SYNTHESIS AND FABRICATION OF MOLECULES FOR MOLECULAR ELECTRONIC DEVICES AND SENSORS

By

KAVITA GARG

(CHEM01200804029)

Homi Bhabha National Institute, Mumbai

A thesis submitted to the

Board of Studies in Chemical Sciences

In partial fulfillment of requirements

For the Degree of

DOCTOR OF PHILOSOPHY

Of

HOMI BHABHA NATIONAL INSTITUTE

JULY, 2013

Homi Bhabha National Institute

Recommendations of the Viva Voce Board

As members of the Viva Voce Board, we certify that we have read the dissertation prepared by **Kavita Garg** entitled "**Synthesis and fabrication of molecules for molecular electronic devices and sensors"** and recommend that it may be accepted as fulfilling the dissertation requirement for the Degree of Doctor of Philosophy.

Chairman-*Prof. S. Chattopadhyay* Date:

Guide/Convener-*Prof. S. K. Nayak* Date:

Guide/Convener -*Prof. D. K. Aswal* Date:

External examiner- *Prof. Amitava Patra* Date:

Member 1- *Prof. A. K. Tripathi* Date:

Member 2- *Prof. S. Banerjee* Date:

Final approval and acceptance of this dissertation is contingent upon the candidate's submission of the final copies of the dissertation to HBNI.

We hereby certify that we have read this dissertation prepared under our direction and recommend that it may be accepted as fulfilling the dissertation requirement.

Guides: Dr. S. K. Nayak **Dr. D. K. Aswal**

Date: **27**th July 2013

Place: Bhabha Atomic Research Centre, Mumbai, India

STATEMENT BY AUTHOR

This dissertation has been submitted in partial fulfillment of requirements for an advanced degree at Homi Bhabha National Institute (HBNI) and is deposited in the Library to be made available to borrowers under rules of the HBNI.

Brief quotations from this dissertation are allowable without special permission, provided that accurate acknowledgement of source is made. Requests for permission for extended quotation from or reproduction of this manuscript in whole or in part may be granted by the Competent Authority of HBNI when in his or her judgment the proposed use of the material is in the interests of scholarship. In all other instances, however, permission must be obtained from the author.

Kavita

Kavita Garg

DECLARATION

I, hereby declare that the investigation presented in the thesis has been carried out by me. The work is original and has not been submitted earlier as a whole or in part for a degree/ diploma at this or any other Institution / University.

Kavita

Kavita Garg

Dedicated to……

………My Parents

ACKNOWLEGEMENT

I would like to express my gratitude to my Guide **Dr. S.K. Nayak** for his advice and support. His superior personality and great passion to work has exceptionally inspired and enriched my growth as a graduate student and a researcher. I would also like to thank **Dr. D. K. Aswal,** co-guide for his guidance in understanding concepts of electronics.

I would like to express my deepest gratitude to head, Bio-Organic Division, **Dr. S. Chattopadhyay** for his inspiration, broad knowledge, invaluable support, continuous encouragement and guidance throughout this project. His faith in me as good student has made this project possible. I would like to thank all my committee members **Dr. A.K. Tripathi** and **Dr. S. Banerjee** for reviewing my project and suggestions.

I am very thankful to **Dr. Ajay Singh** and **Dr. S. P. Koiry** Technical Physics Division for his help in learning experimental set ups of electronics and **Dr. C. Majumdar**, Chemistry Division, BARC, for helping me to understand and carry out theoretical calculation. I am also thankful to all my lab mates especially **Mrunesh Koli** for his help and valuable discussions. I especially thank **Dr. Anubha Sharma** for her friendship, moral support and encouragement during my research work.

Last but not the least I would like to express my deepest tribute to my mom, dad and sisters for their motivation and to be with me in every shade of life. I would like to thank all my friends especially **Nishant, Shilpi Jain** and **Aarti Jain** for supporting me in every phase of my PhD.

Kavita

Kavita Garg

CONTENTS

Synopsis

Silicon industry has undergone a revolution in miniaturization of computational devices with increased speed and memory in the last few decades. However, the difficulty in uniform doping of Si, high power dissipation and economic constraints limit the scaling down of the Si technology to ~20 nm. For example, the power dissipation of a chip having 10^{13} transistors/cm^2 is estimated to be an unacceptably high 100 MW/cm^2. Attachment of small organic molecules to Si would provide organic-inorganic hybrids that are expected to be useful in designing affordable molecular electronic devices. Such a concept is essentially based on using the tunable electronic properties of the organic molecules to control that of the semi-conducting Si atoms. To this end, construction of self-assembled monolayers (SAMs) on the Si-surface is advantageous as the systems can be fabricated easily and their electronic properties can be modulated using the conformational flexibility of the SAMs. Further, proper choice of the organic molecules for selective recognition and binding of analytes would facilitate in constructing chemo-sensors. Using this approach, several prototype devices such as conducting wires, insulating linkages, rectifiers, switches, and transistors have been demonstrated.[1] Extensive theoretical research is also being carried out to develop molecules and molecular assemblies that can offer non-equilibrium electron transport through molecules.

Against this backdrop, the present research work was aimed at designing and constructing molecular hybrids as molecular electronics and gas sensing devices. To this end, all the electronic devices were fabricated on the Si chips, due to the versatility of the semi-conductor over the metals. But, the gas sensing devices were developed employing the operationally simple spin-coating technique of the organic molecules on glass surfaces. The content of the thesis is presented in five chapters, which are briefly summarized in the following.

Chapter 1: Introduction

This chapter deals with the need of molecular electronics according to Moore's law, the practical utility of these devices as well as the challenges in their design.[2] The major emphasis is given on Si-based hybrid nanoelectronics especially with regard to different methods of making monolayers/ multilayers and electrical contacts. A review on the electronic functionalities of the organic molecules, required for the fabrication of such as devices is presented and illustrated citing literature reports on some selected types of molecules. This is followed by a review of the proposed theoretical models in the design of structural and geometrical aspects of the hybrid electronics materials. Finally, the designing of chemo-resistive organic gas sensors is rationalized.

Chapter 2: Methodologies

In the present work, three classes of electron rich organic molecules *viz*. porphyrins, pyrenes and perylenes were electro-grafted on Si substrates to fabricate different electronic devices. Further a bis-porphyrin and its metallated derivative was used as chemo-sensors for two toxic gases, Cl_2 and NH_3. Hence, the synthesis and characterization of all the molecules used in the work is described in details in this chapter.

Various spectroscopic techniques *viz*. Fourier-transform infrared (FTIR), UV-Vis, ^{1}H and ^{13}C NMR spectroscopy, and matrix assisted laser direct ionisation time of flight (MALDI-TOF) were used to elucidate the chemical structures of these molecules. Their purities were confirmed by elemental analyses, and liquid chromatography-mass spectrometry (LC-MS). This is followed by description of the methodology adopted for grafting these organic molecules on the surface of Si wafers. The chemistry of the process is also discussed.

Complete characterization of the organic-Si hybrids is both essential and an extremely challenging task. This is because formation of mono- *vs* multi-layers of the organic molecules can alter the electronics properties of the system. Hence a number of techniques such as FTIR spectroscopy, contact angle measurement**,** ellipsometry, atomic force microscopy (AFM), X-ray photoelectron spectroscopy (XPS), X-ray refraction (XRR), X-ray diffraction (XRD), secondary ion mass spectrometry (SIMS) etc. have been used for this purpose. The procedural details of all these techniques are presented. The experimental related to the fabrication of devices and measurement of the current-voltage (*I*-*V*) characteristics of the devices is also provided. Subsequently, the basis of the theoretical calculations, used to rationalize the observed *I*-*V* properties of the respective devices are provided in this chapter.

Chapter 3: Porphyrin-based Electronic Devices

Large, stable aromatic systems are attractive in molecular electronics because they have HOMO-LUMO energy gaps in a realistic operational range, tend to be stable, and their redox chemistry is reversible under appropriate conditions. The porphyrins possessing 11 π-bonds are particularly important as they have rich electrochemical and photophysical properties amenable to molecular electronics applications. Hence, they are extensively used in fabricating molecular devices.[3-5] According to theoretical calculations, when a single molecule with donor-spacer-acceptor (D-s-A) structure is placed between two electrodes, electrons can flow to the acceptor, and the donor electrons are transferred to the anode. Hence, the system would function as a diode.[3] On the other hand, the $\sigma-\pi-\sigma$ molecular architecture is analogous to the tunnel diode, with a ‘quantum well’ surrounded by thin layer barriers.[6] Thus, the $\sigma-\pi-\sigma$ monolayers, grafted on Si might show negative differential resistance (NDR) effect.[7]

Presently, two new *p*-dialkoxytetraalkylporphyrins **5a** and **5b** with tetraphenylporphyrin (TPP) and a fluoro-derivative of TPP as the respective π moieties and a C_6-alkyl chain and a C_{11}-alkenyl chain as the σ moieties were synthesized, following Lindsey's method.[8] Thus, condensation of pyrrole with the *p*-alkoxyaldehydes **1a/b** furnished the respective dipyrromethanes **2a/b**. Compound **2a** was converted to compounds **4a/b** by coupling with aromatic acid chlorides **3a/b**. Reduction of the keto-group in **4a/b** followed by acid-catalyzed condensation of the resultant diols with **2b** and DDQ oxidation afforded the target porphyrins **5a**/**b** (**Scheme 1.**). The alkenyl chain of these molecules was easily electrografted on Si surface to form the respective hybrid monolayer assemblies. The hybrid systems were subsequently used to construct the devices.

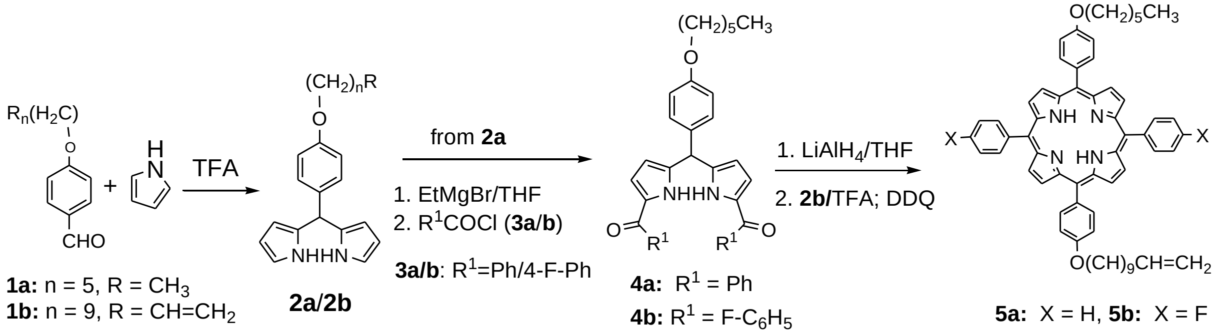

Scheme 1. Synthesis of the unsymmetrical (A_2BC) porphyrins

The AFM, and FTIR analyses revealed that the monolayers of porphyrin **5b** (surface coverage 3.4×10^{12} molecules /cm^2) were more compact than that with **5a** (surface coverage 4.3×10^{11} molecules /cm^2), possibly because of strong van der Waal interactions between F and H of the phenyl rings in the former. Compared to the contact angle (84^o) of deionized water on Si wafers, those with monolayers of **5a** and **5b** were 58^o and ~ 64^o respectively, suggesting tilted arrangements of the porphyrins on the Si surface. The average thicknesses of the monolayers of

5a (2.3 ± 0.2 nm)and **5b** (~ 2.9 ± 0.2 nm), revealed by ellipsometry was also consistent with tilted geometry of the monolayers. The hybrid monolayer assemblies, prepared from **5a** and **5b** showed reversible NDR behavior at room temperature with peak to valley ratios (PVRs) of 10 and 100, and peak positions (voltage) at 1.18 V and 1.09 V respectively. The NDR behaviors were stable during repetitive voltage scan for 8 h in positive and negative bias voltages, without any reduction in current or the effect. However, the reversible NDR effect showed a marginal hysteresis. A schematic diagram of the device and the *I-V* characteristics of the device made from **5a** and **5b** are shown in **Fig. 1a-c** respectively.

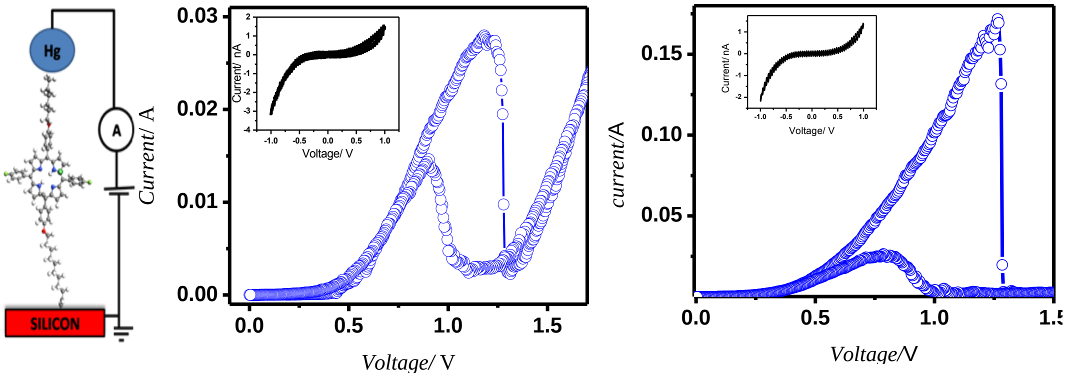

(a) (b) (c)

Fig. 1. (a) *I-V* measurement set up; **(b & c)** *I-V* curves of **5a** and **5b**

The theoretical *I-V* curves of the molecules, calculated using the first-principle non-equilibrium Green's function (NEGF) matched very well with the experimental results. The higher PVR value with **5b** could be explained in terms of the integral of the transmission peak with the molecule. The HOMO-LUMO values of **5a** and **5b** and their respective +1 oxidation states, using ab initio calculation (GAMESS software), and their comparison with the Fermi level of Hg also explained the observed NDR behaviour of the devices.

In order to build up the (D-s-A) structure (**Scheme 2.**), Cu(II)-TPP (**6**) was synthesized by acid-catalyzed coupling between benzaldehyde and pyrrole followed by reaction of the resultant TPP with $Cu(OAc)_2$. A Vilsmeier–Haack formylation of **6** gave compound **7**, which on condensation with the aniline derivatives **8a/8b** and subsequent reduction with $NaBH_3CN$ furnished the amines **9a/9b** respectively.[9] The required anilines were synthesized by *O*-alkenylation of 4-nitrophenol with suitable bromoalkenes and *in situ* reduction with Zn/HCO_2NH_4. The molecules contained the required donor (porphyrin)— spacer (CH_2-NH)— acceptor (phenol derivative) while the C-6/C-11 alkyl appendage was used as the linker for their electrografting on H-terminated Si surfaces to provide the hybrid materials.

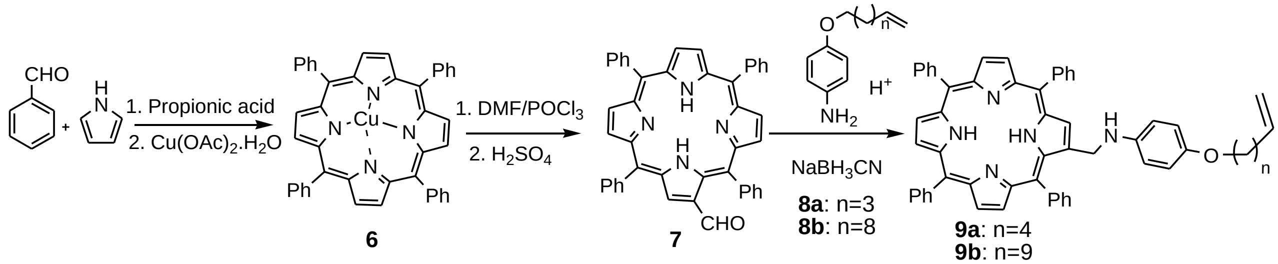

Scheme-2. Synthesis β-pyrrole-substituted porphyrins

The monolayers of **9b** on Si were more compact than that of **9a** with surface coverage of 4.5×10^{14} and 1.11×10^{12} molecules/cm^2 respectively, and less tilted as revealed from thickness 2.5 nm and 3 nm respectively. Both the devices showed stable current rectification during repetitive voltage scanning for 100 scans. The device with **9b** showed much better current rectification (10^7) compared to that (rectification ~100) with molecule **9a**. Possibly a higher linker length with the former (C-11 chain) *vis-à-vis* that of **9a** (C-6 chain) allowed its more compact packing. The experimental results were further verified by theoretical non-equilibrium electron transport calculations (Virtual Nano Lab. Software) for the device using a model Au/molecule/Au systems, which showed similar rectification in the negative bias.

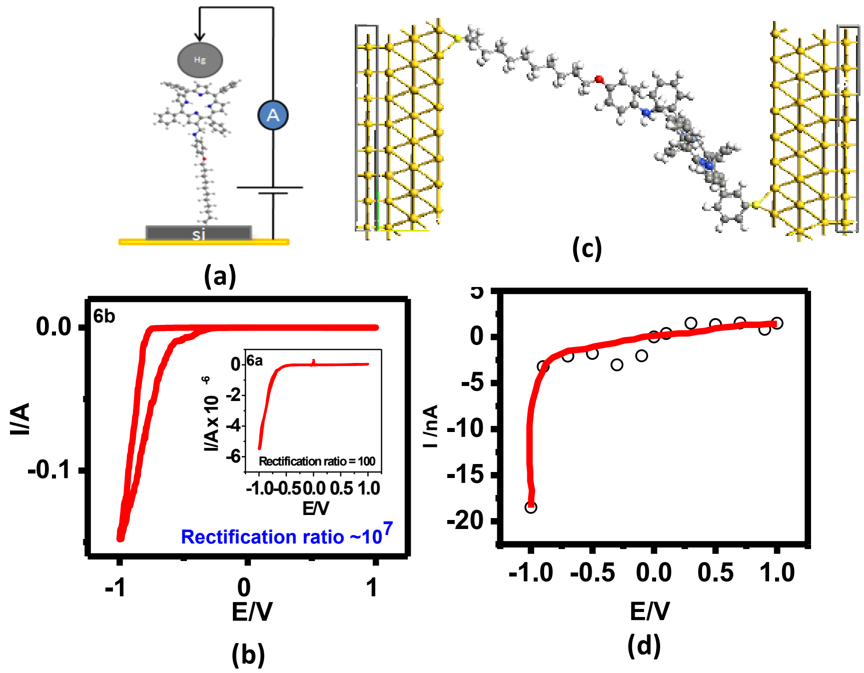

Fig. 2. *I-V* measurement set ups: (a) experimental and (c) theoretical; (b) *I-V* curves of **6b**experimental [inset: *I-V* of **6a**] and (d) theoretical

Chapter 3: Polyaromatic Hydrocarbons (PAHs)-based Molecular Rectifiers

Like porphyrins, other electron-rich PAH molecules such as pyrenes and perylenes are also suitable for organic electronic devices because of their low band gaps, and comparable energy levels as that of contact electrodes. In view of this, two molecular rectifiers were synthesized by grafting some pyrene and perylene molecules on H-terminated Si surfaces, which is described in this chapter.

For this, the pyrene derivatives **12a/b** was synthesized by a base-catalyzed *O*-alkylation of commercially available 1-pyrenemethanol using suitable bromoalkenes **11a/b** (**Scheme 3.**). For the synthesis of the perylene precursor, commercially available perylene was regio-selectively mono-formylated by the Vilsmeier–Haack reaction to furnish the aldehyde **13**, which on $NaBH_4$ reduction afforded the alcohol **14**.[10] Its base-catalyzed *O*-alkylation with the bromide

11b produced the target perylene derivative **15** (**Scheme 4.**). The molecules **12a/b** and **15** were subsequently electrografted on H-terminated Si surfaces and their current rectification property studied.

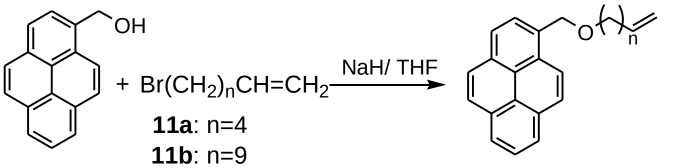

10

12a: n = 9; **12b**: n = 4

Scheme 3. Synthesis of 1-substitutedpyrenes

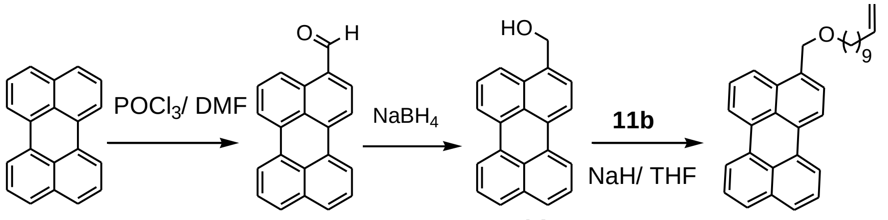

Perylene **13** **14** **15**

Scheme 4. Synthesis of 1-substitutedperylene

Between the pyrenes **12a/b**, the latter with a shorter (C-6) alkyl chain formed more compact monolayers on Si surface than **12a**. This was revealed from the SIMS data where the largest fragment peak the monolayer of **12a** appeared at 215 amu, while the monolayer of **12b** showed the same at 244 amu. Likewise, the tilt angle of the perylene **15**monolayer was more as its largest fragment had two CH_2 groups. The AFM analyses and ellipsometry revealed the thicknesses of the monolayers of **12a/b**, and **15** as ~ 1.8± 0.2 nm, 1.3± 0.2 nm and 2.3 ± 0.2 nm respectively. All the devices showed current rectification in the forward bias. The better compact packing of the pyrene (**12b**)-based monolayers was also reflected in their significantly higher current rectification of (2–5) $\times 10^5$ at 2.0 V compared to that of the **12a**-based monolayers that showed a much less current rectification (~1000) at 1.25 V. The performance of the perylene (**15**)-based device was in between those of the pyrene-based devices with a current rectification ratio 3000-5000 at 1.75 V. However, these devices were stable only up to 5 scans because of instability of these molecules at higher temperature. The results were verified by theoretical calculations using atomic-toolkit and ab-initio calculations.

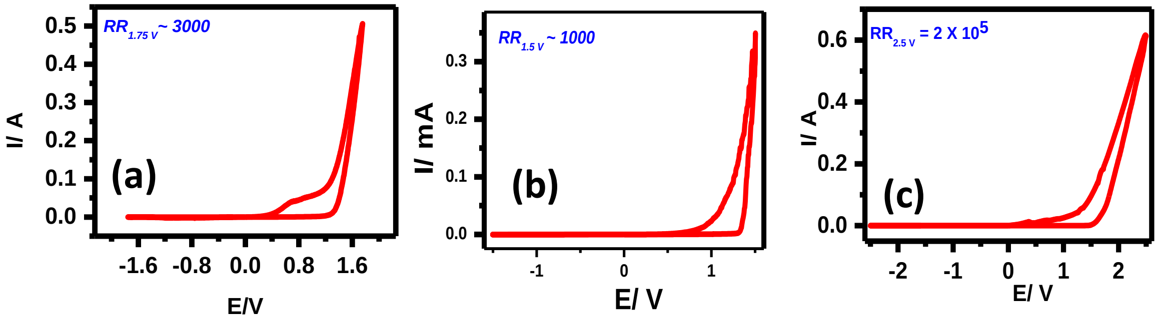

(a) (b) (c)

Fig. 3. *I-V* characteristics: (a) **12a**; (b) **12b**;(c) **15**

Chapter 5: Porphyrins as Gas-sensors

The porphyrins and metallo-porphyrins are highly conjugated p-type organic semiconductors, and can induce charge transfer between various oxidizing or reducing gases and their delocalized π-systems.[11,12] The induced change in the electrical conductance offers the option of developing chemi-resistive gas sensors.[13] Presently, two chemi-resistive sensors for the toxic Cl_2 and NH_3 gases have been developed using a jaw-like bisporphyrin (bis-TPP) molecule and/ or its Zn-derivative as the active layers.

For the synthesis of the bis-TPP molecule, an acid-catalyzed three-component condensation of pyrrole, benzaldehyde and 4-hydroxybenzaldehyde (4:3:1) according to **Rothemund's** method produced (5-(4-hydroxyphenyl)-10,15,20-triphenylporphyrin (**16**). The compound was then esterified with freshly prepared isophthaloyl chloride to get the bis-TPP molecule. This was further reacted with $Zn(OAc)_2$ to get the target Zn-bis-TPP molecule (**Scheme 5.**).

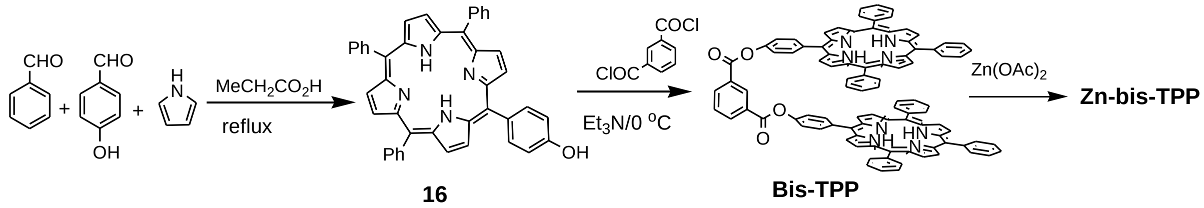

Scheme 5. Synthesis of bis-porphyrin and its Zn-derivative

These molecules were spin coated on glass surfaces to obtain the films that have large number of adsorption sites for the gasses due to their large surface / volume ratio as well as porous structure.[14] The charge mobility in the bis-TPP films was very high (1.8 $cm^2V^{-1}s^{-1}$) compared to that ($1.51x10^{-3}$ $cm^2V^{-1}s^{-1}$) of the Zn-bis-TPP films, which is attributed to the dense packing of the bis-TPP molecules.[15] The bis-TPP films were highly selective to Cl_2 gas at 170^oC and their sensitivity of detection varied linearly between 278 and 1370% in 10-500 ppb range of the analyte. The response time was very low (~ 3 s), while a full recovery to the base conductance took only ~8 min over the above concentration range. The response rate obeyed Elovich equation and a linear correlation has been found between Cl_2 concentration and the response. For the Cl_2 concentrations ≥1000 ppb, the response was irreversible, which was due to chlorination of the bis-TPP molecules. In contrast, the Zn-bisporphyrin films did not sense Cl_2 gas in the ppb range, but showed better response for NH_3 gas, compared to the bis-TPP films at room temperature. The sensitivity of the Zn-bis TPP films for NH_3 (5-40 ppm) varied between 43 and 1890%, the response time was very low (~ 2 s) and a full recovery to base conductance took only ~150 sec.

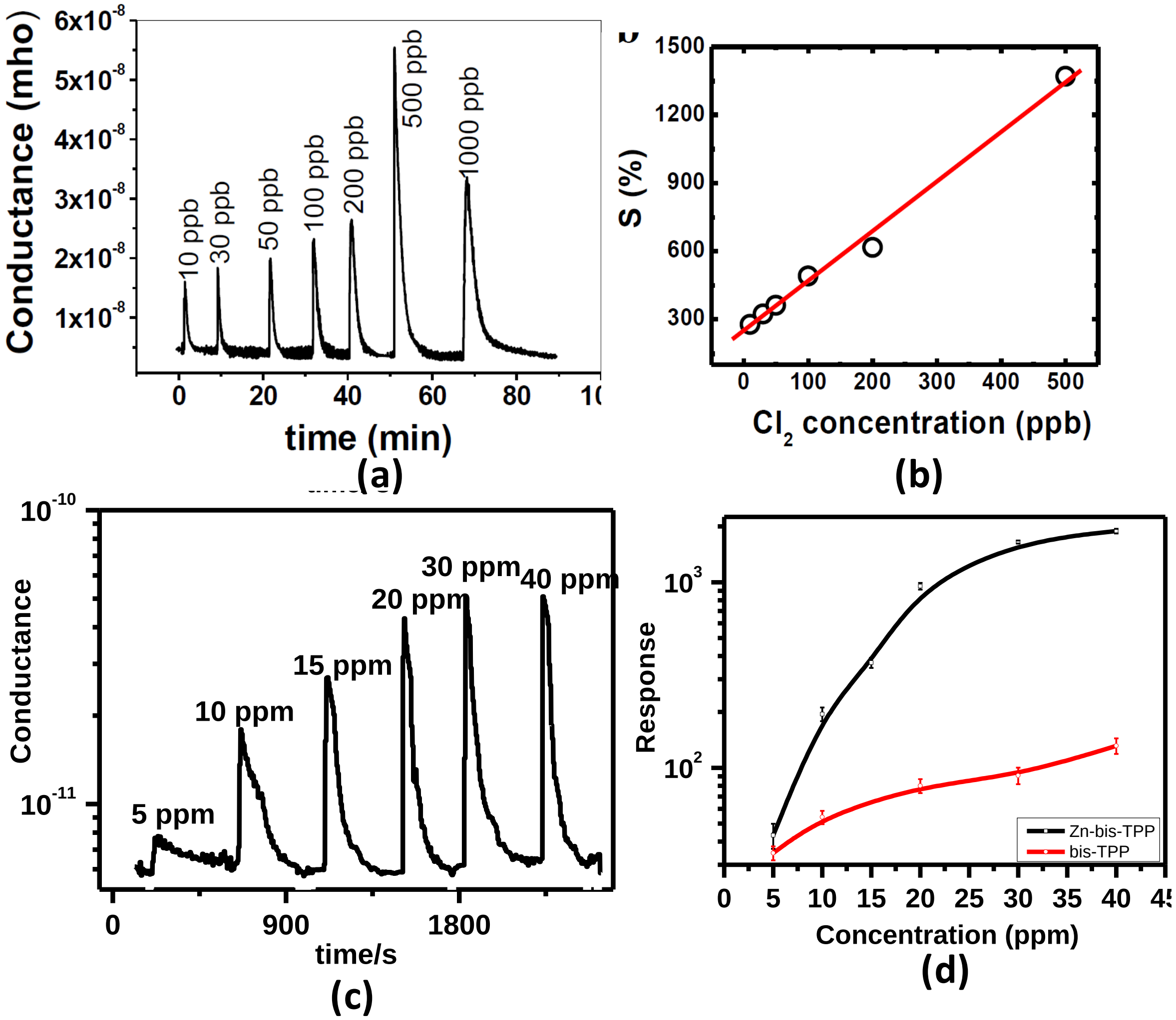

Fig. 4. Conductance and response characteristics of the porphyrin films. (a) Time-dependent conductance changes of (a) bis-TPP with different Cl_2 concentrations, (c) Zn-bis-TPP with different NH_3 concentrations; Response of (b) bis-TPP as a function of Cl_2 concentrations, (d) Zn-bis-TPP/ bis-TPP films as a function of NH_3 concentration.

Finally the results obtained in the present work are briefly summarized, highlighting the major achievements *vis-à-vis* the set objectives in a separate Summary section.

References

1) Aswal, D. K.; Lenfant, S.; Guerin, D.; Yakhmi, J.V.; Vuillaume, D. *Anal. Chim. Acta* **2006**, *568*, 84.

2) Moore, G.E. *Electronics* **1965**,*38*, 1.

3) Aviram, A.; Ratner, M. A. *Chem. Phys. Lett*. **1974**,*29*, 277.

4) Salomon, A.; Cahen, D.; Lindsay, S.; Tomfohr, J.; Engelkes, V. B.; Frisbie, C. D. *Adv. Mater*. **2003**,*15*, 1881.

5) Chen, J.; Reed, M. A.; Rawlett, A. M.; Tour, J. M. *Science***1999**,*286*, 1550.

6) Sze, S. M. *Semiconductor Devices: Physics and Technology*, John Wiley and Sons, New York, 2002.

7) Koiry, S. P.; Aswal, D. K.; Chauhan, A. K.; Saxena, V.; Nayak, S. K.; Gupta, S. K.; Yakhmi, J. V.*Chem. Phys. Lett*. **2008**,*453*, 68.

8) Tamaru, S. I.; Yu, L.; Youngblood, W. J.; Muthukumaran, K.; Taniguchi, M.; Lindsey, J. S. *J. Org. Chem.* **2004**,*69*, 765.

9) Welch, C.; Achibald, S. J.; Boyle, R. W. *Synthesis* **2009**, 551.

10) Skorobogatyi, M. V.; Pchelintseva, A. A.; Petrunina, A. L.; Stepanova, I. A.; Andronova, V. L.; Galegov, G. A.; Malakhov, A. D.; Korshun, V. A. *Tetrahedron***2006**,*62*, 1279.

11) Kang, T. S.; Harrison, B.S.; Foley, T.J.; Knefely, A.S.; Boncella, J.M.; Reynolds, J.R.; Schanze, K.S. *Adv. Mat*. **2003**, *15*, 1093.

12) Savenije, T. J.; Goossens, A. *Phys. Rev. B***2001**, *64*, 115323.

13) Tepore, A.; Serra, A.; Manno, D.; Valli, L.; Micocci, G.; Arnold, D. P. *J. Appl. Phys***1998**,*84*, 1416.

14) Wanga, B.; Zuoc, X.; Wua, Y.; Chena, Z.; Hea, C.; Duana, W. *Sens. Act. B.***2011**,*152*, 191.

15) Nikiforov, M. P. *Nano Lett.* **2008**,*8*, 110.

LIST OF PUBLICATIONS

Published:

- K. Garg, A. Singh, A.K. Debnath, S.K. Nayak, S. Chattopadhyay, D.K. Aswal, Y. Hayakawa, S.K. Gupta, J.V. Yakhmi, *Bis-porphyrin films as ppb level chemiresistive sensors*. Chem. Phys. Lett. **2010**,*488*, 27–31.
- K. Garg, A.Singh, C. Majumder, S. K. Nayak, D. K. Aswal, S. K. Gupta, S. Chattopadhyay. *Room temperature ammonia sensor based on jaw like bis-porphyrin molecules.* Organic electronics**2013,***14, 1021-1224*

Communicated:

- K. Garg, C. Majumder, S. K. Gupta, D. K. Aswal, S. K. Nayak, S. Chattopadhyay Stable Negative Differential Resistance in Porphyrin Based σ–π–σ Monolayers Grafted on Silicon. *J. Org. Chem.*
- K. Garg, C. Majumder, S. K. Gupta, D. K. Aswal, S. K. Nayak, S. Chattopadhyay Modulation of nanoelectronic behaviour porphyrin-silicon hybrid by changing the porphyrin substitution. *Org. Lett.*
- K. Garg, C. Majumder, S. K. Gupta, D. K. Aswal, S. K. Nayak, S. Chattopadhyay Current-rectification behaviours of polyaromatic-monolayered silicon hybrids. *Org. Elec*.

LIST OF CONFERENCE ATTENDED

- K. Garg, S. P. Koiry, S. K. Nayak, D.K. Aswal, S. Chattopadhyay**.** *Negative Differential Resistance behaviour in porphyrin based electrografted* $\sigma\text{–}\pi\text{–}\sigma$ *monolayer.* 10th conference on Material Chemistry at University of Manchester (MC 10), UK.
- K. Garg, S. P. Koiry, S. K. Nayak, D.K. Aswal, S. Chattopadhyay. *Molecular Rectification in Pyrene based Electrografted* $\sigma\text{–}\pi$ *Monolayer.* 2nd International conférence on nanomaterials and nanotechnology (ICANN 2011), IIT Guwahati.
- Attended conference and workshop on Molecular/Organic electronics at Guru Nanak Dev Univeristy, Amritsar.

LIST OF FIGURES

List of schemes

List of tables

Chapter-1

CHAPTER-1

Introduction

1.1. Beyond microelectronics

Silicon industry has undergone a revolution of miniaturization of devices in the past few decades, which lead to increase in the speed and memory of the computational devices.[1,2] Modern computers are classical example of miniaturization- the performance increases several folds in a year without significant change in the price. The process of miniaturization follows Moore's Law, *i.e.*, doubling of bit density in 18 months for memories and 24 months for microprocessors in integrated circuits (ICs).[3] The core component in ICs is the field effect transistor (FET), which consists of a source, a drain and a gate (**Fig. 1.1.**). Miniaturization can be achieved by reducing the distance between source-drain (Channel length, $t_{s\text{-}d}$) and dielectric thickness (t_{di}). Despite being driven by economics, the Moore's law has been successful for last four decades in microelectronics industries. Its extrapolation predicts a channel length <20 nm by 2017. However, several physical as well as economic factors (explained below) would constraint the limit of scaling down.

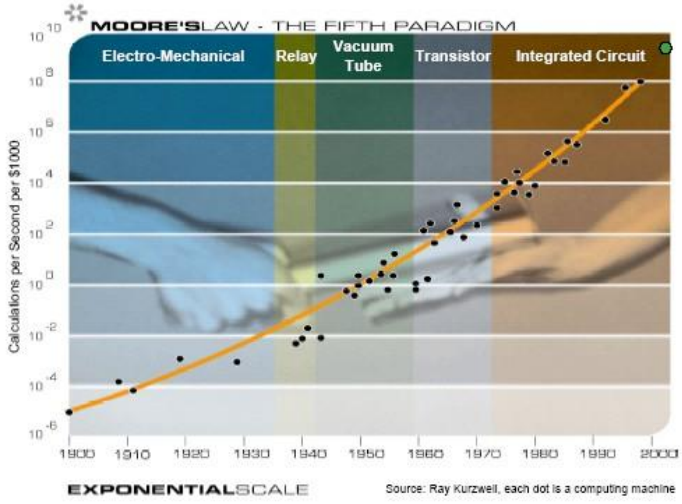

Fig. 1.1. Graphical representation of Moore's law.

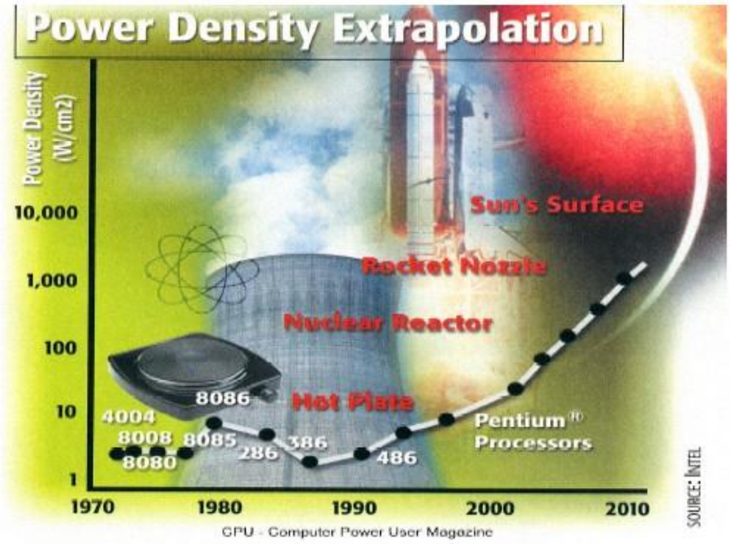

Fig. 1.2. Graphical representation of power dissipation with time.

(i) *Unacceptable power dissipation*: Typical power dissipation for a transistor at a clock frequency of 2 GHz is around 2.5-5 μW. Therefore, a chip with 108 transistor/cm^2 with 2 GHz clock (Pentium IV chip) would have power dissipation of ~50 W/cm^2, assuming 10% of the transistors are switching at a time. The power dissipation for a predicted chip having 10^{13} transistors/cm^2 with clock frequency of 10 GHz (projected for 2017) is estimated to be 100 MW/cm^2 (**Fig. 1.2.**), which exceeds that in a rocket nozzle!. At present, there is no on-chip heat sinking technology in the horizon that can even cope with that. The International Technology Roadmap for Semiconductors has termed this catastrophe as "Red Brick Wall".[4]

(ii) *Electronic structure of the channel*: At the channel width of <20 nm, the band structure of Si is changed. In addition, the uniform doping of Si is very difficult task.[5]

(iii) *Limitation of lithographic techniques*: The existing lithographic techniques used to produce the circuitry on the Si wafers were limited by the wavelengths at which they work, and therefore, creating feature size at nanometre scale is difficult.[5]

(iv) *Economic limitation*: According to Moore's second law, "exponential miniaturization in Si device is achieved by exponential increase in financial investment".[5] Hence, economic factors might also impose severe limitation son the integration process at nanoscale.

1.2. Concept of molecular electronics

Based on the above factors, the problem of scaling limit in Si technology is anticipated in near future.[1] Hence new concepts, radically different from Si technology such as molecular electronics, quantum computing, spin devices, bio-computing, DNA computers, and other theoretically possible information processing mechanisms have emerged. The notion of molecular electronics was envisioned since the first measurement of electron tunnelling through a monolayer of aliphatic chains in 1971,[6] and the prediction by Aviram and Ratner in 1974 that an acceptor-bridge-donor (A-b-D) molecule, where a good organic one-electron donor moiety (D) is linked covalently by a saturated “sigma” bridge to a good organic one-electron acceptor moiety (A) can play the same role as a semiconductor p-n junction.[7] Since then, many groups have reported on the electrical properties of molecular-scale devices from single molecules to monolayers. Molecular electronics, *i.e.*, the information processing at the molecular-scale is envisioned as a promising candidate for the nano-electronics of the future. It is viewed as a technology wherein integrated circuitry (IC) will be constructed from component molecules acting as capacitors, resistors, logic gateways, memory registers, *etc*, joined by molecular wires (such as carbon nanotubes).

> *“Molecular electronics … allows chemical engineering of organic molecules with their physical and electronic properties tailored by synthetic methods”.*[8]

The advantages of such approach electronics are as follows:

i. Size: Molecular electronics has the potential to reduce the IC size dramatically to 0.5 nm - 0.5 μm by tuning the molecular design.

ii. Tunability: Structural modifications of the molecules can alter the electronics properties of the devices as per requirement.

iii. Power: The inefficiency of the modern transistor is because they cannot be stacked into 3D volumes to avoid melting of silicon. Power per calculation will dominate clock speed as the metric of merit for the future of computation.

iv. Manufacturing cost: Many of the molecular electronics designs use simple spin coating or molecular self-assembly of organic compounds. The process complexity is embodied in the synthesized molecular structures, and so they can literally be splashed on to a prepared Si wafer.

v. Low temperature manufacturing: Learning from biological system, it may be possible to fabricate the device at room temperature using cheap plastic substrates instead of expensive Si ingots.

vi. Elegance: Besides these, some of the molecular electronics approaches offer elegant solutions to non-volatile and inherently digital storage. The CMOS silicon often leads to inherently analog and leaky medium that at best approximates a digital and non-volatile abstraction in the design methodology.

Despite these advantages, and availability of the experimental abilities and theoretical ideas in early seventies, work on molecular electronics was not taken up seriously because the limitations on Si-based microelectronics were not felt strongly at that time. Simple molecular electronic test devices usually consist of organic molecules sandwiched between two conducting electrodes. To measure the electronic transport through an organic monolayer, we need a test device as simple as possible. The generic device is a metal/monolayer/metal or metal/molecules/metal (MmM) junction, M can be replaced by a semiconductor. Organic monolayers and sub-monolayers (even single molecules) are usually deposited on the electrodes by chemical reactions in solution or in gas phase using molecules of interest bearing a functional moiety at the ends, which is chemically reactive to the considered solid surface. However, Langmuir-Blodgett (LB) monolayers have also been used for device applications early in the 70s.[9] Thus, the major tasks of constructing molecular devices are (i) making electrical contacts, and (ii) identification of suitable molecules for the designated jobs. However, building electronics solely using molecules appears to be a distant dream at present. Transforming discrete molecular devices into practical circuits, i.e. making billions of molecular devices electrically accessible is a tough task. Thus, a medium term solution, say for next 10–15 years, is to make molecules compatible to Si, so that the nanoscale electronic functionality of molecules can be utilized in Si-based microelectronics. Thus, it is also imperative to design of hybrid devices to enrich the area "hybrid nanoelectronics".[5,10,11]

1.3. Making electrical contacts to the molecules

Making reliable and reproducible contacts between the electrodes and the molecules is a prerequisite for measuring electrical transport through molecules or monolayers deposited on substrates (e.g. Si, Au etc.).Some of the prominent methods developed for this challenging job are schematically shown in **Fig. 1.3.**, and briefly discussed below.

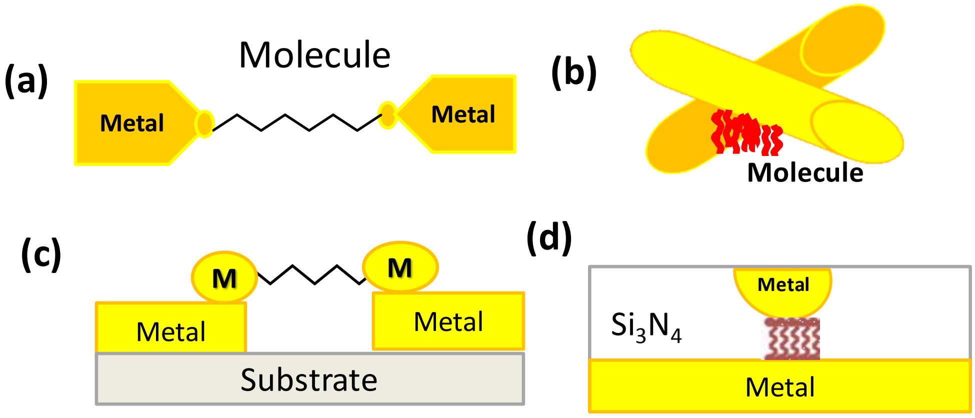

Fig. 1.3. Different methods for attaching molecules to the electrodes:

(a) Break-junction; (b) Cross-wire, (c) Metal-nanoparticles, and (d) Nanopore

1.3.1. Break-junction method

A break junction is an electronic device, which consists of two metal wires separated by a very thin gap of the order of the inter-atomic spacing (~Å). This can be done by physically pulling the wires apart or chemical etching or electromigration.[12] As the wire breaks, the separation between the electrodes can be indirectly controlled by monitoring the electrical resistance of the junction. After the gap formation, its width can often be controlled by bending the substrate upto a precision of picometers.[13]

1.3.2. Cross-wires method

In this, a junction is formed between two thin wires, one passing over the other, and oriented at right angles to it. The distance between the wires is controlled quite accurately down to sub-Å units by a magnetic device. Typically, gold wires of 10μm in diameter are used. One of the wires is covered by a monolayer of the molecule of interest. The wires are brought together until a current is detected. This method, devised by Kushmerick[14] *et al.* is used to study several different types of molecules.[15] The number of molecules forming the bridge between the two wires is unknown (generally <10), but the results are integer multiples of a "lowest curve" which is the current in a *single* molecular bridge.

1.3.3. Metal-nanoparticles method

This technique is similar to the cross-wires method, but metal nanoparticles are used to circumvent the need of fabricating extremely narrow (<1 nm) gaps required for molecules to bridge a gap between two electrodes.[16] The metal nanoparticles on which a monolayer has been deposited are trapped between two closely spaced metal contacts using an alternating electric field (**Fig. 1.3. (c)**).

1.3.4. Nanopore method

In this method, molecules are sandwiched between two metal layers through a small orifice or nano-pore.[17-18] A low stress and low conductivity Si_3N_4 film is grown on a Si wafer. Certain areas of the wafer are then etched away so as to leave free standing Si_3N_4 films. A pore of sub-50 nm diameter is etched through these films, followed by evaporation of Au at the bottom of the wafer. A SAM is assembled from the other side of the membrane on the Au surface, exposed by the pore. Finally, a top metal contact is evaporated onto the monolayer at a reduced temperature.

1.3.5. Planar sandwich geometry

In the planar sandwich geometry, metal counter electrodes are directly fabricated on monolayers, deposited on the conducting substrates, Au or highly doped Si.[19] The ordered monolayers can be formed on Au substrates by using self-assembly of thiol terminated molecules,[20,21] and on Si substrates by self-assembly, thermal evaporation, chemical methods or electrochemical grafting.[5,22,23] It is possible to deposit ~10^{15} molecules/cm^2, and conveniently fabricate two- and/ or three-terminal molecular devices by choosing appropriate electrode configurations by this technique. After forming monolayer, the metal CEs are fabricated without any damage or short-circuit through the monolayer. The types of counter electrodes and their fabrication processes are briefly described below.

(a) Liquid metal or eutectic as contact:[24,25] Hg and In-Ga eutectic can act as soft CEs as these are conducting liquids (**Fig. 1.4.(a)**).Use of liquid metal does not damage the monolayer and helps to improve our understanding of the interfaces and molecular properties. However, they are unsuitable for practical fabrication in the electronics industry.[26]

(b) Conductive probe AFM (CP-AFM) and scanning tunnelling microscope (STM) methods:[27,28] In these methods, a conducting-AFM tip or STM tip is placed in proximity with a monolayer, previously assembled on a conductive substrate. The conducting tip is used as a CE as shown in **Fig. 1.4.(b)**.

(c)Vacuum deposition: Photolithography and electron beam lithography processes can be used for making metal contacts with well-defined structures. The conventional deposition methods such as thermal evaporation, electron-beam evaporation or sputtering can be used for the deposition of metal CEs.[29] However, the required impingement of high energetic metal

flux can damage the monolayer by altering their structures significantly, and/or metal atoms can diffuse through the monolayer causing short-circuits. Two methods can be used to avoid the metal diffusion: (i) Cooling the samples up to liquid N_2 temperature during evaporation,[30] or (ii) Choosing an appropriate surface group of the monolayer, which forms chemical bonds with the metals *e.g.*, CO_2H or OH groups for Al; CO_2, CH_3, OH or CN groups for Ti, the SH group for Au etc.[31,32] Usually Au thickness in the range 20-80 nm thicknesses is suitable as a CE on SH–terminated monolayer. However, this approach produces devices with blurred edges. In order to produce devices with fine features, one can employ the photolithography for micro size features and electron beam lithography for sub-micron size features.

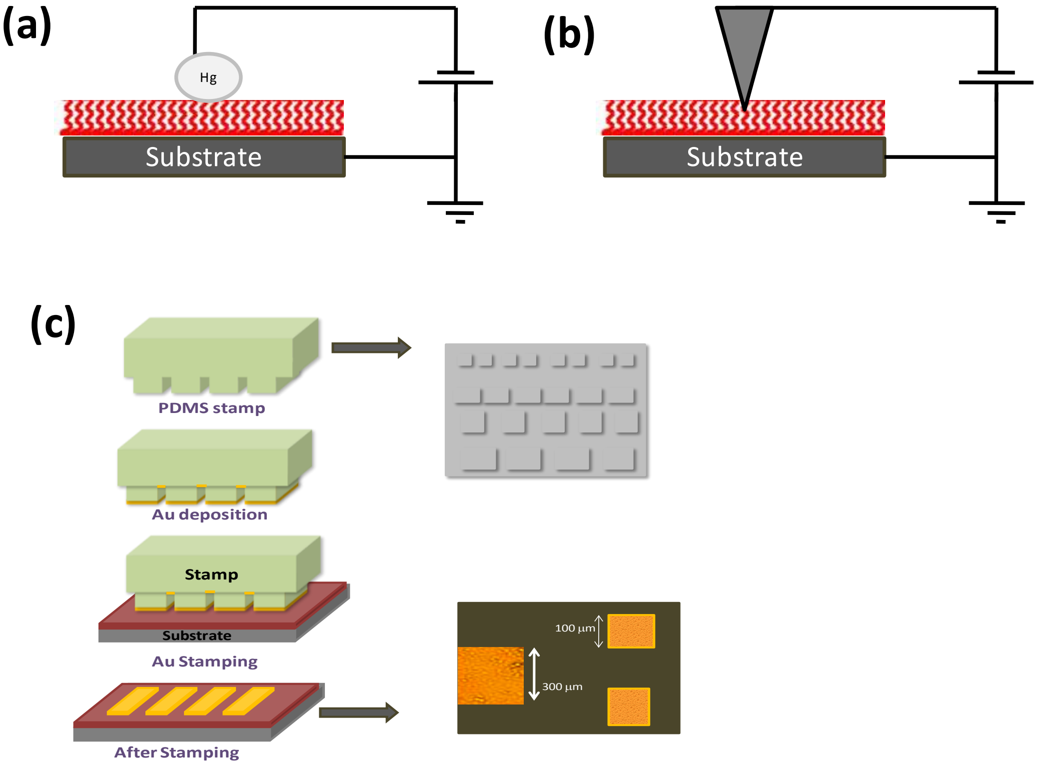

Fig. 1.4. Different methods used for making counterelectrodes on monolayers deposited on conducting substrates:(a) Hg-drop method, (b) conducting AFM or STM tipmethod, and (c) soft lithography.

(d) Soft lithography: "Soft lithography" is a new high resolution patterning technique developed by Whitesides.[29,33] This technique can be used for patterning of SAM on different substrates, pattering of CEs on SAM, etc. Patterning of metal electrodes on the SAM using

soft lithography is known as nano-transfer printing (nTP). It is done by using stamping technique in which a stamp of desired pattern is made from polydimethylsiloxane (PDMS) and followed by etching by perfluorination to make it less adhesive to Au. Then Au was deposited on stamp by thermal evaporation or e-beam evaporation carefully avoiding any crack or buckle in the stamp. Stamping of the monolayer is usually done at room temperature for few tens of seconds. After removal of the stamp, Au patterns are formed on SAM. For this, high density of bonding sites should be present at the monolayer surface that can provide defects free Au contacts.

1.4. Design of molecules for molecular electronics.

Molecules or collections of molecules functioning as electronic components have ample precedents in nature. Voltage, ligand, antibiotic, and other ion conducting channels are digital electronics, self-assembled into biological membranes. They have only 'on' or 'off' positions with unit conductance that is unique to a given channel.[34] Success of molecular electronics devices is decided by the suitable choice of the molecules that has been the subject of muchattention.[35] Current approaches are based on the development of molecular-scale switches, which can be used in both logic and memory circuits. Because the basic paradigm for electronic information storage is retention of charge in a capacitor, the most straightforward approach to molecular scale memory would store charge at the molecular level.

Hence, a molecular approach to information storage employs redox-active molecules tethered to an electro-active surface. Attachment of the molecules to electroactive surfaces requires control over the nature of the tether (linker and surface attachment group). In general classic Columbic charging, the relative spacing of the highest occupied molecular orbital (HOMO) and lowest unoccupied molecular orbital (LUMO), the spin, and the vibrational modes will determine single electron currents through molecules connected to electrodes with tunnelling barriers.[36] Thus, the reversibility of accessible redox states of molecules is important, *e.g.*, in single molecule transistors. The molecular electronic properties are also dependent on the matrix surrounding the molecule and the domain size (number of copies of a molecule in a discrete domain).

Organic molecules made mainly by covalent σ (linear overlap) or π (lateral overlap) bonds. In σ bonds electrons lie between two nuclei and are highly localized, whereas electron density in π bonds is delocalized. According to molecular orbital (MO) theory, linear combination of two atomic orbitals results in one bonding and one anti-bonding orbital, which are filled up by electrons following Pauli's exclusion principle. The energy difference between highest occupied MO (HOMO) and lowest unoccupied MO (LUMO) is related to the band gap of the molecule. The HOMO-LUMO gap for σ bonds is ~eight eV, whereas for the conjugated molecules this gap is in the range of 2-5 eV. Therefore, under an applied electric field, σ-bonded molecules are expected to exhibit no charge transport, and hence may act as dielectrics in nanoelectronics. On the other hand, presence of extended electronic wave function in conjugated (π bonded) molecules would be suitable as semiconducting channels in devices.

It has been recognized that a monolayer of alkyl chains sandwiched between two metal electrodes acts as a tunnelling barrier. Here, the current through the monolayers of alkyl chains follows the usual distance-dependant exponential law, $I=I_oe^{-\pi d}$, where d is the monolayer thickness and π is the distance decay rate. Contrary to this, short oligomers of π-conjugated molecules are considered as the prototype of molecular semiconducting wires. At low bias, when the LUMO and HOMO of the molecules are not in resonance within the Fermi energy window opened between the two electrodes by the applied bias, the conduction is still dominated by tunnelling. However, the decay factor π is lower than in the case of alkyl chains, due to the lower HOMO-LUMO gap of the π-conjugated molecules compared to the alkyl chains, and therefore to a lower energy barrier for charge injections.

Thus, molecules with low HOMO-LUMO gap and with HOMO or LUMO levels close to Fermi levels of the electrodes are suitable for molecular electronics. There are many such systems known with these properties like porphyrins, phthalocyanins, polynuclear aromatic hydrocarbons, carbon nanotubes etc. Following is a brief account of the porphyrins and polynuclear aromatic hydrocarbons (PAHs) that were used for constructing various electronic devices and chemo-sensors.

1.4.1. Porphyrins

Porphyrins and their derivatives are prime candidates for a host of molecular electronics applications. As a class of molecule, they possess distinctive, reversible oxidation and reduction chemistry that potentiates use as wires, switches, transistors, junctions, and photodiodes. The porphyrin macrocycle (**Fig. 1.5.**) consists of four pyrrole rings joined by four interpyrrolic methine bridges to give a highly conjugated macrocycle. The aromaticity of porphyrins has been well established both by its chemical and physical properties. These tetrapyrrolic systems have a closed loop of edgewise overlapping orbitals which interact favourably to stabilize the olefins; the 22 π electrons available in porphyrins make up six different 18 e^- delocalization pathways, which follow Huckel's 4n+2 rule for aromaticity.[37] Positions 5, 10, 15 and 20 are usually referred as *meso*- positions and positions 2, 3, 7, 8, 12, 13, 17, and 18 are called the *β*-positions. The two central pyrrolenine N atoms are capable of accepting the protons to form dications, while the NH groups can lose protons to form dianions. The porphyrin dianions can complex with

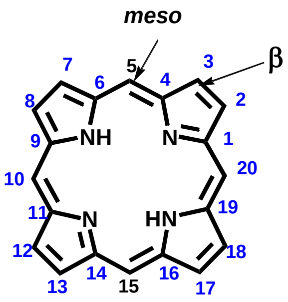

Fig. 1.5. Structure of porphyrin

almost all the metal and semi-metal ions to form metallo-porphyrins of various geometries like in-plane, out-of-plane or bimetallic complexes.[38,39]

Porphyrins and their derivatives are highly coloured with strong (ε ~105 $mol^{-1}L$) absorption in the visible region (~ 400 nm), characteristic of the macrocyclic conjugation, and several weaker absorption bands (Q bands) between 450-700 nm. The main intense absorption band is known as the *Soret* band,[40] named after the biochemist who first observed it in hemoglobin. A disrupted porphyrin macrocycle results in the disappearance of the *Soret* band.[41] A variation in the peripheral substituents of the porphyrin ring normally results in a slight change in the intensity and wavelength of the absorption bands. Each tetra-pyrrolic system can be unique, and therefore, different in colour. Porphyrins that occur naturally are dark red while chlorins, which have reduced tetra-pyrrolic systems are dark green or blue green. Porphyrins are important candidates for molecular devices because

(I) They form stable π-radicals: Porphyrins are 18 π-electron aromatic systems, and the removal of an electron from the π-cloud, leaving an unpaired electron is a facile process. The π-cation radical so generated could be stable because of extensive delocalization over the porphyrin macrocycle.[42a-d]

(II) They can exhibit multiple oxidation states at low redox potentials, which allow multi bit storage with low power consumption.

(III) They have high charge retention periods (up to minimum) in the absence of applied potential that diminishes power consumption further.

(IV) They can withstand high temperatures up to 400 °C without degradation.

(V) They have low HOMO-LUMO gaps which allow charge transport through molecular orbitals.[42e]

(VI) They can be synthesized conveniently and properties can be tuned based on functionalization at *meso* or β positions, or metallation as per requirement.

(VII) They can form ordered films by π–π stacking.

(VIII) They are non-toxic.

1.4.2. Polynuclear aromatic hydrocarbons (PAHs)

PAHs consist of two or more fused benzene rings without any hetero atoms or substituents and show with unique electronic and optoelectronic properties for application in advanced technologies. Large PAHs terminated by H, alkyl substituents, and functional groups are amenable to facile solution processing. Hence, these are promising candidates in organic devices such as light-emitting diodes (LEDs), field-effect transistors (FETs), and photo-volatic cells.[43,44]

The systematic study of PAHs and their application as materials have spurred scientist for several decades. However, only a few selective synthetic methods have been established so far. Fundamental contributions to the directed synthesis and characterization of polycyclic aromatics were pioneered by R. Scholl, E. Clar, and M. Zander, who achieved the synthesis of numerous aromatic compounds under drastic conditions (heat, use of strong oxidizing agents).[45–50] The synthetic break through was achieved as a result of progress of analytical techniques and made the selective synthesis of various PAHs under mild conditions possible.[51] For the present work, only pyrenes and perylene were chosen.

1.4.2.1. Pyrenes

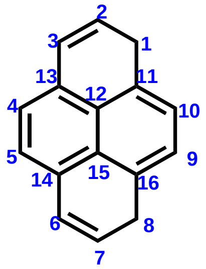

Fig. 1.6. Structure of pyrene

Pyrenes, consisting of four fused benzene rings are the smallest peri-fused PAHs (**Fig. 1.6.**), and are formed during incomplete combustion of organic compounds. These are more resonance-stabilized than fluoanthenes, the five-member ring containing analogues. They have several attributes, making them good candidates for many applications both within and outside the scale of molecular electronics.[52-55] Due to the polarographic half wave oxidation potential at 1.16 V[56] and an ionization potential of 7.41 eV,[57] these molecules are good one-electron donors and is a promising for constructing Aviram and Ratner D-s-A model of rectifiers.[53,52]

However, derivatization of pyrene is very challenging due to many sites of reaction, steric hindrance of crowded protons, poor solubility, and high stability (low reactivity). Electrophilic substitution of pyrene occurs at 1, 3, 6 and 8 positions.[57-61] But the electrophilic substitution reactions (chlorination, nitration, formylation, and Friedal-Craft acylation) take place predominantly at C-1 to afford 1-chloro, 1-nitro, 1-formyl pyrene, and 1-acetylpyrene.So far, most pyrene chemistry has been focused on monosubstituted[62] or symmetrically disubstituted pyrenes.[63] More recently, un-symmetrically substituted compounds such as1-amino-8/6-nitropyrenes have been synthesized.[64] Presently, molecular devices were constructed using 1-alkenylpyrenes.

1.4.2.2. Perylenes

Perylene is a pentacyclic PAH of molecular formula $C_{20}H_{12}$, belonging to the D_{2h} molecular point group (**Fig. 1.7.**). Perylene represent a condensed ring PAHs that contain formal single bonds. Synthesis of perylene from naphthalene[65] led chemist to consider perylene molecule as a combination of two weakly bonded naphthalene nuclei. Structurally, it is distinct from other PAHs due to the number of hydrogen atoms attached to it. It has 22 π electrons, which satisfies the condition of aromaticity of the molecule. However, in 1953, X-Ray determination showed that the length of the bonds, joining the naphthalene nuclei (bond D in **Fig.1.7.**) is 1.50 Å, while all other bonds A, B and C have bond length of 1.38 Å. This indicated that two naphthalenes joined by weak single bonds. It has 32 atoms and is non-

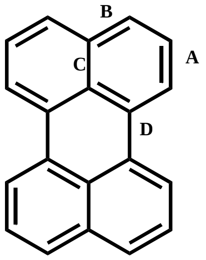

Fig. 1.7. Structure of perylene

planar molecule. Unlike other penta- or hexa-cyclic PAHs that show absorption in the ultra-violet region, perylene absorbs in the visible region ~430 nm.

1.5. Concept of Si-Hybrid-Nano-electronics

Compared to the unimolecular electronics, discussed above, use of hybrid molecular-semiconductor (such as Si) architectures is more of reality. The benefits of these systems over molecular assemblies on metals are due to

(i) Easy handling in view of their crystalline and flat nature.

(ii) Modulation of the electronic properties of Si by changing the dopant (n or p).

(iii) Easy attachment of organic molecules on Si surface through strong Si-O and Si-C (Si-C ~76 kcal mol^{-1}; Si-O ~108 kcal mol^{-1}) covalent bonds.[66]

(iv) Established techniques are available for their preparation and characterization. The inputs available from the existing powerful Si-based IC industry can be used effectively for the development of integrated hybrid devices.

This hybrid approach in a way will not require a complete rethinking of the circuit, as it would be an extension of microelectronics into nanoelectronics, *i.e.* functional molecular components are assembled on a microelectronic frame. The hybrid nanoelectronics, therefore, will be complementary to the traditional electronic devices.

Various molecular devices can be designed taking advantage of σ or π bonds present in the organic molecules. Monolayer deposition of these on highly doped Si (resistivity < 0.001 Ωcm) substrates would provide one electrode required for these devices. The CEs can be formed using liquid Hg drop, thermally evaporated Au/Al pads, CPAFM/STM tip or carbon nanotubes. A variety of devices designed, using this strategy are shown **Fig. 1.8**.

1.5.1 Molecular dielectrics and wires

The two opposite terms, dielectrics and wires describes insulators and conductors

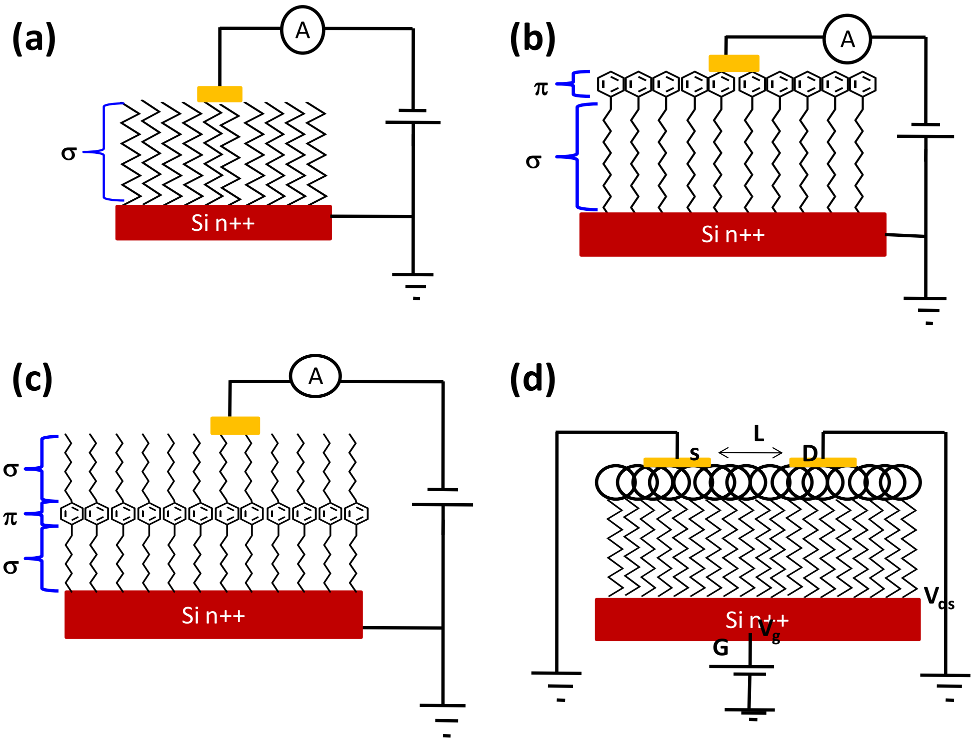

Fig. 1.8. Architectures of Si-hybrid devices: (a) molecular dielectric using alkyl-chains, (b) molecular diodes using σ-π molecules, (c)σ-π-σ resonant tunnel diode, and (d) molecular transistors. The σ components are alkyl-chains of different lengths, and π components are conjugated molecules.

respectively and can be accessed using σ bonds, as in alkyl chains(**Fig. 1.8.(a)**),[6] and π-conjugated molecules, such as, di(phenyleneethynylene) benzenethiolate,[67,68] terthiophene,[68] conjugated oligomers,[69-73] organometallics,[74] porphyrin-oligomers,[75] etc. The semiconductor behaviour of the organic molecules is mainly because of a small HOMO-LUMO gap. The *J*–*V* curves of such molecular wires are generally non-linear with steps (i.e. peaks in the first derivative); corresponding to resonant charge carrier transfer through the MOs of the molecules.[76] The measured conductance corresponds to the conductance through the molecules and the conductance of the molecule/electrode contact. Thus, the influence of the chemical link between the molecules and the electrode is of prime importance.

1.5.2 Molecular diodes

A diode or rectifier is an important component in electronics that allows unidirectional flow of current. As mentioned previously, Molecular diodes were conceived even at the early stage of the molecular electronics by Aviram–Ratner (AR) in their prototype A–b–D molecules. The rectification behaviour of such a molecule, placed between two metal electrodes (MA and MD) arises because of three resonant tunnelling :(HOMO) D→MD, (LUMO) A→ (HOMO) D, and MA→ (LUMO) A, lead to current flow in the forward direction (positive bias to MD). Here, the alignment of the acceptor LUMO and donor HOMO causes resonance tunnelling and hence, a high current flows. In the negative bias, no resonance occurs, and therefore, a very small current flows due to the non-resonant tunnelling.

Based on this concept, several molecular rectifying diodes have been synthesized e.g. hexadecylquinoliniumtricyanoquinodimethanide molecule ($C_{16}H_{33}$-Q-3CNQ) with donor and acceptor moieties linked by a *σ* or π bridge[77] and ω-substituted alkyl-chain, which is essential to allow a LB monolayer formation. These molecular diodes exhibited rectification ratio (RR) [defined by current density at –1 V (in absolute value)/ and current density at +1V] up to

2×10^4. Nevertheless, that may be because of more delocalization of the HOMO handloom as the D and A are separated by π group, and not σ moiety, proposed in the original model. From theoretical calculations, rectification is found to depend on (i) the placement of the HOMO and LUMO levels of the molecule relative to the Fermi levels of the metal electrodes before the bias is applied, and (ii) a shift induced in HOMO/LUMO by the applied bias. Therefore, the electrical rectification can result from the asymmetric profile of the electrostatic potential across the molecule,[78] due to the presence of the alkyl chain. This model has been experimentally verified wherein, simple molecular rectifier with only one donor group and an alkyl spacer chain that is σ-π molecules, grafted on Si (**Fig. 1.8. (b)**) exhibited a RR of ~37.[79]

1.5.3 Molecular memories

A two-terminal device in which the conductance can be reversibly switched between two states with an applied voltage is useful for molecular memory and logicdevices.[80-82] Molecular memories are generally distinguished by three approaches called "conformational memory", "charge-based memory" and resonant tunnelling diode (RTD)-based memory".

I. *Resistive memory:* The resistive memory relies on the idea to store a data bit on two bistable conformers of a molecule, taking advantage of the soft nature of organic molecules. Upon excitation, molecules can undergo conformational changes. If two different conformations are associated with two different conductivity levels of the molecule, this effect can be used to make molecular switches and memories. Such an effect is expected in π-conjugated oligomers used as molecular wires, if one of the monomer is twisted away from, a planar conformation of the molecule.[83] Twisting one monomer breaks the conjugation along the backbone, thus reducing the charge transfer efficiency along the molecule. Electrical bistability has been reported in a number of molecules, such as, rotaxanes,[84,85] catenanes,[86] stearic acid,[87] eicosanoic acid[88] and phenylene–ethynylene oligomers.[89–92]

II. *Capacitive memory*: The capacitive memory works on the principle of charging and discharging of the redox-active molecules into different chemically reduced or oxidized (redox) states.[42c–e,91–93] Molecules, such as metallocenes, porphyrins and triple-decker sandwich coordination compounds, attached on a Si substrate act as charge storage molecular devices.[94-97]

III. *Resonant tunnel diodes (RTD)*: RTD memory utilizes the negative differential resistance (NDR) behaviour of molecules in their current–voltage characteristics due to resonant tunnelling through MOs. The architecture of the molecular RTD device (**Fig. 1.8.(c)**) is analogous to its solid state counter-part:[2] a potential well separated from the electrodes by two tunnel barriers. Here, alkyl-chains can act as tunnel barriers, while a π -moiety acts as the potential well. The advantages of RTD molecular memory compared to ‘resistive’ and ‘capacitive’ molecular memories are fast switching times and possible long-retention times. Only a few σ-π-σ types of molecular RTDs grafted on Si with a small peak-to-valley ratio and low repeatability and reproducibility are reported so far.

1.5.4 Molecular transistors

The concept of molecular transistor (**Fig. 1.8.(d).**) is analogous to the solid-state counterpart of the three-terminal field effect transistors (FETs).[5] The source (S) and drain (D) electrodes, separated by a distance *L*, are deposited on a semiconducting channel made from π moieties. The alkyl chains of length (*t*) act as gate dielectric (G). FETs are based on a gate field modulating the conductance of the semiconducting channel to turn the device “off” and "on." Kagan *et.al.*[98] has investigated the chemical and physical requirements for a successful design and fabrication of molecular FETs. A theoretical analysis using electron tunnelling and device electrostatics place $L > 2.5–3$ nm and minimum gate dielectric thickness $t = L/1.5$for such devices.[98] Till date no molecular-FET has been experimentally demonstrated. However, it has been independently demonstrated that

(i) Alkyl chains work a good dielectric material in FETs made using sexithiophene or pentacene based organic thin film transistors (OTFTs).[99]

(ii) Self-assembled OH functionalized-tetracene monolayer works as an active channel of the transistor.[100] However, in this case a layer of Al_2O_3 (~5 nm) was used to act as both a dielectric layer and a primer for the assembly of the monolayer.

One of the critical requirements for making molecular transistors is availability of π -molecules with exceptionally small (<0.5 eV) HOMO–LUMO gaps, which now have become synthetically achievable targets.[37] Hence, fabrication of a true molecular transistor may not be too far away.

1.6. Scope of thesis

The primary aim of the present investigation was to formulate some organo-Si hybrids as electronic devices. To this end, a few porphyrin, pyrene and perylene derivatives were conceived as the required organic π-systems. The devices were constructed by their covalent attachment to Si (111) wafers, and the electronic behaviour investigated. In addition, given the modern day requirement of chemo-sensors, the change electrical conductance of the organic π-conductors in the presence of redox analytes were used to fabricate chemi-resistive sensors of two toxic gases.

The complete experimental methodologies of syntheses of the target molecules, deposition of their monolayers on Si surface, characterization by various sophisticated instrumental techniques, and device fabrication is presented in Chapter 2. The working principles of the characterization techniques are also provided. In addition, the theoretical techniques, used for understanding mechanisms of charge transport are briefed.

The synthesis and fabrication of two porphyrin-based σ–π–σ systems as resonance tunnelling diodes, and a prototype porphyrin–σ–*p*-hydroxyaniline as an Aviram and Ratnermolecular rectifier, which follows modified model *i.e.* σ-π model is described in Chapter 3. The modulation of tunnelling property by subtle change in the porphyrin motif is also demonstrated, and rationalized by theoretical calculations.

Construction of two pyrene-based and one perylene-based σ–π molecular rectifiers, and their characterization is elaborated in Chapter 4. Comparison of their *J*-*V* behaviour, especially with respect to the chain length of their σ moieties, and electron density is explained theoretically.

Formulation of spin-coated films of two bis-porphyrin molecules and studies on their gas sensing behaviours form the basis of Chapter 5. In particular, the efficiency of bis-porphyrin and its Zn-derivative in detecting Cl_2 and NH_3 gases in air, in terms of detection limit, reversibility, response time and linearity as well as recovery time has been compared. The mechanism of the chemiresistive action of the sensors, and their differential results with respect to the analytes are explained.

Chapter-2

CHAPTER-2

Methodologies

2.1. Synthesis of molecules used in thesis work

General: Reagents and solvents (Sigma-Aldrich or Fluka) of synthetic grade were used after drying and distillation. The IR spectra were recorded with a Jasco model A-202 FT-IR spectrometer and only the pertinent bands are mentioned. The ^{1}H NMR and ^{13}C NMR spectra were scanned with a 200/300/400/600 MHz spectrometer using deuterated solvents as the internal standards and MALDI-TOF/TOF was recorded with Bruker Ultraflex II using cinnamic acid as matrix.

2.1.1. Synthesis of 5-(4-Hexyloxyphenyl),15-(4-undec-10-enyloxyphenyl)-10,20-diphenylporphyrin (Ia) and 5-(4-Hexyloxyphenyl),15-(4-undec-10-enyloxy)-10,20-di-(4-flurophenyl)porphyrin (Ib).

The compounds were prepared according to the following steps (Scheme 2.1).[98-106]

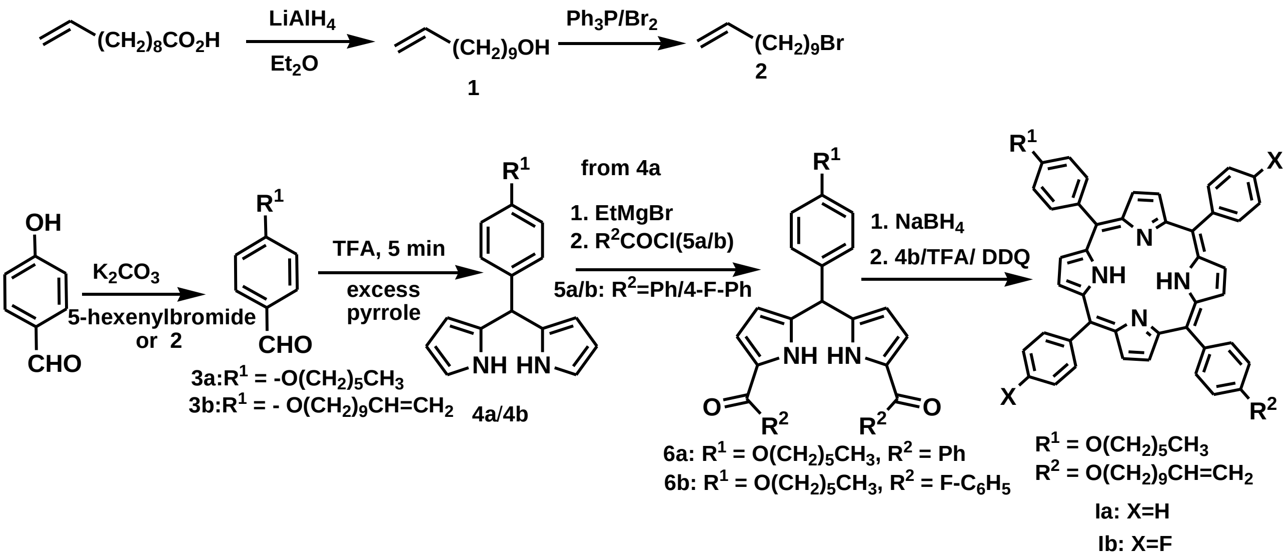

Scheme-2.1. Synthesis of **Ia** and **Ib**

2.1.1.1. Synthesis of 10-undecenol (1)

To a solution of $LiAlH_4$ (3.75 g, 98 mmol) in dry ether (650 ml) was added 10-undecenoic acid (8.28 g, 45 mmol) and refluxed at 40°C for 2 h. The reaction mixture was quenched with ethyl acetate. The solution was filtered and the organic layer was washed with water, brine and dried. After the removal of solvent, the residue was purified by column chromatography (silica gel 0–25% ethyl acetate in hexane) to give pure **1** (7.25 g, 95%). IR: ν_{max} 3340, 3100, 1640, 990, 910 cm^{-1}; ^1H NMR (200 MHz, $CDCl_3$): δ 1.28 (brs, 14H), 1.8–2.1 (m, 2H), 2.48 (s, 1H, D_2O exchangeable), 3.68 (t, J = 7 Hz, 2H), 4.8–6.2 (m, 3H).

2.1.1.2. Synthesis of 1-bromo-10-undecene (2)

To a cooled (0 ^oC) and stirred solution of Ph_3P (13.2 g, 0.055 mol) in CH_2Cl_2 (50 mL) was added bromine (10.0 mL, 0.055 mol, 5.5 M in CCl_4). After stirring for 15 min, the cooling bath was removed and a mixture of **1** (8.5 g, 0.05 mol) and pyridine (5 mL) in CH_2Cl_2 (25 mL) added into the mixture. After stirring for 2 h, the mixture was concentrated, the residue extracted with hexane and the supernatant decanted. The hexane layer was passed through a pad (50 mm) of neutral alumina and concentrated in vacuo to afford pure **2**. (10.0 g, 85%) bp: 100-101 ^oC/5 mm; IR: ν_{max} 3070, 1640, 1460, 990, 910 cm^{-1}; ^1H NMR (200 MHz, $CDCl_3$): δ 1.33 (br. s, 14H), 1.9-2.2 (m, 2H), 3.56 (t, J = 6 Hz, 2H), 4.8-6.3 (m, 3H).

2.1.1.3. Synthesis of 4-(hexyloxy)benzaldehyde (3a) *and 4-(10-undecenyloxy)benzaldehyde* (3b)

A mixture of 4-hydroxybenzaldehyde (4.0 g, 32.7 mmol), 1-bromohexane (39.3 mmol) or 1-bromo-10-undecene (39.3 mmol), K_2CO_3 (5.52 g, 40 mmol) and Bu_4NI (10 mol%) in acetone (100 mL) was refluxed. After completion of the reaction (*cf*. TLC ~ 16 h) the mixture was filtered, concentrated in vacuum, the residue taken in Et_2O (40 mL) and washed with H_2O (2 × 10 mL) and brine (1 × 20 mL), dried and concentrated in vacuo. The residue was purified by column chromatography (silica gel, 5% EtOAc/hexane) to give pure **3a** (6.1 g, 91.2%) and **3b** (8.1 g, 91%).

Compound 3a: Viscous liquid; IR (film): ν_{max} 3019 (s), 2928 (s), 2856 (s), 1687 (s) cm^{-1}; ^{1}H NMR (200 MHz, $CDCl_3$): δ 9.85 (s, 1H), 7.80 (d, *J* = 9.5 Hz, 2H), 6.97 (d, *J* = 9.5 Hz, 2H), 4.01 (t, *J* = 6.2 Hz, 2H), 1.81 (m, 2H), 1.34 (m, 6H), 0.90 (t, *J* = 6.4 Hz, 3H); ^{13}C NMR (50 MHz, $CDCl_3$): δ 190.08, 163.9, 131.5, 129.6, 114.4, 68.1, 31.2, 28.7, 25.3, 22.2, 13.6; MSMS (m/z): 207 (100) $[M+H]^+$ amu; Anal. Calcd. for $C_{13}H_{18}O_2$:C, 75.69; H, 8.80. Found: C, 75.34; H, 9.06%.

Compound 3b: viscous liquid; IR: ν_{max} 3019 (s), 2928, 2856 (s), 1687 (s) cm^{-1}; ^{1}H NMR (200 MHz, $CDCl_3$): δ 9.88 (s, 1H), 7.83 (d, *J* = 8.0 Hz, 2H), 6.99 (d, *J* = 8.0 Hz, 2H), 5.79 (m, 1H), 4.98 (t, *J* = 10.0 Hz, 2H), 4.04 (t, *J* = 6.0 Hz, 2H), 2.05 (m, 2H), 1.82 (m, 2H), 1.38 (m, 12H); ^{13}C NMR (50 MHz, $CDCl_3$): δ 190.6, 164.3, 139.1, 131.9, 129.9, 114.8, 114.1, 68.4, 33.7, 29.4, 29.3, 29.0, 28.9, 25.9; MSMS (m/z): 275.1 (100) $[M+H]^+$ amu; Anal. Calcd. for $C_{18}H_{26}O_2$: C, 78.79; H, 9.55. Found: C, 79.02; H 9.55%.

2.1.1.4. Synthesis of dipyrromethanes **4a** *and* **4b**

A mixture of pyrrole (16 mL, 250 mmol), compound **3a** or **3b** (10 mmol) and trifluoroacetic acid (11 μL, 1 mmol) was stirred under Ar for 5-10 min. The reaction mixture was treated with 0.1 M aqueous NaOH (40 mL) and extracted with EtOAc (100 mL). The organic layer was washed with H_2O (3 × 10 mL) and brine (1 × 5 mL), dried, and concentrated in vacuo. Excess pyrrole was removed by vacuum distillation, and the residue column chromatographed (neutral alumina, 20% EtOAc/hexane) to give the respective products **4a** (1.4 g, 42%) and **4b** (2.0 g, 52%), which were crystallized from hexane.

Compound 4a: White crystals; mp: 58 ^{o}C; IR: ν_{max} 3463 (m), 3019 (s), 2956 (s), 2859 (s), 2399 (w) cm^{-1}; ^{1}H NMR (200 MHz, $CDCl_3$): δ 7.91 (broad s, 2H), 7.13 (d, *J* = 7.8 Hz, 2H), 6.86 (d, *J* = 7.8 Hz, 2H), 6.69 (m, 2H), 6.17 (m, 2H), 5.93 (m, 2H), 5.43 (s, 1H), 3.95 (t, *J* =6.4 Hz, 2H), 1.81 (m, 2H), 1.45 (m, 5H), 0.93 (t, *J* = 6 Hz, 3H);^{13}C NMR (50 MHz, $CDCl_3$): δ 158.2, 134.0, 132.9, 129.3, 117.0, 114.7, 108.4, 107.0, 68.1, 43.2, 31.6, 29.3, 25.7, 22.6, 14.0; MSMS (CI, m/z): 321.2 (100) [M-H]$^{+}$ amu;. Anal. Calcd. for $C_{21}H_{26}N_2O$: C, 78.22; H, 8.13; N 8.69%. Found: C, 78.60; H, 8.17; N, 8.54%.

Compound 4b: White crystals; mp: 64 ^{o}C; IR: ν_{max} 3463 (m), 3019 (s), 2928 (s), 2856 (s), 2399 (w), 1639 (w) cm^{-1}; ^{1}H NMR (200 MHz, $CDCl_3$): δ 7.95 (broad s, 2H), 7.12 (d, *J* = 8.5 Hz, 2H), 6.85 (d, *J* = 8.5 Hz, 2H),6.69 (m, 2H), 6.16 (m, 2H), 5.92 (m, 2H), 5.79 (m, 1H), 5.43 (s, 1H), 4.98 (t, *J* = 9.3 Hz, 2H), 3.94 (t, *J* = 6.4 Hz, 2H), 2.05 (m, 2H), 1.78 (m, 2H), 1.32 (m, 12H), ^{13}C NMR (50 MHz, $CDCl_3$): δ 158.2, 134.0, 132.9, 129.3, 117.0, 114.7, 114.1, 108.4, 107.0, 68.1, 43.2, 31.6, 29.2, 25.7, 22.6; MSMS (CI, m/z): 391.1 (100) [M+H]$^{+}$ amu; Anal. Calcd. for $C_{26}H_{34}N_2O$: C, 79.96; H, 8.77; N, 7.17. Found: C, 79.62; H, 8.77; N, 7.26%.

2.1.1.5. Synthesis of diacyldipyrromethanes 6a and 6b

A solution of EtMgBr in THF (8.1 mmol) was slowly injected to a stirred solution of **4a** (0.520g, 1.62 mmol) in toluene (25 mL) under argon. After stirring for 0.5 h at room temperature, the acid chloride **5a** or **5b** (4.05 mmol) in toluene (2 mL) was injected into the resulting brown solution over 10 min, and stirring continued for an additional 10 min. The reaction mixture was quenched with aqueous saturated NH_4Cl (10 mL) and the mixture extracted with EtOAc (20 mL). The organic extract was washed with H_2O (2 × 10 mL) and brine (1 × 5 mL), dried, and concentrated in vacuo. The residue was column chromatographed (neutral alumina, 25% EtOAc/hexane) to obtain a brown oil as a 4:1 mixture of diacetyl and monoacetyl derivatives of **4a**. The required compounds **6a** (0.532 g, 62%) and **6b** (0.422 g, 46%) were obtained in pure form by triturating the oils with MeOH.

Compound 6a: Light brown powder; mp: 150 ^{o}C; IR: ν_{max} 3225 (m), 3017 (s), 2928 (s), 2856 (s), 1610 (s) cm^{-1}; ^{1}H NMR (200 MHz, $CDCl_3$): δ 11.08 (s, 2H),7.77 (d, *J* = 6.8 Hz, 4H), 7.40 (m, 8H), 6.91 (d, *J* = 6.8 Hz, 2H), 6.60 (m, 2H), 6.00 (m, 2H), 5.60(s, 1H), 3.94 (t, *J* = 6.5 Hz, 2H), 1.71 (m, 2H), 1.38 (m, 6H), 0.89 (t, *J* = 6.5 Hz, 3H), ^{13}C NMR (50 MHz, $CDCl_3$): δ 184.4, 158.6, 141.1, 138.4, 131.6, 131.0, 129.7, 129.4, 128.0, 120.7, 114.9, 111.0, 68.1, 44.1, 31.8, 29.3, 29.2, 26.1, 22.6, 14.0; MS (DI, m/z): 530 [M^{+}] amu. Anal. Calcd. for $C_{35}H_{34}N_2O_3$: C, 79.22; H, 6.46; N, 5.28. Found: C, 79.04, H, 6.52, N, 5.52%.

Compound 6b: Light brown powder; mp: 120 ^{o}C; IR: ν_{max} 3275 (m), 3018 (s), 2932 (s), 2871 (s), 1610 (s) cm^{-1}; ^{1}H NMR (300 MHz, acetone-D_6): δ11.12 (s, 2H), 7.96 (m, 4H), 7.26 (m, 4H), 7.00 (m, 4H), 6.06 (m, 2H), 5.83 (s, 1H), 3.99 (t, *J* = 6.2 Hz, 2H), 1.38 (m, 2H), 0.93 (m, 6H), 0.87 (m, 3H), ^{13}C NMR (75 MHz, acetone-D_6): δ 182.94, 162.5,158.3, 141.0, 131.6, 131.5, 131.3, 130.7, 129.5, 129.2, 120.4, 115.4, 115.0, 114.8, 111.0, 68.1, 43.9, 43.5, 31.6, 29.2, 25.7, 22.5, 13.9; MSMS (CIMS, m/z): 567.4 (100) [M+H]$^{+}$ amu. Anal. Calcd. for $C_{35}H_{32}F_2N_2O_3$: C, 74.19; H, 5.69; N, 4.94. Found: C, 73.78, H, 5.43, N, 4.89%.

2.1.1.6. Synthesis of porphyrins Ia and Ib

To a stirred solution of the respective diacyldipyrromethanes **6a** or **6b** (0.78 mmol) in dry THF/MeOH (10:1, 34 mL) was added $NaBH_4$ (0.037 g, 1.0 mmol) in portions. After the reduction was complete, the mixture was poured into aqueous saturated NH_4Cl (60 mL) and extracted with CH_2Cl_2 (100 mL). The organic layer was washed with H_2O (2 × 5 mL) and brine (1 × 5 mL), dried, and concentrated in vacuo to get the respective dicarbinols as foam like solids.

Mixtures of each of these compounds and the dipyrromethane **4b** (0.305 g, 0.78 mmol) in CH_3CN (350 mL) were stirred to get a homogeneous solution. TFA (1 mL, 9.49 mmol) was slowly added into these under rapid stirring, followed by addition of DDQ (0.531 g, 2.34 mmol) after 5 min. The reaction was stirred for 1 h at room temperature, quenched with Et_3N (0.960 g, 9.49 mmol), passed through a pad of Al_2O_3 and eluted with CH_2Cl_2 until the eluent was colourless. The eluate was concentrated, passed through a silica gel pad that was eluted with CH_2Cl_2 to remove the non-porphyrin products. The purple fractions were combined and concentrated in vacuo to get the porphyrins **Ia** (0.069 g, 10%) and **Ib** (0.143 g, 20%) as purple solids, which were crystallized from $CHCl_3$/MeOH.

Compound Ia: Purple crystals; mp: 230 ^oC; IR: ν_{max} 3433 (s), 3019 (s), 2928 (s), 2399 (w), 1643 (w) cm^{-1}; ^1H NMR (200 MHz, $CDCl_3$): δ 8.84 (m, 8H), 8.13 (m, 8H), 7.75 (m, 6H), 7.26 (m, 4H), 5.81 (m, 1H), 4.97 (t, *J* = 10.0 Hz, 2H), 4.23 (t, *J* = 6.4 Hz, 4H), 1.99 (m, 6H), 1.40 (m, 18H), 0.97 (t, *J* = 6.6 Hz, 3H), -2.79 (s, 2H), ^{13}C NMR (50 MHz, $CDCl_3$): δ 164.5,161.2, 159.0, 139.3, 138.2, 135.6, 135.8, 134.2, 130.8, 120.2, 118.7, 114.2, 113.8, 113.5, 112.7, 68.4, 33.9, 31.8, 29.7, 29.5, 29.2, 28.98, 26.2, 25.9, 22.7, 14.1; MALDI-TOF (m/z): 882 (100) $[M]^+$ amu; MALDI-TOF (HCCA matrix): 882 (100) $[M]^+$ amu; Anal. Calcd. for $C_{61}H_{62}N_4O_2$: C 82.96, H 7.08, N 6.34. Found: C 82.94, H 7.03, N 6.04%.

Compound Ib: Purple crystals; mp: 225 ^oC; IR: ν_{max} 3434 (s), 3019 (s), 2927 (s), 2850 (s), 1643 (w) cm^{-1}; ^1H NMR (200 MHz, $CDCl_3$): δ 8.84 (m, 8H), 8.13 (m, 8H), 7.77 (m, 4H), 7.27 (m, 4H), 5.82 (m, 1H), 4.99 (t, *J* = 10.0 Hz, 2H), 4.23 (t, *J* = 6.2 Hz,4H), 2.00 (m, 6H), 1.46 (m, 18H), 1.07 (t, *J* =6.6 Hz, 3H), -2.81 (s, 2H);^{13}C NMR (50 MHz, $CDCl_3$): δ 164.5, 161.2, 159.1, 138.2, 135.8, 135.6, 134.2, 130.9, 120.2, 118.7, 113.8, 113.6, 112.8, 68.3, 31.9, 31.7, 29.7, 29.5, 29.2, 29.0, 26.3, 25.9, 22.7, 14.2; MALDI-TOF (HCCA matrix): 918 (100) $[M]^+$ amu; Anal. Calcd. for $C_{61}H_6N_4O_2F_2$: C 79.71, H 6.58, N 6.10. Found: C 79.84, H 6.64, N 6.03%.

2.1.2. *Synthesis of 4-undec-10-enyloxyl-N-(5,10,15,20-tetraphenyl porphyrin-2ylmethyl)aniline (IIa) and 4-hex-5-enyloxyl-N-(5,10,15,20-tetraphenylporphyrin-2ylmethyl)aniline (IIb)*(Scheme-2.2)

The compounds were prepared according to the following steps (Scheme 2.2).

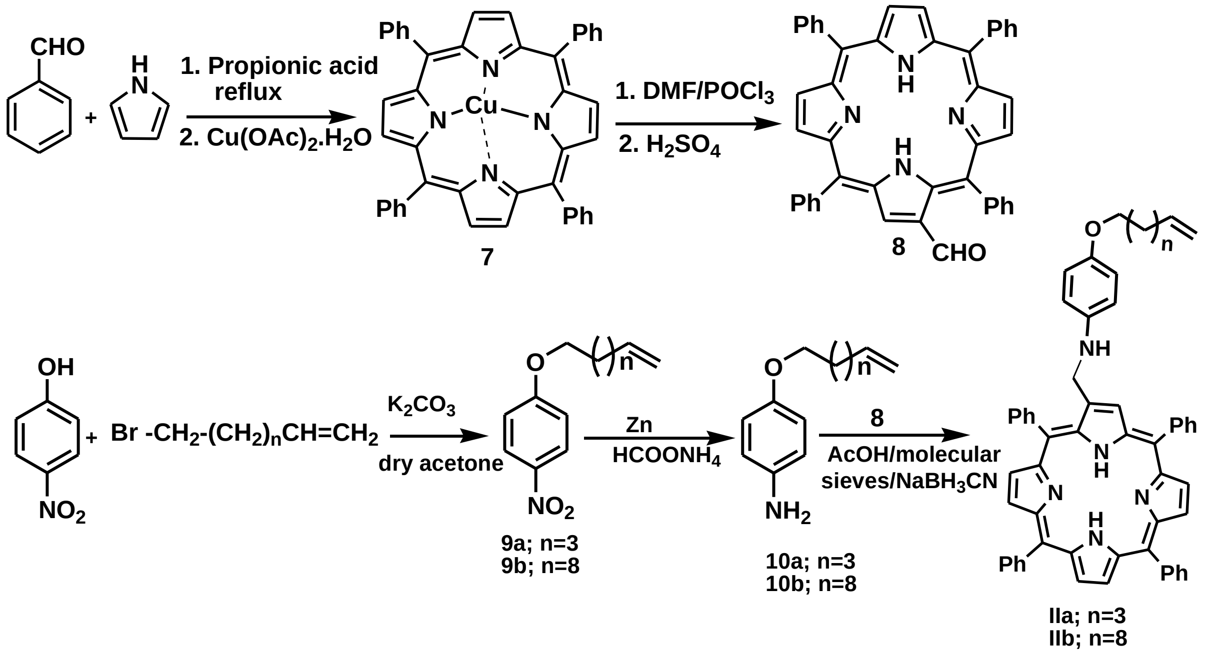

Scheme-2.2. Synthesis of **IIa** and **IIb**

2.1.2.1. Synthesis of 5,10,15,20-tetraphenylporphyrin (TPP)[107]

To a refluxing solution of benzaldehyde (5.30 g, 50 mmol) in propionic acid was added dropwise pyrrole (3.35 g, 50 mmol) in propionic acid. After refluxing for 2h under stirring, the mixture was cooled to room temperature and kept for 12 h. The precipitate was filtered, washed with MeOH, dried in vacuum, and the product column chromatographed (silica gel, 50% $CHCl_3$/hexane). The compound was crystallized from MeOH/$CHCl_3$. 1.62 g, 20%); purple crystals; m.p: >250°C; ^{1}H NMR ($CDCl_3$, 200 MHz): δ -2.78 (broad s, 2H), 8.84 (s, 8H), 8.21 (m, 8H), 7.76 (m, 12H); MALDI-TOF (HCCA matrix): *m/z* (%) 614 d.

2.1.2.2. Synthesis of 5,10,15,20-tetraphenylporphyrinato copper(II) diacetate (7)

A solution of $Cu(OAc)_2.H_2O$ (0.179 g, 0.895 mmol) in MeOH (12 mL) was added to a refluxing and stirred solution of **6** (0.500 g, 0.814 mmol) in $CHCl_3$(75 mL). On completion of the reaction (*cf*. TLC, 30 min), the reaction mixture was brought to room temperature and triturated with MeOH to obtain **7** (0. 647 g, ~quant.). purple powder; m.p: >250°C; MALDI-TOF (HCCA matrix): 795 d. UV-Vis (CH_2Cl_2) λ_{max}: 302, 416, 540, 576, 617 nm.

2.1.2.3. Synthesis of 5,10,15,20-tetraphenylporphyrin-2-carbaldehyde (8)[108]

$POCl_3$ (7.9 mL, 52 mmol) was dropwise added to ice-cooled anhydrous DMF (5.5 mL, 75.6 mmol) to obtain the Vilsmeier complex as a thick golden liquid. A cold suspension of **7** (0.500 g, 0.73 mmol) in CH_2Cl_2 (50 mL) was added, the reaction mixture brought to room temperature, refluxed for 5 h, cooled to room temperature, and left overnight. Concentrated H_2SO_4 (10 mL) was added to the ice-cold mixture, and stirring continued for 10 min. The green mixture was poured into ice cooled 0.625 M NaOH (1 L) with occasional shaking till disappearance of the green colour. It was extracted with $CHCl_3$ (2×200 mL), the organic layer washed with aqueous $NaHCO_3$ (2 × 350 mL) till neutral, and dried over $MgSO_4$. Solvent removal in vacuo followed by column chromatography (silica gel, 40% $CHCl_3$/hexane) of the residue gave **8** (0.085 g, 75%). mp: >250°C; ^{1}H NMR ($CDCl_3$, 600 MHz): δ 9.40 (m, 1H), 9.24 (s, 1H), 8.90 (m, 4H), 8.78 (d, *J* = 2.3 Hz, 2H), 8.25 (d, *J* = 7.0 Hz, 2H), 8.20 (m, 6H), 7.79 (m, 12H); ^{13}CNMR ($CDCl_3$, 75 MHz): δ 189.4, 142.5, 141.9, 141.7, 135.1, 134.7, 133.5, 130.8, 129.1, 128.5, 128.2, 128.0, 127.7, 127.5, 127.1, 126.9, 122.7, 120.7, 120.4, 120.1; MALDI-TOF (HCCA matrix): 642 d; LCMS *m/z* (%): 643.3 amu. Anal. Calcd. for $C_{45}H_{30}N_4O$: C 84.09; H, 4.70; N, 8.72. Found: C 83.84; H, 4.82; N, 8.49%; UV-Vis (CH_2Cl_2): λ_{max} 431, 526, 567, 606, 664 nm

2.2.2.4. Synthesis of 4-undecenyloxy-1-nitro benzene (9a) and 4-hexenyloxy-1-nitro benzene (9b).

A mixture of 4-nitrophenol (0.500 g, 3.59 mmol), **2** (0.920 g, 3.95 mmol) or 1-bromo-5-hexene (0.645 g 3.95 mmol) and K_2CO_3 (0.644 g, 5.14 mmol) in dry acetone was refluxed for 12 h with stirring. The reaction mixture was cooled, filtered over celite, concentrated, and residue dissolved in $CHCl_3$ (20 mL). The organic extract was washed with H_2O (2×20 mL) and brine (1 × 5 mL), and dried. Removal of solvent followed by column chromatography (silica gel, 2% EtOAc/hexane) furnished **9a** (1.0 g, 99%) and **9b** (0.791 g, 99%).

Compound **9a**: Pale yellow crystals; ^{1}H NMR ($CDCl_3$, 600 MHz): δ 8.18 (m, 2H), 6.93 (m, 2H), 5.94 (m, 1H), 4.93 (m, 2H), 4.04 (t, *J* = 6.0 Hz, 2H), 2.04 (q, *J* = 6.0 Hz, 2H), 1.82 (quin, *J* = 6.6 Hz, 2H), 1.28 (m, 14H); ^{13}C NMR ($CDCl_3$, 75 MHz): δ 164.3, 141.3, 139.2, 125.9, 114.4, 114.2, 68.9, 33.8, 29.5, 29.4, 29.3, 29.1, 29.0, 25.9; LCMS *m/z* (%): 292.0 amu. Anal. Calcd. for $C_{17}H_{25}NO_3$: C, 70.07; H, 8.65; N, 4.81; O, 16.47. Found: C, 70.47; H, 8.78; N, 4.59%.

Compound 9b: Pale yellow viscous liquid;^{1}H NMR ($CDCl_3$, 600 MHz): δ 8.18 (m, 2H), 6.93 (m, 2H), 5.83 (m, 1H), 5.01 (m, 2H), 4.06 (t, *J* = 6.0 Hz, 2H), 2.14 (q, *J* = 6.0 Hz, 2H), 1.84 (quint, *J* = 6.8 Hz, 2H), 1.28 (m, 14H); ^{13}C NMR ($CDCl_3$, 75 MHz): δ 164.2, 141.3, 138.3, 125.9, 115.0, 114.4, 68.7, 33.3, 28.4, 25.2; LCMS *m/z* (%): 222.0 amu. Anal. Calcd. for $C_{12}H_{15}NO_3$: C, 65.14; H, 6.83; N, 6.33. Found: C, 65.26; H, 6.77 ; N, 6.33 %.

2.1.2.5. 4-Undecenyloxyl-N-(5,10,15,20-tetraphenylporphyrin-2-ylmethyl)aniline **(10a)** *and 4-Hexenyloxyl-N-(5,10,15,20-tetraphenylporphyrin-2-ylmethyl)aniline* **(10b).**[108]

To a stirred mixture of **9a** (0.200 g, 0.684 mmol) or **9b** (0.151 g, 0.684 mmol) and HCO_2NH_4 (0.068 g) in MeOH (5 mL), was added Zn dust (0.053.6 g, 0.82 mmol) under Ar. After 10 min, the mixture was filtered through celite and washed with Et_2O, the organic layer was washed with H_2O (2×50 mL) and brine (1×5 mL), and dried. Removal of solvent under acuo afforded **10a** (0.162 g, 91%) or **10b** (0.116 g, 89%) as white powders. It turns brown very fast hence used without purification.

2.1.2.6. Synthesis of 4-undecenyloxy-N-(5,10,15,20-tetraphenyl porphyrin-2ylmethyl)aniline (IIa) and 4-hexenyloxy-N-(5,10,15,20-tetraphenylporphyrin-2ylmethyl)aniline (IIb).[110]

A mixture of **8** (0.075 g, 0.12 mmol), **10a** (0.046 g, 0.17 mmol) or **10b** (0.033 mg, 0.17 mmol), molecular sieves 4 Å (0.030 g) and AcOH (2 drops) in THF (5 mL) was refluxed for 2 h when the entire **8** was consumed. $NaBH_3CN$ (0.008 g, 0.15 mmol) in MeOH (5 mL) was added into the mixture, which was refluxed for an additional 3 h. The mixture was diluted with H_2O (5 mL) and extracted with $CHCl_3$ (2 × 25 mL). The organic layer was washed with H_2O (2×50 mL) and brine (1×5 mL), and dried. Removal of solvent in vacuo afforded a residue which was purified by column chromatography (silica gel, 40% EtOAc/hexane) to obtain compound **IIa** (0.080 g, 78%) and **IIb** (0.075 g, 78%) respectively.

Compound IIa: Violet solid; mp: >250^{o}C; ^{1}H NMR ($CDCl_3$, 600 MHz): δ 8.70 (m, 6H), 8.64 (d, *J* = 5.9 Hz, 1H), 8.22 (m, 4H), 8.12 (m, 4H), 7.73 (m, 12H), 6.70 (m, 2H), 6.48 (d, *J* = 8.2 Hz, 2H), 5.81 (dd, *J* = 17.0, 10.0 Hz, 1H), 5.01 (d, *J* = 16.4 Hz, 1H), 4.95 (d, *J* = 10.6 Hz, 1H), 4.45 (broad s, 2H), 3.87 (t, *J* = 7.0 Hz, 2H), 3.74 (broad s, 1H), 2.11 (m, 2H), 1.74 (m, 2H), 1.54 (t, *J* = 8.2 Hz, 2H), 1.20-1.31 (m, 7H); ^{13}C NMR ($CDCl_3$, 75 MHz): δ 151.8, 142.3, 142.2, 142.1, 141.9, 139.3, 134.72, 134.7, 134.7, 134.6, 133.2, 128.5, 127.8, 127.7, 127.3, 126.8, 126.7, 117.4, 115.7, 115.6, 114.7, 114.2, 68.8, 68.7, 33.9, 32.0, 29.8, 29.7, 29.6, 29.5, 29.2, 29.0, 26.1, 22.8, 22.2; MALDI-TOF (HCCA matrix): 888 d. Anal. Calcd. for $C_{62}H_{57}N_5O$: C, 83.84; H, 6.47; N, 8.56. Found: C, 83.40; H, 6.17; N, 8.63%; UV-Vis (CH_2Cl_2) λmax: 411, 514, 548, 589, 646 nm.

Compound IIb: Violet gel; ^{1}H NMR ($CDCl_3$, 300 MHz): δ 8.82 (m, 6H), 8.64 (d, *J* = 4.8 Hz, 1H), 8.17 (m, 8H), 7.73 (m, 13H), 6.72 (m, 2H), 6.48 (m, 2H), 5.83 (m, 1H), 4.98 (m, 2H), 4.45 (s, 2H), 3.88 (t, *J* = 6.6 Hz, 1H), 1.97-2.19 (m, 3H), 1.76 (m, 3H), 1.54 (dt, *J* = 15.3, 7.6 Hz, 5H), 1.49 (broad s, 1H), 1.25 (m, 6H), -2.77 (broad s, 1H); ^{13}C NMR ($CDCl_3$, 75 MHz): δ 151.7, 142.4, 142.3, 142.3, 142.1, 141.9, 138.7, 134.7, 134.6, 133.2, 128.5, 127.8, 127.7, 127.3, 126.8, 126.7, 120.7, 120.3, 119.5, 119.4, 115.7, 114.7, 68.6, 45.1, 33.6, 29.8, 29.0, 25.4; MALDI-TOF (HCCA matrix): 818 d. Anal. Calcd. for $C_{57}H_{47}N_5O$: C, 83.69; H, 5.79; N, 8.56; O, 1.96; Found: C, 83.04; H, 6.08; N, 8.04%; UV-Vis (CH_2Cl_2) λmax: 411, 514, 548, 589, 646 nm.

2.1.3. Synthesis of undec-10-enyl 1-methylperylenyl ether (III)

The compounds were prepared according to the following steps (Scheme 2.3).

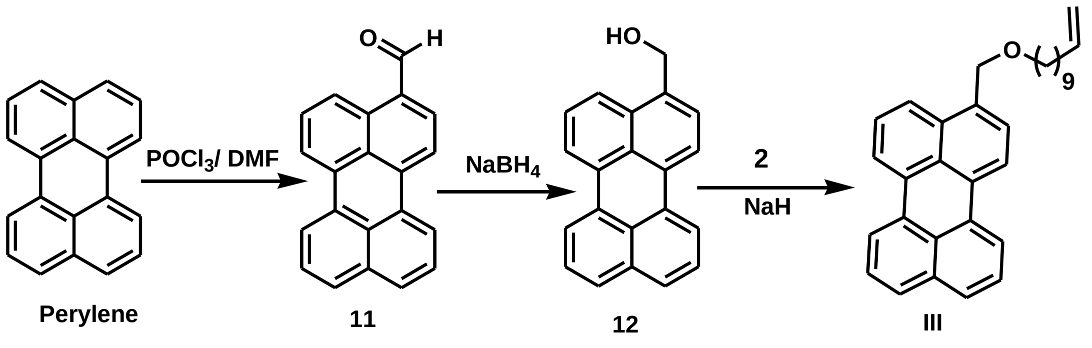

Scheme-2.3 Synthesis of **III**

2.1.3.1 Synthesis of 3-formylperylene (11).[111]

Perylene (0.25 g, 1 mmol) was added to a stirred mixture of anhydrous *o*-dichlorobenzene (0.5 mL) and DMF (0.47 g, 6.5 mmol). The reaction mixture was heated to 100 °C and $POCl_3$ (0.31 g, 20 mmol) added into it in 30 min. After 2 h, the reaction mixture was cooled by an ice bath, and neutralized to Congo red by aqueous 10% NaOAc. After standing on ice for 3 h, the precipitate was collected by filtration, washed with H_2O (3 × 3 mL), air-dried, and purified by column chromatography **(**silica gel, 5% EtOAc/hexane**)** followed by crystallization (hexane/$CHCl_3$) to get **11** (0.2 g, 71.4%). Orange crystalline solid; mp: 235°C, (lit.[14] mp: 236 °C); IR: ν_{max} 2718, 1710 cm^{-1}; ^1H NMR ($CDCl_3$, 500 MHz): δ 10.33 (s, 1H), 9.17 (d, *J* = 8.8 Hz, 1H), 8.36-8.24 (m, 5H), 7.94 (d, *J* = 7.8 Hz, 1H), 7.82 (d, *J* = 7.8 Hz, 1H), 7.76 (d, *J* = 7.8 Hz, 1H), 7.70 (t, *J* = 7.8 Hz, 1H), 7.59-7.52 (m, 2H); ^1H NMR ($CDCl_3$, 125 MHz): δ 192.8, 137.6, 137.2, 134.4, 132.3, 131.3, 130.7, 130.1, 130.0, 129.9, 129.3, 129.0, 128.5, 128.2, 127.0, 126.7, 124.6, 122.8, 121.6, 121.1, 119.1; LCMS: 281 amu.

2.1.3.2. Synthesis of 3-hydroxymethylperylene (12).[112]

To a cooled (0 °C) and stirred solution of **11** (0.13 g, 0.46 mmol) in THF (25 mL) was added dropwise $NaBH_4$ (0.018 g, 0.5 mmol) in MeOH (5 mL) in 2 h. The mixture was stirred for an additional 4 h, concentrated in vacuo, and the residue dissolved in $CHCl_3$ (25 mL).The organic extract was washed with H_2O (3 × 5 mL) and brine (1 × 5 mL), dried and concentrated in vacuo. The residue was purified by column chromatography (silica gel, $CHCl_3$) followed by crystallization (hexane/$CHCl_3$) to get **12** (0.13 g, 98%). Yellow crystalline solid; mp: 207-208°C, (lit.[15] mp: 208-210 °C); IR: ν_{max} 3448 cm^{-1}; ^1H NMR ($CDCl_3$, 300 MHz): δ 8.26-8.13 (m, 4H), 7.95 (d, *J* = 8.4 Hz, 1H), 7.69 (d, *J* = 8.1 Hz, 2H), 7.59-7.45 (m, 4H), 5.10 (s, 2H); ^{1}H NMR ($CDCl_3$, 75 MHz): δ 127.9, 126.9, 126.8, 126.7, 126.6, 126.3, 126.1, 126.0, 124.4, 123.4, 120.4, 120.3, 119.8, 63.8; LCMS: 282 amu.

2.1.3.3. Synthesis of 3-undecenyloxymethylperylene (III)

To a stirred hexane-washed suspension of NaH (0.03 g, 1.1 mmol, 60% suspension in oil) in THF (10 mL) was added compound **13** (0.10 g, 0.35 mmol) in THF (10 mL). After refluxing for 1 h, **2** (0.1 mL, 0.42 mmol) and Bu_4NI (0.1 mmol) was added into the mixture, and refluxing continued till completion of reaction (*cf*. TLC, ~4 h). The mixture was brought to room temperature, treated with aqueous saturated NH_4Cl (1 mL) and extracted with EtOAc (3 × 15 mL). The organic extract was washed with H_2O (2 × 50 mL) and brine (2 × 10 mL), dried and concentrated in vacuo. The residue was purified by column chromatography (silica gel, 5% EtOAc/ hexane) to give the compound **III** (0.12 g, 80%). Pale yellow viscous liquid; IR: ν_{max} 988, 920 cm^{-1}; ^{1}H NMR ($CDCl_3$, 300MHz): δ 8.26-8.15 (m, 4H), 7.96 (d, *J* = 8.4 Hz, 1H), 7.69 (d, *J* = 8.1 Hz, 2H), 7.57-7.45 (m, 4H), 5.82 (ddt, *J* = 17.0, 10.3, 6.7 Hz, 1H), 5.06-4.86 (m, 4H), 3.58 (t, *J* = 6.6 Hz, 2H), 2.03 (q, *J* = 7.1 Hz, 2H), 1.74-1.55 (m, 4H), 1.40-1.16 (m, 10H); ^{13}C NMR ($CDCl_3$, 75 MHz): δ 139.2, 134.6, 133.8, 133.0, 131.5, 131.3, 131.1, 129.0, 128.5, 127.8, 127.0, 126.6, 126.5, 123.9, 120.3, 120.2, 119.6, 114.1, 71.4, 70.5, 33.8, 29.8, 29.7, 29.6, 29.4, 29.1, 28.9, 26.2;MALDI-TOF (HCCA matrix): 434 (100%), 435 (33%); Anal. Calcd. for $C_{32}H_{34}O$: C, 88.43; H, 7.89. Found: C, 88.55; H, 7.94%.

2.1.4. *Synthesis of undecenyl, 1-methylpyrene ether* (IVa) *and hexenyl, 1-methylpyrene ether* (IVb)*.*

The compounds were prepared according to the following steps (Scheme 2.4).

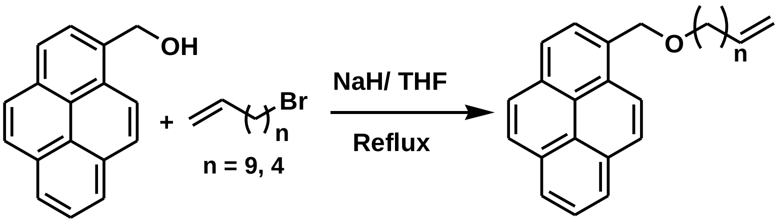

IVa: n = 9
IVb: n = 4

Scheme-2.4. Synthesis of **IVa** and **IVb**

As described for the synthesis of **III**, pyrene-1-methanol (0.20 g, 0.9 mmol) was alkylated with the respective bromides (1.0 mmol) using NaH (0.12 g, 5.1 mmol, 60% suspension in oil) as the base in presence of Bu_4NI (0.1 mmol) in THF (15 mL). Isolation of the product followed by purification column chromatography (silica gel, 5% EtOAc/ hexane) gave **Iva** (0.28 g, 90%) and **IVb** (0.35 g, 90%).

Compound **IVa:** Pale yellow viscous liquid; IR: ν_{max} 991, 921 cm^{-1}; ^1H NMR ($CDCl_3$, 300 MHz): δ 8.38 (d, J = 9.0 Hz, 1H), 8.21-8.10 (m, 4H), 8.06-7.95 (m, 4H), 5.83 (ddt, J = 17.1, 10.1, 6.7 Hz, 1H), 5.22 (s, 2H), 5.02-4.89 (m, 2H), 3.59 (t, J = 6.4 Hz, 2H), 2.00 (quint, J = 6.6 Hz, 2H), 1.65 (quint, J = 6.5 Hz, 2H), 1.45-1.19 (m, 12H); ^{13}C NMR ($CDCl_3$, 75 MHz): δ 138.7, 131.7, 131.2, 131.1, 130.8, 129.2, 127.5, 127.3, 127.2, 126.7, 125.8, 125.1, 125.0, 124.8, 124.7, 124.4, 123.4, 114.5, 71.4, 70.3, 33.5, 29.7, 29.4, 29.3, 25.5, 22.7; LCMS *m/z* (%): 383 (100%), 384 (25%), 385 (12.5%) amu; Anal. Calcd. for $C_{28}H_{32}O$: C, 87.45; H, 8.39. Found: C, 87.77; H, 8.42%.

Compound **IVb:** Pale yellow viscous liquid ; IR: ν_{max} 978, 890 cm^{-1}; ^1H NMR ($CDCl_3$, 200 MHz): δ 8.38 (d, J = 9.0 Hz, 1H), 8.31-7.93 (m, 8H), 5.83 (ddt, J = 17.0, 10.1, 6.7 Hz, 1H), 5.22 (s, 2H), 5.13-4.91 (m, 2H), 3.63 (t, J = 6.4 Hz, 2H), 2.19-2.00 (m, 2H), 1.81-1.47 (m, 4H); ^{13}C NMR ($CDCl_3$, 50 MHz): δ 138.6, 131.7, 131.1, 131.0, 130.7, 129.1, 127.4, 127.2, 127.1, 126.6, 125.7, 125.0, 124.8, 124.6, 124.3, 123.3, 114.4, 71.3, 70.2, 33.4, 29.7, 29.2, 25.5;

LCMS *m/z* (%): 231 (100%), 313 (50%), 314 (12.7%) amu; Anal. Calcd. for $C_{23}H_{22}O$: C, 87.86; H, 7.05. Found: C, 87.55; H, 7.39%.

2.1.5. Synthesis of Bis-porphyrin **V** *and Zn-Bis-porphyrin* **VI.**

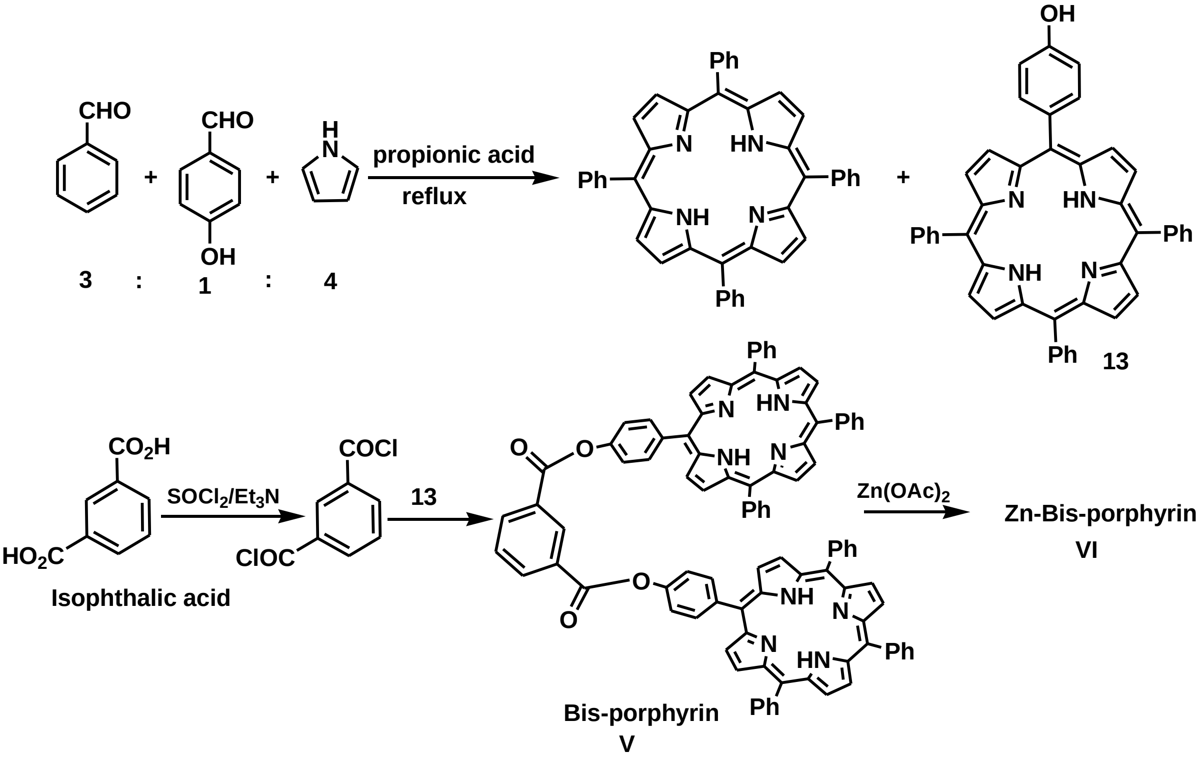

Scheme-2.5. Synthesis of **V** and **VI**

2.1.5.1. Synthesis of V

2.1.5.1.1. Synthesis of mono-hydroxytetraphenylporphyrin (mono-OH-TPP) (**13**).[113]

To a refluxing and stirred solution of pyrrole (2.68 g, 40 mmol) in propionic acid (100 mL) was dropwise added a mixture of benzaldehyde (3.18 g, 30 mmol) and *p*-hydroxybenzaldehyde (1.22 g, 10 mol) in propionic acid (100 mL). After refluxing for 2 h, the mixture was brought to room temperature and kept for 12 h. The precipitate was filtered, washed with MeOH till the filtrate was colourless, dried in vacuum, and column chromatographed (silica gel, 1:1 $CHCl_3$/hexane) to obtain **13** (0.43 g, 7%) along with TPP (%). Purple crystals ($CHCl_3$/MeOH); mp: >240 ^{o}C, (lit.[18] >320 ^{o}C); IR (film): ν_{max} 3429.7, 2976 cm^{-1}; ^{1}H NMR ($CDCl_3$, 200 MHz): δ 8.25 (m, 6H), 8.88 (m, 8H); 8.06 (d, *J* = 8.4 Hz, 2H), 7.75 (m, 9H), 7.14 (d, *J* = 8.4 Hz, 2H), -2.78 (broad s, 2H), ^{13}C NMR ($CDCl_3$, 75 MHz): δ 155.5, 142.3, 135.8, 134.7, 131.3, 127.8, 126.8, 120.2, 113.7; UV ($CHCl_3$): λ_{max} 416.0, 514.6, 549.6, 590.0, 645.8 nm.

2.1.5.1.2. Synthesis of Bisporphyrin **V.**[114]

First, the acid chloride **14** was prepared by dropwise addition of $SOCl_2$ (2.91 mL, 40 mmol) to isophthalic acid (1.66 g, 10 mmol) in dry CH_2Cl_2 (20 mL) and DMF (5 mL) under Ar, followed by refluxing the mixture for 2 h. After distilling off CH_2Cl_2, the DMF was removed from the mixture by vacuum distillation to get **14** as a white solid.

A mixture of **13** (0.10 g, 0.16 mmol) and **14** (0.02 g, 0.08 mmol), and Et_3N (0.01 mL, 0.32 mmol) in CH_2Cl_2 (3 mL) was stirred under Ar at 0 °C. After consumption of **13** (*cf.* TLC, ~4-5 h), the reaction was quenched with H_2O (1 mL), and the mixture extracted with $CHCl_3$ (10 mL). Concentration of the extract in vacuum gave a residue, which on preparative TLC furnished compound **V** (0.06 g, 61%). Purple crystals (MeOH/$CHCl_3$); mp: >220 °C; IR (film): ν_{max} 3434 (NH), 1641 (CO) cm^{-1}; ^{1}H NMR ($CDCl_3$, 200 MHz): δ 8.89 (m, 16H), 8.77 (m, 2H), 8.28 (m, 16H), 9.2 (s, 1H);7.66 (broad s, 23H), -2.76 (broad s, 4H), ^{13}C NMR ($CDCl_3$, 100 MHz): δ 171.1; 150.7, 142.1, 140.2, 135.5, 134.6, 130.5, 127.8, 126.7, 120.3, 120.0, 118.8, MALDI-TOF (HCCA matrix): 1393, 1392,615, 379 d; UV ($CHCl_3$) λ_{max}:416.0, 514.6, 549.6, 590.0, 645.8 nm.

2.1.5.2. Synthesis of Zn- Bisporphyrin VI.[115]

To a refluxing solution of **V** (0.05 g, 0.04 mmol) in $CHCl_3$ (3 mL) was added $Zn(OAc)_2$ (0.02 g, 0.08 mmol) in MeOH (0.6 mL). After stirring for 30 min (consumption of the starting material, *cf.* TLC), the mixture was cooled to room temperature, and **VI** was precipitated with MeOH (0.05 g, 98%).[18] Purple powder; mp > 250 °C; IR (film): ν_{max} 3053

(CH), 1644 (CO) cm^{-1}; ^{1}H NMR ($CDCl_3$, 300 MHz): δ 9.37 (s, 1H), 8.93 (m, 16H), 8.68 (ddt, *J* = 7.7, 1.8 Hz, 2H), 8.27 (m, 16H), 7.74 (m, 23H); ^{13}C NMR ($CDCl_3$, 100 MHz): δ 170.4; 149.9, 143.2, 135.3, 134.4, 131.6, 131.5, 127.1, 126.2, 120.6, 119.4, MALDI-TOF (HCCA matrix): 1392, 1454, 1518 d; Anal. Calcd. for $C_{96}H_{58}N_8O_4Zn_2$: C, 75.94; H, 3.85; N, 7.38; O, 4.22. Found: C, 75.65; H, 3.95; N, 6.97%; UV ($CHCl_3$) λ_{max}:417.4, 547.6, 585.8nm.

2.2. Grafting of organic monolayers on silicon

Grafting of molecular layers under ambient conditions typically involves first passivating the surfaces via either wet-chemical or plasma methods, which produces surfaces in which the unsaturated dangling bonds are terminated with hydrogen, chlorine, or another substituent that reduces the reactivity to facilitate handling in ambient conditions. This process must then be followed by reaction with the organic molecule of interest. In order to form monolayers, it is usually necessary to remove oxide layers and passivate the surface against additional reaction. The goal of the passivation step is to provide all surface atoms with a nearly ideal coordination, thereby reducing their reactivity toward the ambient atmosphere. This is typically achieved using simple monatomic reagents to co-ordinately saturate all surface bonds. The most common passivating agent is hydrogen,[116] because the H-terminated Si surfaces exhibit very low densities of mid-gap surface electronic states, and can be made easily by immersing silicon samples HF or NH_4F solution. HF is excellent in removing surface oxides but does not etch the underlying silicon very quickly. NH_4F etches the silicon as well, but is highly anisotropic. Typically, aqueous ~2%–10% HF and ~40% NH_4F are used to passivate Si<001> and Si<111> surfaces.[117] Because of its anisotropic nature, treatment

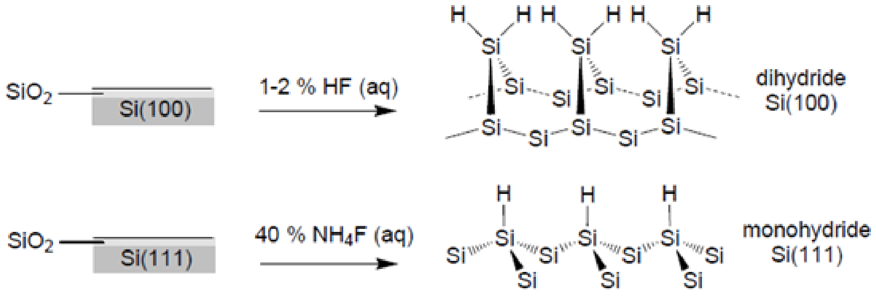

Fig.2.1. Chemical etching processes to obtain H-terminated Si surface

with NH_4F at ambient conditions leads to a spontaneous smoothing of the Si <111> surface, but leads to roughening of the Si<001> surface (**Fig. 2.1.**).[118-120]

Passivation of Si surface by Cl_2[121,122] and I_2[123] is also useful, as organic monolayers can be deposited by coupling with Grignard or organo-lithium reagents on halogen-terminated Si surfaces. After passivation, alkenes and unsaturated hydrocarbon can be grafted, and the required activation or initiation are obtained by Lewis acids,[124,125] diacyl peroxides that forms radicals on heating,[126,127] heating[117,127-129] and photochemically.[130-134] The mechanistically different electro-grafting process is an another useful option to link alkenes and alkynes to the H-terminated Si surfaces.[135,136] This electrochemical method that allows deposition of very thin organic films (typically between one monolayer and 50 nm) is a relatively a new technique, generally carried under inert atmosphere to avoid oxidation of the H-terminated Si surface, and requires a charged Si (*e.g*. highly doped Si) electrode. The Si electrode can be anodic (positive potential) or cathodic (negative potential), but cathodic electro-grafting has a distinct advantage. The negative potential, applied to the Si substrate excludes any oxidation and/or hydrolysis of Si surface during the grafting process, to furnish a clean molecule/Si interface. Moreover, the applied negative potential becomes a controlling parameter for driving the molecules to the Si surface and, therefore, deposition of any impurity is ruled out. It is even possible to generate monolayer patterns using a suitable mask. Another major advantage is that the deposition process can be monitored *in situ* by cyclic voltammetry (CV). In CV the potential (V) between the reference electrode (RE) and the working-electrode (WE) is measured. Current (I) flows between the WE and the counter-electrode (CE), but not through the RE that has a stable and known electrode potential. The high stability of the electrode potential is usually reached by employing a redox system with constant (buffered or saturated) concentrations of each participants of the redox reaction. The commonly used supporting electrolytes include $Bu_4N^+ClO_4^-$(TBAP) or $Bu_4N^+PF_6^-$($TBAPF_6$) in dry and deoxygenated CH_2Cl_2, CH_3CN or MeOH depending on the solvent in which the desired molecule was dissolved. In the current investigation, highly doped Si (111) wafers were used, converted to the required to the Si-H surface and used for electro-grafting the organic molecules as described below.

2.2.1. Passivation of the Si (111) surface

The Si (111) wafers were cleaned by heating them in 3:1 (v/v) of conc. H_2SO_4: 30% H_2O_2 (piranha) for 10 min at 80 °C. The wafers were removed, washed with excess H_2O, and immersed successively in a de-aerated (purged with Ar for 30 min) 40% aqueous NH_4F for 10 min, and in 2% aqueous HF for 2 min. The wafers were further washed with deionized H_2O for 1 min, dried under a stream of N_2 and immediately taken into the electrochemical cell for electro-grafting.

2.2.2. Grafting of monolayers

Presently, electro-grafting of organic molecules to Si surface was carried out using a three-electrode electrochemical setup, as shown schematically in **Fig. 2.2**. The H-terminated Si on which the molecules are to be grafted was used as the WE, while a Pt wire served as the CE. A pseudo RE was prepared by depositing AgCl layer over Ag by the galvanostatic method. For this, a constant current (1mA) between Ag wire and Pt electrode in 1 M HCl was maintained for

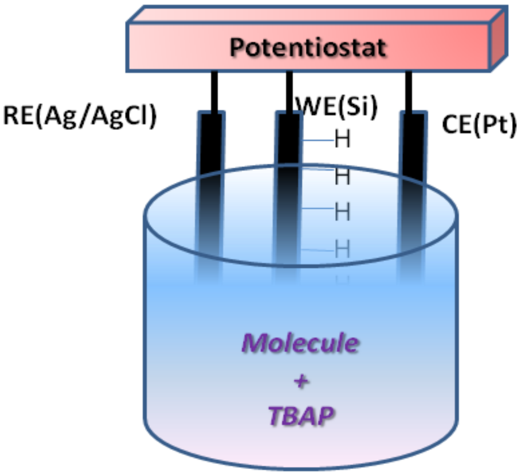

Fig.2.2. Schematic diagram of a three-electrode electrochemical setup for electrografting.

15 min. The AgCl-coated Ag wire was washed thoroughly with de-ionized water to remove the acid, and dried. This was standardized with respect to the redox potential of ferrocene, and used for the experiments. The electro-grafting was carried out using CV by scanning the potential from –1 V to 0 V at a scan rate of 0.05 V/s for number of scans. All the electrochemical experiments were carried out using Potentiostat/Galvanostat system (model: Autolab PGSTAT 30).

2.3. Spin casting of films

In spin coating techniques, a drop of **V** in $CHCl_3$ or **VI** in $CHCl_3$/MeOH (2:1) was applied on freshly cleaned glass substrates, rotating at a speed of 3000 rpm. Due to the rotation, the solution spreads on the substrates and dries rapidly leaving a solid film. The deposited films were dried for 24 h under ambient conditions to obtain the uniformly thick films.

2.4. Characterization of monolayers/multilayers

A complete characterization of the deposited layers in terms of (i) their thickness, (ii) molecular orientation and ordering, (iii) uniformity and coverage, (iv) chemical composition, (v) thermal and chemical stability and (vi) electrical property is essential for further studies on their electronic behaviour. Presently, the monolayers, deposited on Si substrates were characterized by a combination of techniques, such as, ellipsometry, water contact angle measurement, Fourier transform infrared (FTIR) spectroscopy, X-ray photoelectron spectroscopy (XPS), atomic force microscopy (AFM), secondary ion mass spectrometry (SIMS), X-ray reflectivity (XRR) and electrochemically.

Amongst these, SIMS and FTIR are used for chemical analysis, while the SIMS mass fragmentation pattern is also useful in identifying the alignment of the molecules on the Si substrate. The frequencies and intensities of the vibrational modes in the FTIR spectra can provide additional supportive evidence about the molecular alignment. The XPS technique provides excellent information about the elements and their oxidation states, present in the monolayer. Thickness of the organic layers can be determined using ellipsometry and XRR. Contact angle measurements provide information on the surface group of the grafted organic layer. The ordering of the monolayer can be also be assessed by imaging the surface morphology using AFM. Here we present a brief details of the techniques used in the present thesis work.

2.4.1. Wetting measurement

The wetting measurement is used to investigate the surface group by determining contact angle.[137] The contact angle of a water drop on a surface (**Fig. 2.3**) is an interplay of the surface tensions of the solid-liquid, liquid-vapor, and solid-vapor interfaces. When the drop is at equilibrium with the surface and vapor, an infinitesimally small change in area, dA would not produce any change in the surface free energy. Expansion of the drop leads to an increase in the solid-liquid interface area by dA with an equal reduction in the solid-vapor interface area. However, the liquid-vapor interface area of the increases by (cos θ) dA. Each interface has a specific surface tension:γ_{lv} for the liquid-vapor, γ_{sv} for the solid-vapor and γ_{sL} for the solid-liquid interfaces. The sum of the free energy changes due to the infinitesimal area change must be zero and is given by **eq. 2.1.** Rearrangement of the equation yields **eq. 2.2**, often called Young's equation for a contact angle.

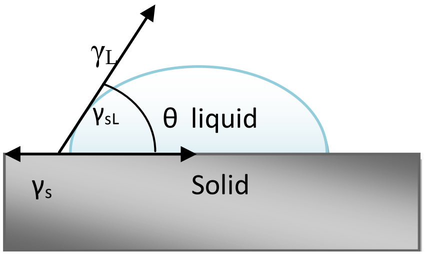

Fig. 2.3. Contact angle measurement diagram

$$\gamma_{sL}\, dA - \gamma_{sv}\, dA + \gamma_{lv}\, dA \cos\theta = 0 \qquad \textbf{(eq. 2.1)}$$

$\gamma_S = \gamma_L + \gamma_{SL.} + \cos\theta$ **(eq. 2.2)**

Despite its utility for predicting contact angles, while the γ_{lv} are easy to measure and can be found in tables, measuring γ_{sv} and γ_{sL} values are difficult. Hence, one often resorts to a model along with contact angles to predict these values. This technique is extremely sensitive to surface group. Values of contact group for different groups are given below in **Table 2.1.**. For the present studies, a drop of de-ionized water was spread on the surfaces of native Si and those containing grafted monolayers. The surfaces were imaged by a CCD camera of a Data Physics System (OCA20) and the contact angle was calculated using suitable software.

Table 2.1. Water contact angle for different surface groups for SAM

Head Group	Contact angle
$CH_3—(CH_2)_n$ (n>10)	110-117
$CH_3—(CH_2)_n$ (n<10)	97-108
$CH_2=CH—(CH_2)_n$ (20>n>10)	95-105
—Thiophene, —phenyl	90-92
$—CO_2CH_3$,$—CO_2CH_2CH_3$,$—CO_2$Benzyl,—thiophene,—anthracene,—pyrene, —EDTM	73-75
—pyridyl	43
—X(Cl, Br, I, F)	80-89
—SH,—S,—S—S	65-71
$—SO_2$	50
$—SO_3H$	30
—SCN	73-75
—OH,—COOH,$—CONH_2—B(OH)_2$	15
$—NH_2$	36
$—NH_3^+$	42
—CN	68-74
$—N_3$	75-79
—C60	65-76

2.4.2. Thickness measurement

Measurement of the layer thicknesses is essential to confirm whether the layer is monolayer or multilayer. For a monolayer, its orientation on the surface can also be determined by comparing the experimental result and the theoretical length of the molecule.

Thickness can be measured by many methods. The thicknesses of Si-grafted layers were measured by ellipsometry and XRR technique. Sinθ = theoretical length/thickness

2.4.2.1. Ellipsometry

In this optical technique, an elliptically polarized light is reflected from a surface and the changes in polarization are measured to obtain the thicknesses and/or refractive indices of thin films. This elliptically polarized light can be represented as the sum of two components, one in the plane of incidence of the light (*p* polarization), the other perpendicular to this plane (*s* polarization). Upon reflection, the amplitude and phase of each of these components is altered, resulting in a change in the overall polarization and amplitude of the light wave. The changes in amplitude and phase are represented by the Fresnel reflection coefficients for the p and s polarizations, $\boldsymbol{r_p}$ and $\boldsymbol{r_s}$. Ellipsometry measures the ratio of these coefficients, *p*. The standard relationships between *p* and the measured analyzer (A) and polarizer **(**P) angles are summarized in **eqs**. **2.3**, **2.4** and **2.5**.[138] *P* is the ratio of the changes in amplitude for the *s* and *p* polarizations of light from an interface on reflection. The angle Δ is the difference in the phase shifts that are experienced by each polarization upon reflection. Specifically, one measures the ratio, tan ψ, of the fraction of the E-fields of *p*- and *s*-polarized lights, reflected from the surface as well as the induced phase angle difference (Δ) between *p*- and *s*-polarized

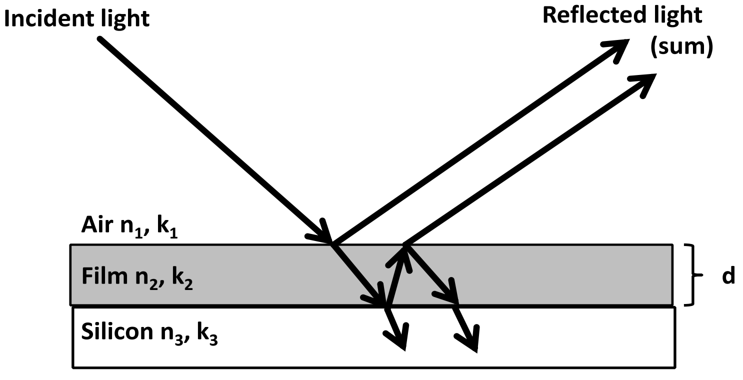

Fig. 2.4. Model used to calculate the thickness of a thin organic layer using ellipsometry.

light. Then one uses an optical model (done by the instrument software) to relate these polarization changes to film and substrate properties. **Fig. 2.4** shows the optical model used to interpret ellipsometry data.

$$p = \boldsymbol{r}_p / \boldsymbol{r}_s = \tan \psi / \exp (i\Delta) \qquad \textbf{(eq. 2.3)}$$

$$\psi = A \qquad \textbf{(eq. 2.4)}$$

$$\Delta = 2P + \pi/2 \qquad \textbf{(eq. 2.5)}$$

For a single film on a reflective substrate (such as a monolayer on silicon), there are three phases *viz*. air, film, and Si. Each of these has a refractive index, n, and an absorption coefficient, k. If we know all of theoretical constants for the system and the thickness of the film, d, we can calculate the values of tan ψ and Δ. It is assumed that the base metal is optically infinitely thick so that no significant amount of light reaches the back side of Si due to its large absorption coefficient. Conversely, if tan ψ and Δ are measured, film thickness and refractive index can be calculated. In this model, two of the four unknown parameters *viz*. film thickness and refractive index and silicon refractive index and absorption coefficient are determined. The k value for air and most organic films is zero as they don’t absorb visible light, and the refractive index of air is nearly 1. For this, the slide of the bare substrate (Si) is thoroughly cleaned and its tan ψ and Δ values are measured to get its n and k values. Next, the film is case on the surface, and the tan ψ and Δ values are measured again. Because we already know n and k for the substrate, this measurement allows calculation of the thickness and refractive index of the organic film. Usually tan ψ and Δ are not especially sensitive to the refractive index of an ultrathin film. Hence, the film thickness is estimated considering the

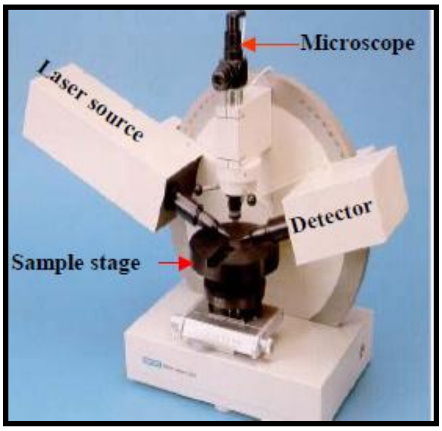

Fig. 2.5. Photograph of the ellipsometer

refractive index of the hydrocarbons as 1.5. The ellipsometer model SE 400 adv of Sentech (**Fig. 2.5.**), consisting of a laser source (632.8 nm), polarizer and rotating analyzer (Glan Prism) and detector (Si and InGaP) was used for the work. For calibration, two models (i) Si/native SiO_2/SAM/Air and (ii) Si/organic layer/Air were designed, and the *n* and *k* values of Si substrate was measured. The models were fitted with the measured *n, k* values of the Si substrate, *n*=1.5and k = 0 for the organic monolayer, its thickness was obtained.[139]

2.4.2.2. X-Ray Reflectivity (XRR)

XRR is a non-destructive and non-contact technique for thickness determination between 2-200 nm with a precision of about 1-3 °A. In addition, this technique is also employed to determine the density and roughness of films and multilayers. Low-angle XRR measures the intensity (R) of the surface-reflected X-rays as a function of the angle θ between the incoming X-ray beam and the sample. In general, the variation of this intensity with θ is given by Fresnel's laws. The intensity also varies as a result of the change in the difference in phase between X-rays reflected from the air-monolayer and monolayer-substrate interfaces. R is related to (d ρ_{ell}/dz) (ρ_{el} is the volume density of electrons) and the average derivative of the electron density along the normal *(z)* axis of the substrate according to **eq. 2.6**.

$$R = R_F \left| \rho_\infty^{-1} \int_{-\infty}^{\infty} (\mathrm{d}\,\rho_{\mathrm{el}} / \mathrm{dz}) \exp(iq_z z)\, dz^2 \right| \qquad \textbf{(eq. 2.6)}$$

$$q_z = 4\pi\lambda^{-1} \sin\theta \qquad \textbf{(eq. 2.7)}$$

Here q_z (**eq. 2.7)** is the change in momentum experienced by the X-ray photons during the reflection process, while ρ the electron density of the bulk substrate. R_F is the Fresnel reflectivity, and gives the intensity of X-rays reflected from a bare substrate whose boundary with a vacuum is sharp and perfectly smooth. If the refractive index of the substrate is known, the form of RF is determined solely by the Fresnel reflection coefficients. This index of refraction is calculated from the critical angle, θ_C, for total reflection of the X-rays.[140] The refractive index in the X-ray region is a linear function of the electron density, ρ_{el}. The change in electron density (d ρ_{ell}/dz), is therefore a direct measure of dη/dz. **Eq.2.6** describes the pattern of interference that results from the reflection of X-rays from an arbitrary electron distribution, ρ_{el}. In the case of two sharp interfaces separated by some distance, the **eq. 2.6** reduces to the familiar interference condition for reflection from parallel surfaces. Since the measured interference pattern depends on the actual distance separating the two interfaces in the monolayer system, this method, unlike ellipsometry, directly measures the thickness of the monolayer. The schematic representation of the XRR experiments (TTRAX3 theta-theta goniometer), performed using Cu-kα as the X-ray source in a fixed monochromator mode is shown in **Fig. 2.6**.

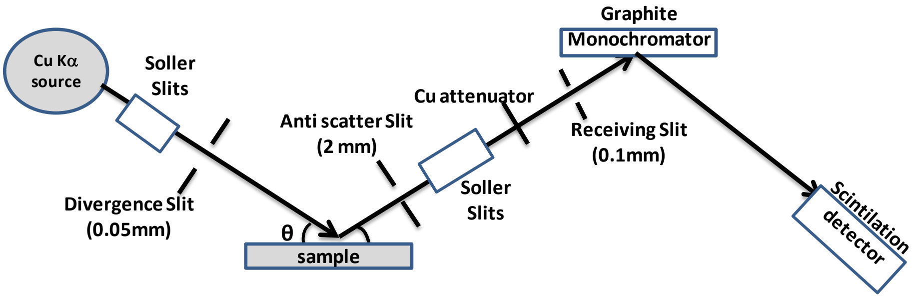

Fig. 2.6. Operating diagram of the XRR set-up

The XRR Data were fitted using MOTOFIT software.[141] The reflectivity data was fitted in a MOTOFIT software, using Parratt's formalism. The scattering length density (SLD) values of the monolayers were calculated from the density of monolayer and molecular formula of molecule according to **eq. 2.8.**Where N_a is Avogadro number, ρ_{mass} is the mass density of the material, M_R is its relative molecular mass and b_{ci} is the bound coherent scattering length of the ith atom of a molecule with n atoms.

$$\rho = \frac{N N_a \rho_{mass}}{M} \times \sum^{n} b_{ci}$$ **(eq. 2.8)**

$$b_i = \frac{e^2}{4\pi \in_0 mc^2} f_{1i}$$ **(eq. 2.9)**

$$\rho = \sum_{i=0}^{N} \frac{\rho_i - \rho_{i+1}}{2} \left(1 + erf \left(\frac{z - z_i}{\sqrt{2}\sigma_i} \right) \right)$$ **(eq. 2.10)**

For X-rays, the scattering length for each atom was calculated using **eq. 2.9**, where e is the charge on a single electron, ε_o is the permittivity of free space, m is the mass of an electron and c is the speed of light. The scattering factor (f_{1i}) for an atom of element *i* is available in literature.[142] Subsequently the SLD profile was calculated using **eq. 2.10** where N is the total number of layers, z is the distance from the top interface and *erf* is the error function. The roughness and thickness values of the grafted layers were determined at the minimum value of χ^2 for the respective monolayers. The Levenberg-Marquardt algorithm (**eq. 2.11**) was used for obtaining the minimum value of χ^2, which defines a surface in a multidimensional error space. The deepest valley in the χ^2 surface signifies minimum coefficient values of the fitting function.

$$\chi^2 = \sum_{n=1}^{L} \frac{1}{L-P} \left(\frac{y_{n,obs} - y_{n,calc}}{y_{n,error}} \right)^2$$ **(eq. 2.11)**

2.4.3. Surface morphology

2.4.3.1. Atomic force microscopy (AFM)

The surface morphology of monolayers is investigated by AFM (NTMDT-Solver P47 model) system, consisting of a cantilever probe with a sharp tip at its end for scanning the specimen surface. Rectangular cantilever of Si_3N_4 (length 200 mm and width 40 mm) having force constant of 3 N/m were employed for the measurements.[143,144]

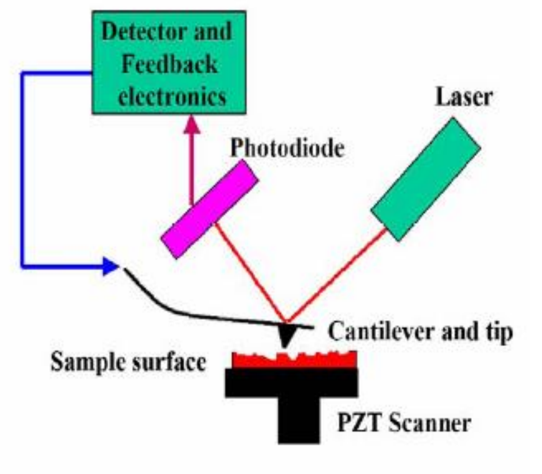

Fig. 2.7. Operating diagram of the atomic force microscope

The probe is typically a silicon or silicon nitride tip with a radius of curvature ~nanometre. When the tip is brought into proximity of a sample surface, the van der Waals force between the tip and the sample leads to a deflection of the cantilever according to Hooke's law. The deflection is measured using a laser spot, reflected from the top of the cantilever into an array of photodiodes. A feedback mechanism is employed to adjust the tip-to-sample distance to maintain a constant force between the tip and the sample. The sample is mounted on a piezoelectric tube that moves the sample in the *z* direction for maintaining a constant force, and the *x* and *d*irections for scanning the sample. The schematic representation of the AFM set up is shown in **Fig. 2.7**. The resulting map of z(*x*, *y*) represents the topography of the sample.

2.4.3.2. X-ray diffraction (XRD)

For the determination of the structure of the deposited films, X-ray diffraction studies, in different configurations were carried out as discussed below.

(a) Powder XRD: An X-ray diffractometer (Seifert XRD 3003TT) in θ-2θ scan mode was used to characterize the orientation and structure of the spin-coated films. **Fig. 2.8.** shows the schematic diagram of the diffractometer, which consists of an X-ray source, and a goniometer for mounting sample, and an-ray detector. The Cu Kα (λ 1.54056Å) selected using Graphite monochromator was used as the X-ray source. For mounting thin films, a specially designed Perspex holder (groove dimension10 ×10 ×1mm^3) was employed. Since the wavelength (λ) of X-rays coincides with the atomic spacing (d) in the solids, it diffracts in those orientations of 2θ, where the Bragg's diffraction condition, $n\lambda = 2d \sin \theta$ (θ being the angle which incident beam makes with the plane of sample) is satisfied.[145] While recording the diffraction pattern with the detector, the sample is synchronously rotated along with the detector, such that the incident X-ray incident beam makes an angle θ with the plane of sample while the detector is at angle 2θ with respect to incident beam. The recorded diffraction pattern is compared with standard patterns to get information about the phase of the samples. The lattice parameters are obtained by fitting the recorded diffraction peaks by least-square fitting software.

(b) Grazing angle XRD In powder or normal geometry contribution from the substrate to diffraction can sometimes overshadow the contribution from the thin films. Therefore the structures of very thin films (<20 nm) were investigated by a Grazing angle X-ray diffractometer. In this configuration, the incident X-ray falls at a very small angle (*e.g.* 0.1°) which is fixed with the sample surface and the detector does a 2θ

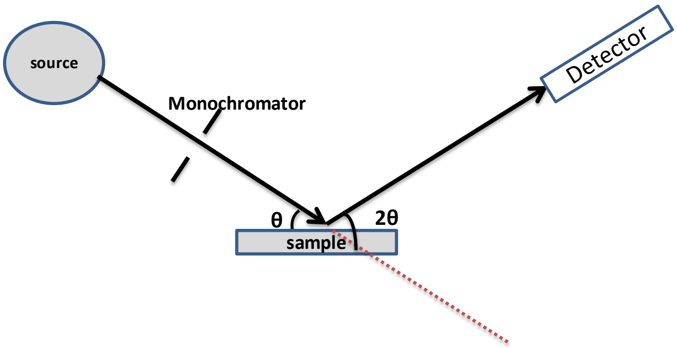

Fig. 2.8. Schematic diagram of the grazing angle XRD

scan. The sampling depth (D) is related to the incidence angle (φ) by the formula, $D = \frac{\lambda}{4\pi q}$ where λ is the X-ray wave length (1.541Å), and

$$q = \left[\sqrt{(\varphi^2 - \varphi_c^2) + 4\delta_i^2} + \varphi_c^2 - \varphi\right]^{\frac{1}{2}} \left(\sqrt{2}\right)^{-1} \qquad \textbf{eq. 2.12)}$$

$\delta_i = \frac{\lambda\mu}{4\pi q}$, φ_c is the critical angle of incidence and μ is the linear absorption coefficient.[146] In the present studies, we have employed φ = 0.1°, which leads to a sampling depth of~ 10 nm; and thus this technique becomes ideal for analyzing the structure of very thin films without having interference from the substrates.

2.4.4. Chemical characterization

Four different techniques, XPS; FTIR; SIMS; and UV-Visible spectroscopy were used to characterize the monolayers.

2.4.4. XPS

XPS was developed as a surface analysis technique in the mid-1960s by Siegbahn *et al.*[50] The core level electrons have the binding energies matching to the energies of the photons that lie in X-ray region.[147,148] XPS are based on the photoelectric effect, through which an atom absorbs a photon with energy (*hv*) in excess of binding energy (E_b) of an electron; a photoelectron is emitted with kinetic energy as shown in **Fig. 2.9**.

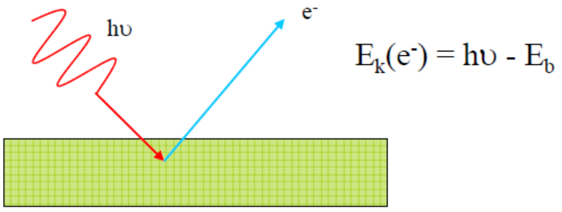

Fig. 2.9. Ray diagram of photoelectric effect

In XPS, a soft X-ray source (Al-Kα and Mg-Kα) is used to ionize electrons (by knocking out the core-level electron) from the surface of a solid sample (top few atomic layers). The binding energies of these electrons, characteristics of the elements are measured. The binding energies also contain chemical information, because the energy levels of core electrons depend slightly on the chemical state of the atom. Such shift in the energies of core level electrons arising due to chemical state of electrons is known as chemical shift. The advantages of XPS technique are (*i*) quantitative analysis of elements and chemical states of all elements except H and He, (*ii*) typical element detection limits are 0.1 atomic percentage from the top few nm, and (*iii*) samples can be conductors, semiconductors or insulators.[149-151] XPS technique provides excellent information about the elements and their bound states present in the monolayer.[152] In addition, it allows determination of thickness of the grafted organic layers. In this work for XPS measurement, a RIBER system (model: FCX 700), consisting of Mg-Kα (1253.6 eV) X-ray source and a MAC-2 electron analyzer (**Fig. 2.10.**) was used. The binding energy scale was calibrated to Au- $4f_{7/2}$ line of 83.95 eV. For charge referencing adventitious C-1s peak set at 285 eV was used. Each data set was first corrected for the non-linear emission background, followed by Gaussian fitting to obtain the peak positions.

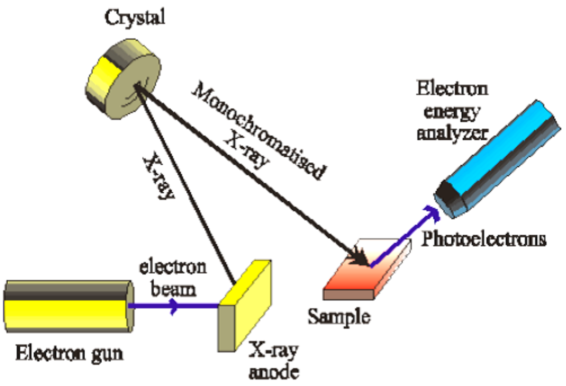

Fig. 2.10. Operational diagram of XPS set-up

2.4.4.2. Fourier Transform Infrared spectroscopy (FTIR)

The frequencies and intensities of the vibrational modes observed by FTIR spectroscopy provide information about the functional groups in the mono/multilayers.[137]

Most of the organic molecules have vibrational frequencies in the mid infrared range of 4000 to 400 cm^{-1}. For the present studies, an FT-IR Bruker Vertex 80 FTIR System, with 3000 Hyperion Microscope and LN-MCT 315-025 as detector in polarized ATR (20X objective) mode for 500 scans was used. In the ATR mode, an infrared beam is directed at a certain angle onto an optically dense crystal with a high refractive index. The internal reflectance creates an evanescent wave (**Fig. 2.11.**) that extends beyond the surface of the crystal into the sample, held in contact with the crystal. This evanescent wave protrudes only a few microns (0.5 μ — 5 μ) beyond the crystal surface and into the sample. Consequently, there must be good contact between the sample and the crystal surface. The evanescent wave is attenuated or altered in the regions of absorption by the sample. The attenuated energy from each evanescent wave is passed back to the IR beam, which then exit the opposite end of the crystal and is passed to the detector in the IR spectrometer to generate an IR spectrum.

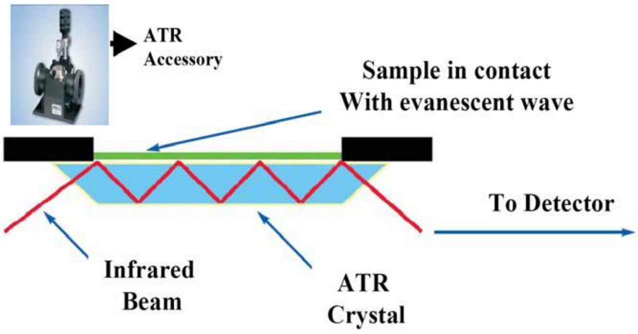

Fig. 2.11. Ray diagram of FTIR measurement in ATR mode.

2.4.4.3. Secondary ion mass spectrometry (SIMS)

SIMS is most sensitive of all the commonly-employed surface analytical techniques, can detect impurities on a surface layer at < 1 ppm concentration, and in bulk at ~1 ppb concentrations, in favorable cases. In SIMS the surface of the sample is subjected to bombardment by high energy ions, ejecting (or *sputtering*) of both neutral and charged (+/-) species from the surface. The ejected species may include atoms, clusters of atoms and molecular fragments (**Fig. 2.12.**). In traditional SIMS, mass analysis of only the positive ions is carried out for practical ease. But, it is unsuitable for quantifying the compositional data since the positive ions are but a small, non-representative fraction of the total sputtered species. The displaced ions have to be efficiently extracted from the sample region, and subjected to energy-filtering before they are mass analyzed (so that only ions with kinetic energies within a limited range are mass analyzed). The mass analyzer may be a quadruple mass analyzer (with unit mass resolution), but magnetic sector or time-of-flight (TOF) mass analyzers are often used. The latter instruments can provide substantially higher sensitivity and mass resolution, and a much greater mass range (albeit at a higher cost). In general, TOF analyzers are preferred for static SIMS, whilst quadruple and magnetic sector analyzers are preferred for dynamic SIMS.

The TOF-SIMS used for this investigation, indigenously developed by Dr. K. G. Bhushan, Technical Physics Division, BARC consists of a 25 KeV, 69Ga mono-isotopic liquid metal ion gun as the primary ion source with a spot size of about 300 nm. For studying larger molecular ions, the primary beam is operated at 10 KeV. Secondary ions are extracted with a wide-acceptance angle that ensures nearly complete extraction of every ion, produced from the sample surface. The sample is pulsed at a high potential (+ 2000 VDC) with a small delay that provides the acceleration energy for the secondary ions produced. A modified Wiley-Mclaren type reflectron produces a uniform electrostatic field over a length of 415mm. The extracted ions with slightly varying kinetic energies are reflected by the reflectron and are eventually time-focused on to a micro-channel detector,

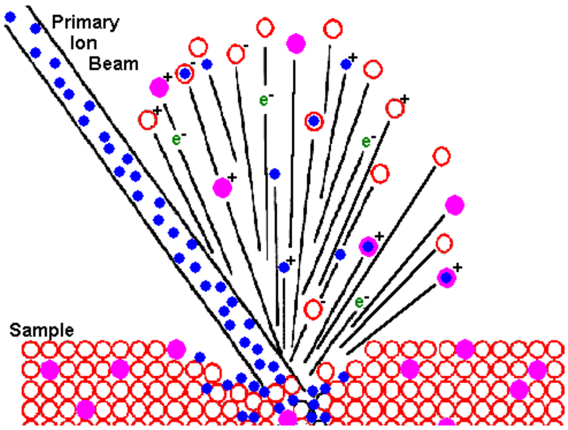

Fig. 2.12. Secondry ion sputtering.

operated in the ion counting mode. A fast pre-amplifier with a rise-time of <500 ps is utilized to detect and amplify the ion signals before being counted by a P7887 (Fast ComTec, Germany) Multi-scaler with a timing resolution of about 300 ps. Three ion pumps are utilized to ensure alow background pressure of < 1 × 10^{-9} mbar in both the analysis chamber and the flight tube.

2.4.4.4. UV-Visible spectroscopy

Absorption of the ultraviolet or visible light by molecules containing π-electrons, σ-electrons or even non-bonding electrons (n-electrons) leads to electronic excitation among various energy levels within the molecules. As a consequence, the wavelength of absorption peaks can be correlated with the type of bonds in the spices.[153] The transition between the bonding and ant bonding levels are of two types:

(i) $\sigma - \sigma^*$ *transition*, requires large energies, most of the transitions occurs below 200nm.

(ii) $\pi - \pi^*$ *transition,* occurs with molecules containing conventional double or triple bond.

Similarly the transitions between non-bonding and antibonding orbitals are $n - \pi^*$ and $n - \sigma^*$.The absorption may sometime occur due to the d and f electrons as well as charge transfer electrons.

The schematic of a double beam single monochromator spectrometer is shown in **Fig. 2.13**. In this spectrometer the intensity (I) of the beam passing through the sample is compared with that (I_0) of a reference beam to get an output of absorbance ($A=log_{10}I/I_0$) *vs.* wavelength. Absorbance is directly proportional to the numbers of absorbing molecules (concentration) in the light-path, and the path length (Beer-Lambert's law), and can be expressed as $A=\varepsilon lc$ where ε is the molar extinction coefficient, *c* is the concentration of the absorbing species and *l* is the path length. The present experiments were carried out with a JASCO B430 spectrometer.

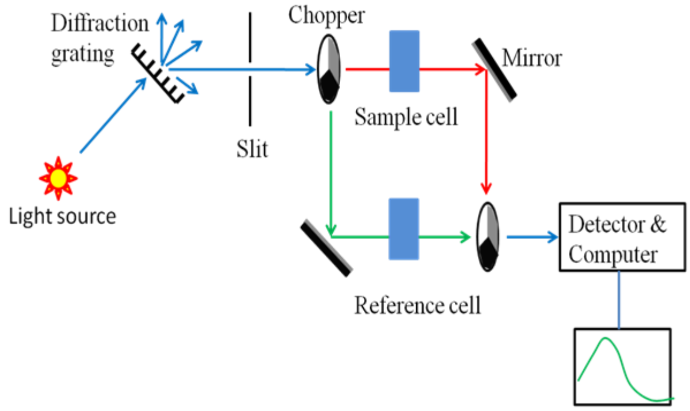

Fig. 2.13. Block diagram of a typical double beam single monochromator UV-spectrometer

2.4.5. Electrochemical characterization

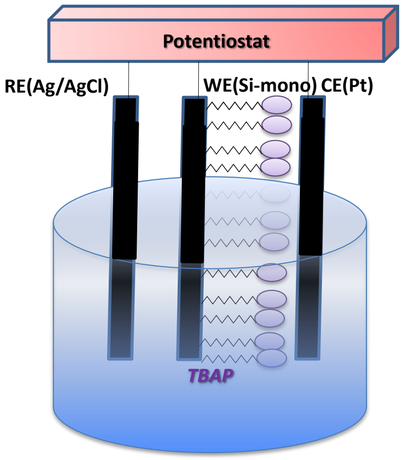

Fig. 2.14. Schematic diagram of a three-electrode electrochemical setup for CV of monolayer.

The electrochemical characterization is a sensitive tool for detection of pinholes and defects in dielectric monolayers.[154] In order to determine the total fraction of pinhole area, one performs cyclic voltammetry using monolayer as working electrode in a solution containing redox species, typically $K_3Fe(CN)_6$, and a supporting electrolyte. An ideal dielectric monolayer with full coverage (*Q*) would completely block the faradic current arising due to electrochemical oxidation of the electrode and exchange of electrons between electrode and redox couples in solution. However, presence of pinholes in the monolayer allows detection of faradic current and this current is then utilized for the determination of area fractions of pinholes (*1-Q*). It may be noted here that the faradic currents are much larger than the tunnelling currents though monolayer. Electrochemical characterization has additional advantage if the monolayer consists of a redox group. Experimentally, the redox property of the monolayer is observed carrying out cyclic voltammetry using fast scan CV (e.g. 30 V/s). For this purpose, we have used three electrode cell: Pt as counter electrode, Ag/AgCl as reference electrode and monolayer deposited Si as working electrode. The electrolyte was the TBAP solution only (cell shown in **Fig. 2.14**). The reduction and oxidation potential can also be used for determination of HOMO and LUMO positions of the monolayers.[155] We also determined the density of molecules in the monolayer using the area under the oxidation peak

2.5. Work-function calculation

2.5.1. Kelvin Probe method

The Kelvin Probe is a non-contact, non-destructive vibrating capacitor device used to measure the work function difference, or for non-metals, the surface potential, between a conducting specimen and a vibrating tip. The Kelvin method was first postulated by the renowned Scottish scientist W. Thomson, later Lord Kelvin, in 1861.[156,157] He described the movement caused by coulomb repulsion within a gold leaf electroscope when zinc and copper plates brought into close proximity while the plates were electrically connected. In 1932, this technique is modified by Zisman as a vibrating capacitor.[158] The Work Function is usually described as being the *'least amount of energy required to remove an electron from a surface atom to infinity or equivalently the vacuum level'*. The Kelvin probe measures the work function indirectly, i.e. via equilibrium not via extracting electrons.[158] The Kelvin probe

(KP) technique measures the contact potential difference (CPD) between surface of sample and KP tip in close proximity. This method of detection is extremely sensitive to noise since the Kelvin Probe signal is diminishing with respect to the noise background. In addition, KP measurements can only detect the CPD, real work function measurements are only possible through calibration i.e. the KP needs to be calibrated against a surface with known work function. For our measurement, we have used Scanning Kelvin Probe system SKP5050 manufactured by KP technology. The Kelvin probe tip (made of gold) and sample mounting stage is shown in **Fig. 2.15.** In our measurements, standard Au/Al sample manufactured by KP technology was used for calibration purpose.

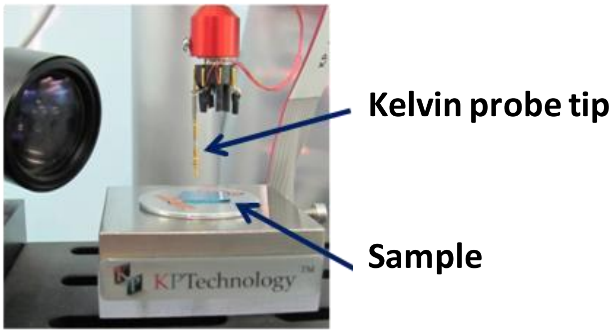

Fig. 2.15. Photograph of Scanning Kelvin probe system.

2.6. *I-V* characteristics for monolayers and multilayers.

Gold pads (size: 2 mm × 3 mm) were deposited by thermal evaporation through a metal mask 12 μm apart, followed by attaching silver wires to them using silver paint. The films were loaded in a vacuum chamber, connected to a turbo molecular pump. To deposit gold electrodes, 99.99% pure gold wire was loaded on a tungsten filament, which was resistively heated by an external power supply. The deposition rate and thickness of the deposited electrodes was monitored through a quartz crystal monitor. The conductance of the films was measured by Keithley 6487 voltage source/picoammeter using the lab-view software. The charge transport measurements were carried out using

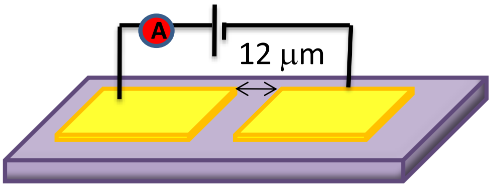

Fig. 2.16. Plane charge transport measurement geometry.

in planar geometry. The in-plane geometry, as shown in **Fig. 2.16.**, has following distinct advantages over the out-of plane geometry in which films is sandwiched between two electrodes.

(i) In the out-of-plane geometry, metal atoms from the electrode can get incorporated in the films, which can act as charge trapping centers, and hence, can give rise to hysteresis in *J*-*V* characteristics.[159] This makes it difficult to isolate the intrinsic hysteretic effect. This problem will not arise in the in-plane geometry, as the electrodes are far apart (12 μm).

(ii) Large electrode spacing also indicates that the contribution of contact resistance is very small compared to the film resistance. Therefore in our studies we measured *J*-*V* characteristics using two-probe in-plane geometry. To measure *J*-*V* characteristics a silver wire is attached to the previously deposited electrode by conducting silver paint. Keithley 6487 picoammeter/voltage source and computer based data acquisition system were used to record the *J*-*V* characteristics. All measurements were carried out in dark to avoid the problem of photoconductivity. In order to rule out the effect of film non-homogeneities, *J*–*V* characteristics were measured on at least three pairs of electrodes deposited on a film at different positions.

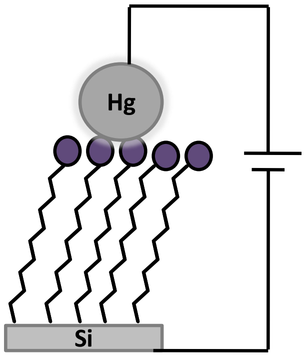

Fig. 2.17. Measurement setup

For the measurement of the electronic transport properties of monolayers deposited on Si, we have used out of the plane measurement in order know the vertical movement of electrons through the molecule for that it is essential to deposit a counter electrode, as schematically shown in **Fig. 2.17.**. An essential criterion for the fabrication of metal counter electrodes is that during the process it should not damage or short-circuit the monolayer. For present work we have used Hg drop contact, in which a small Hg drop was spread over the monolayer using micropipette. The diameter of the drop was measured using contact angle measurement system. Current voltage characteristics were recorded in a dark box using a potentiostat/galvanostat system (model: Autolab PGSTAT 30).

2.7. Gas sensing

The gas sensitivity of the films was measured using a commercially available gas sensitivity measurement setup, as shown in **Fig. 2.18.**. The sensor films are mounted on a heater surface. The temperature of the heater was controlled by an external power supply and temperature controller. The sensor assembly was mounted in a leak tight 1000 ml stainless steel container, and the known amount of gas (to be sensed) was injected into the chamber using a micro syringe. To measure the response of the sensor films for a particular gas, current at a particular bias as a function of time was measured by Keithley make 6487 picoammeter/voltage source and computer based data acquisition system. For the recovery of the sensor, the chamber was exposed to the ambient atmosphere. Commercially available Calibration Gas Standard pressurized (Chemtron Science laboratory Pvt. Ltd., India) cylinder was used and specific volumes of gases were injected in the test chamber to attain the required concentrations. The specifications of the cylinder were as follows: balance gas: N_2, filling pressure: 20 kg/cm^2 (19.4 atm.), preparation method: volumetric, preparation tolerance: ±20% and certification accuracy: ±2%. For the recovery studies, the chamber was exposed to the ambient atmosphere.

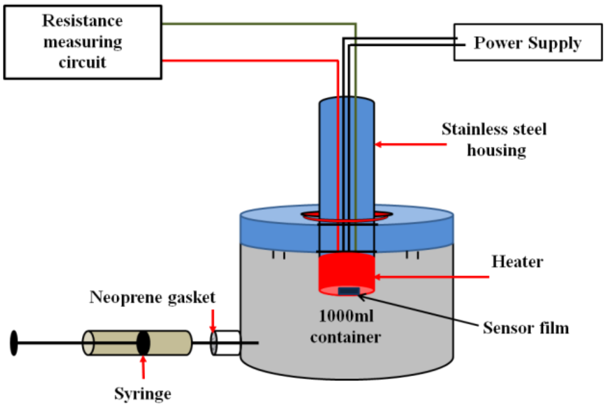

Fig. 2.18. Schematic of gas sensing setup.

2.8. Computational method

2.8.1. Electronic structure of molecules

As described in Chapter 1, typical devices for hybrid nanoelectronics consist of metal-molecular monolayer-Si (highly doped) structures. If the HOMO-LUMO gap is very wide (e.g. ~8 eV for alkane monolayers) and HOMO or LUMO under applied bias do not align with Fermi levels of either of the electrodes, then the charge transport takes place though non-resonant tunnelling. However, for the conjugated molecules the HOMO—LUMO gap is small (<3 eV)) and HOMO or LUMO under applied bias may align with Fermi levels of either of the electrodes. This allows charge transport through molecular orbitals. Therefore, theoretical investigation on the electronic structure of molecules is essential. In the present thesis work, we have used "General Atomic and Molecular Electronic Structure System (GAMESS)" software package to calculate the HOMO and LUMO of the molecules under investigations. GAMESS software utilizes ab-initio molecular orbital theory to calculate the electronic structures of the molecules.[160] The "*ab-initio*" computations are derived directly from theoretical principles, with no inclusion of experimental (empirical) data and are based on quantum mechanics. The time independent Schrödinger equation for a system containing *n* number of electron, and *N* number of nuclei like a cluster or molecule, can be written as

$$\hat{H}(r,R)\,\psi(r,R) = E(r,R)\,\psi(r,R)$$

Where H is the Hamiltonian operator, Ψ is the wave function and E is total energy or Eigen value of the whole system. The wave function, Ψ can be represent as

$$\psi(r, R) = \psi(r_1, r_2 \ldots\ldots\ldots\ldots r_n, R_1, R_2, \ldots\ldots\ldots\ldots R_n)$$

In *ab-initio* method, the Schrödinger equation is solved by selecting a method that in principle leads to a reasonable approximation to the solution. The approximations made are usually mathematical approximations relatively simpler functional form for complex function or getting an approximate solution of differential equation. Inessential part of solving the Schrödinger equation is the Born–Oppenheimer approximation, where the coupling between the nuclei and electronic motion is neglected. The dynamics of a many-electron system is very complex, and consequently requires elaborate computational methods. A simplification is done considering independent particle models, where the motion of one electron is considered to be independent of the dynamics of all other electrons. The interactions between the particles are approximated, by taking all interactions into account in an average fashion in electronic structure theory and this is called Hartree–Fock (HF) theory. In the HF model, single electrons are described by one electron orbital $\chi_n(r_n)$ (single particle functions) consisting of a product of a spatial orbital (molecular orbital) depending on the position of the electron $\psi_n(r_n)$ and a spin function (α or β) depending only on the spin coordinate.

$$\chi_n(r_n)=\psi_n(r_n)\ \alpha\ (n)$$

$$\chi_n(r_n)=\psi_n(r_n)\ \beta\ (n) \text{ where } \alpha = \textit{upspin},\ \beta = \textit{downspin}$$

A many particle wave function describing electrons is forced to obey the Pauli Exclusion Principle. The best set of orbitals is obtained by Variational principle. The HF orbitals give the lowest energy within the restriction of the wave function being a single Slater determinant. The shape of a given molecular orbital describes the probability of finding an electron, where the attraction to all the nuclei and the average repulsion to all the other electrons are included. Since the other electrons are described by their respective orbitals, the HF equations depend on their own solutions, and must therefore be solved iteratively. HF theory only accounts for the average electron–electron interactions, and consequently neglects the correlation between electrons. Density Functional Theory (DFT) in the Kohn–

Sham version can be considered as an improvement on HF theory, where the many-body effect of electron correlation is modelled by a function of the electron density**.** Kohn & Sham proposed a method that involves coupling of wave function and density approach. The key to Kohn–Sham theory is to calculate the kinetic energy under the assumption of non-interacting electrons (in the same sense that HF orbitals in wave mechanics describe non-interacting electrons)). In reality, the electrons are interacting but the difference between the exact kinetic energy and that calculated by assuming non-interacting orbital's is small. To accommodate this, small difference in energy, an exchange–correlation term is introduced, and a general DFT energy expression can be written as

$$E_{DFT} = T_s(\rho) + E_{nc}(\rho\ ) + J(\rho\ ) + E_{Xc}(\rho\ )$$

In this equation, *T* is the kinetic energy term and *S* is kinetic energy when there is no electron electron-electron interaction. *J* and *En c*are potential energy terms and *ρ* are the density. Equating with exact energy, we get *Exc* is the part that remains after subtraction of the non-interacting kinetic energy, and the *Enc* and *J* potential energy term. So

$$E_{\ XC}(\rho) = [T(\rho) - T_s(\rho\ ) - [E_{\ ee}(\rho\ ) - J\ (\rho\ )]$$

First term in the parenthesis is related to kinetic correlation energy, while the last term contains both potential correlation and exchange energy. The exchange–correlation energy, which is a rather small fraction of the total energy, is then the only unknown functional, and even relatively crude approximations for this term provide quite accurate computational models. The simplest model is the local density approximation, where the electron density is assumed to be slowly varying, such that the exchange–correlation energy can be calculated using formulas derived for a uniform electron density. Many more functions have been developed, and the development of more accurate functional is an ongoing process. In practice combinations: e.g. SVWN, RPBE, BLYP, PBELYP, BPW91 etc. are used. All these exchange correlation functional are purely based on density functional. But some hybrid exchange correlations functional are also available in which exchange from Hartree-Fock method is mixed to get better results. A commonly used hybrid pair of functions are Becke's 1988 exchange functional (B88 or B) and the Lee–Yang–Parr (LYP) correlation functional, or the so called B3LYP hybrid functional, which combines the B88 and LYP functions via three parameters (indicated by the 3) with three additional functions.

In this thesis work, the system geometries and total energies were optimized under the density functional theory using the linear combination of atomic orbital (LCAO) approach. A standard 6-31G+(d, p) basis set was employed for this purpose.[161,162] The exchange correlation energy was calculated using Becke's threeparameterfunction.[163] This function consists of Hartree-Fock exchange, Becke's exchange functional and the Lee-Yang-Parr correlation functional.[164] By this method geometry of molecule was optimised then HOMO and LUMO of molecules were calculated and their orbital pictures were drawn using Molkel software.

2.8.2. Simulation of current voltage characteristics

The simulations of current-voltage characteristics of metal-monolayer-Si systems were carried out using Virtual Nano lab (VNL) software package.[165] Numerical calculations in VNL is processed by the Atomistix Tool Kit (ATK), which combines numerical methods, such as, DFT, semi-emperical (extended Huckel), Slater Koster and non-equilibrium Green's functions (NEGF) to describe the detailed electronic structure of nanoscale devices. The most unique capability of VNL is the ability to investigate the electronic transport properties of nanoscale devices. Advanced numerical algorithms enable the application of a bias across the structure and analysis of the current-voltage characteristics of two-probe systems.

Since our systems were very large we donetheoretical calculations of the electronic transport behavior were carried out in two steps. To start with, we have first optimized the ground state geometries of the molecules by *ab-initio* molecular orbital calculations. Using the optimized configuration of these molecules as the central device region, the transport characteristics were calculated by non-equilibrium Green's function method. The ionic optimization of molecules was carried out without any symmetry constraint at the B3LYP/6-31G (d, p) level of theory.

After establishing the equilibrium geometries of molecules, their transmission spectra and the *J-V* characteristics were calculated. For this, a model for a two-probe system was constructed by placing the molecules between two gold electrodes. A thiol end group was used for attachment of the molecule with the electrode. The interface geometry of the thiol-terminated molecule and the electrode was optimized to ensure good overlap between the device and the electrode. Earlier we have performed the calculations using plane wave-based pseudo potential approach with a prototype thiol molecule (methyl thiol) on the periodic Au(111) surface.[166] The distance between the Au (111) surface and the terminal S (or H) atom, located at the hollow site of the Au surface was found to be 2.52 Å. Presently, the two Au(111)-(n × n) (n depends on size of molecule and no. of atoms) surfaces with periodic boundary conditions were used to model the left and right electrodes. The Au/molecule/Au configuration was divided into three parts: left electrode, right electrode, and the central scattering region. In our models, there were n gold layers in each of the left and right electrode unit cells. The scattering region was composed of the isolated molecule together with the respective gold layers on the left and right sides. The electron-transport properties of the Au/molecule/Au systems were investigated using the ATK 11.2.3 program, where a semi-empirical extended Huckel theory in combination with the first-principle non-equilibrium

Green’s function (NEGF) is employed. A k-point sampling of 100 was used in the electron-transport direction (Z direction).[167]

Chapter-3

CHAPTER-3

Porphyrin based molecular electronic devices

3.1. Introduction

The key electronic properties of the organic molecules, required for constructing SAM on Si surface as molecular-level devices have been elaborated in Chapter-1. Many of these are amenable with the porphyrins,[168] and are listed below:

(1) They form stable π radicals, which makes them robust in real world applications;

(2) They exhibit multiple oxidation states, achievable at low voltages;

(3) They have high charge retention abilities;

(4) They can withstand high temperatures (~400°C);[42]

(5) There are eight open β-pyrrole sites and four *meso* sites that can be elaborated further to tune the electronic properties.

In the present investigations, some porphyrin-Si hybrids were synthesized and used to fabricate two types of molecular devices *viz*. resonance tunneling diodes and current rectifiers. These are discussed in this chapter.

3.2. Resonance tunneling diode

Amongst various electronic attributes, the negative differential resistance (NDR) behavior (*i.e.*, an initial rise in current and its subsequent sharp drop even with progressively augmented voltage, as opposed to Ohm's law) has drawn significant attention, because of its potential application in the realization of logic devices and memory circuits,[17,85,90] and is found in a variety of molecular devices.[169,170] In pioneering studies, Lindsay and his group,[171] and Tao[172] reported J–V curves of porphyrins-metal ions combinations that show NDR-like effects.[172,173] Since then, NDR effects have been reported using different types of junctions *viz*. (i) 2'-amino-4,4'-di(ethynylphenyl)-

5'-nitro-1-benzenethiol, sandwiched between two metal electrodes (observed at 60 K),[17] (ii) Pd/ferrocene self-assembled layer/Au structure,[174a] (iii) cyclopentene molecules, deposited on p-type hydrogen free Si(001) (observed at 80 K)[174b] (iv) styrene and 2,2,6,6-tetramethyl-1-piperidinyloxy, deposited on degenerately doped Si(100) 2 × 1 reconstructed surfaces,[174c] and (v) disulfide molecules deposited on Si.[174d]

Impressive progress notwithstanding, the search for alternate single molecules or a finite ensemble of self-assembled molecules showing NDR property at a lower bias is currently the subject of research in molecular electronics. This would enable low-voltage nanoscale analogues of multistate electronic switches. A large peak-to-valley ratio (PVR) in the NDR effect, functioning of the device at room temperature, and high reproducibility are the prerequisites for applications in hybrid nanoelectronics. The reported molecular hybrids, exhibiting the NDR behavior do not fulfill many of these criteria. Further, the measurements were carried out under ultra-high vacuum in certain cases. A rational design of such NDR devices can be realized on understanding the mechanism of NDR behavior. The NDR property can be rationalized as follows. The energy gap (ΔE) between the energy states (LUMO/HOMO) of the molecular bridges and the energy levels (Fermi levels) of the donor and acceptor units control the electron-transfer rate and current flow.[175a,b] For large ΔE, the ET process is dominated by a “through- bond” non-resonant tunneling mechanism, where the organic molecules generally act as poor electron conductors. However, alteration of their electronic structures can induce the ET process via resonance tunneling or a hopping mechanism. The change from a non-resonant to resonant tunneling would result in an abrupt increase in the current, and the measured J–V curves will show NDR characteristics.[175c,d] Resonance tunneling requires a double potential barrier along the electron transfer coordinate. As discussed in Chapter-1, such a double potential barrier might show NDR effect.[176] The $\sigma-\pi-\sigma$ molecular architecture is analog to the tunnel diode, with a ‘quantum well’ surrounded by thin layer barriers.[177] Here, the π–moiety (a conjugated molecule) acts as a quantum well and the σ–moieties (alkyl chains) as the tunnel barriers. The NDR effect in such a monolayer is expected if electrons tunnel through some resonant states of the π–moiety. This hypothesis was substantiated previously from the supervisor's laboratory, using *N*-(2-(4-diazoniophenyl)ethyl)-*N'*-hexylnaphthalene-1,8,4,5-tetracarboxydiimide-tetra-fluoroborate (DHTT) as the σ–π–σ system. However, the device, constructed with Si-DHTT-Hg showed poor NDR effect (~10) with hysteresis.[178]

In view of this, presently the possibility of using the oxidation states of the porphyrin molecules as molecular-scale information storage systems was explored. For this, two new *O*-dialkylated porphyrins **Ia** and **Ib** with tetraphenylporphyrin (TPP) and a fluoro-derivative of TPP derivatives were synthesized and used to form their monolayers on Si (111) surface by electro-grafting. The porphyrin cores served as the respective quantum wells (π moiety), while a C_6-alkyl chain and a C_{11}-alkenyl chain acted as the barriers. Subsequently, the monolayers were characterized by multiple techniques, the efficacy of the new devices in nano-electronics assessed, and the results explained using appropriate theoretical calculations. These are sequentially presented below.

3.2.1. Fabrication of resonance tunnelling diode

3.2.1.1 Synthesis of σ–π–σ porphyrin

Compared to the naturally occurring β-substituted porphyrins, the *meso*-functionalized porphyrins are often used for constructing porphyrin-based SAMs. One the major advantages of this is the rectilinear arrangement of the four *meso* substituents and the ease of their syntheses from pyrrole and simple acyl reactants. In comparison, the β-substituted porphyrins are amenable from the β-substituted pyrroles, the syntheses of which are often cumbersome. The meso-substituted porphyrins are conventionally synthesized by a one-pot reaction between pyrrole and an aryl aldehyde in refluxing propionic acid for 30 min, followed by cooling to obtain the products as glittering purple crystals (**Scheme-3.1.**). This method of Adler and Longo, developed in the 1960's,[179] is a practical version of the sealed-bomb method of Rothemund that requires even higher temperatures.[180]

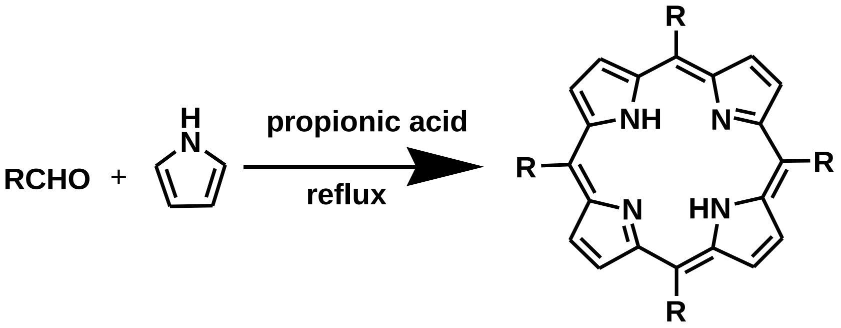

Scheme-3.1. Synthesis of symmetrical porphyrins by Adler and Longo method

However, the scope of the method is primarily limited to the synthesis of symmetric porphyrins, containing an aryl substituent (derived from the aldehyde unit) at each of the four *meso*-positions. Extension of the method to make porphyrins that bear two types of *meso*-substituents relied on an early and widely practiced form of combinatorial chemistry, where condensation of two aldehydes (A-CHO and B-CHO) and pyrrole afforded a statistical mixture of six types (A_4, A_3B, *cis*-A_2B_2, *trans*-A_2B_2, AB_3, and B_4) of porphyrins. The ease of carrying out the reaction was offset by the laborious chromatographic separation required to purify the target porphyrins from the mixture. Thus, the Adler-Longo method presented two significant limitations: (1) harsh reaction conditions that leads to extensive polymerization of pyrrole limiting the yields, and (2) lack of any rational access to porphyrins, bearing two to four distinct *meso*-substituents. For the present work, it was envisaged that the A_2BC-type porphyrins would be ideally suited as the required $\sigma-\pi-\sigma$ systems, because the alkyl groups B and C ring can function as the σ moieties. Further, for the covalent attachment of the porphyrins to the Si (111)-surface, the presence of a terminal alkene function in either B or C ring was also conceived. The alkenyl chain would be particularly useful in electro-grafting of monolayers of the molecules on Si (111) surface. Thus, the overall requirement was porphyrins such as **Ia** and **Ib**, which differ only in presence or absence of a F atom at their respective A_2 phenyl groups (**Fig. 3.1.**)

Lindsey *et.al.* has developed a directed route to synthesize porphyrins with distinct *meso* substituents (ABCD type system) via an intermediate dipyrromethane.[98-107] This method seemed attractive in the present endeavour of synthesizing the required A_2BC type porphyrins, and was adopted. The syntheses started by a base-catalyzed alkylation of 4-hydroxybenzaldehyde with 1-bromoundec-10-ene (**2**) or 1-bromohexaneto afford the aldehydes **3a** and **3b** respectively (**Scheme-3.3.**).The bromide **2**, required for the *O*-alkylation of benzaldehyde was prepared by $LiAlH_4$ reduction of the 10-undecenoic acid followed by bromination of the resultant alcohol **1** with Ph_3P/Br_2 in the presence of pyridine (**Scheme-3.2.**).[181]

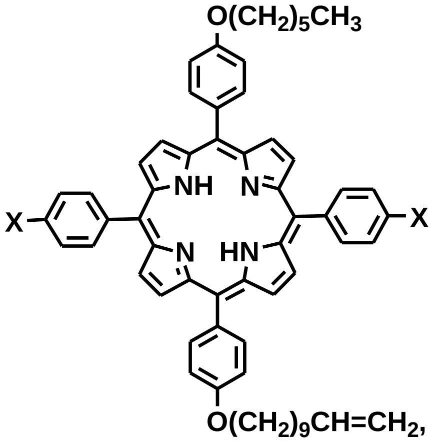

Ia: X=H; **Ib**: X=F

Fig. 3.1. Chemical structures of **Ia** and **Ib**

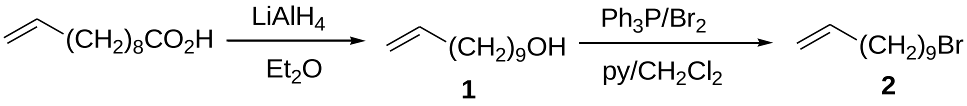

Scheme-3.2. Synthesis of 11-Bromo-undecene

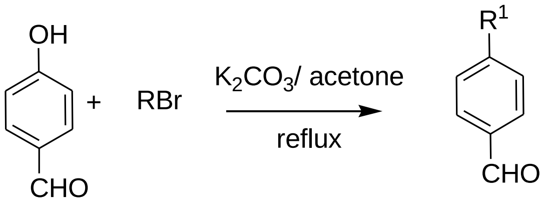

3a :R^1 = -O(C $H_2)_5CH_3$

3b: R^1 = - $O(CH_{2)9}CH=CH_2$

Scheme-3.3. Base catalysed alkylation of p-hydroxybenzaldehyde

Compounds **3a** and **3b** were characterized by ^1H NMR, ^{13}C NMR, LC-MS and CHN analyses. The ^1H NMR spectrum of **3a** (**Fig. 3.2**) showed a singlet at δ 4.01 for the OCH_2 protons, along with the triplets at δ 0.89 for the terminal CH_3 group, besides the resonances due to the CH_2 and aryl protons, and the CHO group. Corresponding peaks of OCH_2 and terminal CH_3 carbon were seen in ^{13}C NMR

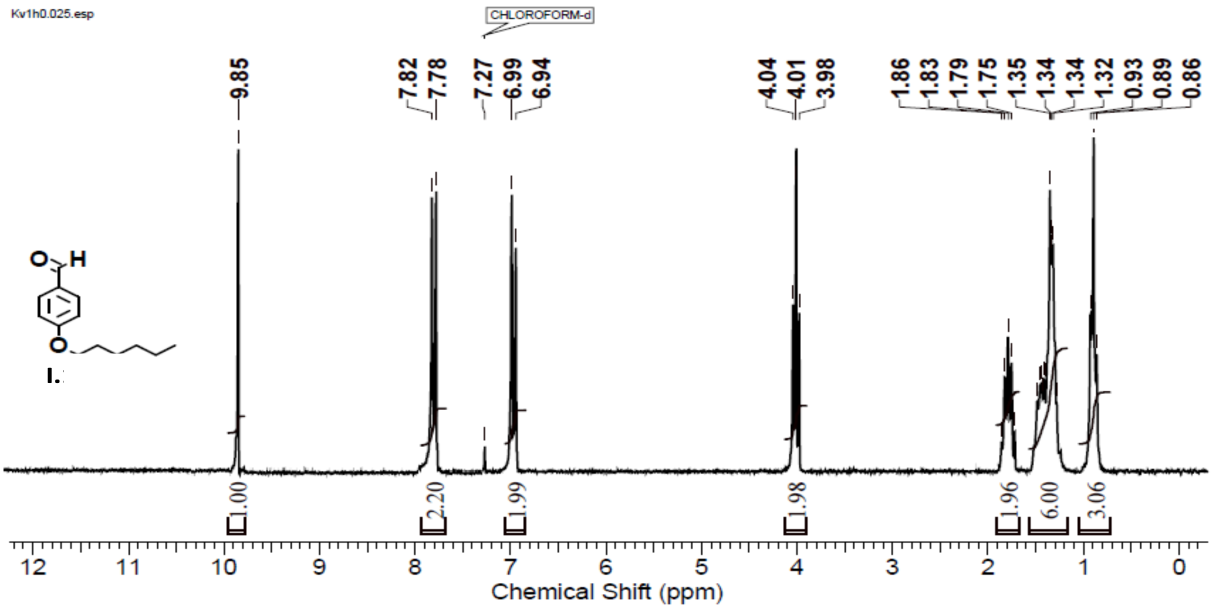

Fig. 3.2. ^{1}H NMR spectrum of **3a**

spectrum at δ 68.06 and 13.62 ppm. Similarly, the ^{1}H/ ^{13}C NMR spectrum of **3b** (**Fig. 3.3**) showed all the above peaks except those for the terminal CH_3 group. Instead, the 1H-multiplets and 2H-triplets at δ 5.8 and 4.9 ppm respectively in ^{1}H NMR spectrum and peaks at δ 139.1 and 114.8 ppm in ^{13}C NMR spectrum accounted for the terminal olefinic moiety.

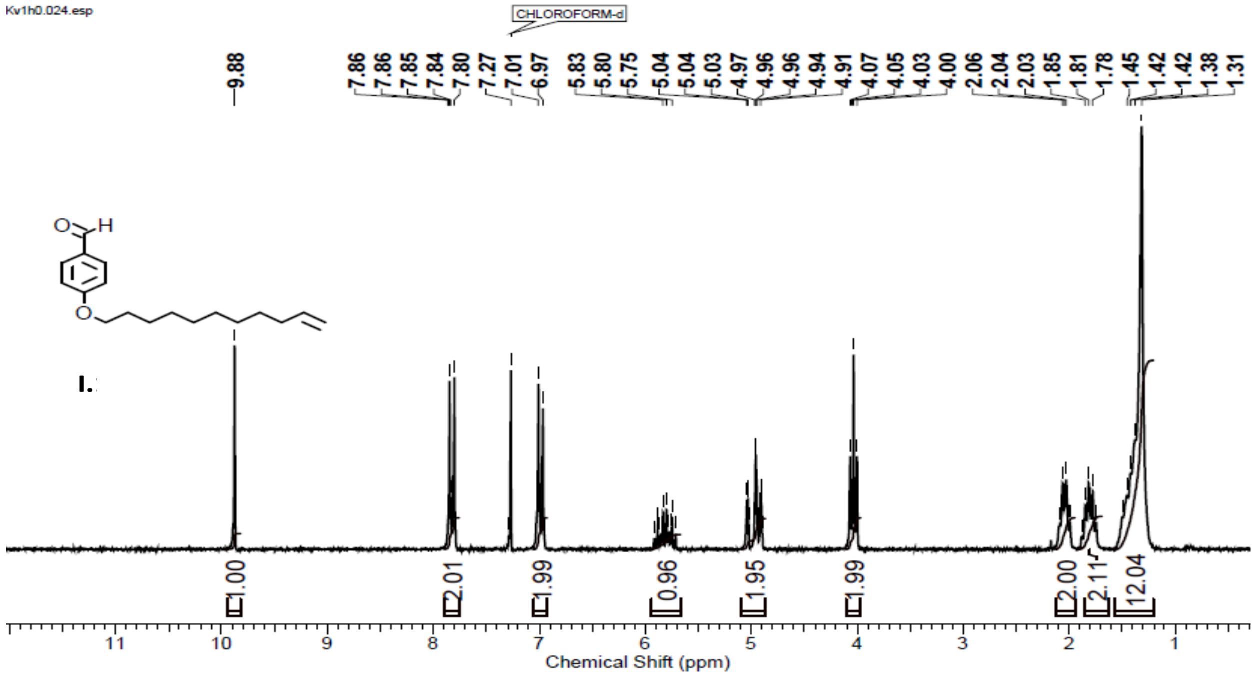

Fig. 3.3. ^{1}H NMR spectrum of **3b**

The next task was to synthesize dipyrromethane using the above aldehydes. Amongst the reported methods, the one-pot method is better because of its expediency and scalability (**Scheme 3.4**).[98-103] Presently this was achieved by condensing the aldehydes **3a** and **3b** with excess pyrrole in the presence of an acid (TFA or $BF_3.O(Et)_2$) as the catalyst at room temperature (**Scheme-3.5**). Maintenance of a high pyrrole/aldehyde ratio (25:1 to 100:1) is obligatory to suppress oligomerization. Here, pyrrole acts both as the reactant and solvent. The reaction afforded the dipyrromethanes **4a** and **4b** respectively. The ^{1}H NMR (**Figs. 3.4** and **3.5**) of **4a** and **4b** showed four singlets at δ 5.43, 5.93, 6.17 and 6.69 corresponding to the *meso*-CH (1H), and pyrrole β- and α-protons (6H) respectively. Similarly,^{13}C NMR spectrum showed peaks at δ 129.3, 107.04, 108.4,

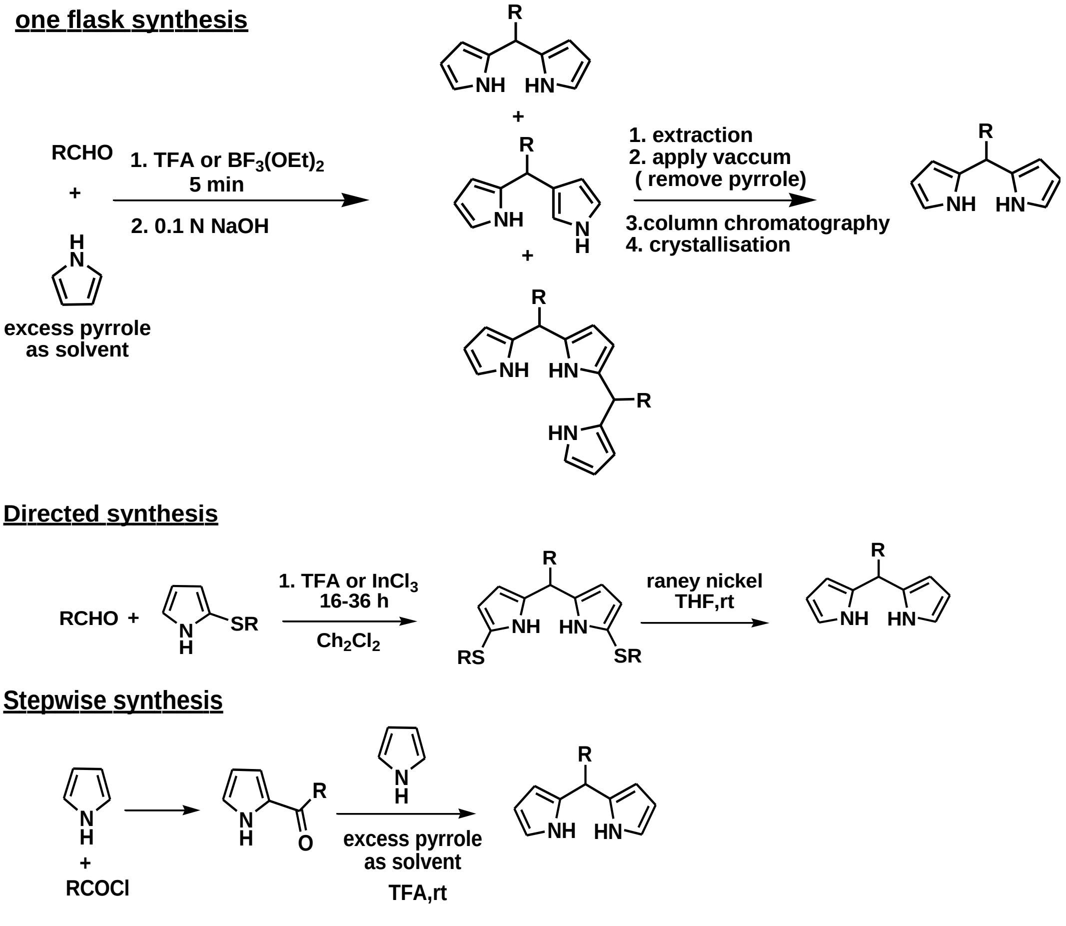

Scheme-3.4. Different methods of dipyrromethane synthesis

132.9 and 134.0 corresponding to the *meso*-C, pyrrole β- and α-C respectively. These confirmed formation of the dipyrromethanes.

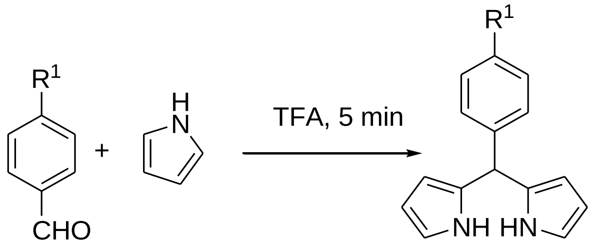

3a :$R^1 = O(CH_2)_5CH_3$

3b: $R^1 = O(CH_2)_9CH=CH_2$

4a/4b

Scheme-3.5. Synthesis of the dipyrromethane **4** by Lindsey method

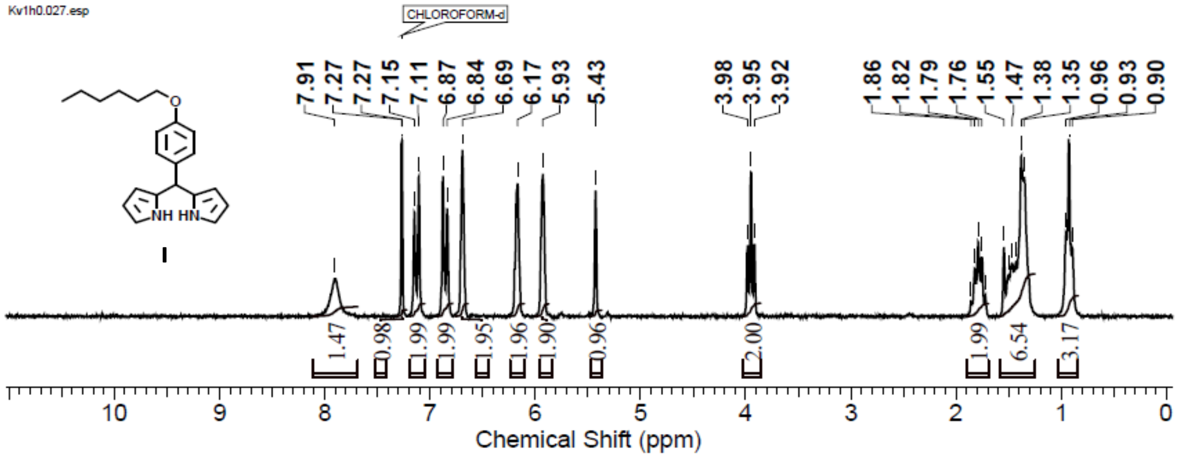

Fig. 3.4. ^{1}H NMR spectrum of **4a**

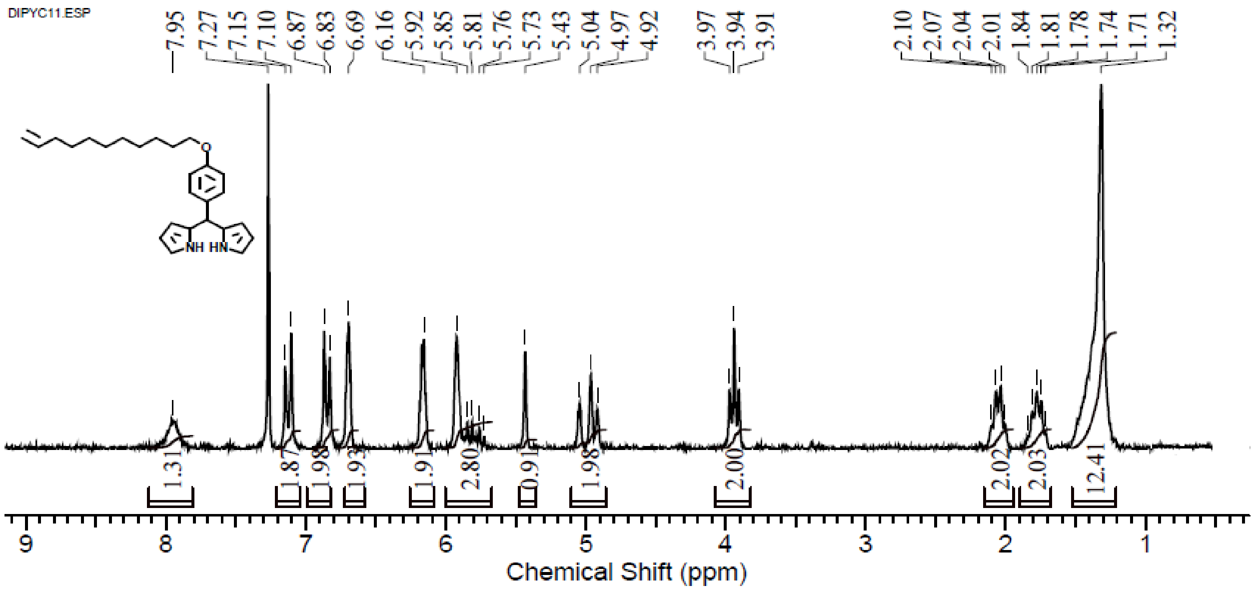

Fig. 3.5. ^{1}H NMR spectrum of **4b**

A simple route for the synthesis of asymmetrical (A_2BC) porphyrins involves acid-catalyzed condensation between a dipyrromethane with an aldehyde, but this approach is often stymied by scrambling processes to produce undesired porphyrin byproducts.[98] Instead, an alternative multi-step route is via (i) diacylation of dipyrromethanes; (ii) subsequent hydride reduction of the dicarbonyl compounds followed by; (iii) condensation of the resultant dicarbinols with another dipyrromethane. Selective introduction of the α-acyl group is the key step in this route. This is best achieved by forming the dipyrromethane-Grignard followed by acylation with an acid chloride.[103] Accordingly, **4a** was treated with 4-5 equiv. of EtMgBr to generate the required Grignard reagent which on reaction with a suitable acid chloride (**5a** or **5b**) afforded the corresponding 1,9-diacyldipyrromethanes (the AB_2 unit of the target porphyrins) **6a** and **6b** respectively along with the monoacyl-dipyrromethanes (**Scheme-3.6.**). The desired diacyl-dipyrromethanes could not be crystallized from the solid foam-like mixture, reducing the yields drastically.

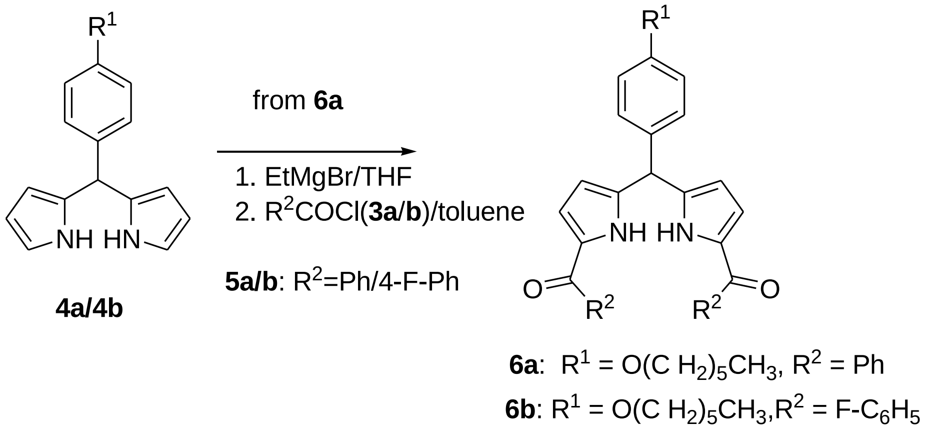

Scheme-3.6. Synthesis of the diacyl-dipyrromethane **6** by Lindsey method

The singlets at δ 6.00 and 6.66 accounting for four pyrrole protons, and absence of pyrrole α-H peak in the ^{1}H NMR spectra of **6a/b** as well as appearance of the carbonyl peak at δ 184.4 in ^{13}C NMR spectrum confirmed the acylation at the two α-positions. Moreover for **6b** the ^{13}C NMR spectra showed additional peak δ 162.5 for C-F. The ^{1}H NMR and ^{13}C NMR spectra of **6a** and **6b** are shown in **Figs. 3.6.** and **3.7.** respectively.

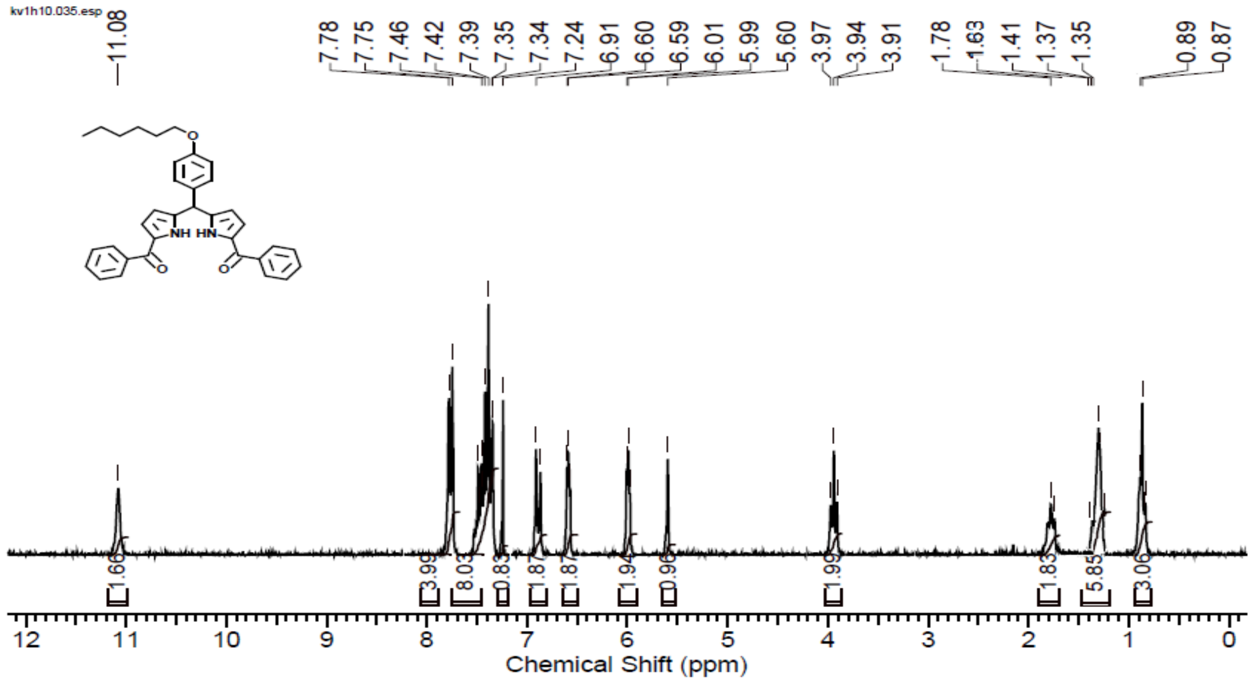

Fig. 3.6. ^{1}H NMR spectrum of **6a**

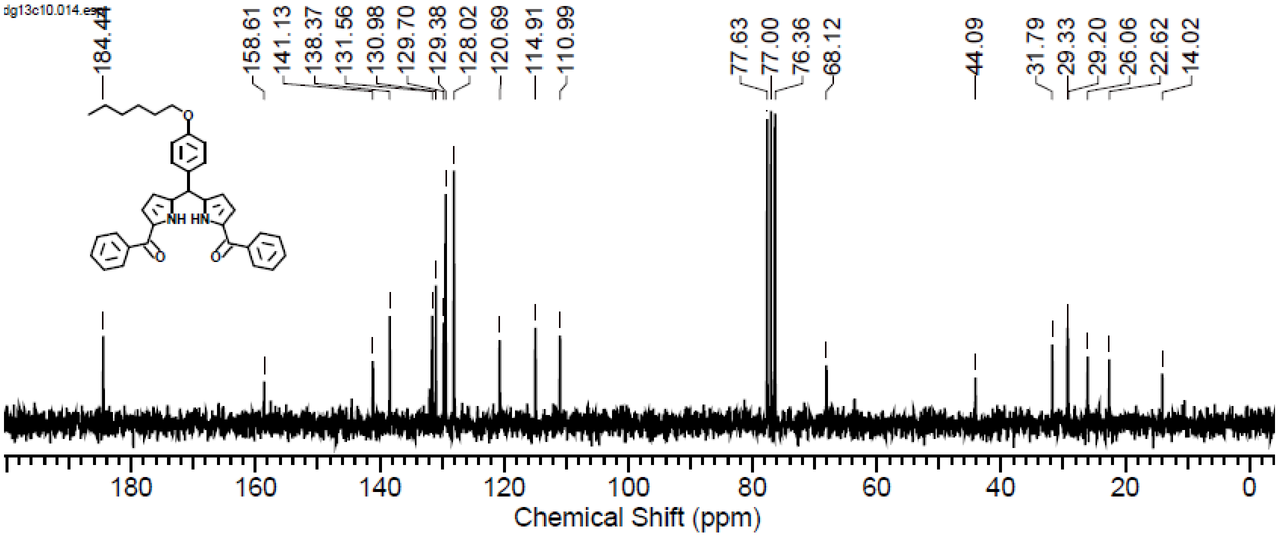

Fig. 3.7. ^{13}C NMR spectrum of **6b**

With the 1,9-diacyldipyrromethanes **6a** and **6b** in hand, the synthesis of an A_2BC-porphyrin was achieved by reduction of **6a**/**6b** with $NaBH_4$ in tetrahydrofuran (THF)/MeOH to obtain the unstable dicarbinols, which on acid-catalyzed condensation with the dipyrromethane **4b** and subsequent oxidation with 2,3-dichloro-5,6-dicyano-1,4-benzoquinone (DDQ) gave **Ia** and **Ib** (**Scheme-3.6**).[104-107]

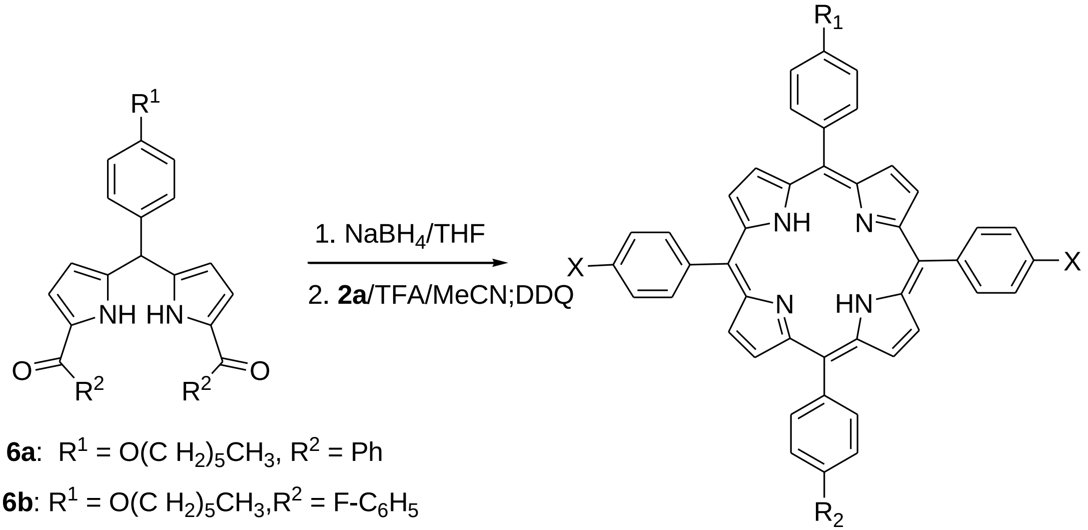

6a: $R^1 = O(CH_2)_5CH_3$, R^2 = Ph

6b: $R^1 = O(CH_2)_5CH_3$,$R^2 = F\text{-}C_6H_5$

Ia: $R^1 = O(CH_2)_5CH_3$, $R^2 = O(CH_2)_9CH{=}CH_2$, X=H

Ib: $R^1 = O(CH_2)_5CH_3$, $R^2 = O(CH_2)_9CH{=}CH_2$, X=F

Scheme-3.7. Synthesis of the target porphyrins

Formation of required porphyrin **Ia**/**Ib** was confirmed by NMR spectra (**Figs. 3.8.—3.11.**) and MALDI-TOF analysis. The ^{1}H NMR peak at δ -2.8 for the NH group is a signature peak of metal free porphyrins, while that at δ 8.88 (8H) corresponded to the pyrrollic hydrogens of porphyrin. Multiplets at δ 5.8 and 5.0 indicated the presence of terminal double bond, whereas triplet at 0.97 confirms terminal CH_3 group. Similarly ^{13}C NMR spectra showed peaks at δ 14.1, 68.4, 112–114, 118–130, 134.1–135.7, 138–139 corresponds to terminal CH_3, OCH_2, *meso*-C, double bond, β-pyrrolic and α-pyrrolic carbons respectively.

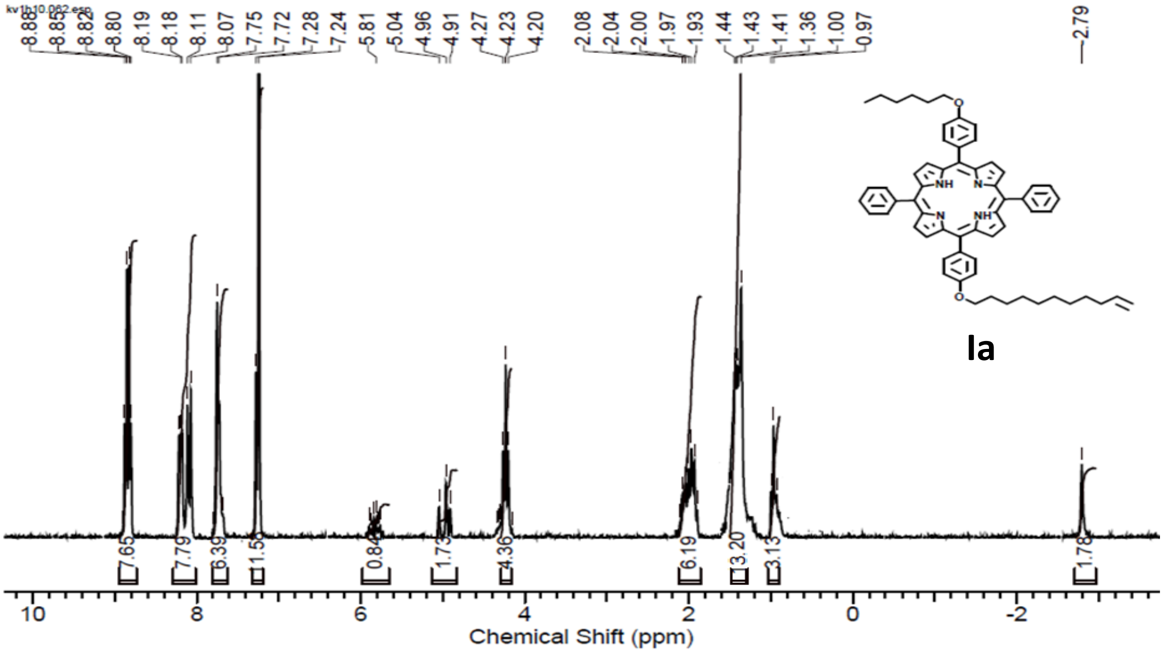

Fig. 3.8. ^{1}H NMR spectrum of **Ia**

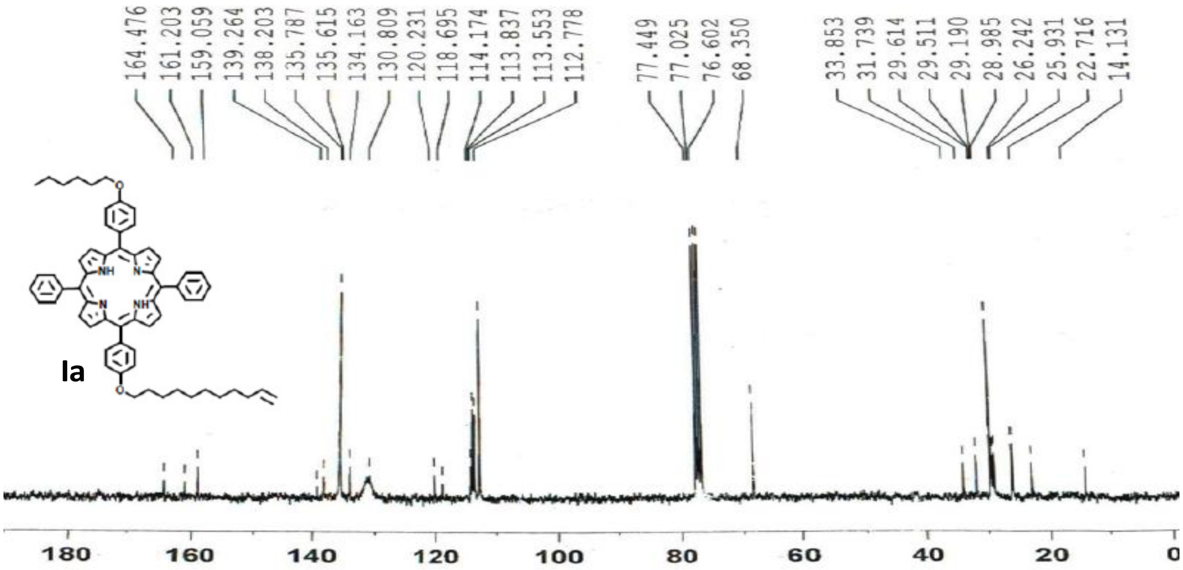

Fig. 3.9. ^{13}C NMR spectrum of **Ia**

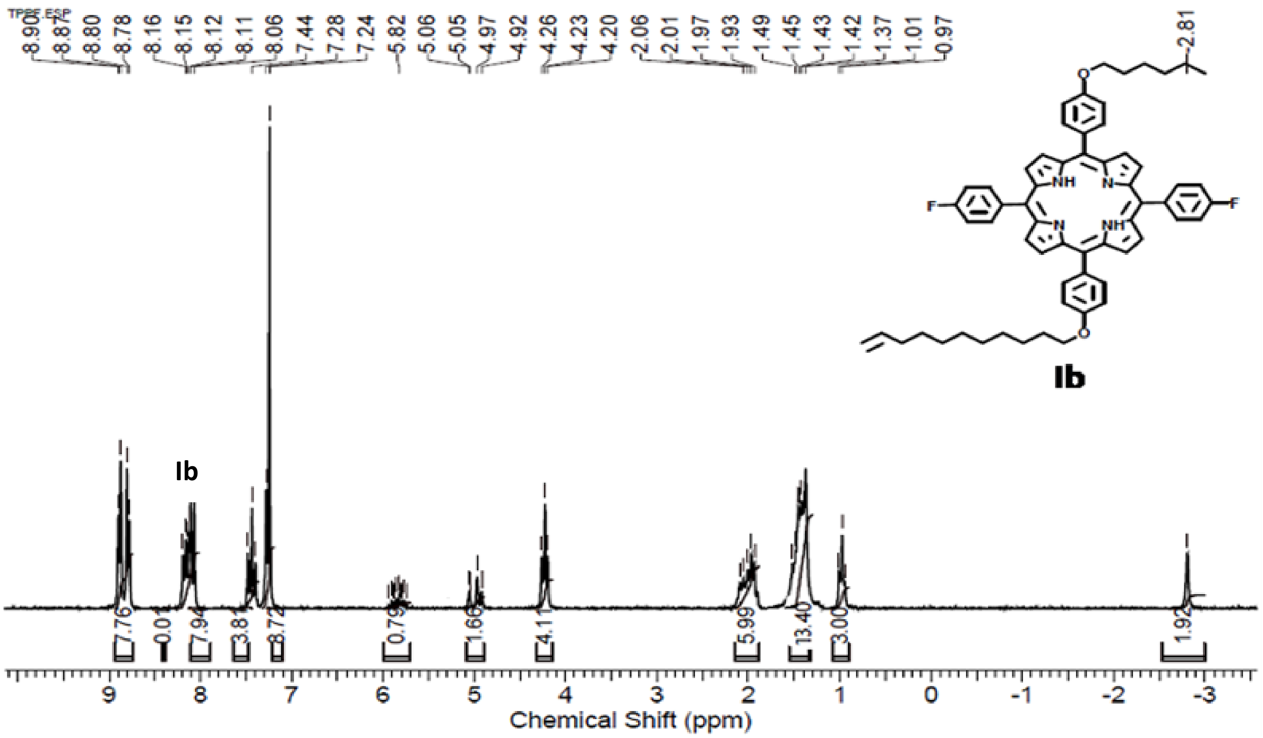

Fig. 3.10. ^{1}H NMR spectrum of **Ib**

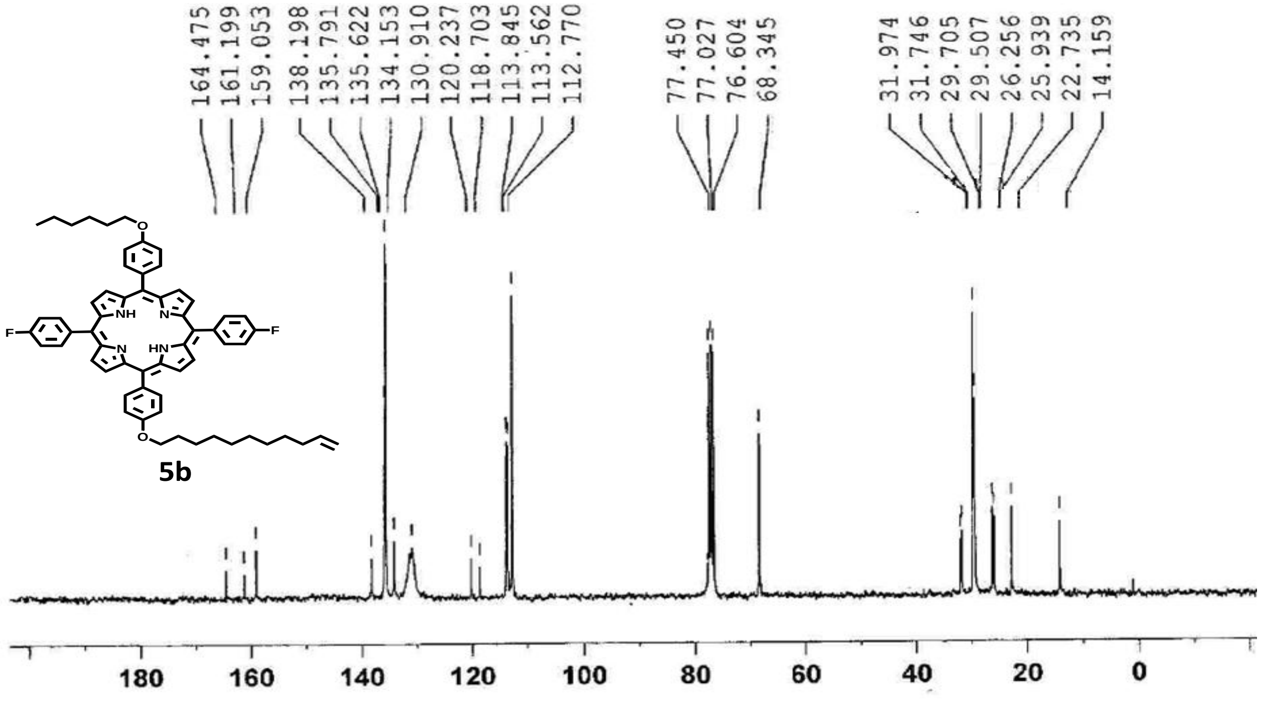

Fig. 3.11. ^{13}C NMR spectrum of **Ib**

3.2.1.2. Preparation of the grafted organic assembly

The electrochemical deposition of **Ia** and **Ib** was carried out by cyclic voltammetry (CV) using the Si-H wafers as the working electrode (WE), Pt as the counter electrode (CE) and Ag/AgCl as the reference electrode (RE). The solution contained 0.1 M Bu_4NP as the electrolyte and **Ia** or **Ib** (1 μM) in dry CH_2Cl_2. The CV was run from 0 to -1 V for 25-50 cycles at a scan rate 0.05 V/s under an inert atmosphere. The CV (**Fig. 3.12.**), recorded during electrochemical deposition of the molecules **Ia** and **Ib** on Si showed an irreversible peak at ~ 0.3 V, indicating covalent attachment of the porphyrin molecules at the H-terminated Si surface. The electrographting procedure and mechanism of Si-H monolayer formation have already been explained in Chapter-2 (section 2.2.2). Using different number of scans (5, 10, 20, 25 and 30); monolayers of **Ia** and **Ib** on Si (111) were prepared. The

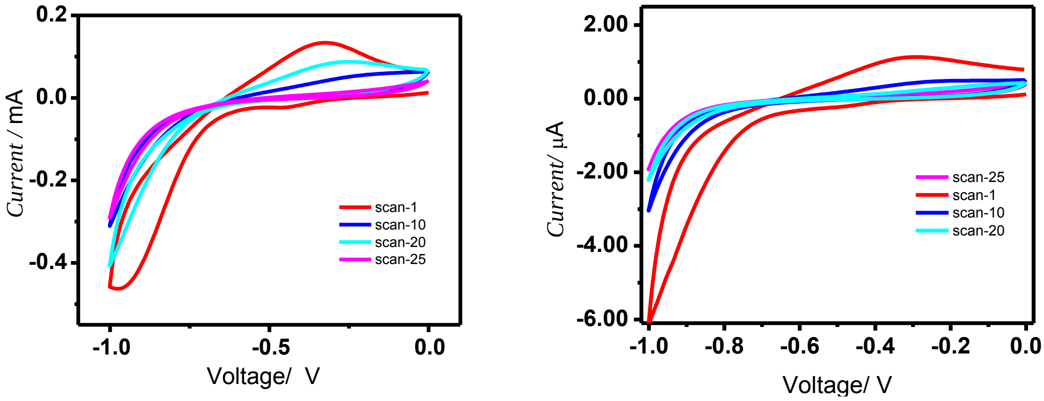

(a) **(b)**

Fig. 3.12. CV of electrochemical deposition of the prophyrins. (a) **Ia**; (b) **Ib**.

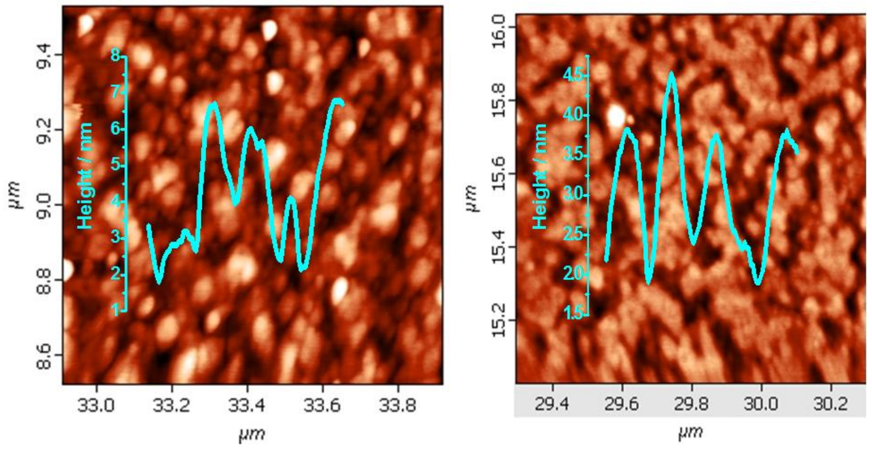

(a) **(b)**

Fig. 3.13. AFM images of the prophyrin-grafted monolayers. (a) **Ia**; (b) **Ib**.

AFM analyses (**Fig. 3.13.**) revealed formation of compact monolayers with both **Ia** and **Ib** at 25 scans, while multilayers were formed at higher scans. The monolayers were more organized with least number of voids and hillocks.

3.2.1.3. Monolayer characterization

In order to ascertain the monolayer deposition on Si surface, the electro-grafted materials were characterized by contact angle measurement, polarized FT-IR spectroscopy, X-ray reflectivity (XRR), ellipsometry, AFM, secondary ion mass spectrometry (SIMS) and electrochemistry. The contact angles of deionized water in case of Si wafers, grafted with **Ia** and **Ib** were ~ 58° and 64° respectively, whereas for the cleaned Si wafer it was 84°. The low contact angles of the monolayers suggested them to be tilted on the surface. This was also confirmed by ellipsometry, where the average thicknesses of respective monolayers were found to be ~ 2.3 ± 0.2 nm in case of **Ia** and 2.9 ± 0.2 nm in **Ib**.

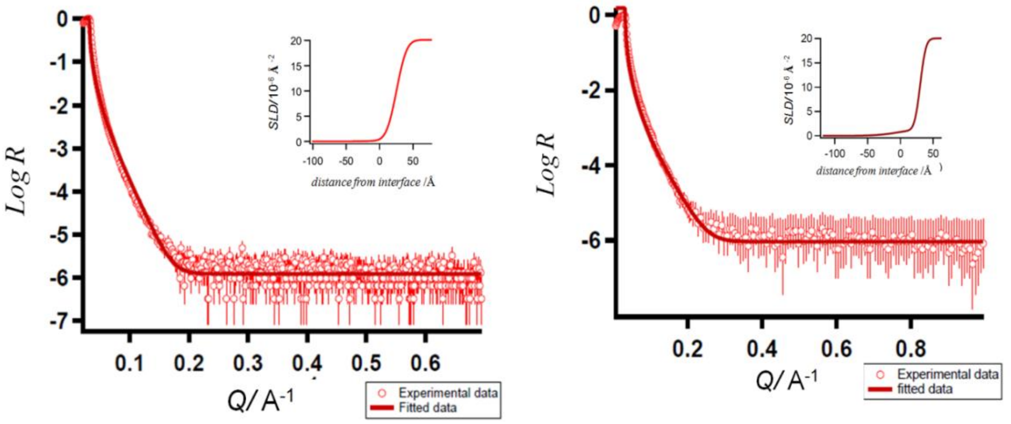

(a) **(b)**

Fig. 3.14. XRR curve of the porphyrins-grafted monolayers.(a) **Ia**; (b) **Ib;** inset: SLD plots

The room temperature XRR experiments further confirmed the thicknesses of the monolayers. The reflectivity data (**Fig. 3.14.**) was fitted using the MOTOFIT software, based on Parratt's formalism. The scattering length density (SLD) values of the monolayers were calculated from the density of monolayer and molecular formula of the molecule. From the plot of SLD *vs.*

interface distance, the thicknesses for **Ia** and **Ib** were found to be 2.54 ± 0.02 nm and 3.05 ± 0.03 nm respectively (**Fig. 3.14. inset**). These values are lower than the theoretically calculated (using Molkel software) length ~3.9 nm of the porphyrins **Ia** and **Ib**. The roughness values for the monolayers of **Ia** and **Ib** *viz*. 24.0 Å (SLD = 0.22 E-6 Å^{-2}, $\chi_{\mathbf{Ia}}^2 = 0.04913$) and 29.7 Å (SLD = 2.23 E-6 Å $^{-2}$ $\chi_{\mathbf{Ib}}^2 = 0.03049$) were close to their thicknesses estimated by ellipsometry. This implied that the molecules **Ia** and **Ib** formed monolayers with some pinholes. The XRR data also indicated that the tilt angles of the monolayers were ~39^{o} and 51.4^{o} for **Ia** and **Ib** respectively. The AFM analyses revealed the void depths of ~ 2.3 nm for **Ia** and 2.9 nm for **Ib** (**Fig. 3.13.**). Compared to that of **Ia**, the monolayers of **Ib** were more compact and uniform with large grain size.

The molecular densities of the monolayers, determined by fast scan (10 V/s) CVs are shown in **Fig. 3.15.**. The CVs exhibited a reversible peak at +0.8 V for the respective porphyrin moieties. The net charge transferred during the oxidation process, calculated from area under the oxidation peak were 4.5 × 10^{-8} C and 8.8 × 10^{-7} C respectively for **Ia** and **Ib**. These amounted to the surface coverage of 4.3 × 10^{11} and 3.4 × 10^{12} molecules/cm^2 respectively for **Ia** and **Ib**. Thus, the surface

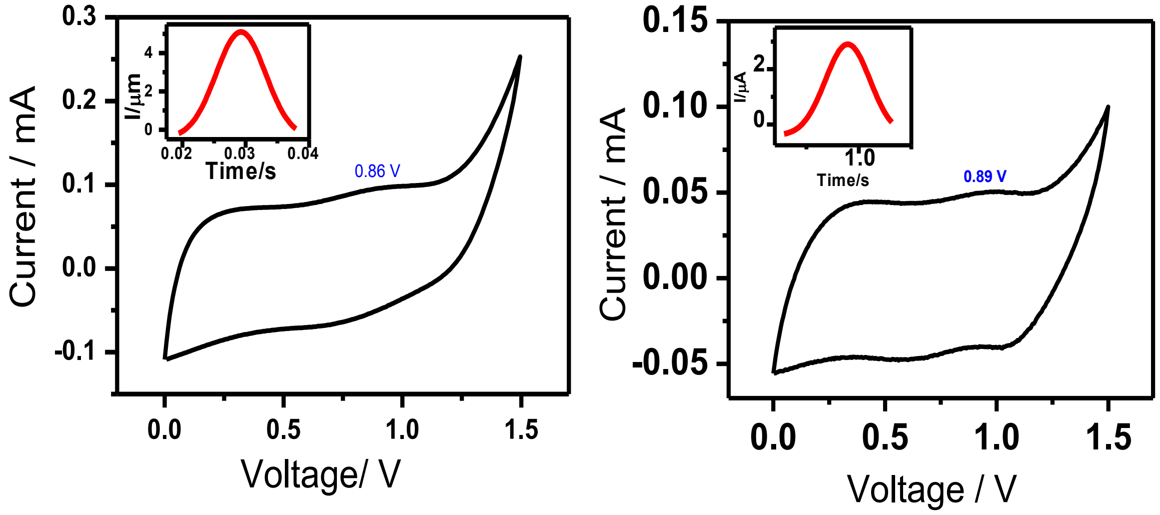

(a) **(b)**

Fig. 3.15. CVs of the prophyrin-grafted monolayers. (a) **Ia**; (b) **Ib**monolayers.Inset: enlarged plot of the oxidation peaks, after background correction and conversion into time scale.

covered by **Ia** was ~ 8 times more than that of **Ib**. These data are consistent with the AFM analyses, both revealing more compact monolayers with **Ib** than **Ia**.

This may be because of hydrogen bonding amongst the F and H atoms of the porphyrin phenyl moieties. Identifying the C–H/F–C interaction as a hydrogen bond is questioned due to the poor acceptor ability of C-bonded F atoms compared to the O- and N-atoms, if present.[182] However, distinct hydrogen bond character has been reported in the layered crystal structure of fluoro-aromatics, where C–H/F–C interactions contribute significantly in stabilizing the layers. This has been attributed to activation of the *ortho*-aromatic protons by the F atom that may override the poor acceptor nature of the C-bonded halogen.[183] In addition, the face-to-face non-covalent interaction in arene–perfluoroarene system is ubiquitous, and widely recognised as one of the major driving forces in forming robust supramolecular assemblies.[184] This primarily involves stabilizing Columbic interactions, and has been reported with several fluoro-aromatic compounds.[185] In the present case, the parallel offset disposition of the fluoro-phenyl moieties of adjacent porphyrin molecules may also be responsible for compact monolayer formed by **Ib.** This may be because of strong van der Waal interactions between F and H of the phenyl rings. Use of such molecular self-assemblies is a preferred approach for the construction of molecular devices.[66,178]

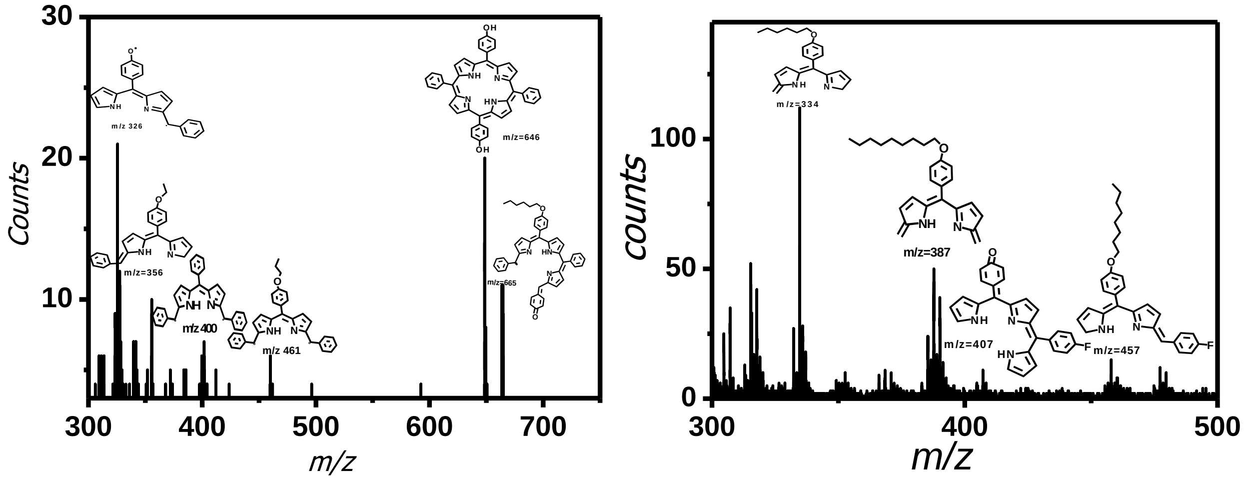

(a) (b)

Fig. 3.16. SIMS of the prophyrins-grafted monolayers. (a) **Ia**; (b) **Ib**.

The SIMS of the monolayer of **Ia** showed peaks due to the porphyrin fragments at m/z 665, 646, 461, 400, 356 and 324 amu. In case of **Ib**, the peaks appeared at a lower mass range *viz*. at m/z 457, 407, 387 and 334 amu. Nevertheless, the SIMS data (**Figs. 3.16. (a)** and **(b)**) of the monolayers of **Ia** and **Ib** confirmed deposition of their respective monolayers on the Si wafers. In case of the **Ia** monolayers, the secondary ions can knock down the porphyrin moiety from the alkyl spacer, attached to the Si surface. Subsequent ionization of the released porphyrin moiety provided the mass fragments at higher masses. Possibly, the secondary ions can't penetrate the more compact **Ib** monolayers, resulting in the fragmentation of the porphyrin moiety in the middle to generate the low molecular weight mass peaks of the truncated porphyrin moiety.

The polarized FTIR spectra (**Fig. 3.17.(a)**) for the monolayer of **Ia** exhibited N-H stretching frequency at 3249 cm^{-1}, symmetric (ν_s) and asymmetric stretching modes (ν_a) of CH_2 group at 2842 and 2910 cm^{-1} and of CH_3 group at 2877 and 2949 cm^{-1}. In contrast, the respective IR absorption peaks (**Fig. 3.17.(b)**) of the monolayer of **Ib** were at 3255 cm^{-1}, 2855 and 2925 cm^{-1}, and at 2871 and 2961 cm^{-1}. In pure solid alkene monolayers, the hydrocarbon chains exist in an all-*trans* configuration such that the carbon backbone of each molecule lies in single planes. However, in liquid form, there is a substantial twisting about the individual bonds; these out-of-plane twists alter the frequency of the methylene ($-CH_2$) vibrational modes.[186] Thus, the IR peaks due to the

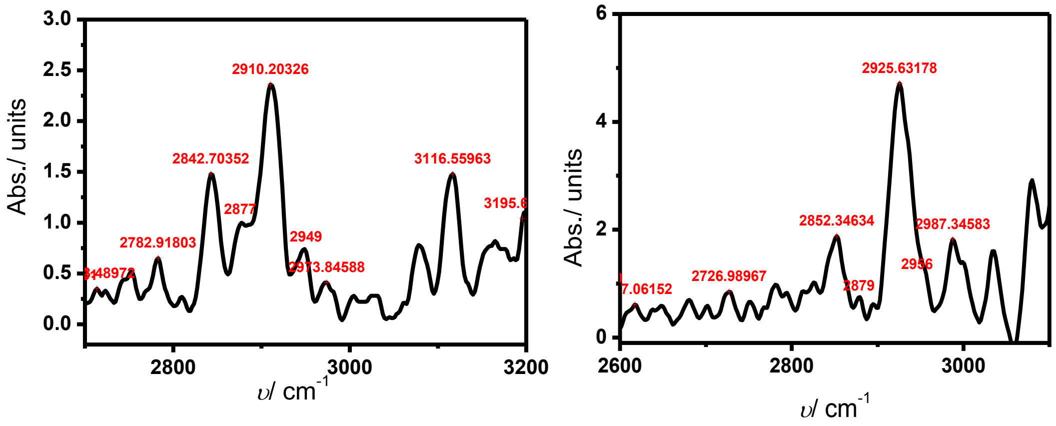

(a) **(b)**

Fig. 3.17. Polarized FTIR spectra of the prophyrin-grafted monolayers. (a) **Ia**; (b) **Ib.**

CH_2vibrational modes can provide better insights about the proposed van der Wall interactions between the porphyrin rings, parallely anchored on Si. Our results showed that the alkyl chains in the monolayers of **Ia** are more rigid like in pure solid alkanes, while that in the monolayers of **Ib** are twisted *i.e.*, more liquid like. Presumably, in case of **Ib**, the phenyl rings of the porphyrin moiety are tightly packed setting the alkyl chains free to twist. But in case of **Ia**, proper packing requires stacking of the porphyrins as well as the alkyl moieties at a tilt angle of 39°. This rigidifies the alkyl chains in **Ia**.

3.2.2. I-V characteristics.

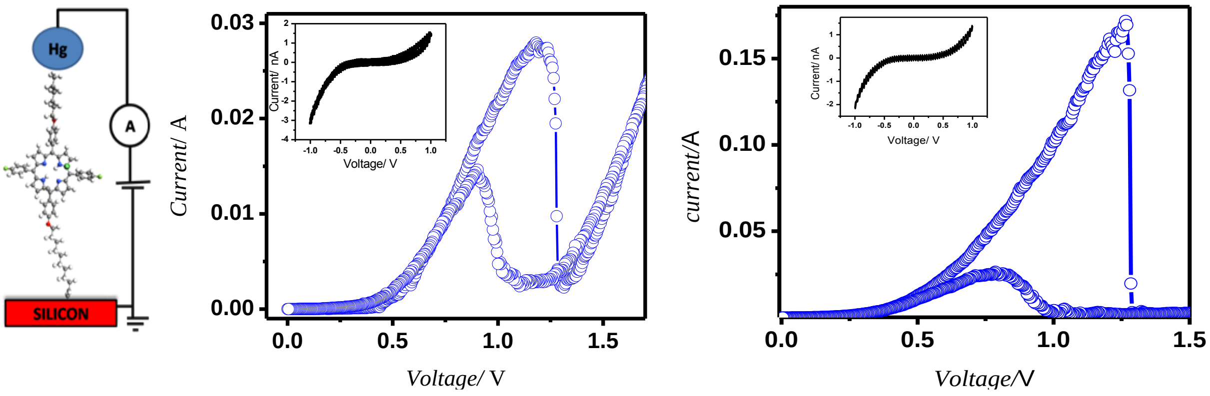

(a) **(b)** **(c)**

Fig. 3.18. Device design and characteristics. (a)*I-V* measurement set up; (b) and (c) *I-V* plots of the prophyrins-grafted monolayers **Ia** and **Ib** respectively.

To measure the *I–V* characteristics, a metal/molecule/Si (n++) structure was completed by using a tiny drop of liquid mercury of diameter 400 μm as the counter electrode as illustrated in **Fig. 3.17. (a)**.The area in contact with the grafted monolayer was 0.2 mm^2. Typical current voltage (*I-V*) curves of Hg/ molecule/ Si (111) wafers are shown in **Fig. 3.18. (b)** and **(c)**. The hybrid assemblies, prepared from **Ia** and **Ib** showed reversible NDR behavior at room temperature with PVRs of 10 and 100, and peak

Table-3.1. Voltages of I-V curve (**Fig. 3.18.**)

Voltages	**Ia (V)**	**Ib (V)**
V_{onset}	**0.38**	**0.32**
V_p	**1.18**	**1.1**
$V_{onset\text{-}rev}$	**0.98**	**0.92**
$V_{p\text{-}rev}$	**0.85**	**0.78**

positions (voltage) at 1.18 V and 1.09 V respectively. Interestingly, both the systems were stable during repetitive voltage scanning for 8 h in positive and negative bias voltages, without any reduction in current or the effect. However, the reversible NDR effect showed a marginal hysteresis. The *I-V* curve details comprising of onset and peak voltages in the forward and reverse directions for the devices are presented in **Table 3.1.**The statistical details about the devices and their PVR characteristics are given in **Table 3.2.**

Table-3.2. Statistics of *I-V* data

Molecules	No. of samples	No. of devices in each sample	Total no. of devices	No. of devices exhibiting NDR	No. of devices with reversible NDR	No. of devices with stable NDR (8h)
Ia	12	8	96	94	94	80
Ib	6	8	48	48	46	43

The *I-V* characteristics of the solid state device can be understood in terms of the molecular properties observed in the solution. Presently, the current flow in both the solid-state devices (**Fig. 3.15.**) as well as the solutions (**Fig. 3.19.**) showed same oxidation peaks. The correspondence between the solution and solid-state results suggested that the fundamental molecular electronic properties of the porphyrins are retained in the solid-state devices. In that case, the forward bias

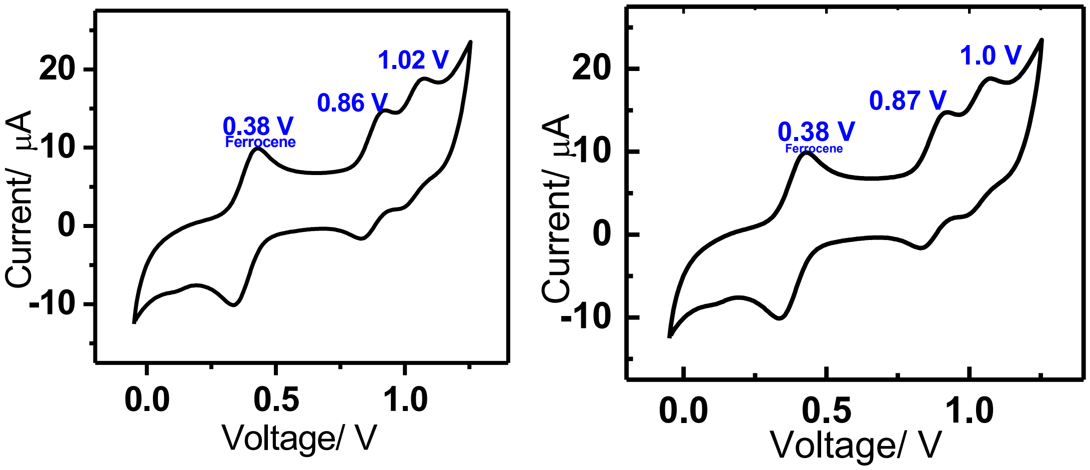

(a) **(b)**

Fig. 3.19. CV of the prophyrins in solution phase using ferrocene as the standard (a) **Ia**; (b) **Ib**.

current-flow should be determined by the HOMO states of the molecules, while their respective LUMO states would dictate the reverse bias current. Thus, the NDR effect in forward bias is a result of alignment of the HOMO levels of the molecules with the Fermi-levels of the electrodes. The NDR mechanism depends on a match (resonant tunneling) between the Fermi levels of electrodes and the HOMO levels of molecule sandwiched between the electrodes, followed by a mismatch of HOMO levels of the oxidized molecule with the Fermi-level. The hypothesis is consistent with a model, proposed by Aviram-Ratner for molecular rectification.[7]

3.2.3. Theoretical Interpretation

Theoretical calculations of the electronic transport behavior were carried out in two steps. To start with, we optimized the ground state geometries of the molecules **Ia** and **Ib** by *ab-initio* molecular orbital calculations. Using the optimized configuration of these molecules as the central device region, the transport characteristics were calculated by non-equilibrium Green's function method. The ionic optimization of molecules **Ia** and **Ib** was carried out without any symmetry constraint at the B3LYP/6-31G (d, p) level of theory. The geometrical parameters of both molecules were found to be same, except for the C-H and C-F bond lengths, which were 1.09 Å and 1.39 Å, respectively.

After establishing the equilibrium geometries of molecules **Ia** and **Ib**, their transmission spectra and the *I-V* characteristics were calculated. For this, a model for a two-probe system was constructed (**Fig. 3.20.**) by placing the molecules between two gold electrodes. A thiol end group was used for attachment of the molecule with the electrode. The interface geometry of the thiol-terminated molecule and the electrode was optimized to ensure good overlap between the device and the electrode. Earlier we have performed the calculations using plane wave-based pseudo potential approach with a prototype thiol molecule (methyl thiol) on the periodic Au (111) surface.[166] The distance between the Au (111) surface and the terminal S (or H) atom, located at the hollow site of the Au surface was found to be 2.52 Å. Presently, the two Au (111)-(8 × 8) surfaces with periodic boundary conditions were used to model the left and right electrodes. The Au/molecule/Au configuration was divided into three parts: left electrode, right electrode, and the central scattering region. In our models, there were six gold layers in each of the left and right electrode unit cells. The scattering region was composed of the isolated molecule together with the respective three gold layers on the left and right sides. The electron-transport properties of the Au/molecule/Au systems were investigated using the ATK 11.2.3 program, where a semi-empirical extended Huckel theory in combination with the first-principle non-equilibrium Green's function (NEGF) is employed. A k-point sampling of 100 was used in the electron-transport direction (Z direction).[167]

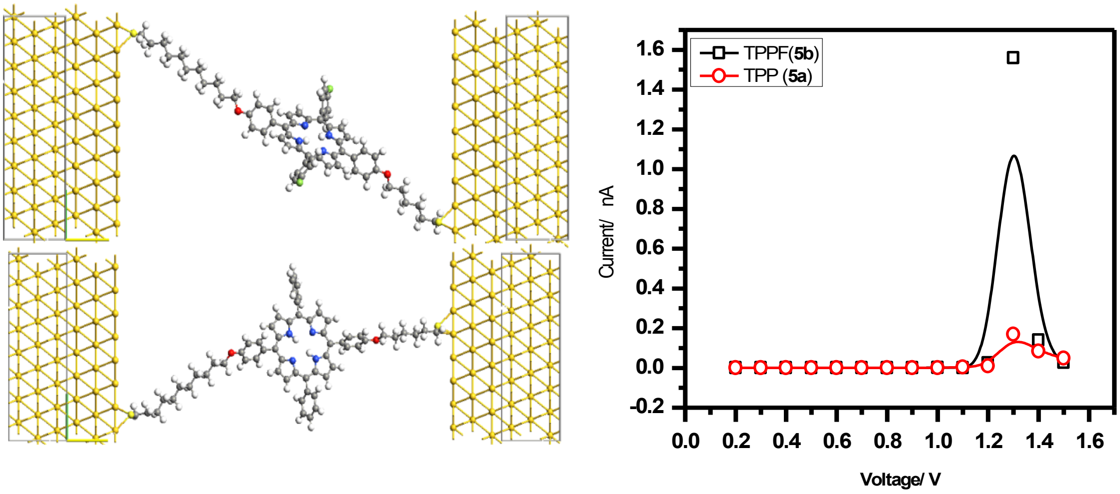

(a) **(b)**

Fig. 3.20. Theoretical device design and characteristics, constructed using Atomix toolkit and Virtual Nanolab software. (a) *I-V* measurement set up; (b) *I-V* plots of the Au/prophyrin/Au devices with **Ia** and **Ib**.

The theoretically calculated *J-V* curve of the molecule **Ib** revealed negligible current flow at the lower voltage up to 1.1 V. Thereafter, there was a sharp increase in the current, followed by a sudden drop, resulting in a peak at 1.3 V. The *J-V* curve of molecule **Ia**, constructed by the theoretical calculations was also similar, but showed a PVR almost 1/10th of molecule **Ib**. This can be explained from the differences in the transmission spectra of these molecules at bias 1.1 V. It was found that at the HOMO level (E_{HOMO} = - 4.7 eV) of molecule **Ib**, the transmission peaks are wider and more intense than that with molecule **Ia**. As the integral of the transmission peak represents the current behavior, molecule **Ib** is expected to show higher PVR. However, the difference in alignment of the respective molecules in the grafted monolayers may also partly contribute to the difference in their PVRs. These results are in excellent agreement with our experimental finding.

Our experimental results revealed that on applying voltage, initially there was a slow rise in the current due to tunneling. But at V_{onset} the HOMO level of the molecule would align in resonance with the Fermi level of Hg. This can explain the eventual sharp increase in current at V_{onset}. At V_p, the molecules get oxidized to the +1 state, causing the misalignment with the Fermi-levels of Hg, and resulting in the current drops. In the reverse scan, when the voltage is reduced, the new device will be Si/porphyrin^{+1}/Hg. At $V_{onset-rev,}$ the Fermi level of Hg would align with the LUMO of porphyrin^{+1}. This induces a sharp increase in the current due to resonance tunneling through the molecule. It again drops at V_{p-rev} as the molecule gets misaligned with the Fermi levels of Hg during its reduction. The observed small hysteresis may be due to conformational changes in the molecule after oxidation. The experimentally observed voltages (Table 3.1) correlated with the theoretically calculated HOMO-LUMO values of **Ia** and **Ib** and their respective +1 oxidation states, using ab initio (GAMESS software) (Table 3.3). The mechanism of NDR effect in **Ia** and **Ib** is explained in **Fig. 3.21**.[42d,e]

Table-3.3. HOMO-LUMO values of **Ia**, **Ib** and +1 their oxidation states

Energy Levels	**Energy in eV**			
	Ia	**Ia^{+1}**	**Ib**	**Ib^{+1}**
HOMO	-4.67	-7.46	-4.77	-7.36
LUMO	-2.02	-5.24	-2.12	-5.33

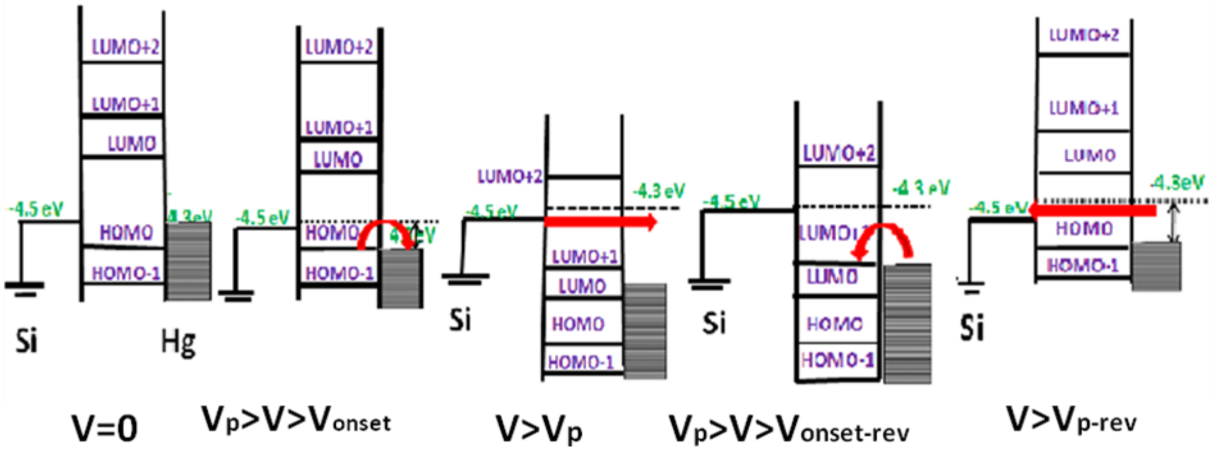

Fig. 3.21. Diagramatic presentation of the NDR mechanism for a σ–π–σ system.

3.2.4. Conclusion

Overall, two dialkylated porphyrin molecules have been designed as prototype σ–π–σ systems, synthesized, and electro-grafted them on H-terminated Si to form monolayers. The presence of the alkenyl chain was particularly useful in electro-grafting monolayers of the molecules on Si (111) surface. The *J–V* characteristics of the monolayers revealed pronounced reversible NDR effects with current PVR of ~ 10 and 100. The NDR effect was quite stable during repetitive voltage scanning for 8 h in the positive and negative bias, without any reduction in current or effect. The higher PVR, observed with the device containing the fluoro-phenyl porphyrin moiety **Ib** suggested its better pre-organization possibly by hydrogen bonding through the F atoms, compared to the device, fabricated using the non-fluorinated porphyrin, **Ia**. Thus, it was demonstrated that the NDR property can be tuned by subtle changes in the porphyrin structure by incorporating an electro-negative substituent (F) at the *meso*-phenyl groups. Theoretical simulations of Si/ porphyrin /Hg device structure showed that the NDR effect is intrinsic to the porphyrin molecules. The NDR effect was explained using the *ab initio* molecular-orbital theoretical calculations.

3.3. Molecular rectifiers

Nonlinear charge transport in organic molecules grafted on Si is a key research area in hybrid nanoelectronics such as molecular diodes, resonant tunnel diodes, memory, molecular transistors etc.[10,175,187] Supramolecular assembly of organic molecules on solid substrates is a powerful `bottom-up' approach for the fabrication of devices for molecular-scale electronics. This is generally achieved by forming Langmuir-Blodgett (LB) films,[188] or self-assembly of monolayers of organic molecules on solid substrates (SAM) via metal/molecules/metal (MMM) junction.[189] However, chemically-grafted organic molecules on semiconductors like Si is most promising for this purpose because the surface potential can be tailored to develop improved hybrid molecular devices.[10] The major advantage of this approach is that the p-n junction threshold voltage for rectification can be adjusted by changing the electronic nature of the organic π group molecules, instead of the classical method of doping.

In view of several favourable electronic attributes, porphyrins have been extensively used as the π molecules to construct storage devices, molecular wires and memory devices. Reports on current rectification by C60-porphyrins combinations also exist. Molecules, showing rectification behaviour with high rectification ratio (RR) is very useful for making diodes. Chemically-grafted organic molecules on semiconductors like Si is most promising for this purpose, as the p-n junction threshold voltage for rectification can be adjusted by changing the electronic nature of the organic π molecules without doping.[10] Current rectification is reported with the hybrids containing σ–π units grafted on Si through an alkyl spacer (σ). A resonant transport between the Si conduction band (CB) and the highest occupied molecular orbital (HOMO) of the π group can explain the rectification behaviour.[5,190,191]Another, well-known model of molecular diode was proposed by Aviram and Ratner.[7] According to this, a single molecule with donor-spacer-acceptor (D-s-A) structure would behave as a diode when placed between two electrodes. The function of the non-conjugated s-bond bridge is to prevent the direct overlap of D and A energy levels.[192,193] For a monolayer to rectify, its molecules must be aligned in register between two electrodes so that they work together when electrons flow from electrode MA (acting as cathode) to A, and exit from D to electrode MD (acting as anode).The extra electron in A’s LUMO then tunnels through the -s- bridge to the vacancy in D’s HOMO to complete the forward-direction flow. If the D and A groups are out of register, the individual molecules would work at cross purposes showing no rectification.

While this model has been experimentally verified by several groups, the porphyrins have never been used for this purpose. In the present investigation two such single molecules **IIa/IIb** were synthesized, grafted on Si-surface using the C-6/C-11 alkenyl chain as the linker, and their *J-V* behaviour studied. In these assemblies that showed high current rectification ratios, the porphyrin and the aniline moieties served as the (A) and (D) units respectively, while the —CH_2-NH— was the required spacer. The fabrication of the device, their characterization and electronic property are described in the following.

3.3.1. Fabrication of molecular rectifier

3.3.1.1. Synthesis of D-σ-A molecule with a linker

Synthesis of the target molecules [porphyrin (A)—CH_2-NH(s)—aryl(D) —C-6/C-11 alkyl chain (linker)] warrants availability of the porphyrins with a mono-substitution that can be attached to the donor aryl moiety containing the linker. However, synthesis of the mono-functionalized porphyrins by the conventional Adler and Longo mixed condensation method is cumbersome because it provides a statistical mixture of products from which isolation of the required product is tedious. Further, the method is limited tithe choice of substitution, and furnishes the unsymmetrical porphyrins as the minor products. The other option of selective fictionalization of the porphyrin moiety is also difficult, because unlike other aromatic compounds, porphyrins are inactive towards conventional electrophilic reactions like Friedal-Craft alkylation and acylation reaction. On the other hand, halogenation[194] and nitrations[108] of the symmetrical porphyrins leads to di- or higher substituted products. In exception to these, the Vilsmeier-Haack reaction of the porphyrins proceeds regioselectively at the pyrrole ring to furnish mono-formyl-porphyrins. The Vilsmeier complex, formed by the interaction between $POCl_3$-DMF reacts with the Cu(II) complex of the porphyrins to formylate at the *β*-position. Metallation is required to prevent protonation of the inner nitrogens, and direct the electrophilic attack of the chloromethyleneiminium salt towards the *β*-pyrrolic position.[195]

It was envisaged that such a *β*-formylporphyrin would be amenable to attachment of the aryl donor group containing a ω-alkenyl spacer. The attachment would provide the required spacer, while the alkenyl group can be used for covalent attachment to Si-surface as used earlier. With this hypothesis in mind, the Cu(II)-tetraphenylporphyrin(Cu-TPP)**7** was synthesized by an acid-catalyzed condensation between benzaldehyde and pyrrole under heating, followed by reaction of the resultant TPP with a Cu(II) acetate.[103]

Formyltion of **7** with $POCl_3$ in DMF, and subsequent hydrolysis of the intermediate iminium salt furnished the aldehyde of the Cu(II)-TPP in excellent yield (~95%). However, its attempted using sulphuric acid produced a mixture of degraded porphyrinic compounds instead of the expected free base porphyrin. It was postulated that sulfonation and/or a secondary reaction of the formyl group was responsible for the result.[196] Later, the anomalous result was found to be due to the intramolecular cyclization of the formyl group at the *ortho*-postion of the adjacent phenyl ring under the acidic conditions.[197] Surprisingly the intermediate iminium salt was found to be stable in the presence of acidic demetallating conditions.[108] Hence the intramolecular cyclisation problem was avoided by directly demetallating the Cu(II)-salt of formyl-TPP with an acid, followed by hydrolysis

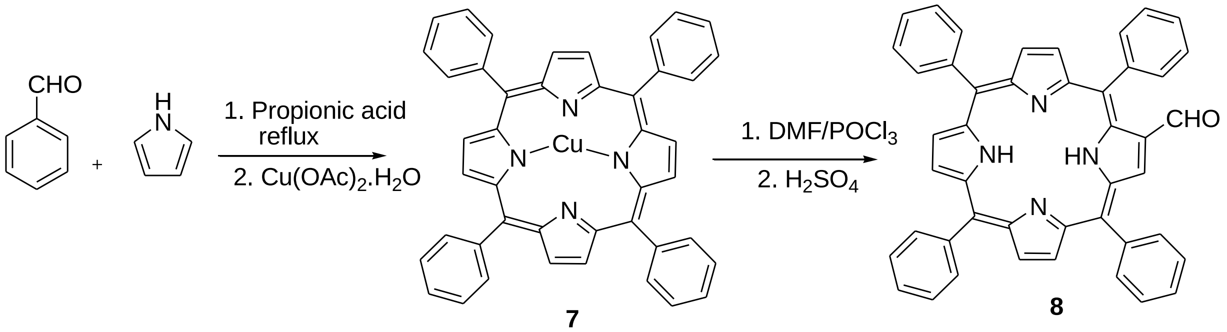

Scheme-3.8. Synthesis of β-formyl porphyrin by Vilsmeier-Haack reaction of the iminium salt *in situ* to obtain the metal-free 2-formyl-TPP **8** (**Scheme-3.8.**).Following essentially the same procedure, compound **8** was prepared. The ^{1}H NMR spectrum (**Fig. 3.22.**) of **8** displayed of the expected resonances for the TPP moiety along with the two 1-H-singlets at δ 9.43 and δ 9.24, respectively for the CHO and neighbouring *β*-pyrrolic protons was in agreement with the previously reported data.[108] The carbonyl peak at δ 189.2 in its ^{13}C NMR spectrum (**Fig. 3.23.**) also confirmed the presence of C=O group.

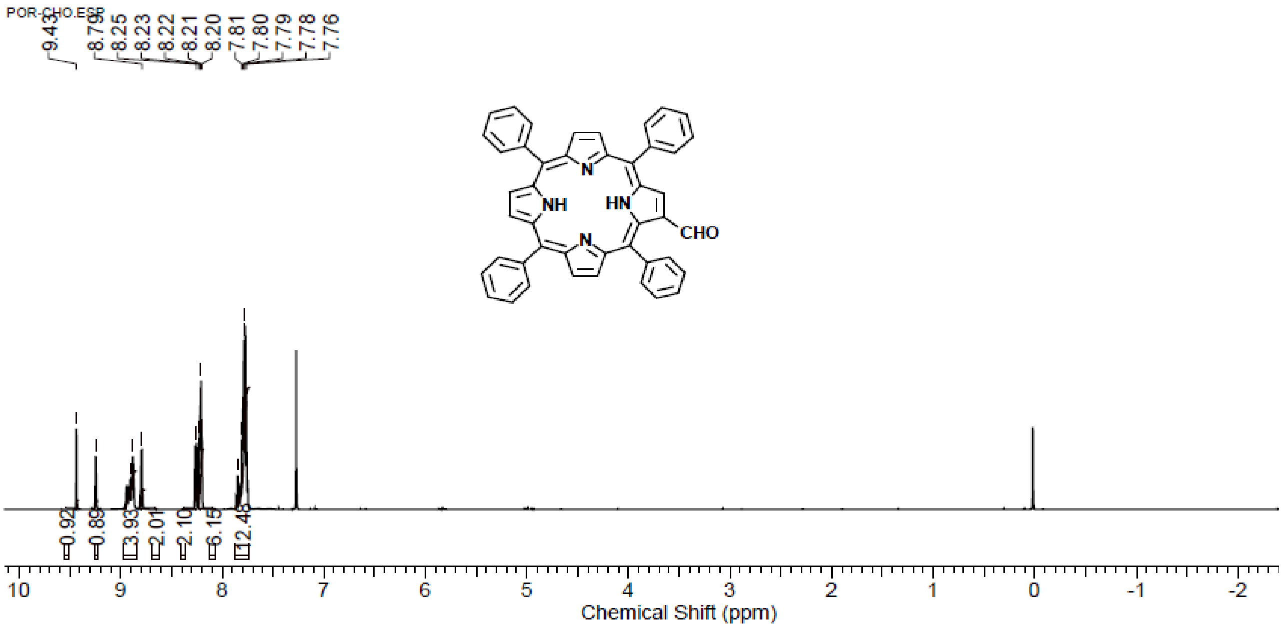

Fig. 3.22. ^{1}H NMR spectrum of **8**

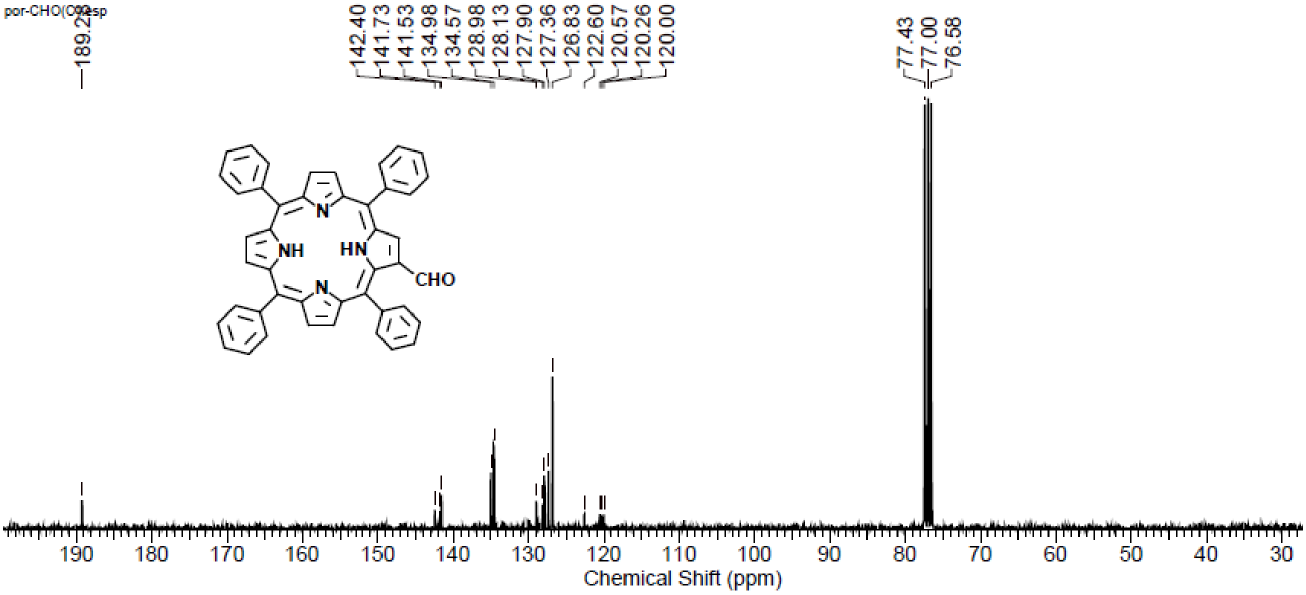

Fig. 3.23. ^{13}C NMR spectrum of **8**

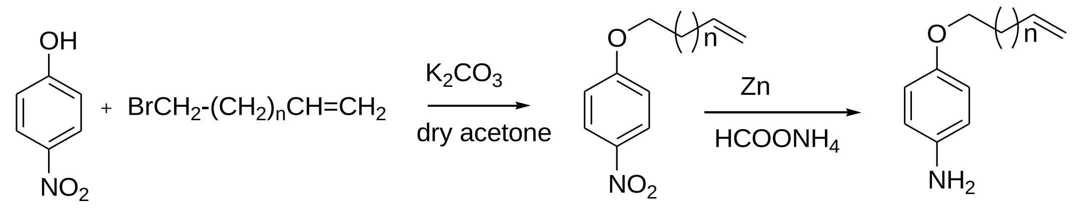

9a; n=3
9b; n=7

10a; n=3
10b; n=7

Scheme-3.9. Synthesis of 4-alkenyloxyaniline

As per the synthetic plan, a reductive amination of **8** with a suitable aniline derivative was conceived for the attachment of the acceptor π group. The *para*-alkenyloxy anilines **10a** and **10b** appeared well-suited for this purpose, as it would ensure the incorporation of the spacer and the linker, required for grafting on Si-surface. Hence, *para*-nitrophenol was subjected to a base-catalyzed alkylation with 5-hexenyl bromide and 10-undecenyl bromides **3** separately to furnish compounds **9a** and **9b**. ^{1}H NMR spectra of both the molecules showed doublet of doublet at δ 7.55 (4 H), triplet at δ 4.0 (2 H) ppm and multiplets at δ 5.78 and 4.96 ppm indicating p-substituted benzene, OCH_2 group and terminal double bond respectively. Similarly, ^{13}C NMR spectra showed peaks at δ 164.1, 141.9, 114.9, 114.28 and 68.57 ppm indicating ArC-NO_2, ArC-O, terminal double bond Carbon and OCH_2 respectively.

Reduction of their NO_2 group under a catalytic transfer hydrogenation conditions with Zn and HCO_2NH_4[198] furnished the *para*-alkenyloxy anilines **10a** and **10b** uneventfully (**Scheme-3.9.**). The next task was the reductive amination of the aldehyde **8** with the anilines **10a** and **10b**. The reductive amination type reaction of **8** and a variety of primary amines, including aniline has been achieved using acetic acid as the catalysis. The reaction was carried out in THF or toluene, and the resultant imines is reduced *in situ* with $NaBH_3CN$, prior as well as post-imine formation. The reactions, performed in toluene used a Dean-Stark trap to remove water, driving the reaction towards formation of the imine intermediate.[110] We followed the latter method, but used molecular sieves to remove the H_2O, formed during the imine formation (**Scheme-3.10.**). This improved the yield and the reaction could be performed much faster (4 h) compared to that (72 h) in the reported procedure. The ^{1}H

NMR spectrum of **IIa** and **IIb** showed multiplets at δ 8.51 (7 H), 5.82 (1 H) and 5.00 (1 H), singlet at 4.45 (2 H) and triplet at δ 3.88 (2 H) corresponding to the pyrrolic protons, terminal double bond, CH_2NH and OCH_2 groups respectively. Similarly, ^{13}C NMR spectra showed corresponding peaks for terminal double bond, CH_2NH and OCH_2 groups at δ 114.6, 115.5, 68.5 and 45.0 ppm respectively. The representative ^{1}H and ^{13}C NMR spectra of **IIb** are shown in **Figs. 3.26.** and **3.27**.

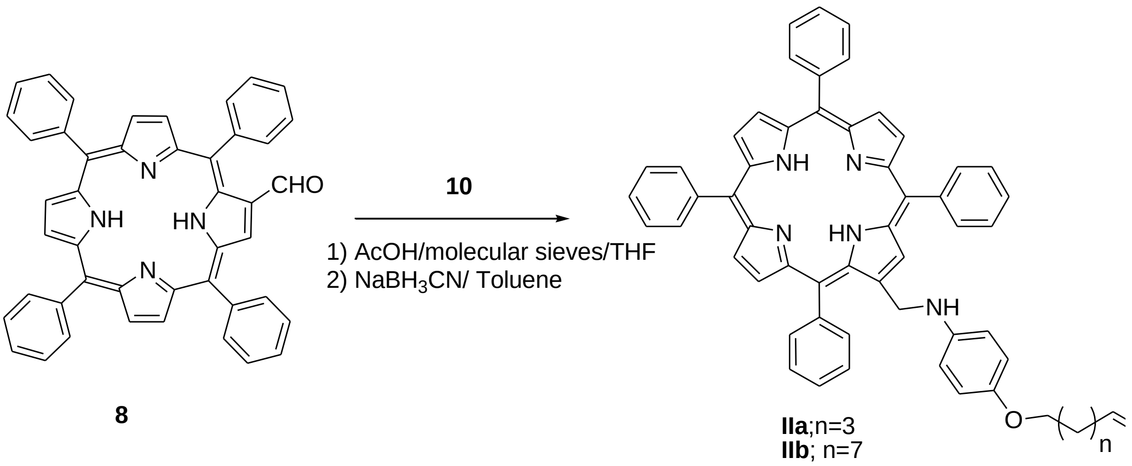

Scheme-3.10. Reductive amination of **8** with **10a** and **10b**.

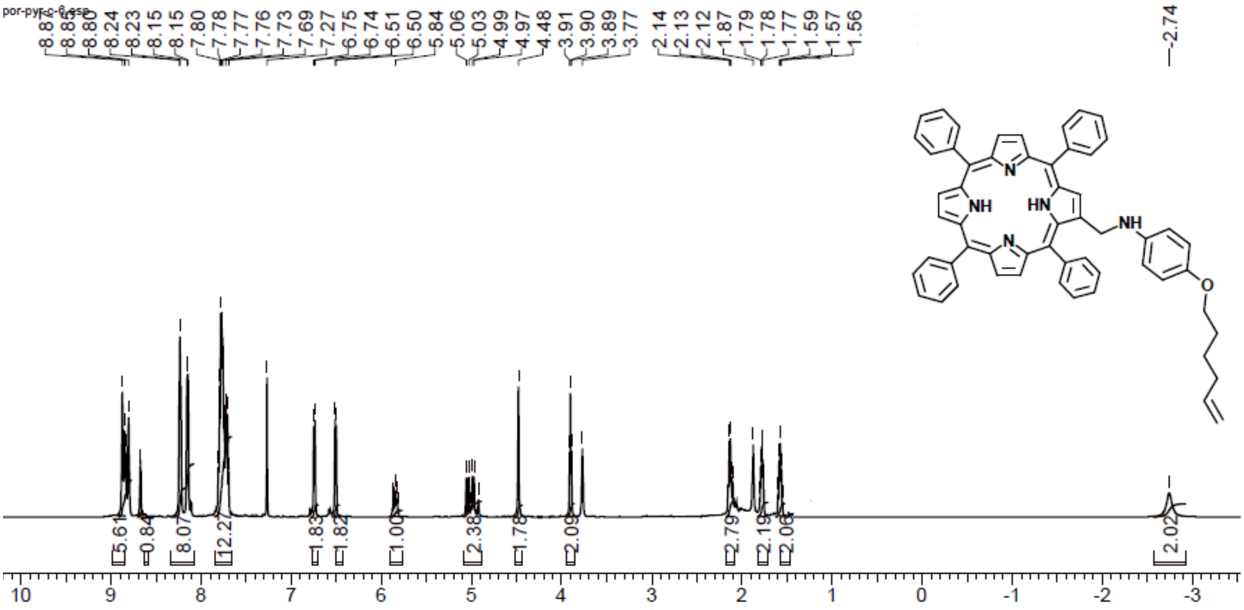

Fig. 3.24. ^{1}H NMR spectrum of **IIa**

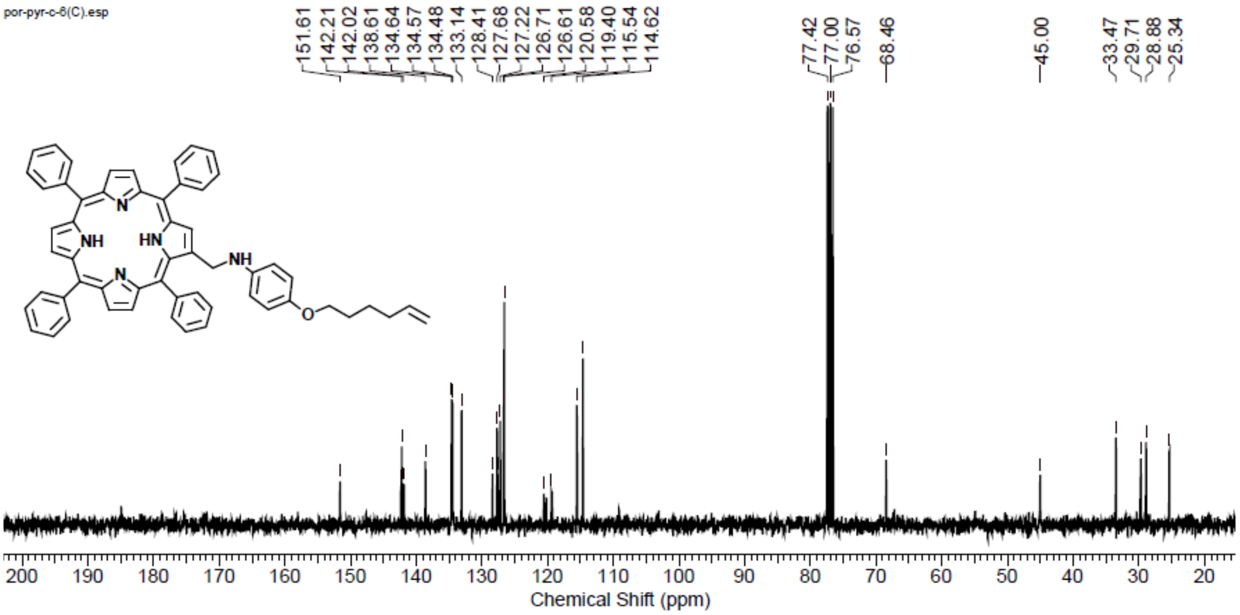

Fig. 3.25. ^{13}C NMR spectrum of **IIa**

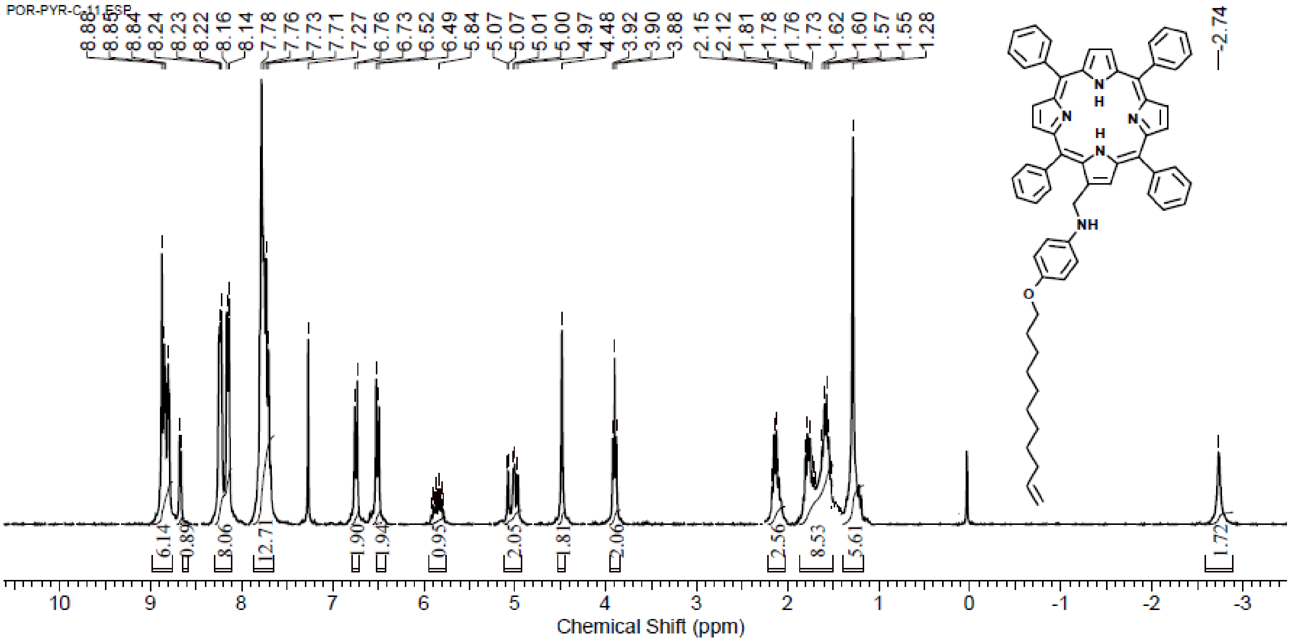

Fig. 3.26. ^{1}H NMR spectrum of **IIb**

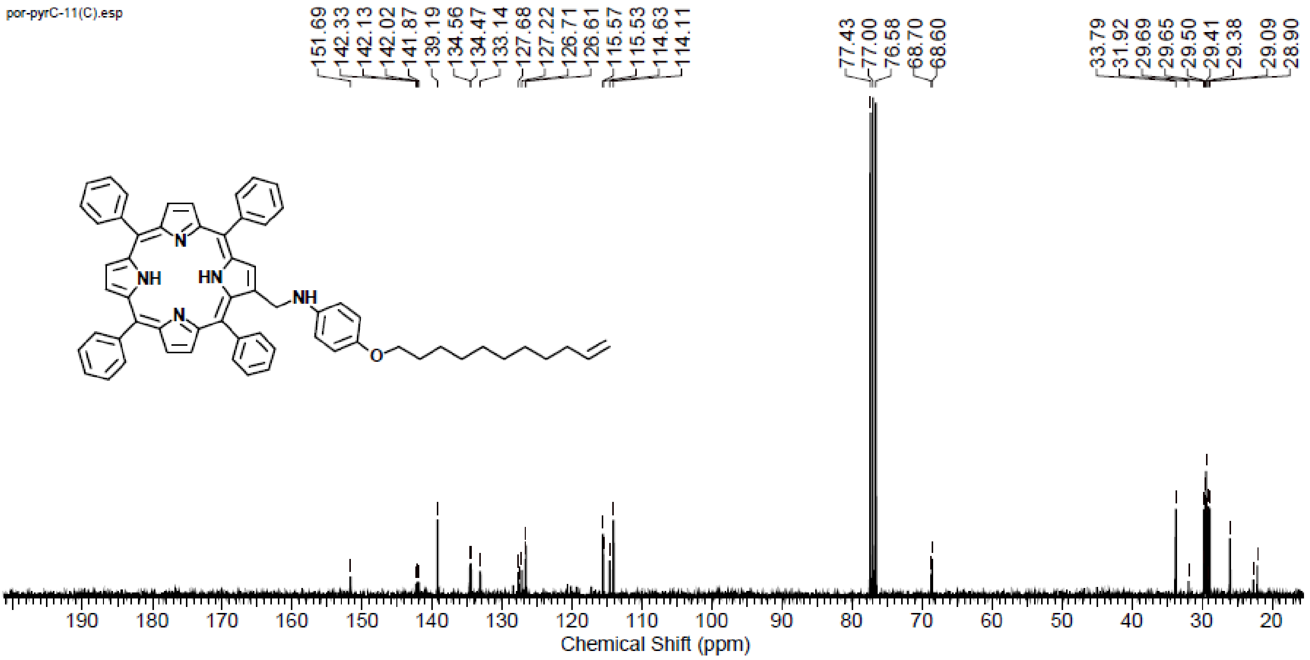

Fig. 3.27.^{13}C NMR spectrum of **IIb**

3.3.1.2 Preparation of the grafted organic assembly

As described in section. 3.2.1.2, the compounds **IIa** and **IIb** was electro-grafted on hydride terminated Si, and the representative CV of depositing **IIb** is shown in **Fig. 3.28** along with the design of the electrochemical cell.

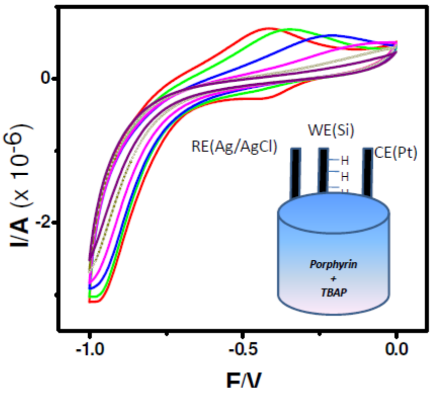

Fig. 3.28. Electrochemical deposition of **IIb**
[inset: electrochemical cell].

3.3.1.3 Characterization of monolayer

The deposited monolayers were characterized as earlier. The contact angles of deionized water at the Si surface grafted with **IIa** and **IIb** were 55° and 64° respectively, *vis-à-vis* that (84°) of the cleaned Si wafer. The low contact angles of the monolayers suggested them to be tilted on the Si-surface. The ellipsometry data revealed average monolayer thicknesses of 2.4±0.1 nm for **IIa** and 2.9±0.2 nm in case of **IIb**. The AFM images (**Fig. 3.29.**) revealed that 30 CV scans produced the most organized monolayer with least number of voids and hillocks, and the void depths were ~ 2.5 nm for **IIa** and 3 nm for **IIb**. Compared to **IIa**, the monolayers of **IIb** were more compact and uniform with large grain size.

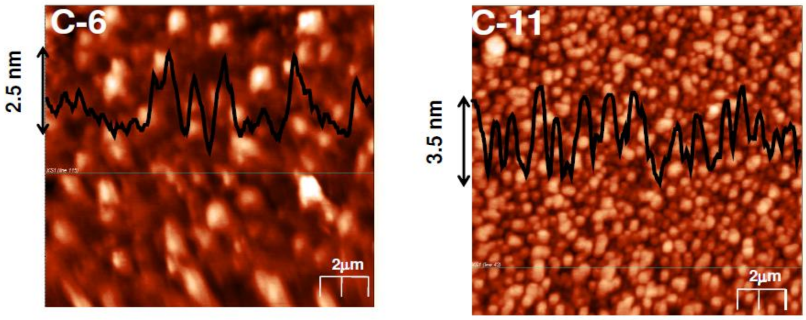

(a) (b)

Fig. 3.29. AFM images of the monolayers. (a) **IIa**; (b) **IIb**.

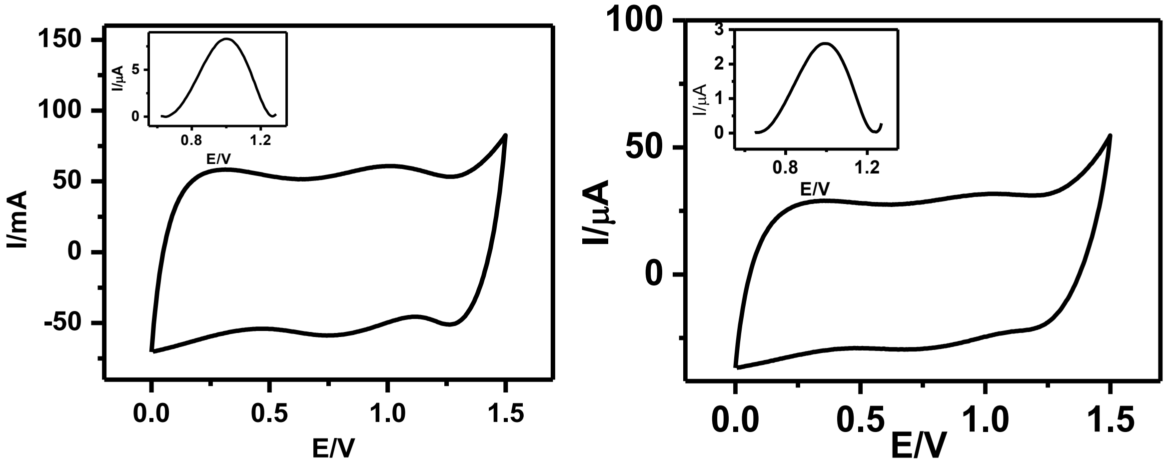

(a) (b)

Fig. 3.30. CV of monolayers (a) **IIa** and (b) **IIb**.

The fast scan (10 V/s) CVs (**Fig. 3.30**) of the monolayer exhibited a reversible peak at +0.8 V for the respective porphyrin moieties. The net charge transferred during the oxidation process, calculated from area under the oxidation peak were 8.6×10^{-7} C and 2.45×10^{-6} C respectively for **IIa** and **IIb**.

These amounted to a surface coverage of 1.11 × 10^{12} and 4.5 × 10^{14} molecules /cm^2 respectively for **IIa** and **IIb**, confirming AFM data of more compact monolayers with **IIb** than **IIa**.

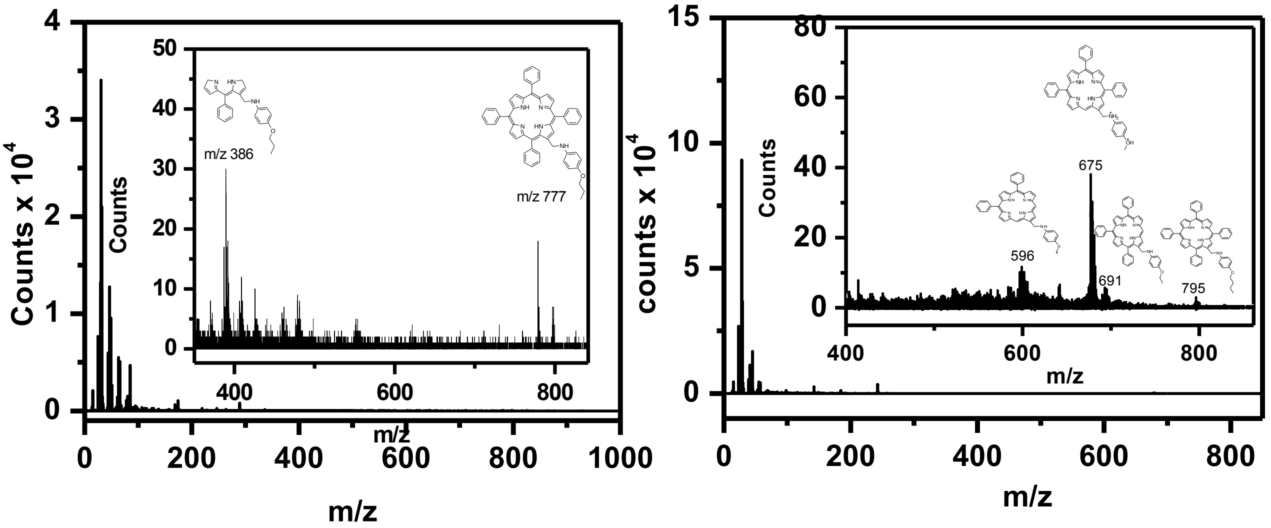

(a) (b)

Fig. 3.31. SIMS of (a) **IIa** and (b) **IIb**

The SIMS of the **IIa** monolayers showed peaks (**Fig. 3.31.**) at m/z 777 and 386 amu, while the SIMSfor **IIb** showed peaks at 795, 691, 675 and 596amu. The mass peaks at 777 and 795 amu confirmed that the TPP moiety (m/z 614) remained intact during grafting process for both **IIa** and **IIb**. Moreover, the larger mass fragments in case of the C-11 monolayers **IIb** indicated these were more tilted on the Si-surface. The polarized FTIR spectra (**Fig. 3.32.**) for the monolayers of **IIa** exhibited N-H stretching frequency at 3251 cm^{-1}, symmetric (ν_s) and asymmetric stretching modes (ν_a) of CH_2 group at 2856 and 2927 cm^{-1}. In contrast, the respective IR absorption peaks of the monolayers of **IIb** were at 3255 cm $^{-1}$, 2840and 2921 cm^{-1}. Our results showed that the alkyl chains in the monolayers of **IIb** are more rigid like in pure solid alkanes due to betterpacking,[176] while that in the monolayers of **IIa** are twisted *i.e.*, more liquid like. The layers were devoid of any SiO_2, as their XPS data

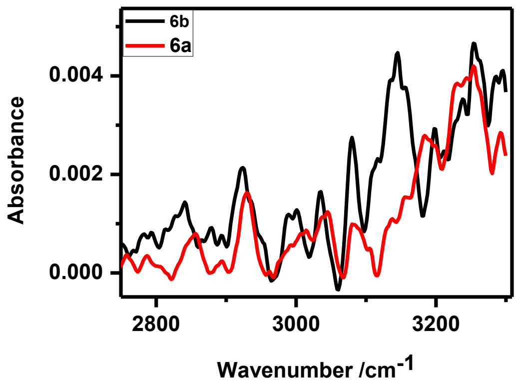

Fig. 3.32. FTIR spectra of **IIa** and **IIb**

showed the presence of the elements, C, N and O, but absence of 103 eV peak (Si-O). Further, the Si-C bond peak at 99.5 eV confirmed grafting of the TPP derivatives on the Si-surface.

3.3.2 I-V characteristics

To measure the *I–V* characteristics, a metal/molecule/ Si (n++) structure was completed by using a tiny drop of liquid mercury as illustrated in **Fig. 3.33.(a)**. The area in contact with the grafted monolayer was 200 µm^2. The current voltage (*I-V*) curves of Hg/ molecule (**IIa** or **IIb**)/ Si (111) wafers (**Fig. 3.33 (b)**) showed current rectification by both the devices. But the device with C-11 alkyl chain showed significantly better RR (10^7) due to its compact packing, compared to that (RR ~100) observed with **IIa** (C-6alkyl chain). Nevertheless, both the systems showed stable current rectification during repetitive voltage scanning for 100 scans. Statistics of I-V data is shown in **Table-3.4.**

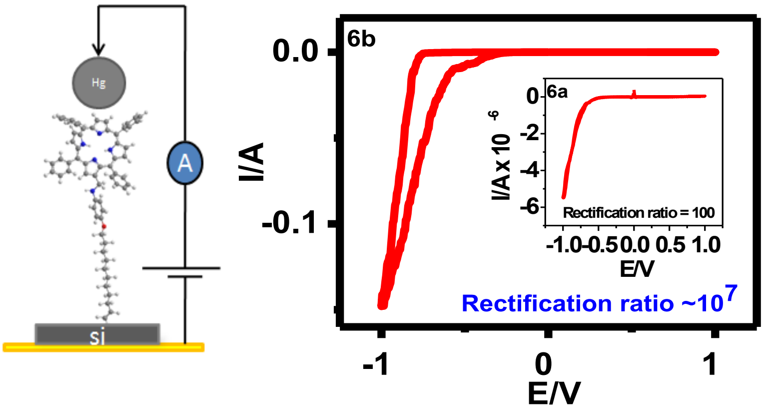

(a) **(b)**

Fig. 3.33. (a) *I-V* measurement set up; (b) *I-V* curve of **IIb;** [**inset**: *I-V* of **IIa**].

Table-3.4. Statistics of *I-V* data

Molecules	**No. of samples**	**No. of devices in each sample**	**Total no. of devices**	**No. of devices rectification**	**No. of devices with high rectification**
IIa	8	8	64	64	42
IIb	5	8	40	40	29

3.3.3 Theoretical calculations

As discussed earlier, the forward bias current-flow is determined by the HOMO states of the molecules, while their respective LUMO states dictate the reverse bias current. Thus, the rectification in reverse bias is a result of alignment of the LUMO levels of the molecules with the Fermi-levels of the electrodes. The hypothesis was verified by theoretical calculations, wherein the HOMO and LUMO energy levels of **IIb** were determined using ab-initio method (GAMESS software).The ionic optimization without any symmetry constraint was carried out at the B3LYP/6-31G (d, p) level of theory where the exchange correlation functions are expressed using hybrid density functional theory.

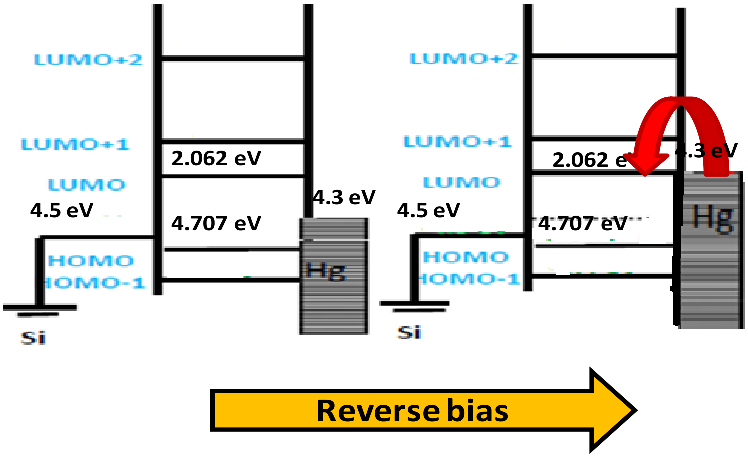

Fig.3.34. Mechanism of rectification

The results revealed that the HOMO levels of the molecules are located at the phenyl moiety of TPP, while the LUMO levels reside at the porphyrin ring (**Fig. 3.35. (a)**). Due to the different locations of the HOMO and LUMO levels, and their separation by the CH_2-NH spacer, current can't flow in the forward bias. However, in the reverse bias, the Fermi levels of Hg would align themselves with LUMOs of the molecules, as LUMO is more delocalized than HOMO. As a result, the flows of electrons would be from mercury to the porphyrin ring and from the phenyl ring to Si. This implies that as against conventional direct of current flow, the electrons would flow from mercury to silicon, accounting for the observed unidirectional current or rectification.

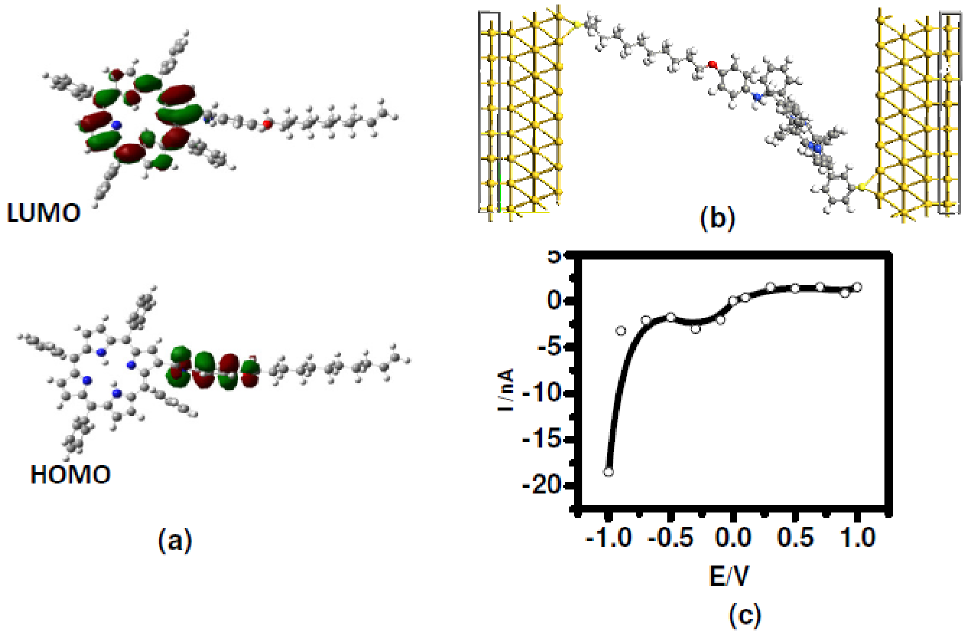

Fig. 3.35. (a) HOMO-LUMO diagram of **IIb**; (b) Measurement setup (Au/Molecule/Au); (c) I-V curve of **IIb**.

Quantification of the theoretical J-V curve was confirmed by calculating the transmission spectra. For this, a model for a two-probe system was constructed with four gold layers on each side of the molecule (**Fig. 3.35. (b)**)(Au/molecule/Au systems) as discussed earlier in section 3.2.3. The theoretically calculated curve also showed rectification in reverse bias (**Fig. 3.35. (c)**).

3.3. Conclusion

Based on Aviram and Ratner model, two D-s-A systems were designed and synthesized. Both the systems were promising in terms of high current rectification and stability. The newly designed rectifiers showed significantly better material attributed, compared two other reported molecular rectifiers. Although the molecular design followed Aviram and Ratner model, theoretical simulation suggested that the rectification effect is intrinsic, and can be explained by alignment mercury levels with LUMO of molecule in reverse bias. In other words, consideration of this as a σ-π system can adequately explain the rectification behavior.

Chapter-4

CHAPTER-4

Molecular rectifiers based on polyaromatic hydrocarbons (PAHs)

4.1. Introduction

It is well established that high-performance bulk organic electronic devices can be developed by using π-conjugated molecules as active components.[199] Molecular-sized rectifiers hold promise for the miniaturization of electronic circuits as engineering approaches the scale of nanotechnology.[77,187] As discussed in the previous chapter, covalent attachment of electron rich π molecules on Si surface through an alkyl spacer (σ) furnishes the σ–π hybrids that show rectification behavior.[5,190,191] A resonant transport between the Si conduction band (CB) and the highest occupied molecular orbital (HOMO) of the π group can explain the rectification behaviour in such systems.The Fermi level pinning at the metal/ π-group interface plays a key role in the electrical behavior of these molecular rectifying junctions. The advantage of these systems over the well-acclaimed Aviram and Ratner model[199b] is the ease of their syntheses, especially from commercially available π-molecules. One of the challenges in this area is to develop devices that are environmentally stable, and show high-mobility and easy processability.

Because of their high band gap and low electronic affinity, most of the “classical” organic semiconductors (pentacene, anthracene, phthalocyanines, and most of the conjugated polymers) are p-type or transport holes. However, the performance and stability of organic n-type materials have significantly lagged behind their p-type counterparts. Amongst the common air-stable n-type organic semiconductors, some perylene-diimides are particularly attractive because of their robust nature, flexible molecular orbital energetics, and excellent charge transport properties. Along with the advantages of perylene-diimides, however, comes a major disadvantage. Their poor solubility (typically 1-2 mg/L) limits the amount of useful chemistry that can be accomplished with them.[200] This restricts their applications in nanoelectronics. Attachment of the alkyl (σ) moiety to the polyaromatic hydrocarbons including the perylenes improved their solubility enormously.[201-203] Due to their high ionization energies and band gaps, the perylenes/pyrenes are suitable π-moieties for making rectifying diodes, and several such systems have been constructed.[85,89,204,205]

Our group has active interest in fabricating chemically-bonded organic molecules on H-terminated Si surface for molecular electronics applications.[22] It was hypothesized that use of a pre-synthesized alkenylpyrene/ perylene as the σ–π molecule would be advantageous to obtain the required organo-Si hybrids. The alkenyl group was expected to increase the solubility of the molecule, and also provide the required functionality for electro-grafting the monolayers on Si surface. To this end, two alkylated pyrenes and one perylene molecules were synthesized, deposited on H-terminated Si (111) wafers to form their respective monolayers, and their current rectification behaviour was investigated. In these hybrids, the pyreneand perylene groups served as the π moieties, while the alkenyl chain acted as the σ moiety. This chapter describes these aspects sequentially.

4.2. Synthesis of σ–π molecules

4.2.1 Perylene-based

To synthesize the alkyl perylene **III**, an $AlCl_3$-catalyzed Friedel-Craft acylation of perylene at its most electrophilic C-3 centre with 10-undecenoyl chloride was attempted. The acid chloride was prepared by reaction of 10-undecenoic acid with excess of $SOCl_2$. The product was isolated by vaccum distillation. It was then used to acylate perylene using triethylamine as base at 0^oC. The acylation gave a mixture of mono- and di-acyl perylenes along with the starting compound. In view of the poor solubility of reaction products, we were unable to separate yields are given based on literature.[48]

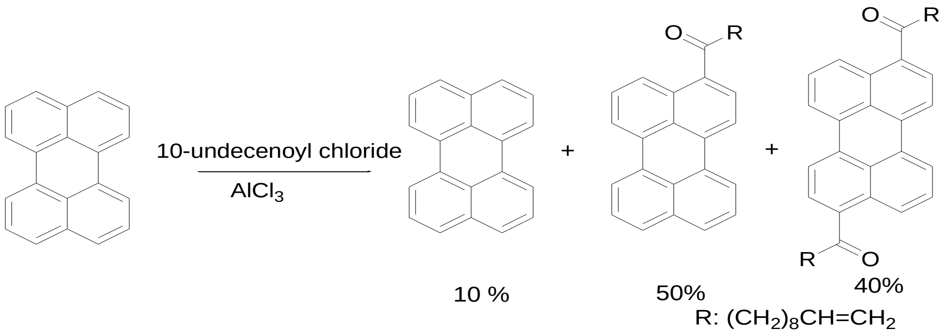

Scheme 4.1. Friedel-Craft acylation of perylene.

Earlier, Buu Hoi and Dewar reported that Vilsmeier-Haack formylation of perylene in *o*-dichlorobenzene at 100°C proceeds region-selectively at C-3. Presently, the same protocol was used to obtain 3-formylperylene (**11**) as the sole product (Scheme 4.2). The ^{1}H NMR

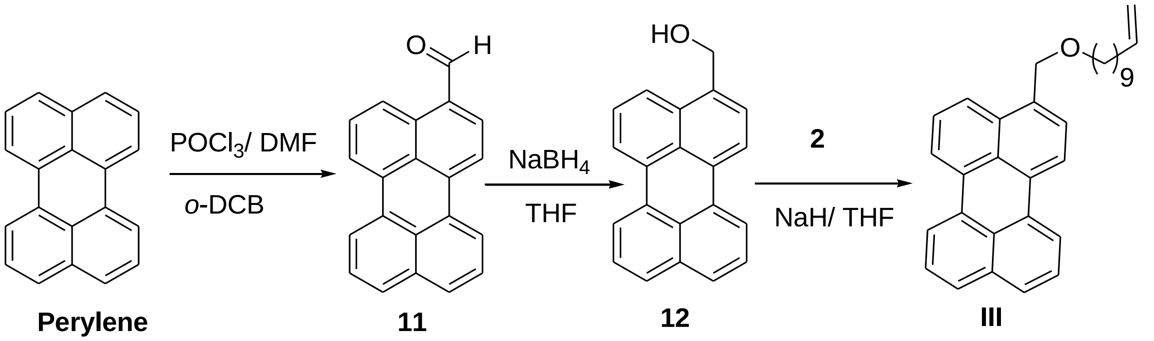

Scheme-4.2. Synthesisof the perylene derivative **III**.

singlet (1H) at δ 10.3 for the –CHO proton and the ^{13}C NMR peak at δ 192.0 along with the expected resonances due to the aromatic moiety (**Figs. 4.1.** and **4.2.**) were consistent with the reported data,[112] and established its structure. The LCMS molecular ion peak at 281 amu as the base peak further confirmed its formation.

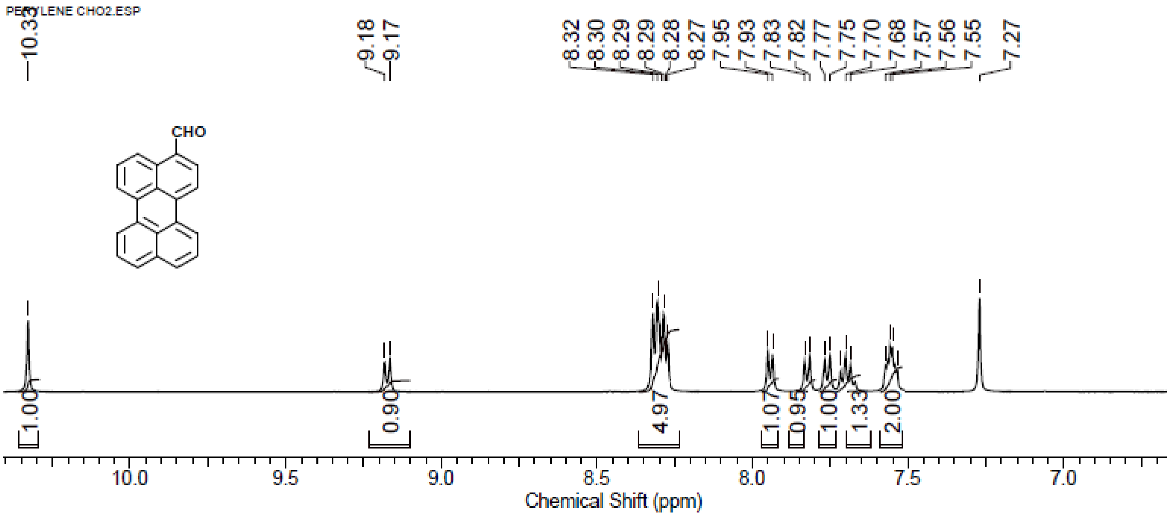

Fig. 4.1. ^{1}H NMR spectrum of 3-perylenecaboxyldehyde (**11**)

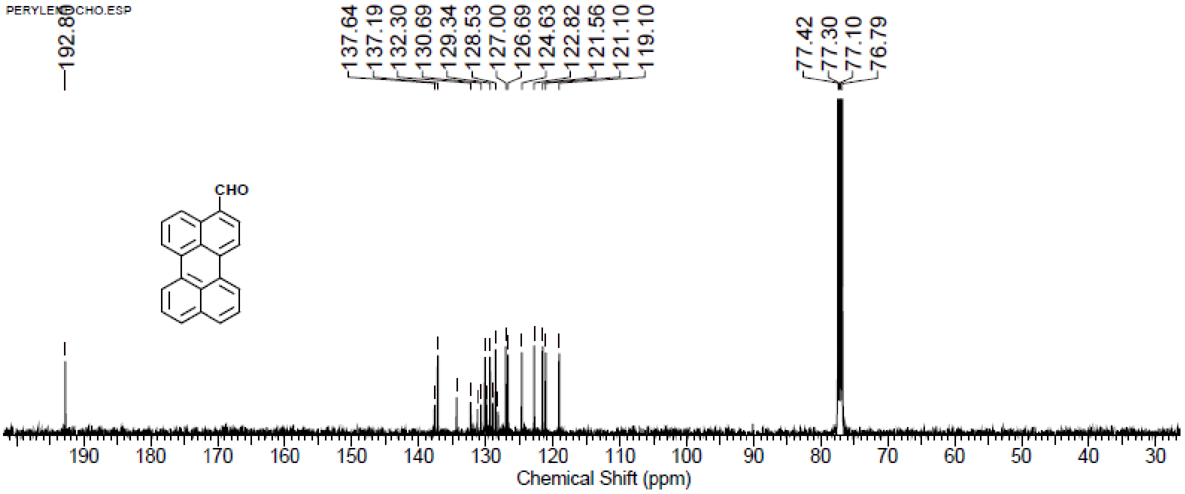

Fig. 4.2. ^{13}C NMR spectrum of 3-perylenecabaldehyde (**11**)

Compound **11** was reduced with $NaBH_4$ in THF at room temperature to obtain the known alcohol **12**.[111] This was characterized by its FTIR absorbance at cm^{-1} (OH) and the ^{1}H NMR two proton-singlet at δ 5.10 for the -C**H**$_2$OH protons. The alcohol**12** was then subjected to *O*-alkylation with **2** in THF using NaH as the base to afford **III**. Compound **III** was than characterized by spectroscopy. The ^{1}H NMR multiplets at δ 5.82 (1H) and at δ 4.94 (4H) accounted for three olefinic protons and the CH_2 protons flanked between the oxygen atom and the perylene moiety. In addition, the ^{1}H NMR triplets at δ 3.56 for the OCH_2 moiety along with the resonances for the aromatic protons (**Fig. 4.3.**) are in agreement with the structure of **III**. The ^{13}C NMR peaks (**Fig. 4.4.**) at δ 70.5 and δ 71.4 for the –O-**C**H_2- and –O-**C**H_2-perylene moieties further confirmed the structure. The molecular ion peak at 434 amu as the base peak in the MALDI-TOF spectrum (**Fig. 4.5.**) of **III** confirmed its identity.

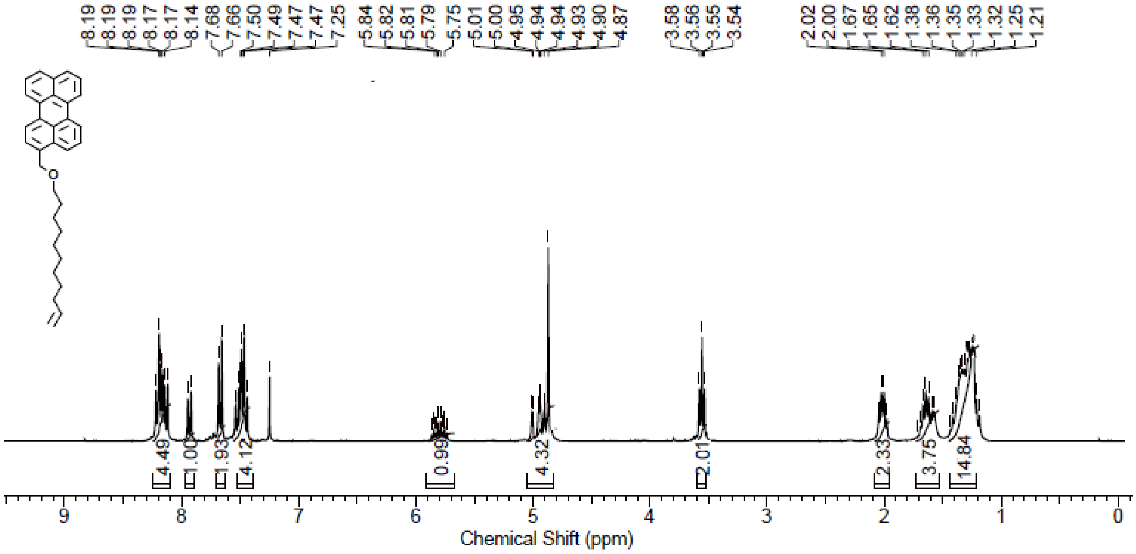

Fig. 4.3. ^{1}H NMR spectrum of 3-undecenyloxyperylene (**III**)

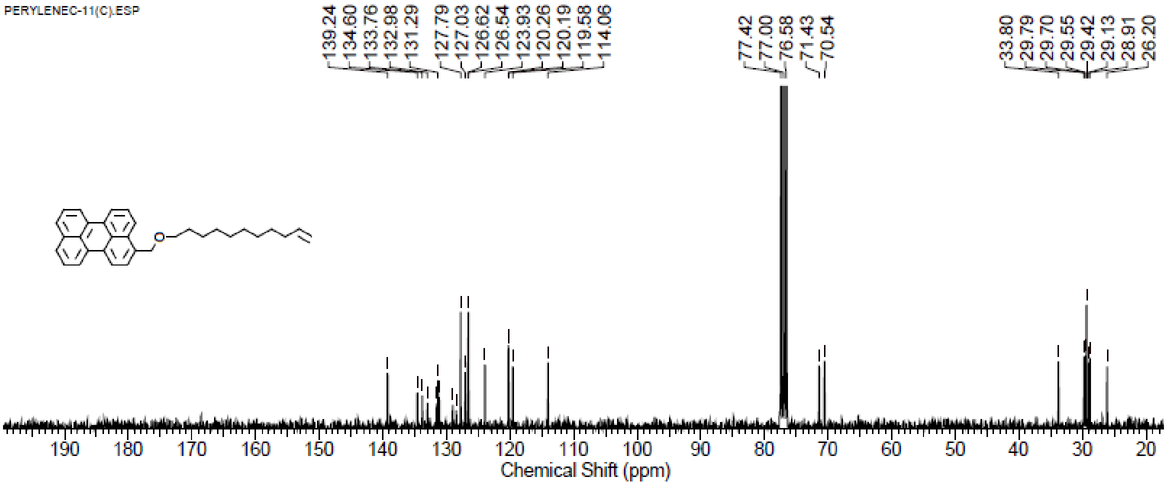

Fig. 4.4. ^{13}C NMR spectrum of 3-undecenyloxyperylene (**III**)

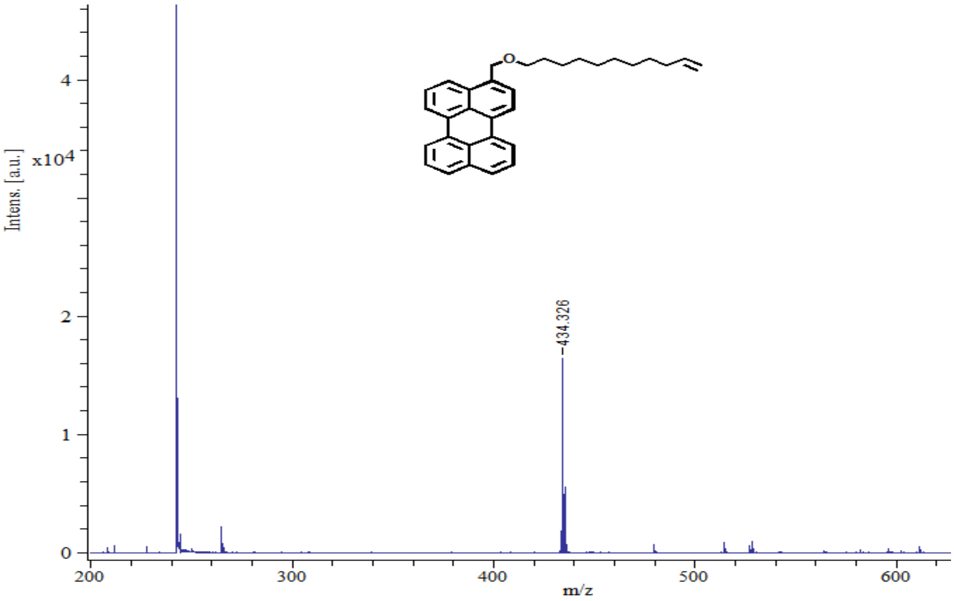

Fig. 4.5. MALDI-TOF of 3-undecenyloxyperylene(**III**)

4.2.2. Pyrene-based

The polycyclic aromatic hydrocarbon, pyrene is (PAH) the smallest peri-fused PAH (one where the rings are fused through more than one face), and contains a flat aromatic system of four fused benzene rings. Pyrene and its derivatives are commercially used to make dyes, while its derivatives are excellent molecular probes due to high fluorescence quantum yields and lifetimes. As opposed to the ground state, its excited state has a non-planar structure resulting in high sensitivity of the emission spectrum towards the solvent polarity.

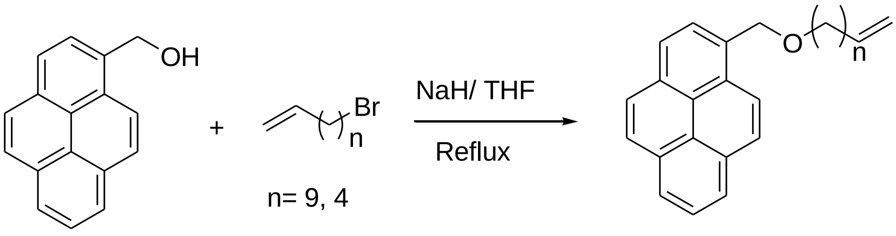

IVa: n = 9
IVb: n = 4

Scheme-4.3. Syntheses of the *O*-alkylatedpyrene-1-methanols **IVa** and **IVb**

The gap states in the pyrene derivatives can pin the Fermi level. Hence these are also suitable for nano-electronic applications, but less explored.[206] For synthesizing the required pyrene-based organic π-system, commercially available 1-pyrene methanol was subjected to a base-catalyzed *O*-alkylation with **2** or 1-bromo-5-hexene (**Scheme-4.3.**) to obtain the compounds **IVa** and **IVb** respectively.

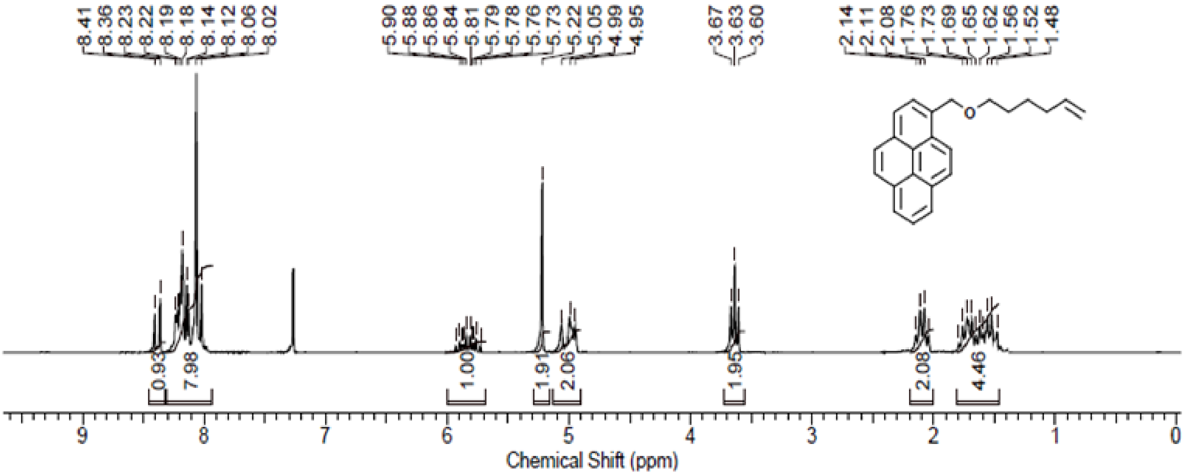

Fig. 4.6. ^{1}H NMR spectrum of **IVb**

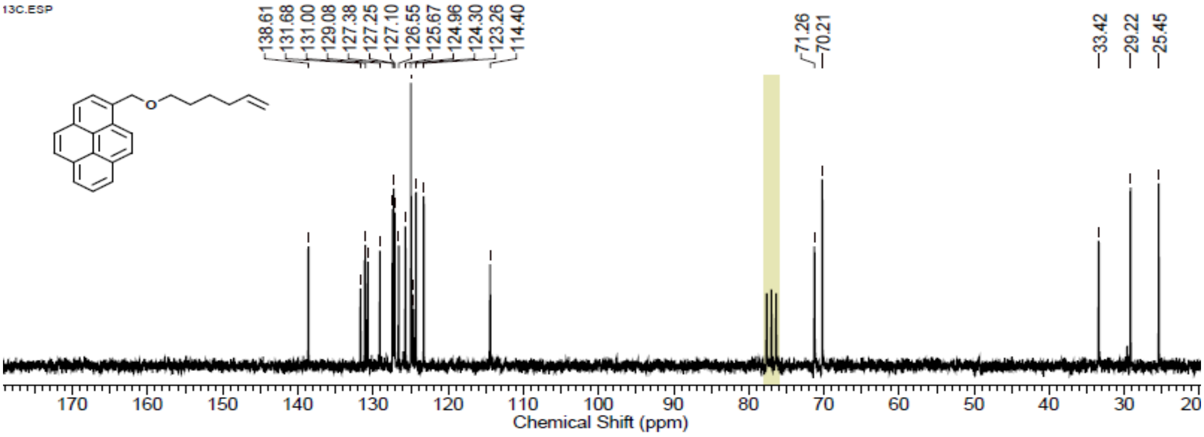

Fig. 4.7. ^{13}C NMR of spectrum of **IVb.**

Both the products were characterized by spectroscopy, and the ^{1}H NMR, ^{13}C NMR, LCMS spectra of **IVb** are presented in **Figs. 4.6**. The ^{1}H NMR spectrum showed the terminal olefinic multiplets at δ 5.82 (1H) and at δ 4.99 (2H), while the triplets at δ 3.63 indicated the presence of O-CH_2- group of the alkyl moiety. Its ^{13}C NMR spectrum was also consistent with the structure, showing peaks at δ 70.2 and 71.3 for the –O**C**H_2 moieties. The LCMS showed the molecular ion peak at 313 amu.

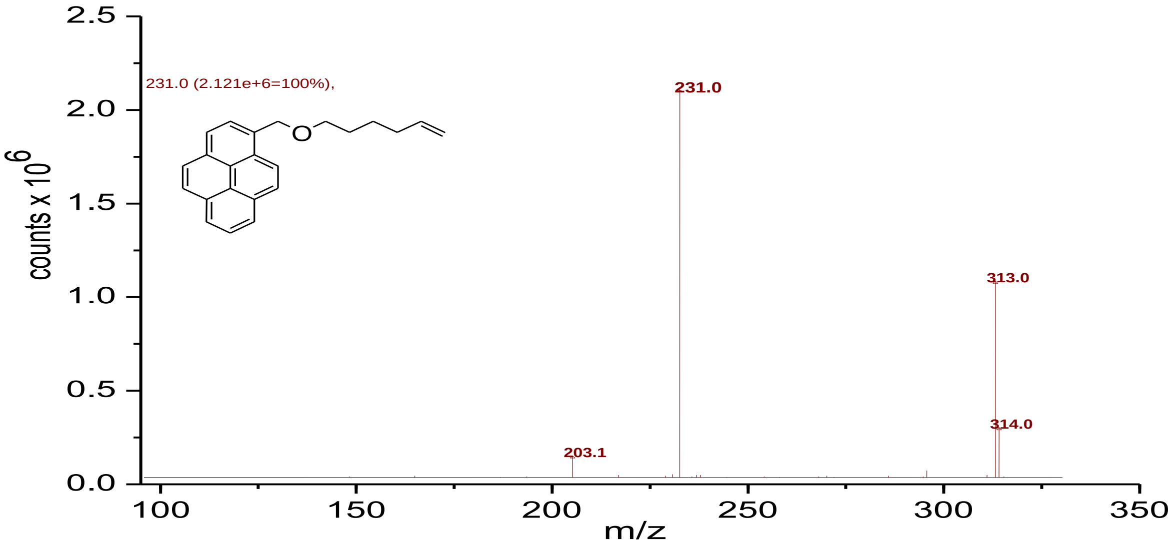

Fig. 4.8. LC-MS of **IVb**

4.3. Fabrication of devices

4.3.1. Electrografting of monolayers on Si

As earlier, the electro-deposition of the molecules **III**, **IVa**, and **IVb** on the H-terminated Si surface was accomplished by CV that showed the characteristic irreversible peak at ~0.3 V confirming covalent attachment (**Fig.4.9.**). Formation of the respective monolayers was optimized using different number of scans (5, 10, 20, 25, 30 and 50). Compounds **III** and **IVa** required 50 scans, while **IVb** required only 25 scans to form compact monolayers, as revealed by AFM (**Fig. 4.10.**). At higher scans, formation of multilayers was evident by AFM analysis.

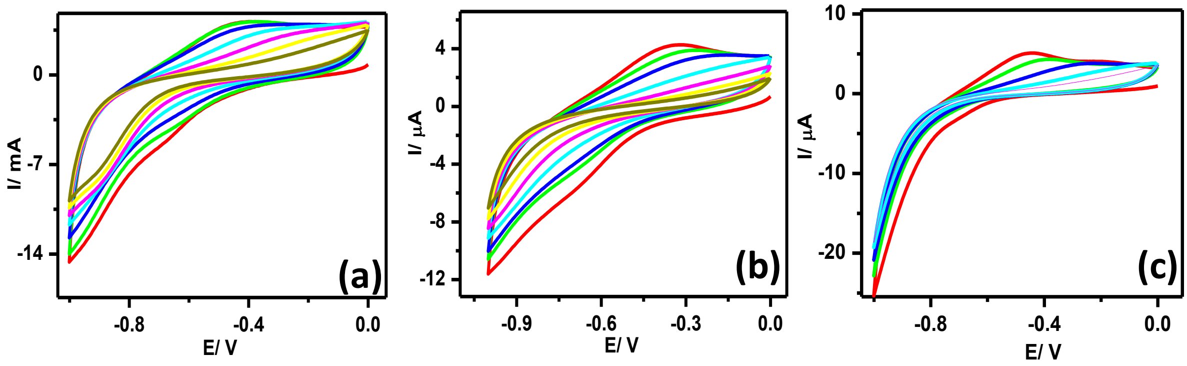

Fig. 4.9. Electrochemical deposition of (a) **IIIa**; (b) **IIIb**; (c) **IV.**

4.3.2. Characterization of the monolayers

The contact angles of deionized water in case of Si wafers, grafted with **III**, **IVa** and **IVb**were 68°, 74° and 80° respectively, as against 84° for the cleaned H-terminated Si wafers. The low contact angles of the monolayers suggested them to be tilted on the surface. The average thicknesses of respective monolayers were found to be 2.4 ± 0.1 nm for **III**, ~1.9 ± 0.2 nm for **IVa** and 1.2 ± 0.1 nm for **IVb** by ellipsometry, confirming tilting of the molecules on the Si surface. The experimental data matched well with theoretically calculated thickness values were 2.7, 2.1 and 1.4 nm for **III**, **IVa** and **IVb** respectively. In consideration of the lengths of the molecules, the calculated tilt angles were 58.3°, 58.9° and 54.3° for the monolayers of **III**, **IVa** and **IVb** respectively. The AFM analyses revealed that the monolayers of **IVb** were more compact and uniform with larger grain size, compared to that of **IVa**. The void depths of the monolayers were 2.3 nm for **III**, 1.8 nm for **IVa** and ~ 1.3 nm for **IVb** (**Fig. 4.10.**), suggesting that the monolayers of **IVb** were more organized with least number of voids and hillocks.

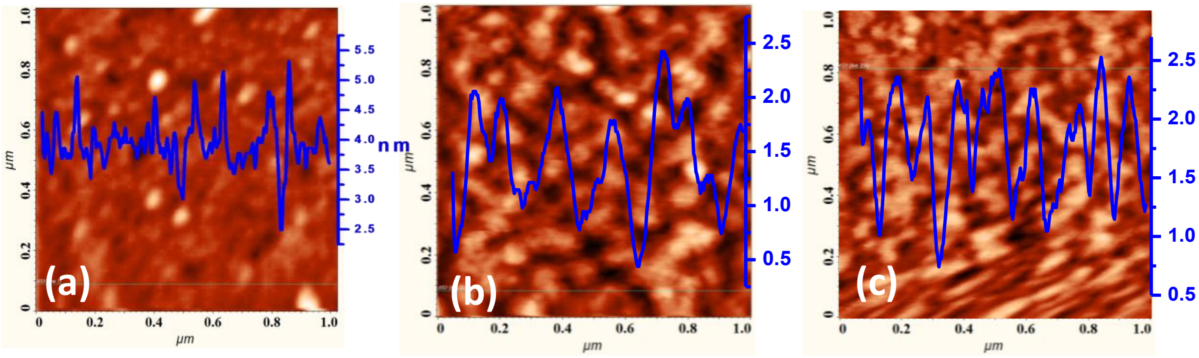

Fig. 4.10. AFM images of monolayers. (a) **III**; (b) **IVa**; (c) **IVb.** (Overlay: roughness profiles)

The molecular densities of the monolayers, determined by fast scan (10 V/s) CVs (**Fig. 4.11.**) exhibited a reversible peak at +0.8 V. The net charge transferred during the oxidation process, calculated from the areas under the oxidation peaks were 3.62×10^{-8}, 3.5×10^{-8} and 1.72×10^{-6} C respectively for **III**, **IVa** and **IVb**. These amounted to the surface coverage of 2.52×10^{11}, 5.62×10^{12} and 1.59×10^{13} molecules/cm^2 for **III**, **IVa** and **IVb**. Thus, the surface covered by **IVb** was ~ 2.8 times that of **IVa**. These data are consistent with the AFM analyses, both revealing more compact monolayers with **IVb** than **IVa**. The XPS data showed absence of SiO_2 peak at 103 eV, and presence of a peak at 99.5 eV due to the Si-C bond in the monolayers.

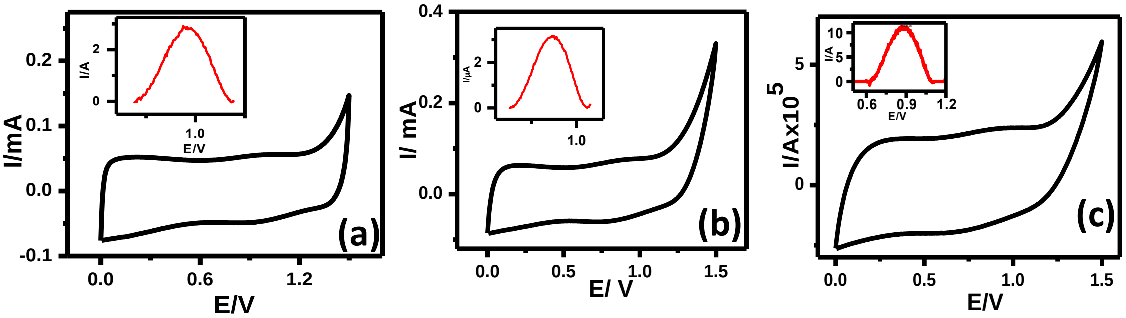

Fig. 4.11. Cyclic voltammetry of the grafted monolayers.(a)**III**; (b) **IVa**; (c) **IVb.**

The SIMS of the monolayer of **III** showed peaks due to the perylene fragments at 310, 295, 285, 270 and 258 amu (**Fig. 4.12. (a)**). In case of the compound **IVa**, the peaks due to the pyrene fragments appeared at m/z 215, 181, 164 and 114 amu (**Fig. 4.12. (b)**). But the peaks appeared at a higher mass range *viz.* at m/z 244, 206, 184, 147, 142 and 116 amu (**Fig. 4.12.(c)**) with compound **IVb**. Besides confirming the deposition of the monolayers, the SIMS data also explained their orientation. It is expected that when the monolayer is tilted more, the ions from the top have higher probability to hit the surface and knock down the aromatic moiety from the alkyl spacer. Because the **IVb** monolayer was more tilted compared to that of **IVa**, its largest mass fragment appeared at a higher mass (244 amu) *vis-à-vis* **IVa** (fragment at 215 amu). Considering the molecular weight of 1-pyrenemethanol as 232 amu, the mass fragment peak at e/z 244 amu can be represented as ([pyrene-CH_2OCH_2]-1]. Consistent with this, the monolayer of **III** with a high tilt angle showed the largest mass fragment peak at 282 amu, attributed to the ([perylene-$CH_2OCH_2CH_2$]-1) unit.

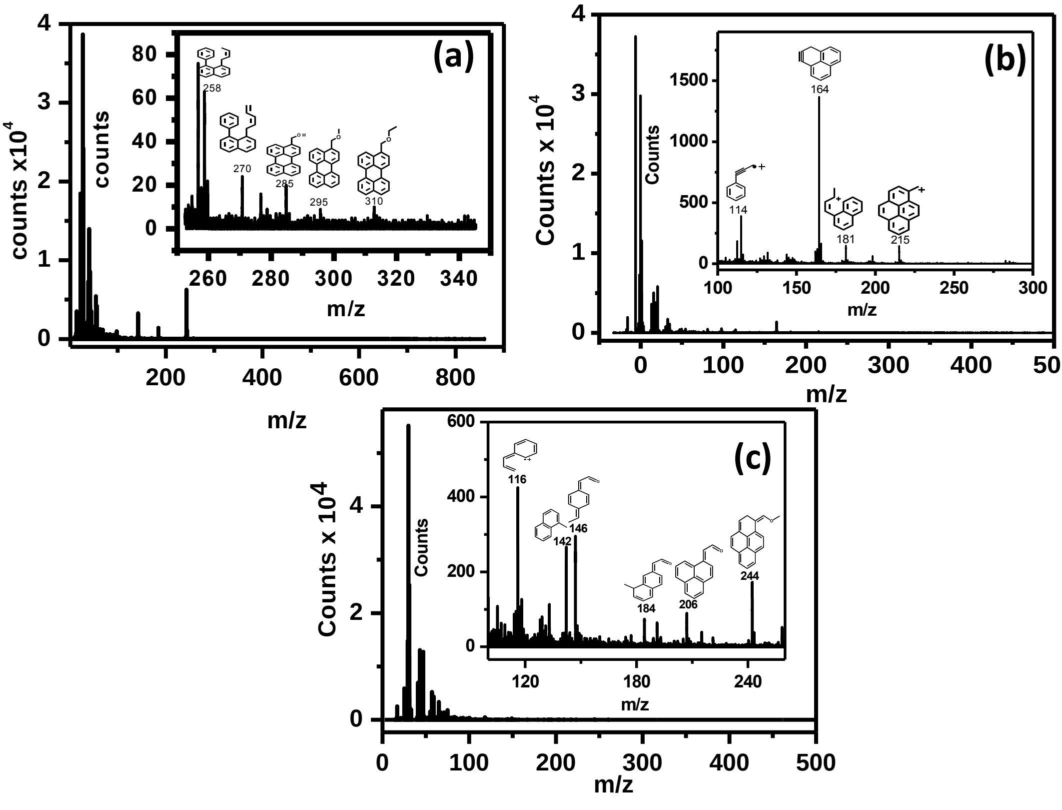

Fig. 4.12. SIMS data of grafted monolayers.(a) **III**; (b) **IVa**; (c) **IVb.**

In pure solid alkene monolayers, the hydrocarbon chains exist in an all-*trans* configuration such that the carbon backbone of each molecule lies in a single plane to maximize the enthalpic gain (~ 2 kcal/mol per CH_2 unit).[207,208] However, in liquid form, there is substantial twisting about the individual bonds. These out-of-plane twists alter the frequency of the CH_2 vibrational modes.[186] Thus, the IR peaks due to the CH_2 vibrational modes provide good insights about the proposed van der Waals interactions. The polarized FTIR spectra (**Fig. 4.13.**) for the monolayers showed the symmetric (ν_s) and asymmetric stretching (ν_a) CH_2 vibrations (i) at 2853 and 2923 cm^{-1} for compound **IVb**; and (ii) at 2847 and 2920 cm^{-1} for compound **IVa**. These suggested that the alkyl chains in the monolayers of **IVa** (containing a C_{11}-alkyl unit) are more rigid like in pure solid alkanes, while that in the monolayers of **IVb** (containing a C_6-alkyl unit) are twisted *i. e.*, more liquid like. In other words, there is an increase in the van der Waals interactions between neighboring molecules in case of the **IVa-**monolayers compared to that with **IVb-**monolayers. This is consistent with our SIMS data as well as the tilt angle values of the respective monolayers. In case of the perylene derivative **III**, the ν_s and ν_a CH_2 vibrations appeared at 2853 and 2926 cm^{-1}, indicating twisted monolayers. Possibly, the non-planarity of perylene moiety precludes tight stacking of the monolayers. This is also substantiated by the high tilt angle of its monolayers.

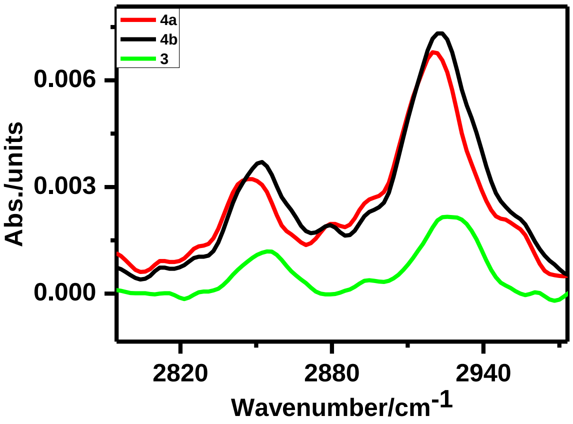

Fig. 4.13. Polarised FTIR spectra of the **III, IVa** and **IVb** monolayers.

4.4. *I-V characteristics*

The *I-V* curves of Hg/ molecule (**III**, **IVa** and **IVb**)/ Si (111) devices wafers (**Fig. 4.14.**) showed current rectification in the forward bias. The pyrene-based device with a C-6 alkyl chain (**IVb**) showed excellent results with a RR value of 2–5 × 10^5 at 2.0 V due to compact packing as compared to that with the C-11 pyrene (**IVa**)-based device (RR ~ 1000 at 1.25 V). The device made of the perylene **III** showed a RR of 3000-5000 at 1.75 V. In the present case, rectification in the forward bias is a result of resonance tunnelling through HOMO of the molecules at bias > 1 V.

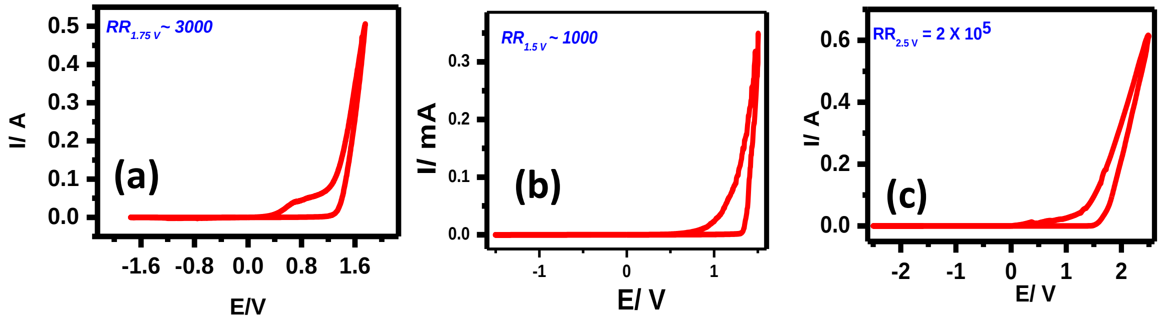

Fig. 4.14. *I-V* characteristics of the devices.(a) **III**; (b) **IVa**; (c) **IVb**.

Molecular stacking is very important for the electrical behaviour of the organic semiconductors as the overlapping of electrons clouds favours the charge carriers generation and transport to induce intrinsic conductivity. Our results showed rms roughness of 2.3 nm for **III**, 1.8 nm for **IVa** and ~ 1.3 nm for **IVb**, indicating more and/or larger defects in case of **III** and **IVa** than of **IVb** due to the longer alkyl bridge.[187] consequently, maximum RR was observed with the **IVb** monolayers.

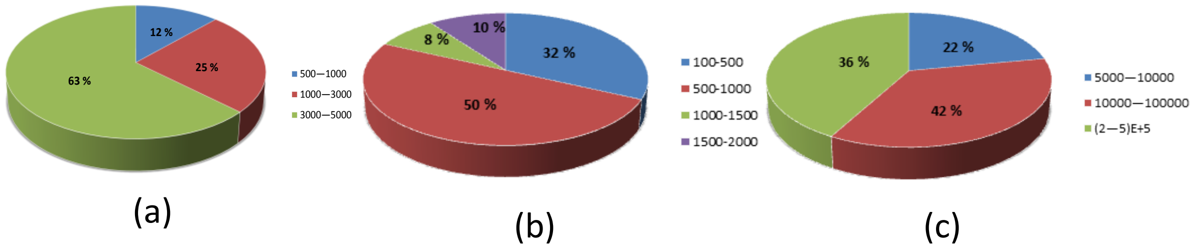

Fig. 4.15. Statistics of rectification ratios.

All the systems were stable during repetitive voltage scanning up to 15 scans without significant reduction in current or the effect. A gradual drop of RR was observed with all the devices in the subsequent scans. The statistics of the *I-V* data are shown in **Fig. 4.15.** and **Table 4.1**. Compared to the previous reports by Lenfant and his group,[89] the magnitude of

Molecules	No. of samples	No. of devices/ sample	Total no. of devices	No. of devices exhibiting Rectification
III	6	8	48	48
IVb	6	8	48	48
IVa	6	8	48	48

Table 4.1 Statistics of *I-V* measurement

current in the present devices was much higher. Hence the device temperature shoot up that might alter the geometry of the molecular assembly, explaining the results.

4.5. Theoretical calculations

In general, the forward bias current flow should be determined by the HOMO states of the molecules, while their respective LUMO states would dictate the reverse bias current. Thus, the rectification in forward bias in case of the pyrenes and perylene is a result of alignment of the HOMO of the molecules with the Fermi-levels of the electrodes (**Fig. 4.16.**). To verify this, we have theoretically calculated the HOMO and LUMO energy levels of **III**, **IVa** and **IVb** using *ab initio* method (GAMESS software). The geometry optimization without any symmetry constraint was carried out at the B3LYP/6-31G (d, p) level of theory where the exchange correlation functions are expressed using hybrid density functional theory. The HOMO-LUMO values (**Table 4.2.**) of the molecules revealed a higher HOMO-LUMO gap (3.77) with the pyrene molecules compared to that of the perylene derivative (3.01). Hence more rectification is expected with the device made of the pyrenes **IVa** and **IVb** than the perylene **III**, as was observed experimentally. In case of **III** and **IVa** the spacer length is more, hence rectification was observed at lower biases than that with **IVb**. On the other hand, the molecule **IVb**

Molecule	HOMO	LUMO
III	-4.89 eV	-1.877 eV
Iva	-5.51 eV	-1.74 eV
IVb	-5.52 eV	-1.75 eV

Table 4.2. Theoretically calculated molecular orbital energies for **Fig. 4.16**

possesses a small alkyl spacer, and the gap between its HOMO level and the Si Fermi level is larger. Consequently, the current rectification with **IVb** was observed at a higher voltage (2.5 V).

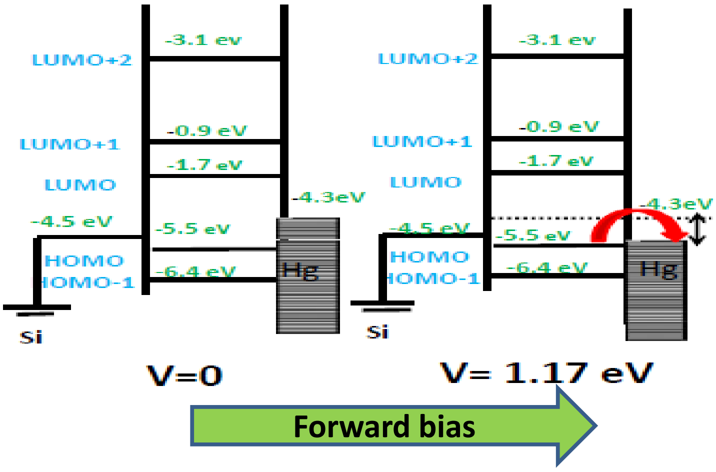

Fig. 4.16. Mechanism of rectification of devices made with **IVb**.

As described earlier, a model for a two-probe system containing the molecules between two gold electrodes via a thiol end group was constructed (**Fig. 4.17.**). After optimizing the interface geometry of the thiol-terminated molecule and the electrode for best overlap between the device and the electrode, the transmission spectra and theoretical *I-V* curves of the devices were calculated. A similar calculation with the prototype molecule, methyl thiol on the periodic Au (111) surface revealed the distance between the Au (111) surface and the terminal S (or H) atom, located at the hollow site of the Au surface as 2.52 Å.[166] Presently, the two Au (111) - (4 × 4) surfaces with periodic boundary conditions were used to model the left and right electrodes. The Au/molecule/Au configuration was divided into three parts: left electrode, right electrode, and the central scattering region. In our models, there were four gold layers in each of the left and right electrode unit cells. The scattering region was composed of the individual isolated molecules together with the respective three gold layers on the left and right sides.

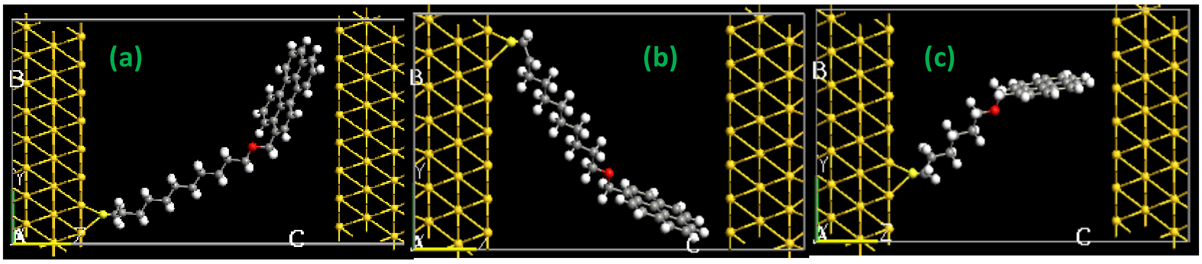

Fig. 4.17. Theoretical measurement set up Au/molecule/Au devices. (a)**III**; (b) **IVa**; (c) **IVb**.

The electron-transport properties of the Au/molecule/Au systems were investigated using the ATK 11.2.3 program, where a semi-empirical extended Huckel theory in combination with the first-principle non-equilibrium Green's function (NEGF) is employed. A k-point sampling of 100 was used in the electron-transport direction (Z direction).[167] The theoretically calculated curve also showed rectification in positive bias (**Fig. 4.11.**) for **III**, **IVa** and **IVb** with RRs as 2000, 400 and 8000 respectively at 2 V. This confirmed that the rectification is intrinsic property of the molecules.

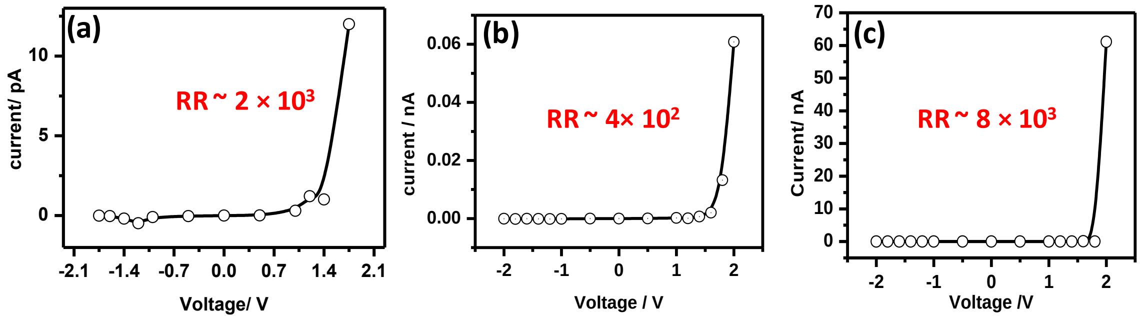

Fig. 4.18. Theoretical *I-V* characteristics of Au/molecule/Au devices.(a) **III**; (b) **IVa**; (c) **IVb**.

4.6. Conclusions

Overall, three alkenylated polyaromatic molecules *viz.* a C-11-perylene (**III**), and the C-6- and C-11-alkenylated pyrenes (**IVa**and **IVb** respectively) were synthesized as prototype σ–π systems, and individually electro-grafted on H-terminated Si surfaces to form monolayers. The *I–V* characteristics of the monolayers revealed pronounced current rectification in the positive bias. To the best of our knowledge such a high RR value is not reported till date. The rectification by the hybrid systems was stable and reproducible property, and could be tuned by subtle changes in alkenyl chain lengths that determined the packing of the monolayers on the Si surface. In the previous studies,[85,89] the σ–π systems were attached on Si wafers by silanization of native oxide with n-alkenyltrichlorosilanethat produced much less RR (~35). In those case, the attachment of the σ–π systemsthrough the strong Si-O-Si linkages (Si-O ~108 kcal mol^{-1}),[175c] would rigidize the molecular assemblies on the surface. This may prevent proper stacking, creating voids and resulting in poor RR values. In comparison, our devices were built through Si-C bonds (Si-C ~76 kcal mol^{-1}), as confirmed from the XPS data. Hence, it is expected to offer more flexibility to the molecules on the Si-surface for more van der Waals interactions, ensuring better packing to show better rectification. Theoretical simulations of Au/ molecule (**III**, **IVa** or **IVb**)/Au structure demonstrated that the rectification is intrinsic to the molecules.

Chapter-5

CHAPTER-5

Porphyrin based chemical sensing devices

5.1. Introduction

The ability to sense or detect and quantify a chemical entity, and in particular accomplish this through the use of chemical means, has become a topic of extensive research in modern society. The rapid growth in chemosensing is driven largely due to their applications in medical diagnostics, environmental monitoring, and toxicological analysis, and the need to develop probes that allow for the in-depth understanding of the relationships between the presence of chemical or biological marker and its biological implications. A chemosensor functions on a molecular level, generating a signal upon binding with certain chemical stimuli selectively. At the heart of almost all mechanisms of molecular sensing is a binding event of some kind, supramolecular (through weak interactions) or covalent bond formation with the analytes.[209]

As discussed in a previous chapter, porphyrins and their derivatives are highly conjugated p-type organic semiconductors. Their electrical as well as optical properties can be changed by interaction with various gases,[210] hence they have been used to develop chemi-resistive or optical gas sensors. Their sensitivity to gas molecules may be tuned by manipulation of the central metal, and by substitution of functional groups on the organic ring.[211] Exposure to oxidizing or reducing gases causes charge to be transferred between the gas and the delocalized π-system of the porphyrin molecules. This charge transfer significantly modifies the optical absorbance spectrum as well as electrical conductance of the films, which provide the basis for simplistic gas sensing methods.[210,212] A big disadvantage of optical method of gas sensing is that it requires an expansive and bulky spectrophotometer. On the other hand, measuring the change in electrical conductance on exposure to gas (*i.e.* chemi-resistive sensor) is much simpler. The gas sensors of these materials was normally fabricated by depositing their thin films using chemical (Langmuir-Blodgett, spin coating etc.) or physical (thermal evaporation) techniques.[213-215] Of these, the spin coating method is simple, economical and mostly used for soluble organic materials. In general the spin-coated films have porous structures with large surface/volume ratio, hence large number of adsorption sites for gas and active layer interaction. Therefore these are very useful for gas sensing applications.[216]

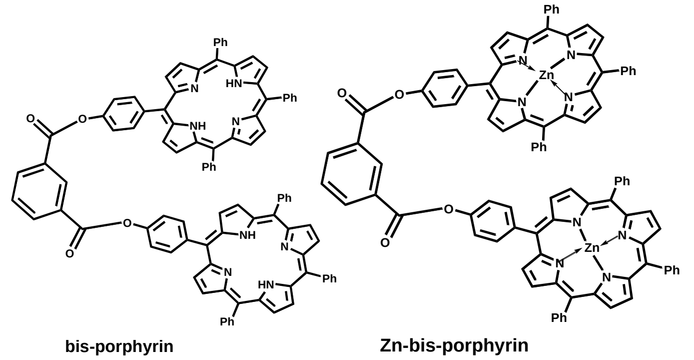

bis-porphyrin

Zn-bis-porphyrin

Fig. 5.1. Structure of bis-porphyrin **V** and Zn-bis-porphyrin **VI**

The application of porphyrins in molecular electronics was demonstrated by constructing several Si-porphyrin hybrid devices with current rectification and/ or NDR properties. During the present investigations, two new porphyrin derivatives *i.e.* a bis-porphyrin and its Zn-derivative were synthesized, spin-coated on glass surface, and their potential as chemi-resistive sensors of two toxic gases, Cl_2 and NH_3 were assessed. These are discussed in this chapter. Regarding the molecular design, it was envisages that rather than a simple mono-porphyrin, if two of these molecules are tethered at two ends of a spacer, the resultant bisporphyrin molecule would possess a jaw-like structure enabling it to be a more effective hosts for the analyte. This, in turn, may induce better binding, depending on the cleft size and other interactions to offer higher selectivity for the target analyte. With this rationale, the bisporphyrin **V** and its Zn-derivative **VI** (**Fig. 5.1.**) were chosen as molecular hosts. It was envisaged that the chosen molecules will provide the following advantageous in developing chemi-resistive sensors

i. The solubility of bisporphyrin in polar solvent is expected to be high,[217] assisting the film formation by spin coating;

ii. The molecules would have net dipole moments due to the presence of the ester group with asymmetric oxygen structure; and

iii. The jaw like structure would offer more open area inside the films, hence more sensitive gas sensing characteristics.

5.2. Synthesis of the gas sensing molecules

5.2.1. Synthesis of Bisporphyrin (V).

Compound **V** was synthesized in two steps. In the first step, 5-(4-hydroxyphenyl)-10,15,20-triphenylporphyrin **13** was synthesized by the classical Adler and Longo method. This involved condensation of 4 equivalent of pyrrole with two different aldehydes (benzaldehyde and 4-hydroxybenzaldehyde) in 3:1 equivalent ratio in propionic acid to furnish the mono-hydroxy-TPP **13** (**Scheme-5.1.**).[218] The product was characterized by ^{1}H NMR, UV-Vis and FTIR spectra. Its ^{1}H NMR resonances comprising of (i) a broad singlet at δ -2.75 (porphyrin

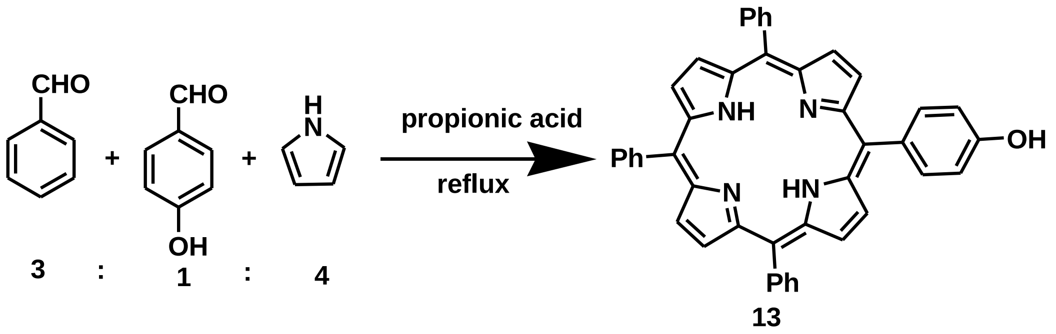

Scheme-5.1. Synthesis of mono-hydroxytetraphenyl porphyrin **13**

NH), (ii) two doublets at δ 7.14 and 8.15 (*p*-substituted benzene), (iii) 8H-multiplets at δ 8.87 ppm (β-pyrrolic protons), and (iv) multiplets at δ 8.24 (6H) and at δ 7.77 (9H) (three phenyl moieties) were consistent with its chemical structure. The UV-Vis spectrum of porphyrin display *etio* type allure with a typical Soret (B) band at 416.0 nm, and the four Q-bands in the visible region displaying absorption maxima (λ_{max}) around 514.6, 549.6, 590.0 and 645.8 nm. The Soret band is generated by the transition from a_{1u} (π) – e_g^* (π), and the four Q bands correspond to a_{2u} (π) – e_g^* (π) transitions. The FTIR spectra showed peaks at 3429 (NH), 3019(CH), 2976 (CH), 2399(CN) and 1215 (CO) cm^{-1}.The MALDI-TOF showed the mass peak at 630 d, confirming its formation.

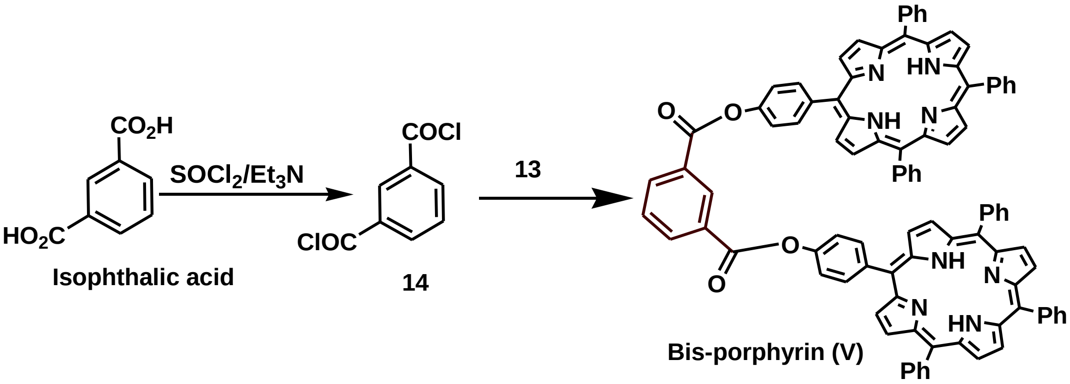

Scheme-5.2. Synthesis of **V**

For the synthesis of compound **V**, isophthalic acid was reacted with $SOCl_2$ in DMF to afford isophthaloyl chloride **14** that was purified by vaccum distillation. Reaction of 1 equiv. of the acid-chloride **14** with two equivalents of **13** in the presence of Et_3N furnished a mixture of the mono and di-esters of isophthalic acid. This on thin layer chromatography (TLC) gave compound **V**. Its ^{1}H NMR showed a broad porphyrin NH singlet at δ -2.78, a singlet at δ 9.3 corresponding to isophthalic acid

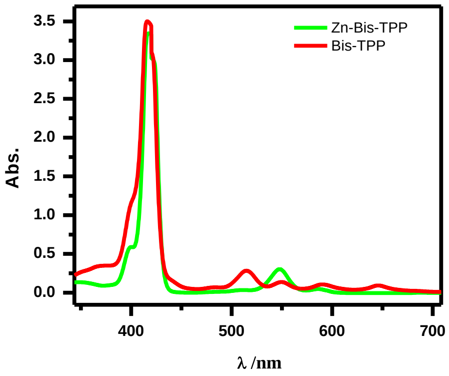

Fig. 5.2. UV spectrum of **V** and **VI**

aromatic H-2, multiplets at δ 8.92 (16H) for the β-pyrrolic protons, and phenyl multiplets at δ 8.65 (2H), 8.31 (16H) and 7.74 (23H). The UV-Vis spectrum of **V** displayed a typical Soret band at 416.0 nm, and four Q-bands at 514.6, 549.6, 590.0 and 645.8 nm (**Fig. 5.2.**). The FTIR peaks at 3434, 3019, 2399, 1641 and 1215 cm^{-1}accounted for the NH, CH, CN and CO functionalities respectively, while the molecular ion MALDI-TOF at 1392 d as the base peak confirmed its structure.

5.2.2 Synthesis of Zn- bisporphyrin (VI)

Compound **VI** was synthesized by metalation of compound **V** with Zn(OAc)$_2$ (**Scheme-5.3**.).[219] Amongst the methods for metalation of porphyrins, reaction of metal acetates in acetic acid and porphyrin in methanol is often used. However, the workup poses problem with water-soluble porphyrins. Hence presently, the reaction between compound **V** and Zn(OAc)$_2$ was carried out in MeOH-CHCl$_3$ mixture under a refluxing condition, omitting acetic acid. As usual, compound **VI** was characterized by ^{1}H NMR, UV-Vis and MALDI-TOF spectroscopy. The absence of the of the porphyrin NH peak in the ^{1}H NMR spectrum indicated its metalation (**Fig. 5.3.**) that further was confirmed from the [M]$^+$ peak at 1518 d in

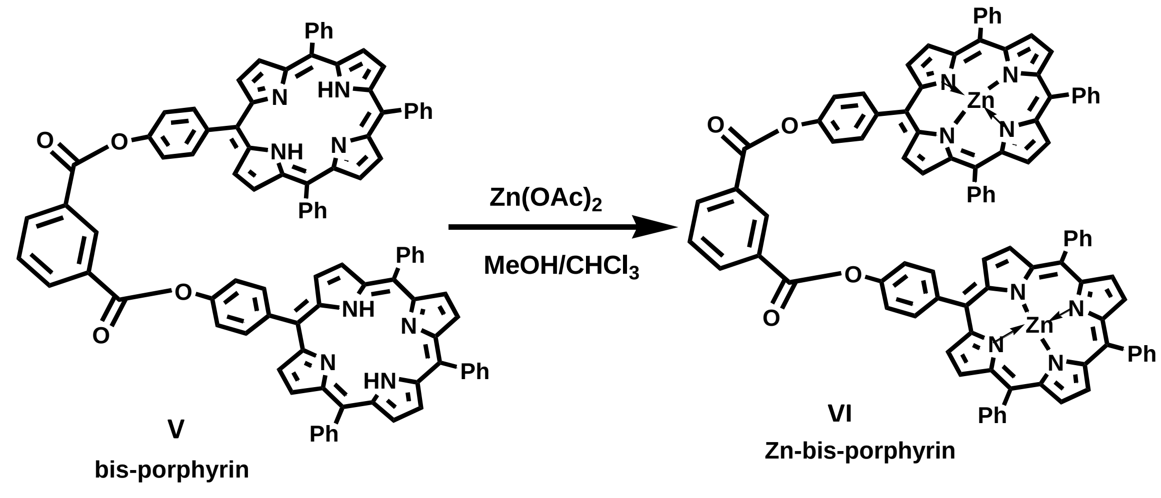

Scheme 5.3. Synthesis of **VI**

the MALDI-TOF spectrum (**Fig. 5.4.**). The typical ^{1}H NMR porphyrin resonances, FTIR peaks for the CN and CO functionalities, and the UV-Vis Soret band at 417 nm and Q bands at 547 and 585 nm were also observed (**Fig. 5.2.**).

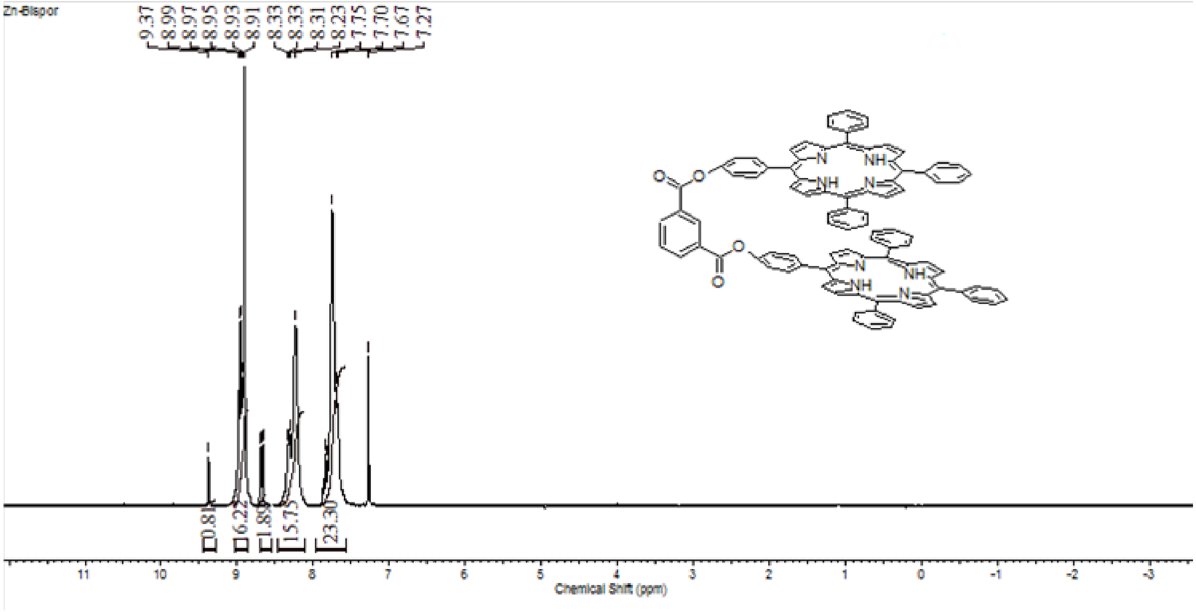

Fig. 5.3. ^{1}H NMR of **VI**

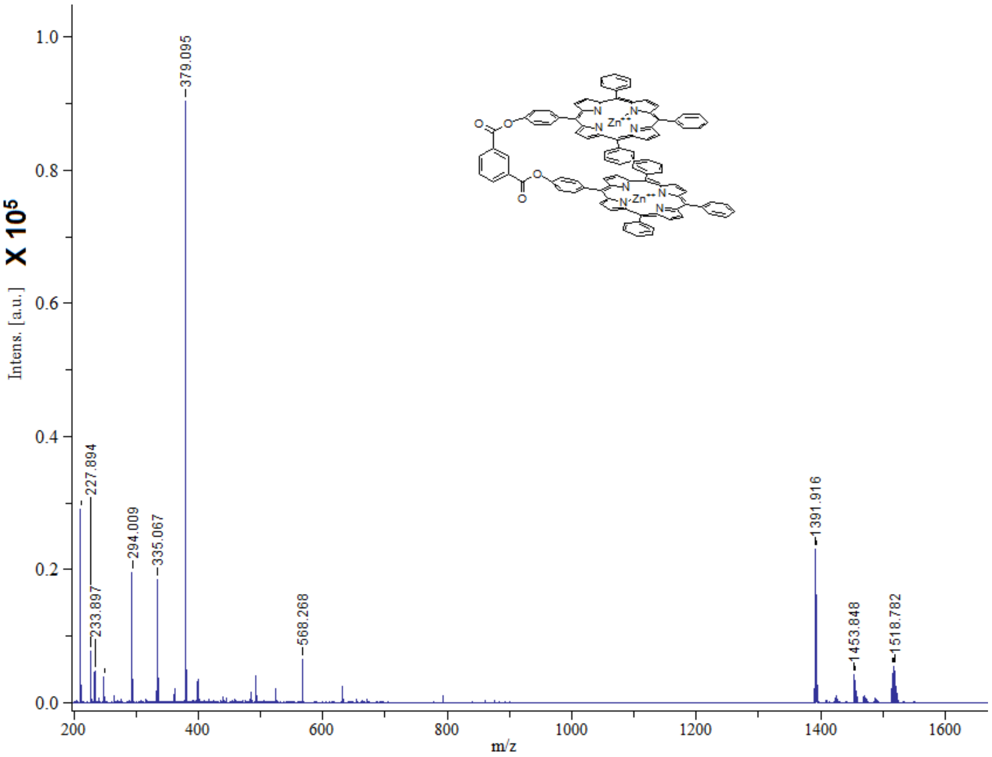

Fig. 5.4. MALDI-TOF of **VI**

5.3 Sensor fabrication

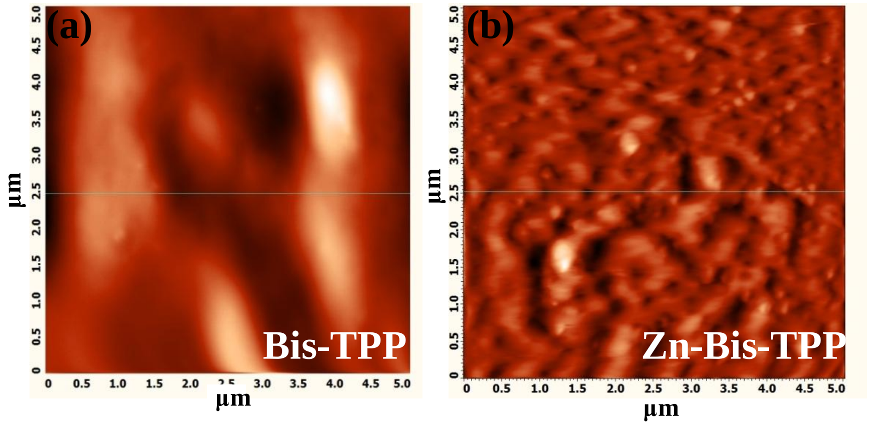

(a) **(b)**

Fig. 5.5. AFM of **V** and **VI** fims

Thin films of **V** and **VI** (thickness~1 µm) were deposited by spin casting (details given in **Chapter-2**). Typical AFM images (size; 5 µm × 5 µm) of the spin-coated films of **V** and **VI** are shown in **Figs. 5.5. (a)** and **(b)** respectively. The analysis of surface morphology for both films revealed the rms surface roughness of ~10 nm for **V** films, while for the films with **VI**, the roughness was ~ 20 nm. Formation of such a uniform film is attributed to the dipole moment associated with these molecules, which favours the strong π-π interactions between the porphyrin rings. Moreover higher roughness for **VI** indicated poor structural ordering in these films, which is possibly due to more non planar nature of the **VI** subunits.

The structural ordering of both the films was confirmed by XRD pattern (**Fig. 5.6.**). The presence of sharp diffraction peaks for **V** films indicated their poly-crystalline nature, while absence of any diffraction peaks for the **VI** films revealed their amorphous nature. Since both films were prepared under identical experimental conditions, the amorphous nature of **VI** is attributed to the influence of Zn^{2+} ion on the bis-porphyrin core.

The ramification of morphology and crystallinity of the films is also revealed in the room temperature current-voltage (*J-V)* characteristics, as shown in **Fig. 5.7**. The *J-V* characteristics for both the films were highly nonlinear, exhibiting two different power law ($J{\sim}V^2$) behaviour as a function of applied bias with varying α values. At room temperature, for low bias (< 20 V) α ~1 indicated ohmic conduction; while for high bias (>20 V), α ~ 2 indicated space charge limited conduction (SCLC). SCLC occurs if the injected carrier density is higher than thermally generated carrier concentration and *J* depends on applied bias *V* through the relation: $J = \frac{9}{8}\varepsilon\mu\frac{V^2}{d^3}$, where ε is permittivity of films.[220] As shown in the inset of each **Figs. 5.7.(a)** and **(b)**, the data of the J-V^2 plots showed linear fits at a high bias (>20 V). This indicated that the charge transport in these films is governed by trap-free SCLC. From the slope of the linear fit to J-V^2 data, and assuming the literature value of ε (3×10^{-11}F/m),[221] the calculated value of μ (at 300K) for **V** films was 1.76 $cm^2V^{-1}s^{-1}$. Similar analysis of *J-V* data for **VI** films indicated the μ as $1.51\times10^{-3}cm^2V^{-1}s^{-1}$.The low mobility values are due to the amorphous nature of these films.[222] From the Ohmic region of *J-V* characteristics, the respective free carrier concentration was calculated using the Ohmic relation, $J = n_0 e\mu E$, where n_0 is the thermally generated hole concentration, *e* is electronic charge, μ is the hole mobility and *d* is the electrode separation.[220] The room temperature values of n_0 for the **V** and **VI** films were 2.3 × 10^{14} cm^{-3} and 1.6 × 10^{13} cm^{-3} respectively. The low values of μ and n_0 for the **VI** is an outcome of their poor structural ordering.[223]

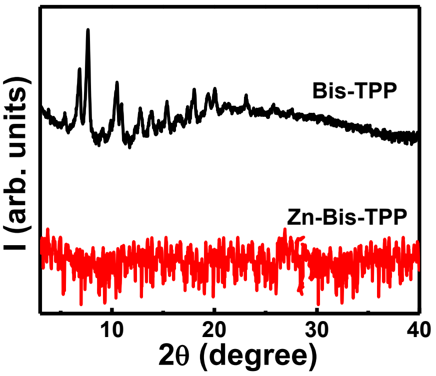

Fig. 5.6. XRD of **V** and **VI** fims

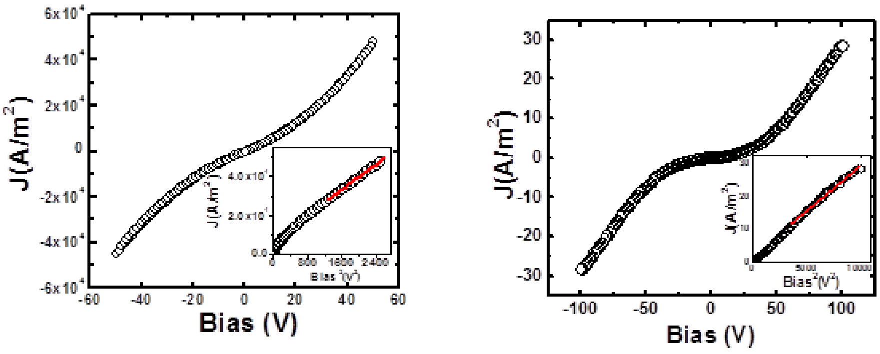

(a) (b)

Fig. 5.7. J-V characterstics of (a) **V** (b) **VI** films

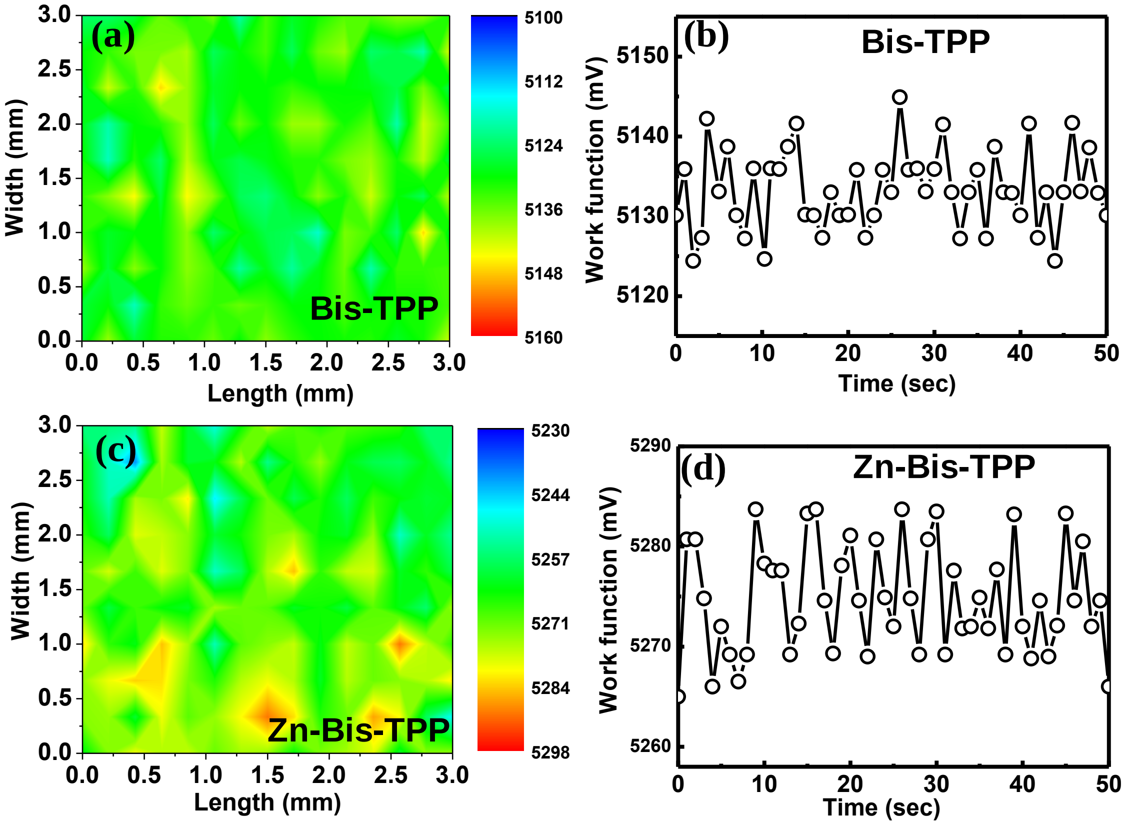

Fig. 5.8. Work function images of (a) **V** and (c) **VI** films. (b) and (d) shows the work function measured at 50 point of films for (a) and (c) respectively.

The work function values of the films were recorded using Kelvin-probe microscopy and the results are shown in **Fig. 5.8.**. **Figs. 5.8. (a)** and **(c)** show the work function images (3 mm × 3 mm) of the **V** and **VI** films. **Figs. 5.8. (b)** and **(d)** show the work function for **V** and **VI** films, measured at 50 different points on the films surface. From these data the estimated average values of work functions for **V** and **VI** were calculated as 5132 and 5275 meV respectively with a standard deviation of 20 meV. The work function values are close to that of gold (5.1 eV), indicating that gold electrode and the films can have Ohmic contacts that is necessary to describe charge transport by SCLC mechanism discussed earlier.[224]

The UV-Vis absorption spectrum of the **V** and **VI** molecules in chloroform solutions and spin coated films is shown in **Fig. 5.9**. The absorption spectra of both the films are relatively broad and red shifted, compared to that of molecules in solutions. This suggested occurrence of an incoherent interaction in the surroundings of the dense film. For the **V** film, the Soret band appears at 432 nm as compared to the 418 nm observed for the free base monomers (solution phase). The weak Q-bands at 518, 555, 594, and 651 nm were also observed for the **V** films. The red-shifts of the Soret and Q bands confirmed formation of J-aggregates, as H-aggregation results in the blue-shift.[225] In case of the **V** and **VI** films, the J-aggregation may be due to π–π stacking leading to the formation of ladder type structures. In case of the **VI** films, the presence of a strong high-energy absorption shoulder of the Soret band (at 431 nm)[225] is usually assigned to the orthogonal transition dipole to the aggregation axis. This suggested that the slipping distance (d) is quite short in case of **VI**, which is possible due to the non-planarity of Zn-porphyrin subunits. Therefore, the J-aggregation of **VI** with small slipping distance can yield rough structure, as observed in the AFM images.

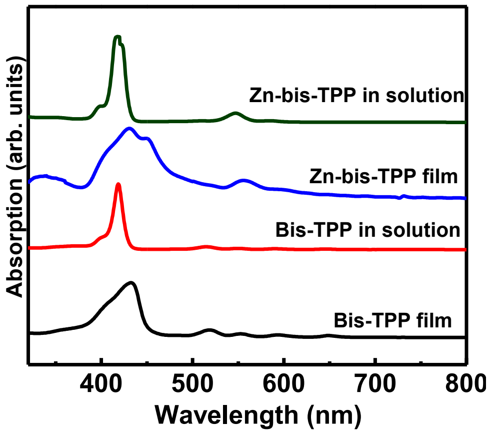

Fig. 5.9. UV-Vis spectrum of **V** and **VI** in CHCl$_3$ solution as well as in films forms

5.4. Gas sensing by the films

5.4.1. Chlorine sensing

Chlorine is used in many applications including water disinfection and for treating sewage effluent, bleaching of pulp in paper mills, disinfecting of equipment and utensils in beverage and food processing plants and is used in the manufacture of a number of products including rubber, antifreeze, household cleaning agents, and pharmaceuticals. In addition, one of the most common uses of chlorine is to keep pool water safe for swimming. Most of us use products that contain chlorine on a regular basis without concern. However, chlorine may bring negative impact to human health when it emits into environment.[226] Cl_2 is a strong irritant in humans affecting the eyes, upper respiratory tract, and the lungs. These include nose and throat tickling, stinging or dryness, and burning of the conjunctiva at the sub-ppm levels. At ~1 ppm level, the discomfort ranges from ocular and respiratory irritation to coughing, shortness of breath, and headaches. Higher levels of Cl_2 exposure results in the following effects in humans; 1 to 3 ppm; mild mucous membrane irritation; 30 ppm; chest pain, vomiting, shortness of breath, cough; 46 to 60 ppm; toxic pneumonitis and pulmonary edema; 430 ppm; lethal after 30 minutes; 1000 ppm fatal within a few minutes. Hence, detection of Cl_2 gas in environment is necessary for the human safeguards.

In recent years, some metal oxides and complex metal oxides have been used as chlorine gas sensors that work at high For example, Wang *et al.*[227] synthesized mesoporous SnO_2-based sensor which was sensitive to chlorine gas at 370 ^{o}C. The In_2O_3 sensor showed better sensitivity to Cl_2 gas at 300,[228] while the $CdIn_2O_4$ sensors[229] showed faster response to Cl_2 gas at 220–300 °C. $CdSnO_3$, used as an electrochemical material was found attractive for sensing various gases including chlorine. However, depending on the method of synthesis, these inorganic sensors show may have different morphology, and varying efficiencies.[230]

Therefore, it is necessary to improve the property of Cl_2 gas sensors in order to decrease the working temperature, and also have a reliable and sturdy device. Considering the high toxicity of gaseous Cl_2, the present studies were carried out using Cl_2 gas in the concentration range (10-1000 ppb). The **V** films showed an increased conductance on exposure to Cl_2 gas even at room temperature. However, the response and recovery times were too large to be of any use. It was gratifying to note that the response was enhanced significantly with increasing temperature, and the optimum temperature for Cl_2 sensing was 170ºC. A typical response curve recorded at 170 ºC for different Cl_2 concentrations is shown in **Fig. 5.10**.

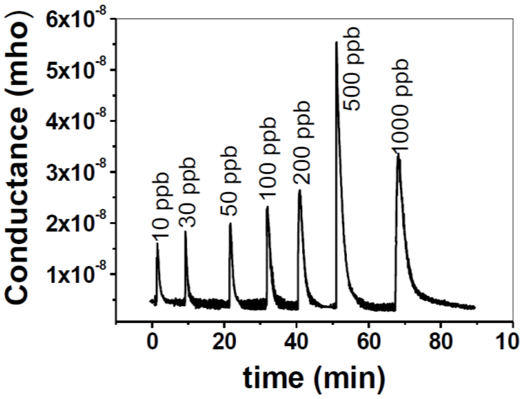

Fig. 5.10. Response curves of **V** films

Reversible response is a prerequisite for chemi-resistive sensors. Presently the response curve to the **V** films showed a linear response for Cl_2 gas in the chosen concentration range (10-500 ppb), the response was highly reproducible, with a very fast response time (~ 3 s) and a complete recovery in 8 min. The sensitivity of the sensors is defined as $S = \{(C_e\text{-}C_0)/C_0\} \times 100$, where C_0 and C_e are the conductance values in air and at the saturation level of the exposed gas. The variation of S as a function of Cl_2 concentration (10-500 ppb) (**Fig. 5.11.**) revealed the S varied linearly between 278 and 1370%. However, at 1000 ppb of Cl_2, the S value started decreasing, and the recovery was also not complete.

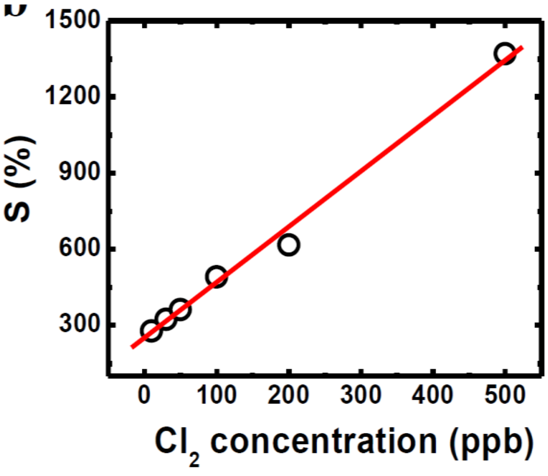

5.11. Variation of sensitivity (S) with Cl_2 concentration

The mechanism of response of the films to the exposure of Cl_2 gas can be explained on the basis of the formation of a charge transfer (CT) complex between the oxidizing, electrophilic molecule Cl_2 and the π-electron system of the **V** films. A charge-transfer complex (CT complex) or electron-donor-acceptor complex is an association of two or more molecules, or of different parts of a large molecule, in which a fraction of electronic charge is transferred between the molecular entities.[231] The resulting electrostatic attraction provides the stabilizing force for the molecular complex. The nature of the attraction in a charge-transfer complex is not a stable chemical bond. The association does not constitute a strong covalent bond and is subject to significant temperature, concentration, and host, e. g., solvent, dependences. Charge-transfer complexes exist in many types of molecules, inorganic as well as organic, and in all phases of matter, i.e. in solids, liquids, and even gases. The CT complex are of contemporary interest in developing novel functional materials such as solar cell, sensors etc.

Formation of the CT complex alters the conjugation properties, such as, conjugation length and number of π-electrons, resulting in a conductance change. The adsorptions sites of the Cl_2 molecules on the **V** films are not identified, as the attachment can take place at the centre of the conjugated rings or between the two rings. Also, the number of Cl_2 molecules per porphyrin ring that constitute the CT complex is also known. Given our interest on developing a gas sensor, these aspects were not included in the present studies. Nevertheless, irrespective of the adsorptions sites on **V** films, the adsorption rate would decrease with time due to an increase in surface coverage, according to the Elovich equation: $d\theta / dt = a \exp(-b\theta)$, where θ is the amount of gas adsorbed at time t and a, b are constants.[223,232] In the Elovich equation, constant 'a' is regarded as the initial adsorption rate because $d\theta/dt$ approaches a when θ approaches 0, and it depends on the activation energy. The constant 'b' is related to a measure of the extent to which the surface has been screened by the potential barrier for successive adsorption. In the present case, assuming that the change in the conductance (ΔC) is proportional to the amount of adsorbed Cl_2 molecules (θ), the Elovich equation in its integrated form can be written as: $\Delta C = \frac{1}{b'}\ln a'b' + \frac{1}{b'}\ln[t + (1/a'b')]$, where *a'* and *b'* are constants. As shown in **Fig. 5.12(a)**, the plots of ΔC vs ln*t*, derived from **Fig. 5.6** are linear after a time (i.e. ln*t* > 0.65), indicating that the interaction obeys the Elovich equation. From the slopes, the values of *b'* were calculated for different Cl_2 concentration. As shown in the **Fig. 5.12(b)**, log *b'* versus log [Cl_2] plot is linear in nature. Therefore, apart from the sensitivity plot (**Fig. 5.11**), the Cl_2 concentration can also be determined from the *b'* value, derived from the response rate $\Delta C/dt$. The irreversible response of the films at higher Cl_2 concentrations (>1000 ppb) indicated its chemical reaction with the **V** molecules. Hence the process will be irreversible unless energy and presence of other species are available, as observed in the present case. In order to confirm the chemical reaction of **V** with Cl_2 gas, the XPS, FTIR and UV-Vis spectra of the freshly prepared films and after exposure to a high dose (5000 ppb) of Cl_2 were recorded. The core level N-1s XPS spectrum of fresh **V** films (**Fig. 5.13. (a)**) indicated the presence of N in two different chemical states. The peaks at 398.9 eV and 402.4 eV corresponded to nitrogen in C-N and N-H bonds of **V**, respectively.[233] However, appearance of a single N peak in the XPS spectrum at 397.6 eV in the Cl_2-exposed films indicated an identical environment for all the nitrogen atoms. This can possibly happen if the Cl_2 molecules, at higher concentrations, diffuse between the two porphyrin wings of the **V** molecules and oxidize it. The presence of Cl_2 p peak (**Fig. 5.13.(b)**) in the exposed films verified the existence of chemisorbed

Cl_2.[234]

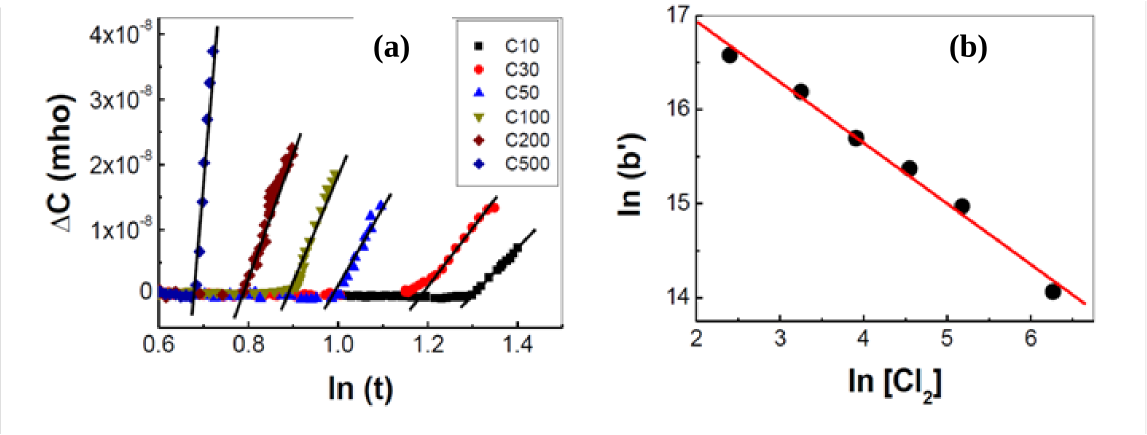

Fig. 5.12. (a) Change in conductance (ΔC) as a function of ln (t.) (b) Linear correlation between ln*b'* and ln [Cl_2].

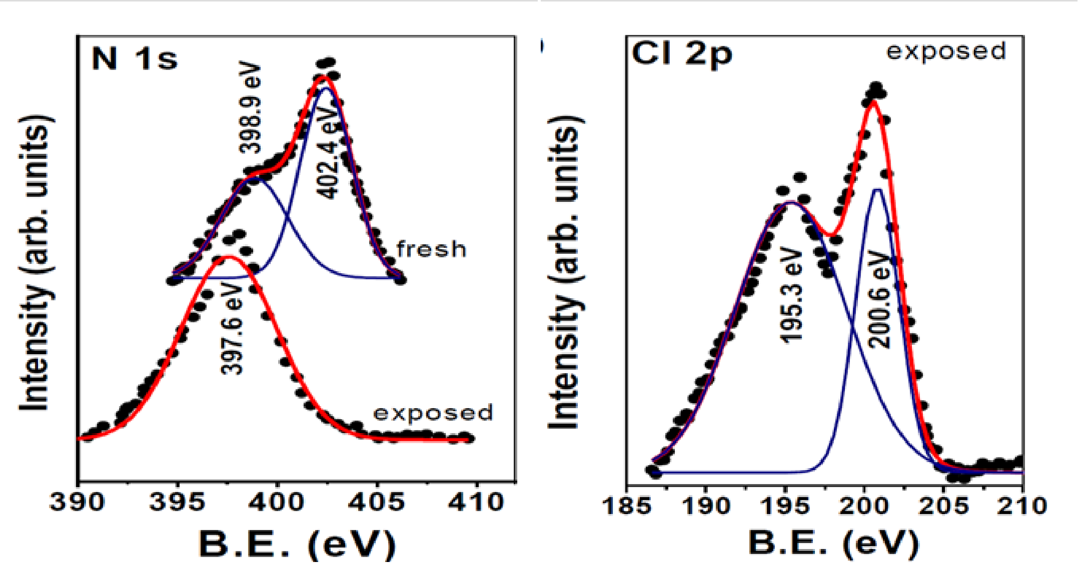

(a) (b)

Fig. 5.13. XPS data of fresh and 1000 ppb Cl_2 exposed **V** films. (a) N-1s and (b) Cl-2p

The inference was further supported by the FTIR data presented in **Fig. 5.14(a)**. For the fresh film, the noticeable peaks were: 3313 cm^{-1} (N-H stretching bond), 1600 cm^{-1} (phenyl C=C stretching) 1548 cm^{-1} (in plane N-H bending) and 1743 cm^{-1} (ester C=O stretching).[235,236] However, on Cl_2 exposure the peaks at 3313 cm^{-1} and 1548 cm^{-1}almost vanished. This indicated possible transforms of N-H bonds to N-Cl bonds, which was also evident from the absence of the N-1s XPS peak corresponding to the N-H bond (**Fig. 5.13.(a)**). However, the possibility of direct aromatic ring chlorination can't be excluded. More evidence for the chemical bond formation between Cl_2 and **V** films comes from UV-Vis spectra, as shown in **Fig. 5.14.(b)**. Fresh films show sharp and intense band around 417 nm (Soret band or B band) and four bands of lower wavelength at 513, 548, 590 and 645 nm (Q bands). After Cl_2 exposure, all bands show a red shift (by 7 nm) along with a decrease in intensity. In addition, a new band develops at 710 nm. Red shift of the spectra reflects the transfer of electrons density porphyrin rings to the chlorine.[211,212]

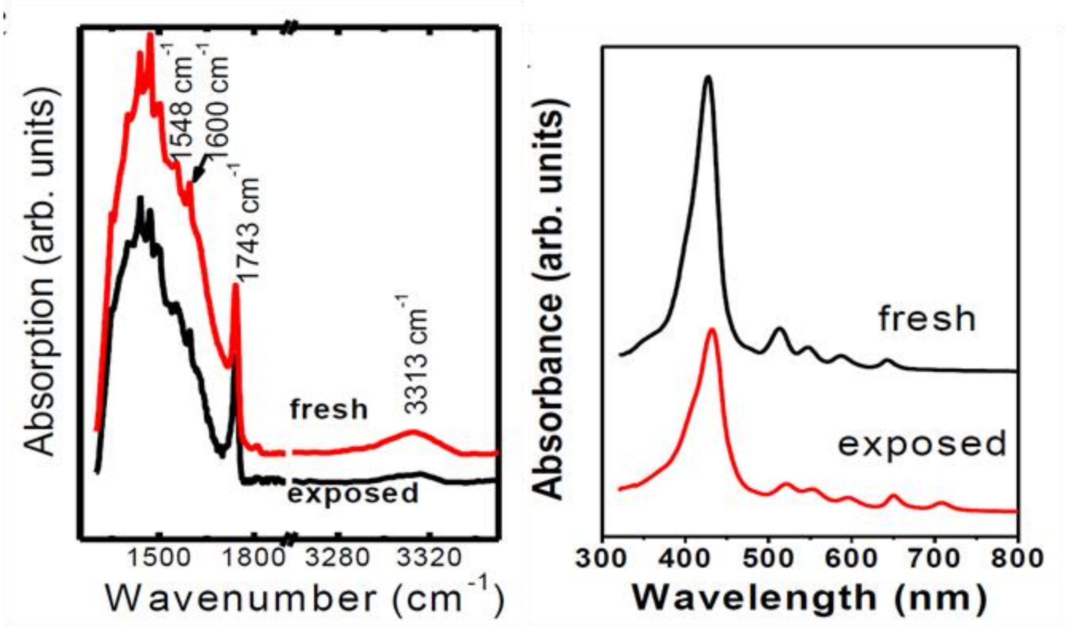

(a) **(b)**

Fig. 5.14. (a) FTIR and (b) UV-Vis spectra of **V** films.

5.4.2. Ammonia sensing

Ammonia is widely used in chemical industries, fertilizer factories and refrigeration, and can be produced by deteriorating/decomposing food/fruit bodies. It is highly toxic to human, can affect the immune system, and is one of the major causative factors of respiratory diseases such as sneezing, pneumonia etc. Hence, considerable attention is given to develop ammonia sensors for their multipurpose uses in monitoring environment and food quality, as well as in medical sciences.[237] Further, ammonia detection can provide a fast and non-invasive technique to diagnose diseases such as ulcers and kidney disorders.[238] Various types of ammonia detectors based on polymers *viz*. polyaniline, Nafion and polypyrrole as well as metal oxides *viz*. SnO_2, $CdSnO_3$, TiO_2, In_2O_3 thin films coatings have been formulated. These rely primarily on the changes in the optical and electrical properties of a sensitive area of the films in the presence of the analyte. However, the polymeric sensors often show time-dependent reduction in sensitivity, while the ceramic sensors lack selectivity to a particular gas. Moreover, many of these the metal oxides-based NH_3 sensors function at higher temperature.[237,239] The combination of nanostructured inorganic materials and conducting polymers appears best suited for fabricating gas sensors. Some of these materials have been reported to sense NH_3 at room temperature, but their preparation requires sophisticated techniques such as tuning the nanoporous structures of metal oxides, synthesis of polymer nanofibres etc.[240,241] Gong *et al*. fabricated a unique sensor with PANI nanograins enchased on TiO_2 microfibers surface that can detect NH_3gas even at 50 ppt in air.[242] To the best of our knowledge, this is the best sensitivity reported so far in detecting NH_3 gas.

It was envisaged that porphyrin thin films may provide a room temperature ammonia gas sensor that is simple and cheap to fabricate, shows reproducible and reversible response over a wide range of partial gas pressures, and is stable under ambient conditions. Free as well as metalo- monomeric and dimeric porphyrins have earlier been used to construct ammonia gas sensors.[213,243,244] Herein, the time response curves of the constructed two thin film chemi-resistive ammonia gas sensors, were recorded at room temperature for different gases *viz*. Cl_2, H_2S, NH_3, CH_4, CO, NO_2 and NO (each 5 ppm) (details of gas sensing experiment given in **Chapter-2**). A total of six spin-coated samples of each molecule were prepared in three batches. Each sample contained 5 gold pads (measurement points), and the measurements at the designated NH_3 concentrations were carried out. The response data are mean ± s. d.

The plots of conductance of the **V** and **VI** films as a function of time revealed that amongst the chosen gases, only NH_3, H_2S and Cl_2 exhibited response at room temperature at 5 ppm concentration. However, due to irreversible response of both the films at the higher concentrations of H_2S and Cl_2, these are not suitable for sensing the designated gases at room temperature. In contrast, both the films exhibited reversible response to NH_3 over a concentration range of 5-40 ppm. The response curves of all the samples were similar, and the representative response curves for these films are shown in **Figs. 5.15. (a)** and **(b)**. The response times, defined by time required to reach 90% of the highest conductance were 8 sec and 2 sec respectively for the **V** and **VI** films. Reversibility is an important property for sensors. Our room temperature desorption experiments revealed the recovery times (time required to reach 10% of the base conductance value) as 450 sec and 150 sec respectively for the **V** and **VI** films. The results indicated that the current of the films was restored to the original baseline at room temperature for the repeated use of the device.

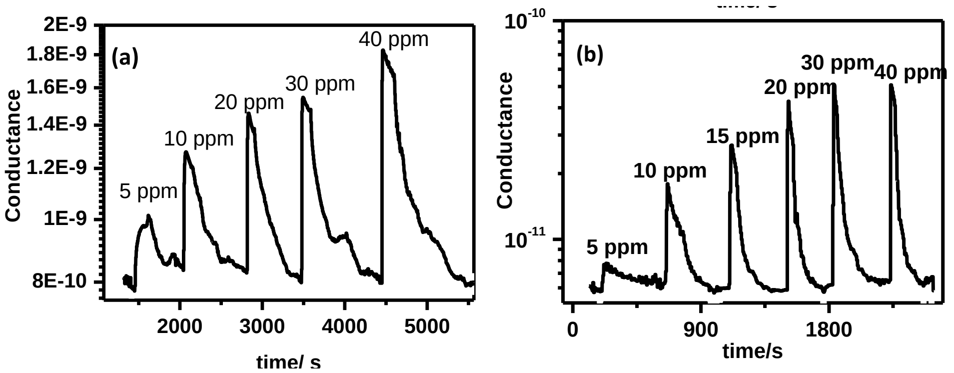

Fig. 5.15. Conductance versus time data (5-40 ppm of NH_3) for (a) **V**, (b) **VI** films.

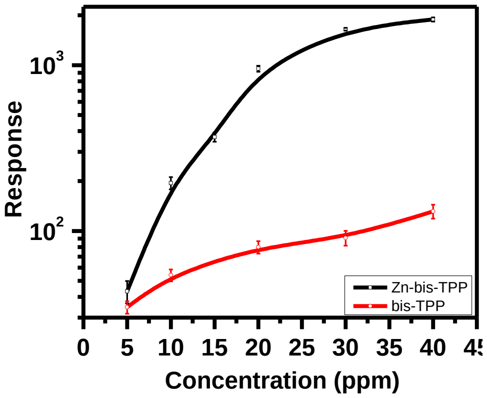

Fig. 5.16. Dependence of Response as a function of NH_3 concentration for **V** and **VI** films.

The response of the sensors can be calculated from $R = \{(C_e - C_0)/C_0\} \times 100$, where C_0 and C_e are the conductance values in air and at the saturation level of the analyte gas. The variation of R (mean ± s. d.) as a function of NH_3 concentration (**Fig. 5.16.**) revealed that for 5-40 ppm of NH_3, R varied almost linearly from 34% to 131% with the **V** films. However, with the **VI** films, the curve was almost linear up to 20 ppm of NH_3, with much higher (43 to 952%) R values. Beyond this NH_3 concentration, the **VI** films showed even higher (up to 1890% at 40 ppm NH_3) response that varied non-linearly. Overall, the response of **VI** films for NH_3 was about 14 times that of the **V** films.

The interaction between organic films and gases is quite complex, and the proposed models are empirical and qualitative. When the film is exposed to test gas in air, the adsorption and the desorption processes occur simultaneously. Possibly, during the physical adsorption/desorption of the gas molecules, the van der Waals force between them and the film changes to induce the electrical response.[245-247] Porphyrins are generally electron donors and hole transporters. Thus, their direct interaction with ammonia is expected to trap the holes and decrease current. However, the unusual behavior of increased conductance has been previously reported with some porphyrin-based NH_3 sensors.[212,216,236] Similar current behaviour has also been observed with various organic FET-based sensors.[248,249] In the present case, the increased current in both the **V** films on exposure to NH_3 suggested an interaction of the analyte with some solvent molecules, trapped in the TPP films during spin coating. Possibly, the trapped solvent molecules are responsible for low hole conduction. Hence their deactivation by the NH_3 molecules would increase the conductance of films. We have chosen Zn metal for the present studies as this has maximum d electrons and largest size in the 3d metal series that would facilitate charge conduction.[250] Further, compared to the **V** films, the **VI** film exhibits highly porous macrostructure. This would provide more interaction area for the analyte, and allow its easy entry and exit from the thin film. As a result, the **VI** films showed faster response and recovery.

5.5. Conclusion

In summary, we have synthesized the bis-porphyrin molecules **V** and **VI**, which consists of two porphyrin rings coupled to a benzene ring through ester group. Good solubility of these molecules in the polar solvents allows facile fabrication of their thin films using spin coating method. Due to dense packing, the charge mobility in **V** films was very high (1.8 $cm^2V^{-1}s^{-1}$) as compared to the **VI** ($1.51x10^{-3}$ $cm^2V^{-1}s^{-1}$) films. These films were highly selective to Cl_2 gas sensing, and their sensitivity varied linearly between 278 and 1370% with Cl_2 gas in the concentration range of 10-500 ppb. The response time was also very low (~ 3 s) and a full recovery to the base conductance took only ~8 min. The response rate obeyed Elovich equation, showing a linear correlation with Cl_2 concentration. However, for concentrations ≥1000ppb, the response was irreversible, possibly due to chlorination of bis-porphyrin molecules.

The sensors, fabricated with **V** and **VI** films, both showed excellent selectivity towards NH_3 gas and reversibility. Although the **VI** films did not show Cl_2 gas sensing in the ppb range, they sensed NH_3 (5-40 ppm) with high response, very low response time (~ 2 s) and a complete recovery within ~150 sec. Moreover, their sensitivity (varying linearly between 43 and 1890%) in NH_3 gas detection was better than that of the **V** films.

Summary

Summary

The objective of the present work was to develop some covalently linked organic monolayers on Si surface and to study the feasibility using of such hybrids in molecular electronics. The design characteristics of the devices was based on three basic models: (i) a $\sigma-\pi-\sigma$ molecular architecture is at tunnel diode analog, with a ‘quantum well (a π conjugated molecule)’ surrounded by tunnel barriers (σ alkyl chains), and hence may show NDR behavior; (ii) a single molecule with donor-spacer-acceptor (D-s-A) structure would behave as a diode when placed between two electrodes; and (iii) a $\sigma-\pi$ system grafted on Si would function as a current rectifier due to a resonant transport between the Si conduction band and the HOMO of the π group.The NDR property have its potential application in the realization of logic devices and memory circuits, while molecules, showing rectification behaviour with high rectification ratio (RR) are very useful for making diodes. The other aim of the investigation was to use the redox property of the organic molecules to construct chemi-resistive sensors for some hazardous gases (Cl_2 and NH_3) using economically viable spin-coated thin films of these molecules on glass surfaces. The achievements are highlighted below.

I. Two unsymmetrical ABC_2 type porphyrins containing of two dialkylated *meso*-phenyl moieties as the AB groups and the *meso*-phenyl/4-flurophenyl moieties as the C_2 group were synthesized as the prototype $\sigma-\pi-\sigma$ systems, and electro-grafted on H-terminated Si to form monolayers. The hybrid assemblies showed pronounced reversible, stable (up to 8 h of voltage scanning) and room temperature NDR effects with PVRs of ~ 10 (at 1.18 V) and 100 (at 1.09 V) respectively.

II. The NDR effect in the forward bias was due to alignment of the HOMO levels of the molecules with the Fermi-levels of the electrodes (resonant tunneling), and a mismatch of HOMO levels of the oxidized molecule with the Fermi-levels.

III. The higher PVR, observed with the device containing the fluoro-phenyl porphyrin moiety may be due to its better organization by hydrogen bonding through the F atoms, compared to the device fabricated using the non-fluoroporphyrin.

IV. Two prototype porphyrin-based D-s-A structures, synthesized by the Vilsmeier-Haack reaction of TPP followed by the reductive amination of *β*-formyl TPP with *p*-alkenyloxy (C-6/C-11) aniline, and subsequent electro-grafting on H-terminated Si (1 1 1) wafers.These devices showed RR up to 10^7 in reverse bias as a result of alignment of the LUMO levels of the molecules with the Fermi-levels of the electrodes.

V. Taking advantage of their high ionization energies and band gaps, some alkenylated perylenes/pyrenes organic n-type materials with good solubility and easy processability were used to construct σ–π systems-grafted Si hybrids that showed high RR values, the performance of the perylene-based device was in between that of the pyrene-based devices.

VI. Using a bis-porphyrin along with its Zn^{2+}-derivative two densly-packed spin-coated thin films were fabricated. The bis-porphyrin films were used as highly selective, reversible chemoresistive Cl_2 gas (10-500 ppb) sensors, with very low (~ 3 s) response time and complete recovery in ~8 min. The irreversible response at higher (≥1000 ppb) Cl_2 concentrations was attributed to N-chlorination of the bis-porphyrin molecules. Formation of a charge transfer (CT) complex between the oxidizing, electrophilic molecule Cl_2 and the π-electron system of the films has been suggested to explain the sensing behavior.

VII. The sensors, fabricated with bis-porphyrin and its Zn^{2+}-derivative showed excellent selectivity and reversibility in room temperature sensing of NH_3 gas, with linear variation of sensitivity for NH_3 (5-40 ppm), very low response time (~ 2 s) and a complete recovery within ~150 sec. The significantly better performance of the Zn^{2+}-bis-porphyrin sensor was attributed to its highly porous macrostructure, providing more interaction area for the analyte, and allowing its easy passage.

References

References

1) International Technology Roadmap for Semiconductors (IRTS), 2007 <http://www.itrs.net/reports.html>.

2) Sze, S. M. Semiconductor Devices: Physics and Technology, John Wiley & Sons, New York, 2002.

3) Moore, G. E. *Electronics* **1965**, *38*, 1.

4) Peercy, P. S. *Nature* **2000**, *406*, 1023 and reference cited therein.

5) Aswal, D. K.; Lenfant, S.; Guerin, D.; Yakhmi, J. V.; Vuillaume, D. *Anal. Chim. Acta*. **2006**, *568*, 84.

6) Mann, B.; Kuhn, H. *J. Appl. Phys*. **1971**, *42*, 4398.

7) Aviram, A.; Ratner, M. A., *Chem. Phys. Lett.*, **1974**, *29*, 277.

8) Reed, M. A.; Lee, T. Molecular Nanoelectronics: *Stevenson Ranch, CA: American Scientific Publishers*, 2003.

9) Ulman, A. An introduction to ultrathin organic films: from Langmuir-Blodgett to Self-assembly, *Boston, Academic press*, 1991.

10) Joachim, C.; Gimzewski, J. K.; Aviram, A. *Nature* **2000**, *408*, 541.

11) Cerofolini, G. F.; Romano, E. *Appl. Phys. A* **2008**, *91*, 181.

12) From Molecular Electronics to Proteonics: Break Junctions for Biomarker Detection - IEEE Life Sciences". *Lifesciences. ieee. org. 2009-04-11. Retrieved 2011-11-29.*

13) Parks, J. J.; Champagne, A. R.; Hutchison, G. R.; Flores-Torres, S.; Abruña, H. D.; Ralph, D. C. *Phys. Rev. Lett*. **2007**, *99*, 026601.

14) Kushmerick, J. G.; Holt, D. B.; Yang, J. C.; Naciri, J.; Moore, M. H.; Shashidar, R. *Phys. Rev. Lett* .**2002**, *89*, 243.

15) Schull, T. L.; Kushmerick, J. G.; Petterson, C. H.; George, C.; Moore, M. H.; Shashidar, R. *J Am. Chem. Soc.* **2003**, *125*, 3202.

16) Bezryadin, A.; Dekker, C.; Schmid, G. *Appl. Phys. Lett.* **1997**, *71*, 1273.

17) Chen, J.; Reed, M. A.; Rawlett, A. M.; Tour, J. M. *Science* **1999**, *286*, 1550.

18) Ralls, K. S.; Buhrman, R. A.; Tiberio, R. C. *Appl. Phys. Lett.* **1989**, *55*, 2459.

19) Salomon, A.; Yellin, R. A.; Shanzer, A.; Karton, A.; Cahen, D. *J. Am. Chem. Soc.* **2004**, *126*, 11648.

20) Nuzzo, R. G.; Allara, D. L. *J. Am. Chem. Soc.* **1983**, *105*, 4481.

21) Love, J. C.; Estroff, L. A.; Kriebel, J. K.; Nuzzo, R. G.; Whitesides, G. M. *Chem. Rev.* **2005**, *105*, 1103.

22) Aswal, D. K.; Koiry, S. P.; Jousselme, B.; Gupta, S. K.; Palacin, S.; Yakhmi, J. V. *Physica E: Low-dimensional Systems and Nanostructures* **2009**, *41*, 325.

23) Maoz, R.; Sagiv, J. *J. Colloid Interf. Sci.* **1984**, *100*, 465.

24) Selzer, Y.; Salomon, A.; Cahen, D. *J. Phys. Chem. B* **2002**, *106*, 10432.

25) Liu, Y. -L.; Yu, H. -Z. Chem. *Phys. Chem.* **2002**, *19*, 799.

26) Jung, D. R.; Czanderna, A. W.; Herdt, G. C. *J. Vac. Sci. Technol. A* **1996**, *14*, 1779.

27) Xu, B.; Tao, N. J. *Science* **2003**, *301*, 1221.

28) Wold, D. J.; Frisbie, C. D. *J. Am. Chem. Soc.* **2001**, *123*, 5549.

29) Fisher, G. L.; Walker, A. V.; Hooper, A. E.; Tighe, T. B.; Bahnck, K. B.; Skriba, H. T.; Reinard, M. D.; Haynie, B. C.; Opila, R. L.; Winograd, N.; Allara, D. L. *J. Am. Chem. Soc.* **2002**, *124*, 5528.

30) Metzger, R. M.; Xu, T.; Peterson, I. R. *J. Phys. Chem. B* **2001**, *105*, 7280.

31) Aswal, D. K.; Lenfant, S.; Guerin, D.; Yakhmi, J. V.; Vuillaume, D. *Small* **2005**, *1*, 725.

32) Herdt, G. C.; Czanderna, A. W. *J. Vac. Sci. Technol. A* **1995**, *13*, 1275.

33) Xia, Y.; Whitesides, G. M. *Angew. Chem. Int. Ed.* **1998**, *37*, 550.

34) Hille, B. *Ion Channels of Excitable Membranes. 3.* Sinauer Associates; Sunderland: 2001.

35) Collier, C. P.; Wong, E. W.; Belohradsky, M.; Raymo, F. M.; Stoddart, J. F.; Kuekes, P. J.; Williams, R. S.; Heath, J. R. *Science* **1999**, *285*, 391. (b) **17**

36) Kubatkin, S.; Danilov, A.; Hjort, M.; Cornil, J.; Bredas, J. L.; Stuhr-Hansen, N.; Hedegard, P.; Bjornholm, T. *Nature* **2003**, *425*, 698.

37) Hodgkin, D. R.; Hodder, O. J. R.; Harrison, H. R. *J. Chem. Soc. B.* **1971**, 640.

38) Hoard, J. L. *Porphyrins Metalloporphyrins* **1975**, 317.

39) Buchler, J. W. *Porphyrins Metalloporphyrins* **1975**, 157.

40) Ghosh, A.; Jynge, K. *Chem. Eur. J.* **1997**, *3,* 823.

41) (a) Johnson, A. W.; Kay. I. T. *J. Chem. Soc.* **1965**, 1620. (b) Paolesse, R.; Sagone, F.; Macagnano, A.; Boschi, T.; Prodi, L.; Montalti, M.; Zaccheroni, N.; Bolletta, F.; Smith, K. M. *J. Por. Phthalo*. **1999**, *14,* 69.

42) (a) Roth, K. M.; Dontha, N.; Dabke, R. B.; Gryko, D. T.; Clausen, C.; Lindsey, J. S.; Bocian, D. F.; Kuhrb, W. G. *J. Vac. Sci. Technol. B.* **2000**, *18*, 2359. (b) Gryko, D.; Li, J.; Diers, J. R.; Roth, K. M.; Bocian, D. F.; Kuhr, W. G.; Lindsey, J. S. *J. Mater. Chem.* **2001,** *11*, 1162. (c) Roth**,** K. M.; Lindsey, J. S.; Bocian, D. F.; Kuhr, W. G. *Langmuir* **2002**, *18*, 4030. (d) Roth, K. M.;Yasseri, A. A.; Liu, Z.; Dabke, R. B.; Malinovskii, V.; Schweikart, K.-H.; Yu, L.; Tiznado, H.; Zaera, F.; Lindsey, J. S.; Kuhr, W. G.; Bocian, D. F.*J. Am. Chem. Soc.* **2003**, *125,* 505. (e) Liu, Z.; Yasseri, A. A.; Lindsey, J. S.; Bocian, D. F. *Science* **2003**, *302*, 1543.

43) Watson, M.; Fechtenkötter, A.; Müllen. K. *Chem. Rev.* **2001**, *101*, 1267.

44) Wu, J.; Pisula, W.; Müllen. K. *Chem. Rev.* **2007**, *107*, 718.

45) Scholl, R.; Seer, C. *Justus Liebigs Ann. Chem.* **1912**, *394*, 111.

46) Scholl, R.; Seer. C. *Ber. Dtsch. Chem. Ges.* **1911**, *44*, 1233.

47) Clar, E. *Ber. Dtsch. Chem. Ges.* **1929**, *62*, 1574.

48) Clar, E. *Polycyclic Hydrocarbons*, Vols. 1 and 2, John Wiley, New York, 1964.

49) Clar, E.; Zander. M. *J. Chem. Soc.* **1958**, 1577.

50) Zander. M. *Handbook of Polycyclic Aromatic Hydrocarbons*, Marcel Dekker, New York, 1983.

51) Hagen, S.; Hopf. H. *Top. Curr. Chem.* **1998**, *196*, 44.

52) Musa, A.; Sridharan, B.; Lee, H.; Mattern, D. L. *J. Org. Chem*. **1996**, *61*, 5481.

53) Metzer, R. M. *J. Mat. Chem*. **1999**, *9*, 2027.

54) Inouye, M.; Itoh, M. A. S.; Nakazumi, H. *J. Org. Chem*. **1999**, *64*, 9393.

55) Psysh, E.; Yang, N. C. *J. Am.Chem. Soc.* **1963**, *85*, 2124.

56) Clar, E.; Robertson, J. M.; Schlogl, R. *J. Am. Chem. Soc.* **1981**, *103*, 1320.

57) Vollmann, H., Becker, H., Corell, M., Streeck, H. *Just. Liebig. Ann. Chem.* **1937**, *531*, 1.

58) Streitwieser, A.; Lawler R. G.; Schwaab, D. *J. Org. Chem*, **1965**, 30, 147.

59) Moyle, M.; Ritchie, E. *Aust. J. Chem*. **1985**, *11*, 211.

60) Harvey, R. G.; Pataki J.; Lee, H. *Org. Prep. Proc.* **1984**, *16*, 144.

61) Minabe, M.; Takeshige, S.; Soeda, Y.; Kimura, T.; Tsbota, M. *Bull. Chem. Soc. Jpn*. **1994**, *67*, 172.

62) Inouye, M.; Fujimoto, K.; Furusyo, M.; Nakazumi, H. *J. Am. Chem. Soc.,* **1999**, *121*, 1452.

63) Vandana, P.; Basu, A. K. *Org. lett.* **2000**, *2*, 1871.

64) Clar, E. *Elseveir Science: Amesterdam, 2^{nd} ed*. 1952, 5.

65) Donaldson, D. M.; Robertson, J. M.; White, J. G. *Proc. Roy. Soc. London* **1953**, *220*, 311.

66) Dubois, L. H.; Nuzzo, R. G. *Annu. Rev. Phys. Chem.* **1992**, *43*, 437.

67) Bumm, L. A.; Arnold, J. J.; Cygan, M. T.; Dunbar, T. D.; Burgin, T. P.; Jones II, L.; Allara, D. L.; Tour, J. M.; Weiss, P.S. *Science* **1996**, *271*, 1705.

68) Ashwell, G. J.; Urasinska, B.; Wang, C.; Bryce, M. R.; Grace, I.; Lambert, C. J. *Chem. Commun.* **2006**, *45*, 4706.

69) Reed, M. A.; Zhou, C.; Miller, C. J.; Burgin, T. P.; Tour, J. M. *Science* **1997**, *278*, 252.

70) Weber, H. B.; Reichert, J.; Weigend, F.; Ochs, R.; Beckmann, D.; Mayor, M.; Ahlrichs, R.; von Lohneysen, H. *Chem. Phys.* **2002**, *281*, 113.

71) Bahr, J. L.; Tour, J. M. *J. Mater. Chem.* **2002**, *12*, 1952.

72) Patrone, L.; Palacin, S.; Charlier, J.; Armand, F.; Bourgoin, J. -P.; Tang, H.; Gauthier, S. *Phys. Rev. Lett.* **2003**, *91*, 096802.

73) Seferos, D. S.; Trammell, S. A.; Bazan, G. C.; Kushmerick, J. G. *Proc. Nat. Acad. Sci*. **2005**, *102*, 8821.

74) Paul, F.; Lapinte, C. *Coord. Chem. Rev.* **1998**, *431*, 178.

75) Reimers, J.; Lu, T. X.; Crossley, M. J.; Hush, S. *Nanotech*. **1996**, *7,* 424.

76) Nitzan, A.; Ratner, M. A. *Science* **2003**, *300*, 1384.

77) Metzger, R. M. *Chem. Rev.* **2003**, *103*, 3803.

78) Krzeminski, C.; Allan, G.; Delerue, C.; Vuillaume, D.; Metzger, R. M. *Phys. Rev. B* **2001**, *64*, 085405.

79) Lenfant, S.; Krzeminski, C.; Delerue, C.; Allan, G.; Vuillaume, D. *Nano Lett.* **2003**, *3*, 741.

80) Tour, J. M. *Molecular Electronics: Commercial Insights, Chemistry. Devices, Architecture and Programming,* World Scientific Publishing Co. Pvt. Ltd. Singapore, 2003.

81) Cuniberti, G.; Fagas, G.; Richter, K. *Introducing Molecular Electronics*, Springer, Berlin, 2005.

82) Aswal, D. K.; Koiry, S. P.; Yakhmi, J. V. Monolayer for hybrid nanoelectronics in Molecular and organic electronics devices, Aswal, D. K.; Yakhmi, J. V. (eds.), Nova Science Publisher, New York, 2010.

83) Venkataraman, L.; Klare, J. E.; Nuckolls, C.; Hybertsen, M. S.; Steigerwald, M. L. *Nature* **2006**, *442*, 904.

84) Collier, C. P.; Wong, E. W.; Belohradsky, M.; Raymo, F. M.; Stodart, J. F.; Kuekes, P. J.; Williams, R. S.; Heath, J. R. *Science* **1999**, *285*, 391.

85) Chen, Y.; Ohlberg, D. A. A.; Li, X.; Stewart, D. R.; Williams, R. S. *Appl. Phys. Lett.* **2003**, *82*, 1610.

86) Collier, C. P.; Mattersteig, G.; Wong, E. W.; Luo, Y.; Baverly, K.; Sampaio, J.; Raymo, F. M.; Stoddart, J. F.; Heath, J. R. *Science* **2000**, *289*, 1172.

87) Lau, C. N.; Stewart, D. R.; Willaims, R. S.; Bockrath, M. *Nano Lett.* **2004**, *4*, 569.

88) Stewart, D. R.; Ohlberg, D. A. A.; Beck, P. A.; Chen, Y.; Willaims, R. S. *Nano Lett.* **2004**, *4*, 133.

89) He, J.; Chen, B.; Flatt, A. K.; Stephenson, J. J.; Doyle, C. D.; Tour, J. M. *Nat. Mater.* **2006**, *5*, 63.

90) Donhauser, Z. J.; Mantooth, B. A.; Kelly, K. F.; Bumm, L. A.; Monnell, J. D.; Stapleton, J. J.; Price, D. W.; Rawlett, A. M.; Allara, D. L.; Tour, J. M.; Weiss, P. S. *Science* **2001**, *292*, 2303.

91) Rawlett, A. M.; Hopson, T. J.; Nagahara, L. A.; Tsui, R. K.; Ramachandran, G. K.; Lindsay, S. M. *Appl. Phys. Lett* **2002**, *81*, 3043.

92) Reed, M. A.; Chen, J.; Rawlett, A. M.; Price, D. W.; Tour, J. M. *Appl. Phys. Lett.* **2001**, *78*, 3735.

93) Li, Q.; Mathur, G.; Homsi, M.; Surthi, S.; Misra, V.; Malinovskii, V.; Schweikart, K. -H.; Yu, L.; Lindsey, J. S.; Liu, Z.; Dabke, R. B.; Yasseri, A. A.; Bocian, D. F.; Kuhr, W. G. *Appl. Phys. Lett.* **2002**, *81*, 1494.

94) Gupta, S. K.; Koiry, S. P.; Chauhan, A. K.; Padma, N.; Aswal, D. K.; Yakhmi, J. V. *Appl. Surf. Sci.* **2009**, *256*, 407.

95) Polymeropoulos, E. E. *J. Appl. Phys.* **1977**, *48*, 2404.

96) Polymeropoulos, E. E.; Sagiv, J. *J. Chem. Phys.* **1978**, *69*, 1836.

97) Wold, D. J.; Frisbie, C. D. *J. Am. Chem. Soc.* **2000**, *122*, 2970. **chap2**

98) Littler, B. J.; Miller, M. A.; Hung, C.-H.; Wagner, R. W.; O'Shea, D. F.; Boyle, P. D.; Lindsey, J. S. *J. Org. Chem.* **1999**, *64*, 1391.

99) Laha, J. K.; Dhanalekshmi, S.; Taniguchi, M.; Ambroise, A.; Lindsey, J. S. *Org. Process Res. Dev.* **2003**, *7*, 799.

100) Thamyongkit, P.; Bhise, A. D.; Taniguchi, M.; Lindsey, J. S. *J. Org. Chem.* **2006**, *71*, 903.

101) Muresan, A. Z.; Thamyongkit, P.; Diers, J. R.; Holten, D.; Lindsey, J. S.; Bocian, D. F. *J. Org. Chem.* **2008**, *73*, 6947.

102) Cho, W.-S.; Kim, H.-J.; Littler, B. J.; Miller, M. A.; Lee, C.-H.; Lindsey, J. S. *J. Org. Chem.* **1999**, *64*, 7890.

103) Tamaru, S. -I.; Yu, L.; Youngblood, W. J.; Muthukumaran, K.; Taniguchi, M.; Lindsey, J. S. *J. Org. Chem.* **2004**, *69*, 765.

104) Zaidi, S. H. H.; Loewe, R. S.; Clark, B. A.; Jacob, M. J.; Lindsey, J. S. *Org. Process Res. Dev.***2006**, *10*, 304.

105) Rao, P. D.; Dhanalekshmi, S.; Littler, B. J.; Lindsey, J. S. *J. Org. Chem.* **2000**, *65*, 7323.

106) Lee, C.-H.; Li, F.; Iwamoto, K.; Dadok, J.; Bothner-By, A. A.; Lindsey, J. S. *Tetrahedron* **1995**, *51*, 11645.

107) Lindsey, J. S. *The Porphyrin Handbook*; Kadish, K. M.; Smith, K. M.; Guilard, R. (eds.); Academic Press: SanDiego, CA 2000, Vol. *1*, pp. 45.

108) Bonfantini, E. E.; Burrell, A. K.; Campbell, W. M.; Crossley, M. J; Gosper, J. J.; Harding, M. M.; Officer, D. L.; and Reid, D. C. W. *J. Por. Phthalo*. **2002,** *6*, 708.

109) Gowda, D.; Mahesh. B; Shankare. G. *Ind. J. Chem. Sect. B* **2001**, *4*, 551.

110) Welch, C.; Achibald, S. J.; Boyle, R. W. *Synthesis* **2009**, 551.

111) Skorobogatyi, M. V.; Pchelintseva, A. A.; Petrunina, A. L.; Stepanova, I. A.; Andronova, V. L.; Galegov, G. A.; Malakhov, A. D.; Korshun, V. A. *Tetrahedron* **2006**, *62*, 1279.

112) Grechishnikova, I. V.; Johansson, L. B. A.; Molotkovsky, J. G. *Chem. Phy. Lipids* **1996**, *81*, 87.

113) Grama, S.; Hurduc, N.; Fagadar-Cosma, E.; Vasile, M.; Tarabukina, E.; Fagadar-Cosma, G. *Digest J. Nanomat. Biostruct.* **2010**, *5*, 959.

114) Garg, K.; Singh, A.; Debnath, A. K.; Nayak, S. K.; Chattopadhyay, S.; Aswal, D. K.; Hayakawa, Y.;Gupta, S.K.; Yakhmi, J. V. *Chem. Phys. Lett.* **2010**, *488*, 27.

115) Dunbar, A. D. F.; Richardson, T. H.; McNaughton, A. J.; Hutchinson, J.; Hunter, C. A. *J. Phys. Chem. B* **2006**, *110*, 16646.

116) Yablonovitch, E.; Allara, D. L.; Chang, C. C; Gmitter, T.; Bright, T. B. *Phys. Rev. Lett.* **1986**, *57*, 249.

117) Sieval, A. B.; Demirel, A. L.; Nissink, J. W. M.; Linford, M. R.; van der Maas, J. H. *Langmuir* **1998**, *14*, 1759.

118) Higashi, G. S.; Becker, R. S.; Chabal, Y. J.; Becker, A. J. *Appl. Phys. Lett.* **1991**, *58*, 1656.

119) Dumas, P.; Chabal, Y. J.; Gunther, R.; Ibrahimi, A. T.; Petroff, Y. *Prog. Surf. Sci.* **1995**, *48*, 313.

120) Dumas, P.; Chabal, Y. J. *Chem.Phys. Lett.* **1991**, *181*, 537.

121) Bansal, A.; Lewis, N. S. *J. Phys. Chem. B* **1998**, *102*, 1067.

122) Bansal, A.; Li, X. L.; Lauermann, I.; Lewis, N. S.; Yi, S. I.; Weinberg, W. H. *J. Am. Chem. Soc.* **1996**, *118*, 7225.

123) Cai, W.; Lin, Z.; Strother, T.; Smith, L. M.; Hamers, R. J. *J. Phys. Chem. B* **2002**, *106*, 2656.

124) Buriak, J. M. Allen, M. J. *J. Am. Chem. Soc.* **1998**, 120, 1339

125) Buriak, J. M.; Stewart, M. P.; Geders, T. W.; Allen, M. J.; Choi, H. C. *J. Am. Chem. Soc.* **1999**, *121*, 11491.

126) Linford, M. R.; Chidsey, C. E. D. *J. Am. Chem. Soc.* **1993**, *115*, 12631.

127) Linford, M. R.; Fenter, P.; Eisenberger, P. M.; Chidsey, C. E. D. *J. Am. Chem. Soc.* **1995**, *117*, 3145.

128) Perring, M.; Dutta, S.; Arafat, S.; Mitchell, M.; Kenis, P. J. A.; Bowden, N. B. *Langmuir* **2005**, *21*, 10537.

129) Sieval, A. B.; Linke, R.; Zuilhof, H.; Sudholter, E. J. R. *Adv. Mater.* **2000**, *12*, 1457.

130) Effenberger, F.; Gotz, G.; Bidlingmaier, B.; Wezstein, M. *Angew. Chem. Int. Ed***.** **1998**, *37*, 2462.

131) Strother, T.; Cai, W.; Zhao, X. S.; Hamers, R. J.; Smith, L. M. *J. Am. Chem. Soc.* **2000**, *122*, 1205.

132) Strother, T.; Hamers, R. J.; Smith, L. M. *Nucleic Acids Res.* **2000**, *28*, 3535.

133) Cicero, R. L.; Linford, M. R.; Chidsey, C. E. D. *Langmuir* **2000**, *16*, 5688.

134) Stewart, M. P.; Buriak, J. M. *J. Am. Chem. Soc***.** **2001**, *123*, 7821.

135) Robins, E. G.; Stewart, M. P.; Buriak, J. M. *Chem. Comm.* **1999**, 2479.

136) Wang, D.; Buriak, J. M. *Surf. Sci.* **2005**, *590*, 154.

137) Carter, F. L.; Siatkowski, R. E.; Wohltjen, H. (eds.); *Molecular Electronic Devices*: Proc. 3rd Int. Symp. On Molecular Electronic Devices, North-Holland, New York, 1989.

138) McCrackin, F. L.; Passaglia, E.; Stromberg, R. R.; Steinberg, H. L. *J. Res. Natl. Bur. Stand., Sect. A* **1963**, *67*, 363.

139) Azzam, R. M. A.; Bashara, N. M. *Ellipsometry and Polarized Light*, North Holland, Amsterdam, 1977.

140) Als-Nielsen, *J. Physica* **1986**, *140A*, 376.

141) Nelson, A. *J. Appl. Cryst*. **2006,** *39*, 273.

142) http://www-phys.llnl.gov/Research/scattering/asf.html

143) Aswal, D. K.; Muthe, K. P.; Tawde, S.; Chodhury, S.; Bagkar, N.; Singh, A.; Gupta, S. K.; Yakhmi, J. V. *J. Cryst. Growth.* **2002**, *236*, 661.

144) Instruction Manual, SPM Solver P47, NT-MDT Co., Zelenograd Research Institute of Physical Problems, Moscow, Russia.

145) Cullity, B. D. *Elements of X Ray Diffraction*, BiblioBazaar, 2011.

146) Toney, M. F.; Haung, T. C.; Brennan, S.; Rek, Z. *J. Mater. Res.* **1988**, *3*, 351.

147) Zhang, S.; Li, L.; Kumar, A. *Material Characterisation Techniques*, CRC Press, 2009.

148) Woodruff, D. P.; Delchar, T. A. *Modern Techniques in Surface Science*, Cambridge Univ. Press, 1994.

149) Briggs, D.; Seah, P. *Progress in Surface Analysis by Auger and X-ray Photo-electron Spectroscopy*, Wiley, 1983.

150) John J. W.; Watts, F. *An Introduction to Surface Analysis by XPS and AES*, John Wiley and Sons, 2003.

151) Moulder, J. F.; Chastain, J. *Handbook of X-ray Photoelectron Spectroscopy*, Physical Electronics, 1995.

152) Finklea, H. O.; Robert, A. (eds.) *Meyers Encyclopedia of Analytical Chemistry*, John Wiley & Sons Ltd, Chichester, 2000.

153) Skoog, D. A.; Holler, F. J.; Crouch, S. R. *Principles of Instrumental Analysis*, Thomson Brooks/Cole, 2007.

154) Sabatani, E.; Rubinstein, I. *J. Phys. Chem.* **1987**, *91*, 6663.

155) Johansson, T.; Mammo, W.; Svensson, M.; Andersson, M. R.; Inganas, O. *J. Mater. Chem.* **2003**, *13*, 1316.

156) Kelvin, L. *Phil. Mag. Ser. 5* **1898**, *46*, 82.

157) Subramanyam, A. *Kelvin Probe For Surface Engineering: Fund And Design*, Ane Books Pvt. Ltd., 2010.

158) Zisman, W. A. *Rev. Sci. Inst*. **1932**, *3*, 367.

159) Kao, K. C.; Hwang, W. *Electrical Transport in Solids: With Particular Reference to Organic Semiconductors*, Pergamon Press, 1981.

160) (a) Schmidt, W.; Baldridge, K. K.; Boatz, J. A.; Elbert, S. T.; Gordon, M. S.; Jensen, J. H.; Koseki, S.; Matsunaga, N.; Nguyen, K. A.; Su, J. S.; Windus, T. L.; Dupuis, M.; Montgomery, J. A. *J. Comput. Chem.* **1993**, *14*, 1347. (b) Jensen, F. *Introduction to Computational Chemistry,* John Wiley & Sons London, 2007.

161) Francl, M. M.; Petro, W. J.; Hehre, W. J.; Binkley, J. S.; Gordon, M. S.; De Frees, D. J.; Pople, J. A. *J. Chem. Phys.* **1982**, *77*, 3654.

162) Hariharan, P. C.; Pople, J. A. *Theor. Chim. Acta.* **1973**, *28*, 213.

163) Becke, A. D. *Phys. Rev A* **1988**, *38,* 3098.

164) Lee, C.; Yang, W.; Parr, R. G. *Phys. Rev. B* **1988**, *37*, 785.

165) Atomistix Tool Kit version 2011.11.2.3, Quantum Wise A/S (www.quantumwise.com).

166) Majumder, C.; Mizuseki, H.; Kawazoe Y. *J. Chem. Phys*. **2003**, *118*, 9809.

167) Stokbro, K.; Peterson, D. E.; Smidstrup, S.; Blom, A.; Ipsen, M. *Phys. Rev. B.* **2010**, *82*, 075420. **Chapter 3**

168) Holmlin, R. E.; Ismagilow, R. F.; Haag, R.; Mujica, V.; Ratner, M. A.; Rampi, M. A.; Whitesides, G. M. *Angew. Chem. Int. Ed*. **2001**, *40*, 2316.

169) Esaki, L. *Phys. Rev*. **1958**, *109*, 603.

170) (a) Seabaugh, C.; Kuo, Y.C.; Yuan, H. T. *IEEE Electron Dev. Lett*. **1992**, *13*, 479. (b) Chow, D. H.; Dunlap, H. L.; Williamson III, W.; Enquist, S.; Gilbert, B. K.; Subramaniam, S.; Lei, P.-M.; Bernstein, G. H. *IEEE Electron Dev. Lett*. **1996**, *17*, 69. (c) Inokawa, H.; Fujiwara, A.; Takahashi, Y. *Appl. Phys. Lett*. **2001**, *79*, 3618 (d) Yu, L. W.; Chen, K. J.; Song, J.; Wang, J. M.; Xu, J.; Li, W.; Huang, X. F. *Thin Solid Films* **2007**, *515*, 5466.

171) Han, W.; Durantini, E. N.; Moore, A. L.; Gust, D.; Rez, P.; Leatherman, G.; Sealey, G. R.; Tao, N. J.; Lindsay, S. M. *J. Phys. Chem. B* **1997**, *101*, 10719.

172) Tao, N. J. *Phys. Rev. Lett.* **1996**, *76*, 4066.

173) Duati, M.; Grave, C.; Tcbeborateva, N.; Wu, J.; Müllen, K.; Shaporenko, A.; Zharnikov, M.; Kriebel, J. K.; Whitesides, G. M.; Rampi, M. A. *Adv. Mater.* **2006**, *18*, 329.

174) (a) Mentovich, E. D.; Kalifa, I.; Tsukernik, A.; Caster, A.; Rosenberg-Shraga, N.; Marom, H.; Gozin, M.; Richter, S. *Small* **2008**, *4*, 55. (b) Pitters, J. L.; Wolkow, R. A. *Nano Lett*. **2006**, *6*, 390. (c) Guisinger, N. P.; Greene, M. E.; Basu, R.; Baluch, A. S.; Hersam, M. C. *Nano Lett*. **2004**, *4*, 55. (d) Salomon, A.; Yellin, R. A.; Shanzer, A.; Karton, A.; Cahen, D. *J. Am. Chem*. Soc. **2004**, *126*, 11648.

175) (a) Newton, M. D. *Chem. Rev.* **1991**, *91*, 767. (b) Davis, W. B.; Svec, W. A.; Ratner, M. A.; Waseliewski, M. R. *Nature* **1998**, *396*, 60. (c) James, D. K.; Tour, J. M. *Top. Curr. Chem.* **2005**, *257*, 33. (d) Simonian, N.; Li, J.; Likharev, K. *Nanotechnol*. **2007**, *18*, 424006.

176) Koiry, S. P.; Aswal, D. K.; Chauhan, A. K.; Saxena, V.; Nayak, S. K.; Gupta, S. K.; Yakhmi, J. V. *Chem. Phys. Lett*. **2008**, *453*, 68.

177) Sze, S. M. *Semiconductor Devices: Physics and Technology*, John Wiley and Sons, New York, 2002A.

178) Koiry, S. P.; Aswal, D. K.; Jousselme, B.; Majumdar, C.; Gupta, S. K.; Palacin, S.; Yakhmi, J. V. *Physica E* **2010**, *70*, 135.

179) Adler, A. D.; Longo, F. R.; Finarelli, J. D.; Goldmacher, J.; Assour, J.; Korsakoff, L. *J. Org. Chem.* **1967**, *32*, 476.

180) Rothemund, P. *J. Am. Chem. Soc.* **1936**, *58*, 625.

181) Sankaranarayanan, S.; Sharma, A.; Kulkarni, B. A.; Chattopadhyay, S. *J. Org. Chem.* **1995**, *60*, 4251.

182) Dunitz, J. D.; Taylor, R. *Chem. Eur. J.* **1997**, *3*, 89.

183) Thakur, T. S.; Kirchner, M. T.;Blaser, D.; Boese, R.; Desiraju, G. R. *Cryst. Eng. Commun*. **2010**, *12*, 2079.

184) (a) Williams, J. H. *Acc. Chem. Res*. **1993**, *26*, 593. (b) Dahl, T. *Acta. Chem. Scand*. **1994**, *48*, 95. (c) Meyer, E. A.; Castellano, R. K.; Diederich, F. *Angew. Chem. Int. Ed*. **2003**, *42*, 1210.

185) (a) Bacchi, S.; Benaglia, M.; Cozzi, F.; Demartin, F.; Filippini, G.; Gavezzotti, A. *Chem. Eur. J.* **2006**, *12*, 3538. (b) Cozzi, F.; Bacchi, S.; Filippini, G.; Pilati, T.; Gavezzotti, A. *Chem. Eur. J.* **2007**, *13*,7177. (c) Annunziata, R.; Benaglia, M.; Cozzi, F.; Mazzanti, A. *Chem. Eur. J.* **2009**, *15*, 4373.

186) (a) Taylor, J.; Guo, H.; Wang, J. *Phys. Rev. B.* **2001**, *63*, 245407. (b) Sieval, B.; Demirel, A. L.; Nissink, J. W. M.; Linford, M. R.; van der Maas, J. H.; de Jeu, W. H.; Zuilhof, H.; Sudhölter, E. J. R. *Langmuir* **1998,** *14*, 1759.

187) Metzger, R. M. *Acc. Chem. Res.* **1999**, *32*, 950.

188) Ulman, A. *An Introduction to Ultrathin Organic Flms: From Langmuir-Blodgett to Self- assembly*, Academic Press, Boston, 1991.

189) Schreiber, F. *Prog. Surf. Sci.* **2000,** *65*, 151.

190) Salomon, A.; Cahen, D.; Lindsay, S.; Tomfohr, J.; Engelkes, V. B.; Frisbie, C. D. *Adv. Mater*. **2003**, *15*, 1881. Electronic devise measurement.

191) Vuillaume, D.; Lenfant, S.; Guerini, D.; Delerue, C.; Petit, C.; Salace, G. *Pramana J. Phys*. **2006**, *1*, 17.

192) Metzger, R. M.; Panetta, C. A. *New J. Chem.* **1991**, *15*, 209.

193) Mallouk, T. E.; Lee, H. *J. Chem. Educ.* **1990**, *67*, 829.

194) Giraudeau, A.; Callot, H. J.; Jordan, J.; Ezhar, I.; Gross, M. *J. Am. Chem. Soc*. **1979**, *101*, 3857.

195) Hombrecher, H. K.; Gherdanm, V. M.; Ohm, S.; Cavaleiro, J. A. S.; Neves, M. G. P. M. S.; Condesso, M. F. *Tetrahedron* **1993**, *49*, 8569.

196) Momenteau, M.; Loock, B.; Bisagni, E.; and Rougee, M. *Can. J. Chem.* **1979**, *57*, 1804.

197) Callot, H. J.; Schaeffer, E.; Cromer, R.; Metz, F. *Tetrahedron* **1990**, *46*, 5253.

198) Gowda D.; Mahesh, B.; Shankare, G. *Ind. J. Chem. Sect. B* **2001**, *40*, 75.

199) (a) Petty, M. C.; Bryce, M. R.; Bloor, D.; Eds. *Introduction to Molecular Electronics*; Oxford University Press: New York, 1995. (b) Aviram, A.; Ratner, R. (eds.); *Molecular Electronics: Science and Technology, Ann. N. Y. Acad. Sci.* **1998**, *852*. (c) Alivisatos, A. P.; Barbara, P. F.; Castleman, A.W.; Chang, J.; Dixon, D. A.; Klein, M. L.; McLendon, G. L.; Miller, J. S.; Ratner, M. A.; Rossky, P. J.; Stupp, S. I.; Thompson, M. E. *Adv. Mater.* **1998**, *10*, 1297. (d) Cahen, D.; Hodes, G. *Adv. Mater.* **2002**, *14*, 789. (e) Aviram, A.; Ratner, R.; Mujica, V. (eds.); *Molecular Electronics II, Ann. N. Y. Acad. Sci.* **2002**, *960*.

200) Langhals, H. *Heterocycles* **1995**, *40*, 477.

201) Langhals, H.; Demmig, S.; Potrawa, T. *J. Prakt. Chem.* **1996**, *333*, 733.

202) Belfield, K. D.; Schafer, K. J.; Alexander, Jr., M. D. *Chem. Mater.* **2000**, *12*, 1184.

203) Wescott, L. D.; Mattern, D. L. *J. Org. Chem.* **2003**, *68*, 10058.

204) Martiny, A.; Sambles. J. R. *Nanotech.* **1996**, *7*, 401.

205) Brady, A. C.; Hodder, B.; Martin, A. S.; Sambles, J. R.; Ewels, C. P.; Jones, R.; Briddon, P. R.; Musa, A. M.; Panetta, C. A.; Mattern, D. L. *J. Mater. Chem.* **1999**, *9*, 2271.

206) Metzer, R. M. *Mat. Sci. Eng.* **1995**, *C3*, 277.

207) Rabe, J. P.; Buchholz, S. *Science* **1991**, *253*, 424.

208) Hentschke, R.; Schürmann, B. L.; Rabe, J. P. *J. Chem. Phys.* **1992**, *96*, 6213.

209) Wang, B.; Anslyn, E. V. (eds.), *Chemosensors: Principles, Strategies, and Applications*, John Wiley & Sons, Inc., 2011.

210) Biesaga, M.; Pyrynska, K.; Trojanoweiz, M. *Talanta* **2000**, *51*, 209.

211) Dunbar, A. D. F.; Richardson, T. H.; McNaughton, A. J.; Hutchinson, J.; Hunter, C. A. *J. Chem. Phys. B* **2006**, *110*, 16646.

212) Tepore, A.; Serra, A.; Manno, D.; Valli, L.; Micocci, G. *J. Appl. Phys.* **1998**, *84*, 1416.

213) Spadavecchia, J.;Ciccarella, G.;Siciliano, P.; Capone, S.; Rella, R. *Sens. Act. B* **2004**, *100*, 88.

214) Perez-Morales, M.; de Miguel, G.; Bolink, H. J.; Martin-Romero, M. T.; Camacho, L. *J. Mater. Chem.* **2009**, *19*, 4255.

215) Noh, Y.Y.; Kim, J. J.; Yase, K.; Nagamatsu, S. *Appl. Phys. Lett.* **2003**, *83*, 1243.

216) Wang, B.; Zuo, X.; Wu, Y.; Chen, Z.; He, C.; Duan, W. *Sens. Act. B.* **2011**, *152*, 191.

217) Micali, N.; Villari, V.; Castriciano, M. A.; Romeo, A.; Scolaro, L. M. *J. Phys. Chem. B* **2006**, *110*, 8289.

218) Garg, K.; Singh, A.; Debnath, A. K.; Nayak, S. K.; Chattopadhyay, S.; Aswal, D. K.; Hayakawa, Y.; Gupta, S. K.; Yakhmi, J. V. *Chem. Phys. Lett.* **2010**, *488*, 27.

219) Plater, M. J.; Aiken, S.; Bourhill, G. *Tetrahedron* **2002**, *12*, 2415.

220) Gould, R. D. *Coord. Chem. Rev.* **1996**, *156*, 237.

221) Samanta, S.; Singh, A.; Debnath, A. K.; Aswal, D. K.; Gupta, S. K.; Yakhmi, J. V.; Deshpande, S. K. *J. Appl. Phys.* **2008**, *104*, 073717.

222) Nikiforov, M. P. *Nano Lett.* **2008**, *8*, 110.

223) Debnath, A. K.; Samanta, S.; Singh, A.; Aswal, D. K.; Gupta, S. K.; Yakhmi, J. V. *Chem. Phys. Lett.* **2009**, *480*, 185.

224) Mahapatro, A. K.; Ghosh, S. *App. Phys. Lett.* **2002**, *80*, 4840.

225) Okada, S.; Segawa, H. *J. Am. Chem. Soc.* **2003**, *125*, 2792.

226) (a) Gao, Z. –X.; Li, H. –F.; Liu, J.; Lin, J. –M. *Anal. Chim. Acta* **2008**, *622*, 143. (b) Chu, X. F.; Cheng, Z. M. *Sens Act.* **2004**, *98*, 215. (c) Patil, D. R.; Patil, L. A. *Sens Act. B* **2007**, *123*, 546.

227) Wang, D.; Hu, P.; Xu, J.; Dong, X.; Pan, Q. *Sens. Act. B* **2009**, *140*, 383.

228) Belysheva, T. V.; Bogovtseva, L. P. *J. Anal. Chem*. **2006**, *61*, 494.

229) Lou, X.; Shi, D.; Liu, S.; Peng, C. *Sens. Act. B* **2007**, *123*, 114.

230) Xing-Hui, W.; Yu-De, W.; Yang-Feng, L.; Zhen-Li, Z. *Mater. Chem. Phys*. **2003**, *77*, 588.

231) IUPAC Recommendations.*Pure Appl. Chem.***1995**,*67*, pp. 1328.

232) Tongpool, R.; Yoria, S. *Thin Soild Films* **2005**, *477*, 148.

233) Sarno, D. M.; Matienzo, L. J.; Jones, W. E. *Inorg. Chem.* **2001**, *40*, 6308.

234) Moulder, J. F.; Stickle, W. F.; Sobol, P. E.; Bombson, K. D. *Handbook of X-ray Photoelectron Spectroscopy*, Physical Electronics Inc., Minnesota, 1995.

235) Limbach, H. H.; Hennig, J.; Stultz, J. *J. Chem. Phys.* **1983**, *78*, 5432.

236) Thomas, D. W.; Martell, A. E. *J. Am. Chem. Soc.* **1967**, *89*, 1992.

237) Timmer, B.; Olthuis, W.; van den Berg, A. *Sens. Act. B* **1994**, *107*, 666.

238) Kearney, D. J.; Hubbard, T.; Putnam, D. *Dig. Dis. Sci.* **2002**, *47*, 2523.

239) Zeng, Y.; Lou, Z.; Wang, L.; Zou, B.; Zhang, T.; Zheng, W.; Zou, G. *Sens. Act. B* **2011**, *156*, 395.

240) Saroch, M.; Srivastava, S.; Fink, D.; Chandra, A. *Sensors* **2008**, *8*, 6355.

241) Stamenov, P.; Madathil, R.; Coey, J. M. D. *Sens. Act. B* **2012**, *161*, 989.

242) Gong, J.; Li, Y.; Hu, Z.; Zhou, Z.; Deng, Y. *J. Phys. Chem. C* **2010**, *114*, 9970.

243) Ma, X.; Sun, J.; Wang, M.; Hu, M.; Li, G.; Chen, H.; Huang, J. *Sens. Act. B* **2006**, *114*, 1035.

244) Arnold, D. P.; Manno, D.; Micocci, G.; Serra, A.; Tepore, A.; Valli, L. *Langmuir* **1997**, *13*, 5951.

245) Misra, S. C. K.; Mathur, P.; Yadav, M.; Tiwari, M. K.; Garg, S. C.; Tripathi, P. *Polymer* **2004**, *45*, 8623.

246) Jiang, D. P.; Lu, A. D.; Li, Y. J.; Pang, X. M.; Hua, Y. L. *Thin Solid Films* **1991**, *199*, 173.

247) Wright, J. D. *Prog. Surf. Sci.* **1989**, *31*, 1

248) Huang, Y.; Fu, L.; Zou, W.; Zhang, F.; Wei, Z. *J. Phy. Chem. C.* **2011**, *115*, 10399.

249) Kong, H.; Jung, B. J.; Sinha, J.; Katz, H. E. *Chem. Mater.* **2012**, *24*, 2621.

250) Wang, B.; Chen, Z.; Zuo, X.; Wu, Y.; He, C.; Wang, X.; Li, Z. *Sens. Act. B* **2011**, *160*, 1.